Study of Electrical Strength and Lifetimes of Polymeric Insulation for DC Applications

A thesis submitted to The University of Manchester for the Degree of

Doctor of Philosophy

In the Faculty of Engineering and Physical Sciences

2016

Ibrahim Iddrissu

School of Electrical and Electronic Engineering

Table of Contents

Word count: ~ 64,000

List of Figures

List of Tables

Abstract

Polymeric insulating materials are being re-evaluated in the context of the re-emergence of HVDC and its advantages in bulk power transfer over long distances. This has been met with new sets of requirement such as; the use of polymeric insulation, compaction of HV equipment (e.g. HV cables), and innovations in converter technology. This equipment requires high power rating and hence will be exposed to high electric stresses. One of the properties of polymeric DC insulation is its ability to retain injected charges at high DC fields leading to local field modification and subsequent breakdown of the insulation through electrical treeing. Electrical treeing is one of the important failure mechanisms of solid polymeric insulations resulting from high voltage stresses and a precursor to failure of electrical equipment. Hence, the performance and reliability of polymeric insulation designs will be affected by electrical treeing. Literature shows that electrical trees initiate easily with switching voltages such as impulses, voltage surges and reversal of power flow direction. Innovations in converter technology employs fast switching devices such as insulated gated bipolar transistors (IGBTs) which generates substantial amount of harmonics and may also impact insulation systems reliability.

This research investigates the reliability of epoxy resin (LH/HY 5052) for suitability in HVDC applications due to its excellent properties as jointing compound in medium and high voltage cables systems. The development of test facilities for short term breakdown strength, space charge measurement and electrical treeing experiment have allowed short term breakdown strength on homogeneous layers of thin epoxy-epoxy samples and long term breakdown through electrical treeing under DC, AC and AC superimposed on DC to be investigated so that an understanding of the link between space charge, material strength and life times can be clarified.

The results on short term breakdown showed the layered samples have 6% reduction in strength compared to un-layered samples. For long term treeing test, 100% of the samples stressed with negative DC did not fail while 67% of the sample stressed with positive DC failed with average lifetime of 250 minutes. Samples stressed under AC showed forward and reverse directions of tree growth with average lifetime of 143 minutes from 70% failed samples. For AC superimposed on ±DC all samples failed

with average lifetimes of 54 and 78 minutes for positive and negative bias tests, respectively.

It is concluded that, the differences in lifetime obtained under positive and negative pure DC tests and that of the positive and negative DC bias tests are associated with space charge causing field relief under negative DC and negative bias tests. The huge reduction in lifetimes under AC superimposed on DC as ripples tests highlights the potential threat of power quality issues on the reliability of DC systems. Electrical tree growth from the ground planer electrode (reverse tree) observed under AC test was associated with relatively low voltage under AC test compared with the other tests see Table 8-1 for test voltages employed.

Declaration

No portion of the work referred to in this thesis has been submitted in support of an application for another degree or qualification of this or any other university or institute of learning.

Copyright statement

The author of this thesis (including any appendices and/or schedules to this thesis) owns certain copyright or related rights in it (the "Copyright") and s/he has given The University of Manchester certain rights to use such Copyright, including for administrative purposes.

Copies of this thesis, either in full or in extracts and whether in hard or electronic copy, may be made only in accordance with the Copyright, Designs and Patents Act 1988 (as amended) and regulations issued under it or, where appropriate, in accordance with licensing agreements which the University has from time to time. This page must form part of any such copies made.

The ownership of certain Copyright, patents, designs, trademarks and other intellectual property (the "Intellectual Property") and any reproductions of copyright works in the thesis, for example graphs and tables ("Reproductions"), which may be described in this thesis, may not be owned by the author and may be owned by third parties. Such Intellectual Property and Reproductions cannot and must not be made available for use without the prior written permission of the owner(s) of the relevant Intellectual Property and/or Reproductions.

Further information on the conditions under which disclosure, publication and commercialisation of this thesis, the Copyright and any Intellectual Property and/or Reproductions described in it may take place is available in the University IP Policy[1], in any relevant Thesis restriction declarations deposited in the University Library, The University Library's regulations[2] and in The University's policy on presentation of Theses

---

[1] See http://www.campus.manchester.ac.uk/medialibrary/policies/intellectual-property.pdf
[2] See http://www.manchester.ac.uk/library/aboutus/regulations

Acknowledgement

Firstly I would want to thank Almighty Allah (God) for granting me, my family and everyone involved in this project good health throughout this journey.

Secondly I would like to thank my supervisor Professor Simon Rowland for his guidance, support, encouragement, patience and zeal for research as well as my personal development. I am privileged to have you as my supervisor, thank you Simon! To Dr. Antonios Tzimas thank you for introducing me to the Pulsed Electro-Acoustic Technique during your time with us in the department.

Many thanks to all the people at the Mechanical and Electronic Workshop in the School of Electrical and Electronic Engineering for assisting in the development of my experimental work. To our Safety and Laboratories manager Mr. Frank Hogan and his team I say thank you for the day to day support and help in the laboratory. To all the academics/staff and my colleagues at the Ferranti Building thanks for your help in various forms. You made this journey an enjoyable one. Thank you all. To Dr. Roger Schurch and Dr. Qi Li thanks for help with the family. Amina, Sabir and Humu say thank you.

 A special thanks to Dr. Amidu Mohammed and Chief Issaka for visiting all the way from Ghana. To Uncle Imran, thanks for checking up on me on weekly basis.

To my father Alhaji Iddrissu Mohammed (RIPP); it was your last words "go to school" that kept me going thank you Dad. To my uncle Alhaji Sadik Hussien (RIPP) thank you for supporting my educational needs with eagerness without which I would not have reached this far.

Finally and most especially, I would like to thank my wife Humu K. Rufai for her encouragement throughout this journey. Your input with the kids at home is more demanding than mine at the University. This is for you as well as me. To Amina and Sabir I hope you will grow and achieve more than me and thank you for your understanding.

Dedicated to my father: Alhaji Iddrissu Mohammed

1. Introduction

1.1 Top and Tail

"Transformation of the Top and Tail of Energy Networks" more commonly known as "Top and Tail" was a collaborative project consisting of 8 Universities including the University of Manchester and funded by The Engineering and Physical Sciences Research Council (EPSRC) UK [1]. The overall aim of "Top and Tail" is to develop the technologies to transform physical infrastructure in energy networks, required to move the UK to a low carbon economy, and achieve the Government's target in CO_2 emission to 80% of the 1990's level by 2050. The two areas in the existing energy networks that require radical change have been identified as:

1. The "Top of the network" where the highest transmission voltages occur. A radical innovation in converter technology and the need to increase cable capacity is urgently needed in order to take advantage of diversity in renewable sources to enable power exchange between UK, Europe and elsewhere and also to meet the demands in diversity of loads.

2. The "Tail of the network", where the low voltage distribution assets exists, including behind-the-meter wiring into consumer premises. There is a need to re-engineer the existing assets in response to energy consumption behaviour without digging up buried cables and pipes in the ground.

This study is at the top of the "Top and Tail" project and is part of the work package 1.3, which envisages HVDC cable transmission links of the order of 20 GW. In response to this, work package 1.3.1 is looking into the possibilities of developing HVDC cable and converter technology of ratings up to 1 MV/5 kA, and this study is focused on polymeric insulating material for HVDC use.

1.2 Overview of HVDV transmission

The re-emergence of high voltage direct current (HVDC) can be traced back to 1954 when the first commercial submarine cable, (100 km/20MW±100 kV) using mercury arc converter stations was installed between the Swedish mainland and island of Gotland [2].

Even though HVDC technology has been in existence since 1882 [3], the progress in HVDC technology has been slow due to cost of converter stations and technological

barriers such as low power rating of converters and inability to efficiently reduce voltage levels using DC-to-DC converters [2]. On the other hand, the ability to use transformers to efficiently step voltages up and down with minimal losses, has resulted in the worldwide embrace of AC power transmission systems [4]. Thus, to date, most of the power system grid all around the world is interconnected with AC systems, and DC is only employed where the use of AC system is not feasible such as water crossings, bulk power transfer over long distances and connection of unsynchronised AC systems [2].

Recent advances in converter technology and competition in the market place have resulted in increased power rating of converters with decreased cost of installation. The low cost/high power rating in converter technology, together with government policies to reduce CO_2 emission by encouraging green and clean energy generation and transmission lead to increase in HVDC projects installation around the world. These are mostly point to point connection. In the UK for example, apart from the existing HVDC links: BritNed 1000MW/260km, Moyle Interconnector 2x250MW/64km and England-France Interconnector (IFA) 2000MW/73km, several transmission reinforcement strategies have been proposed, with some under construction in an anticipation to meet the government target of 15% of energy demand coming from renewable sources by 2020 [5]. Most of these interconnectors are either underground cable or subsea cables. An example of a reinforcement projects is the western link project between Scotland and Wales with power rating of 2200MW/422 km long scheduled for 2016 completion. Several others documented in [5].

1.3 **Current trends in HVDC transmission cables**

HVDC transmission is the economical and technically viable means of bulk power transfer over long distances compared to HVAC where the distance of transmission is limited by the coaxial capacitance in cables [2]. HVDC transmission can be accomplished by using overhead lines and underground cables (mainland transmission) or submarine cables for sea crossing. Usually, at the transmission voltages, overhead lines are employed due to their lower cost compared to underground cables which are mostly used in the distribution network. Even though HVDC overhead lines require narrower transmission corridors compared to HVAC, in general acquiring permit for overhead lines is difficult as compared to

underground cables especially in crowded cities due to their visual and environmental impact.

Traditionally paper insulation impregnated with oil has been employed for HVDC cable insulation, and they prove to be very reliable with good service records. However, manufacturing processes and maintenance of these cable types are expensive compared to extruded cables. As such, extruded cables are now considered as a potential alternative for HVDC due to their excellent physical, thermal and electrical properties. Extruded cables have been used successfully for HVAC transmission up to 500 kV [6]. However, under DC transmission, there are some drawbacks which are due to space charge accumulation in polymeric dielectrics [7].

1.4 Limitation of Extruded HVDC cable

1.4.1 Effect of space charge

A significant issue with the use of polymeric insulating material for HVDC application is its ability to trap electrical charges at structural discontinuities [8-9]. These trapped charges (space charge) are the net localised charges present in the bulk of an insulating material which may be coming from electrode injection or from dissociation of ionic impurities in the bulk of the insulating material [10]. These space charges whether trapped or mobile can cause local field enhancement, and on energised loaded cables leads to field inversion and accelerated ageing resulting in failure [8, 10-11].

Unlike under AC where the frequency of the applied voltage is too quick (40 ms every half-cycle of the applied waveform) to allow enough time for space charge to accumulate in the insulation, as shown by Takada in [12], for measurement of space charge at frequency range of 0.0002 Hz to 50 Hz. Under DC stress, space charge will slowly build up locally due to the constant direction of electric field and may increase throughout the polymeric insulation lifetime [8,10]. Electric field distribution in DC insulation is non-uniform and depends on the conductivity (resistivity) and temperature due to space charge build-up [10-11]. This situation is very serious on polarity reversals due to field inversion causing higher field at the vicinity of the conductor than the outer screen as shown in [11]. The issues with space charge has brought into question of using the recommended DC voltages [13],

on routine diagnostic test on AC power cables due to pre-mature failures experienced by utilities on 5 kV to 35 kV extruded power cables which is believed to be caused by space charge accumulation [12].Thus an alternative on-site test technique using very low frequency (VLF) 0.1 Hz which require further clarification on frequency dependency on space charge has been adopted [12-14]. It is evident from above that space charge is a big issue with regard to the use of polymeric insulation for HVDC application. It is reported in [9] that an ideal dielectric insulation for HVDC cable should possess the following properties:

- High DC breakdown strength, particularly under superimposed impulse conditions.

- Stable insulation resistance that does not change in the presence of an electric field or thermal gradient.

- Low space charge retention properties.

- Low thermal resistance.

However, no single material has been identified so far to possess all these properties [9]. It is summarised in [8] that the success of mass impregnated paper insulation under applied DC field compared to polymeric insulation is that, the accumulated charge in polymeric insulating material takes much longer time to dissipate than in mass impregnated paper insulation on removal of the applied field. This is the main limitation of the use of polymeric insulating cables for HVDC transmission compared to HVAC transmission as discussed above.

1.4.2   Converter technology and power quality

Another drawback of the use of polymeric insulation for HVDC application is the converter technology barrier at higher voltages. Converters are required at the sending (rectification) and the receiving (inversion) ends of DC link as shown in Figure 1-1.
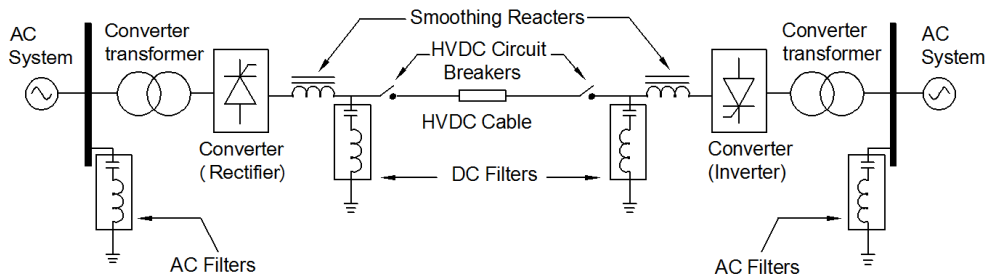
Figure 1-1: Typical HVDC system [2].

The proven technology for converter stations is the traditional line commutated converters (LCC) which have so far been used up to ± 800 kV on mass impregnated paper insulated cables [15]. To reverse power flow direction using LCC converter, the polarity of the voltage needs to be reversed. This is one of the main operations of DC transmission and this will present a threat to cable insulation if not well managed due to space charge injection, especially where polymeric insulation is employed. An example of this threat was experienced in the early 1970's in Japan when a project which was intended to use cross-linked polyethylene (XLPE) cable for DC transmission between Hokkaido and Honshu was abandoned due to the effect of space charge during pre-installation tests [7]. This project was later completed by using the traditional oil-filled cable in 1978.

Recent voltage source converter (VSC) technology eliminates the need to reverse voltage polarity to achieve reversed power flow direction. However, VSC technology, which employs insulated gated bipolar transistor (IGBT) devices, has a lower voltage rating compared to LCC which uses thyristors. The world's first extruded cable HVDC link was installed in 1999 on the island of Gotland and has voltage rating of ± 100 kV, 50 MW [16]. Since then, a lot of progress in voltage VSC technology has been made and voltage rating is now available up to ± 500 kV. The highest rating of a VSC HVDC link installed so far is the 500 kV/715MW for the Skagerrak 4 project between Norway and Denmark awarded to ABB in 2011 [15]. These advances in voltage ratings of converter stations, together with a breakthrough in HVDC circuit breakers capable of interrupting short circuit current up to 16 kA within 5 milliseconds [17], has eliminated most of the barriers of HVDC transmission and resulted in increased installation of HVDC projects around the

world. Thus the use of polymeric insulation for cables at higher voltages requires more investigation.

Converters produce substantial amount of harmonics from the fast switching operation of the semiconductor devices employed in both LCC and VSC. It is known that harmonics cause voltage distortions which impact power quality with consequential effect on cable insulation. Thus costly filters are installed on both the AC and DC sides of the converter to reduce voltage distortion and other interference (such as from telephony) [2] [18] as shown in Figure 1-1. Power quality will influence insulation ageing and the key question is "how do we know the role the various disturbances play in ageing and failure processes of this insulation?" [19]. Electrical insulation is one of the extensively researched areas of HV electrical equipment because it is one of the vulnerable parts of the overall system. As a result, insulation design is usually based on wide margin of safety a situation dubbed as "the factor of ignorance" by Miner [20]. The move toward HVDC transmission and the quest for more compact and reliable equipment means electrical insulation is going to be exposed to higher electrical fields than before [21].

Electrical treeing is one of the important mechanism that cause failure of insulation of high voltage electrical equipment such as cables, electrical machines, switchgear and transformers bushings and is a major concern to the electrical generation, transmission and distribution industries [22-23]. Treeing is the name given to the type of long term progressive damage through a dielectric insulation section under electrical stress, so that, if visible, its path looks something like a tree [24]. Generally treeing is more associated with AC or impulse voltages [24], but it is reported to have been observed under high DC voltage stress under wet experimental condition in [24].

This means more research is needed to better understand and improve insulation design for more compact and reliable HVDC links.

This study looks at how various high electrical stresses (AC, DC and composite AC and DC) affect ageing of polymeric insulation in relation to electrical tree growth resistance, electric breakdown strength, and vulnerability to charge injection at interfaces.

1.5 **Research aim and objectives**

The main aim of this research is to develop understanding of the potential issues of using solid Polymeric insulating material for HVDC application, and in particular, the response of the material to high DC electric stress. The specific objectives are to investigate:

- The electric strength of thin homogeneous layers of polymeric (epoxy resin) insulating material.
- The vulnerability of polymeric insulating material to charge accumulation at layer interfaces under DC field.
- The nature of electrical tree growth and their contribution to failure in solid polymer samples exposed to AC and DC fields.
- The use of combined AC and DC fields to investigate how a superimposed AC component (noise) on DC impacts electrical tree growth.

The outcome of this research will report on the electric performance of the studied polymer samples, under various electric stress conditions which is hoped will ultimately lead to increased knowledge of reliability and design of solid polymeric insulation for HVDC application.

1.6 **Overview of methodology**

Epoxy resin was used in this research due to its range of properties which makes it suitable for use as an insulating material in HV electrical equipment. Its transparency and ease of moulding into different shapes makes it one of the materials normally used for experimental work where imaging and sample fabrication is required.

Sample preparation: Reproducibility of experiments will always depend on how well the samples under test were fabricated. In this study, a lot of effort has been made to standardise the sample fabrication procedure as much as possible. The procedure for sample fabrication for this study is reported in chapter 3. Two sample types were fabricated using epoxy resin. For short-term breakdown and space charge measurement, thin films of epoxy up to about 250 μm were fabricated, while for electrical tree growth investigation, the traditional point-to-plane sample configuration was used.

Electric strength: A test cell was designed and developed to investigate short-term breakdown tests on fabricated thin/layered samples. Test was performed under

AC/50 Hz and DC (positive and negative polarity) to compare the performance of single-layer and layered thin samples. Chapter 4 reports the development of the experimental set up and outcome of test results.

Space charge measurement: It is often the case that interfaces are locations for charge accumulation leading to local field enhancement and material degradation. The pulsed electro-acoustic method of charge measurement has been developed to investigate charge dynamics in thin layered samples and is reported in chapter 5.

Electrical treeing: A new system has been developed capable of simultaneously monitoring electrical tree growth through image capture and partial discharge measurement. Electrical trees were grown by applying either AC voltage at 50 Hz, DC, or AC superimposed on either positive or negative DC voltages. The development of the experiment is reported in Chapter 6.

1.7 Main contributions

This research project yielded the following achievements:

- Three experimental systems were successfully designed, built and operated which facilitate means of dielectric material ageing, monitoring and lifetimes investigations under AC, DC and composite waveforms

- Successful and well control method sample preparation was developed resulting in consistency of obtained experimental results.

- Electrical tree was successfully grown under DC with repeatable results.

- Capturing of electrical tree growth from counter electrode (reverse tree) repeatedly has resulted in the 5 stage model of tree growth proposed in this study.

1.8 Outline of the thesis

This thesis consists of ten chapters:

- **Chapter 1:** Introduces the overall Top and Tail project, its aim and objectives and where this study fits.

- **Chapter 2**: Presents background knowledge on polymeric insulating materials. Literature reviews on ageing mechanism and breakdown processes of solid polymer insulation is presented.

- **Chapter 3:** The procedure developed for consistent sample preparation is reported for both planar and point to plane samples

- **Chapter 4:** Reports on the development of a system and measurement procedure for short-term breakdown tests on thin layered and un-layered epoxy resin samples of about ~200 μm.

- **Chapter 5:** The system developed for measurement of space charge on planer samples using the pulsed-electro acoustic technique together with measurement results is presented.

- **Chapter 6:** Development of a system for long-term breakdown tests which incorporates simultaneous imaging and partial discharge measurement is reported.

- **Chapter 7:** This chapter presents preliminary tests on treeing degradation and partial discharge measurements before a protocol for further testing is outlined.

- **Chapter 8:** This chapter presents a protocol adopted for treeing tests under various voltage regimes.

- **Chapter 9:** Results on the treeing tests and partial discharge measurement is presented in this chapter.

- **Chapter 10:** Discussions on the test results is presented, from which conclusions from this study was drawn and areas identified for future work proposed.

2. Background knowledge

2.1 **Introduction**

In this chapter, background knowledge of polymeric insulating materials and their electrical properties are discussed. References are made to polymeric insulating materials in general such as polyethylene (PE), cross-linked polyethylene (XLPE) and epoxy resins as they are the polymeric insulating materials most frequently used in HV equipment. Epoxy resin is the material used in this study, and where necessary it will have more emphasis.

2.2 **Polymeric insulating materials**

Increased use of polymeric insulations for insulating high voltage equipment is a testimony to their excellent physical, chemical and electrical properties [25-26]. These materials have been used in applications such as power cables, transformers and rotating machines as a result of these excellent properties. However, their complex nature also presents new sets of challenges with regard to charge injection, trapping/transport and storage especially at high voltages where contact with other materials is inevitable. Thus understanding their properties is essential to the performance and reliability of HV equipment in which they are employed.

2.2.1 Polyethylene

Polyethylene is one of the most studied polymeric insulating materials. It consists of long-chain of macromolecules with a repeating base unit called ethylene (C_2H_4) from which polyethylene ($C_2H_4)_n$, is derived, where n is the degree of polymerisation [8] [27]. Branching of the main polymer backbone (linkage along the length of the polymer) influences physical properties, because it reduces the potential for regular molecular packing leading to smaller crystalline regions and more amorphous regions which in turn lowers the material density [8]. This can present trapping sites for charges injected at high fields, leading to ageing processes [8]. For example, different types of polymer with varying degrees of densities can be produced by controlling the branching of the back bone of polyethylene resulting in materials such as; linear low density polyethylene (LLDPE), low density polyethylene, (LDPE) and high density polyethylene (HDPE). HDPE exhibits higher mechanical

strength than its corresponding counterparts (LLDPE and LDPE). Also the physical and chemical properties of polyethylene can be modified by a process called cross-linking which result in a thermosetting material called crosslinked polyethylene (XLPE) with superior electrical properties [8].

2.2.2 Epoxy resin

Epoxy resins are a group of thermosetting polymers in which two components (the resins and the hardener) are mixed to form an end product with superior electrical properties for high-voltage electrical insulation [28]. Curing or hardening of an epoxy resin is the process by which a curing agent or hardener is mixed with the resin to convert the compounds into a thermoset form. The action of the curing agents is to open and join into the epoxide rings to form a strong covalent bond, and it is in this form that the resins are mostly used [26, 28]. Epoxy resins have a time after mixing within which it must be applied to the job concerned called the "pot life". The pot life is the time taken from the initial mixing of the resin and the hardener to the point when the viscosity of the material is so high that if not applied to the intended job it render the mixture useless [26].

2.2.3 Properties of epoxy

Epoxy resins can be cured both at room temperature and at higher temperatures when required. Cured epoxies are mechanically strong and, usually among the polymeric insulating materials, are able to withstand long-term exposure to temperatures of the orders 210-260 °C [26]. For example only 1.08% weight loss was observed when cast epoxy system was kept at 210 °C for 500 h and a 9.20% weight loss after 200 h at 260 °C [26]. Table 2-1 shows the maximum operating temperatures of some polymers.

Table 2-1: Maximum operating temperatures for some polymers [26].

Plastic	Temperature [°C]
Phenolic moulding materials	150-250
Epoxy casting	50-260
PTFE	260
Polypropylene	120
Polycarbonate	120
Rigid PVC	90-100
Nylon 66	90
Polysterene	65-85
Polyurethane	88

This property makes epoxy resins find use in many electrical applications such as rotating machines, distribution switchgear, transformers, cable jointing, printed circuit boards, bushings, encapsulation of electronic devices as well as indoor/outdoor insulators.

To improve their properties further and reduce cost, most epoxy insulation systems are filled with micro-particulate inorganic materials. Most commonly used is silicon oxide (silica), which prevents chemical reaction on the material surfaces. Aluminium trihydrate is also used as flame retardant and anti-tracking filler because it degrades endothermically at elevated temperatures. Inorganic fillers are also used to improve thermal, mechanical and electrical properties. Aluminium oxide (alumina) for example is used to improve thermal conductivity of epoxy resin components [29]. Some of the properties which recommend epoxy resins for use in HV electrical applications are [26]:

- The ability to cure with negligible shrinkage and absence of volatiles.
- High mechanical strength, which is retained at elevated temperatures.
- High dielectric strength, volume and surface resistivity.
- High resistance to chemical and atmospheric attack and to absorption of water.
- High heat resistance and dimensional stability.
- Good adhesion to metals, glass, porcelain, rubber and other materials.

2.2.4 Amorphous and crystalline polymers

Most polymers are amorphous above their melting temperature, where irregular packing of molecular chains is observed, and crystalline below their glass transition temperature where orderly packing of the molecular chains is observed. Polymers may contain both amorphous and crystalline regions for example PE and PP. The amorphous (low density) and crystalline (high density) regions can act as traps for electrons and holes leading to increase in local space charge concentration which may influence the electrical properties of the polymer [8]. Figure 2-1 (A) and (B) schematically shows crystalline and amorphous regions in polyethylene [27].
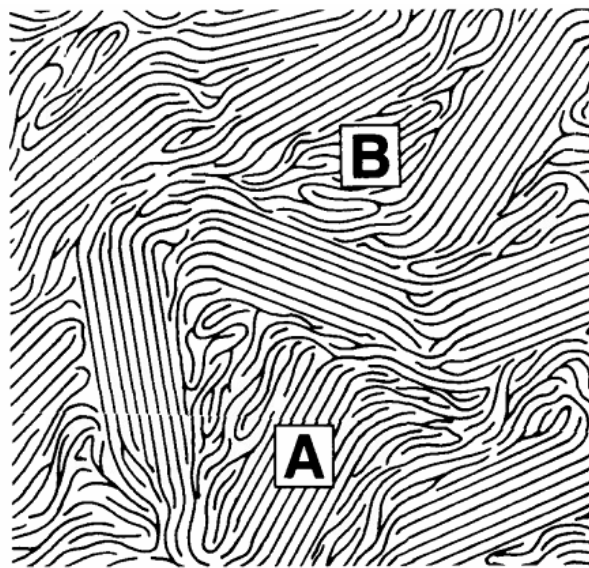
Figure 2-1: Schematic of: (A) crystalline and (B) amorphous regions in polyethylene [27]

2.2.5 Glass transition temperature

A glass transition temperature (T_g) is a temperature above which polymers are rubbery and below which they exhibit a glassy state as shown in Figure 2-2. A semi-crystalline polymer will have a sudden change in specific volume when it is cooled from its liquid state through the melting temperature, which is an indication of closer regular packing of molecules into crystalline structures. For amorphous polymers, the change in specific volume is gradual and there is no observable melting temperature until the glass transition temperature is reached. Also in the region between the glass transition temperature and melting temperature, both amorphous and semi-crystalline polymers are mechanically rubbery. They exhibit continuous

decrease in specific volume at a slower rate below the glass transition temperature [8].
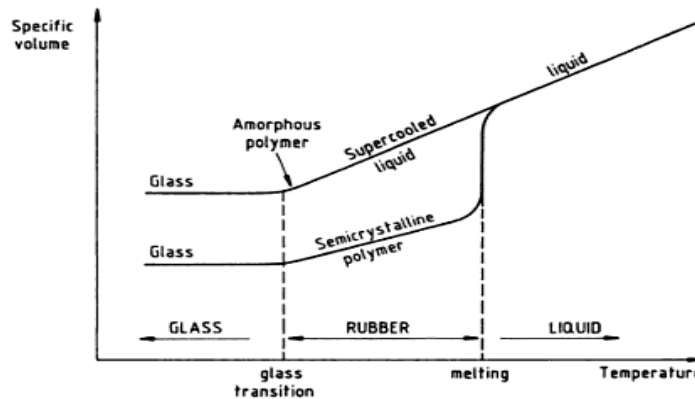
Figure 2-2: A schematic diagram showing the variation of specific volume with temperature for an amorphous and a semi-crystalline polymer [8]

2.3 **Response of a polymer dielectric to an electric field**

The response of a dielectric to an applied electric field is defined as their electrical properties [30-31]. Ku and Leipins [30], summarised these responses into two main parts: firstly as dielectric properties and secondly as bulk conductive properties. They listed four fundamental parameters characterising both the dielectric and bulk conductive properties as:

- Dielectric constant; representing polarisation or movement of bound charges.

- Tangent of dielectric loss angle; representing relaxation phenomena or energy conversion/loss.

- Dielectric strength; representing breakdown phenomena

- Conductivity; representing electrical conduction (movement of non-localised charges).

These fundamental properties form the basis of understanding the extent to which dielectrics respond to an applied electric field. Dielectrics are employed in various electrical and electronic applications where they perform different functions. Examples are electrical energy storage as in capacitors, or insulating electrical parts as in cables.

A simple parallel plate capacitor as shown in Figure 2-3 is considered. At low fields when a voltage is applied across its plates, charge build up is realised on the plates in response to the applied field due to various types of polarisation (electronic, atomic and molecular) of the bound charges which depend on whether the material between the plates is polar or non-polar.
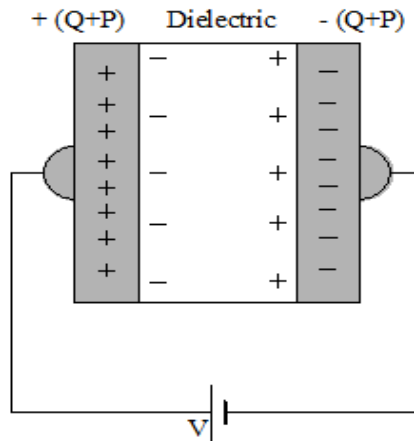
Figure 2-3: A simple parallel plate capacitor with dielectric between its plates.

Two important equations representing polarisation shown as equations (2.1) and (2.2) can be derived (see [30-31] for more details) as:

$$P = \varepsilon_o E(\varepsilon - 1) \qquad\qquad (2.1)$$

$$P = n\alpha E_L \qquad\qquad (2.2)$$

Where:

P; is the various polarisations in the material (electronic, atomic or molecular).

E; is the applied electric field.

$\varepsilon_o\varepsilon$; is the absolute permittivity and ε is the dielectric constant.

E_L; is the local electric field including from the various polarisations.

α; is the polarizability defined as the average molecular polarised dipole moment produced under action of an electric field and

n; is the number of contributing elementary entities per unit volume of the dielectrics.

Equations (2.1) and (2.2) give two alternative expressions for polarisation and together they permit polarisability (α) and dielectric constant (ε) to be related. The dielectric constant ε is a macroscopic quantity, whereas polarisability α is a microscopic quantity, which is related to the molecular structure of the dielectrics. Thus the field acting on individual polarisable entity such as atom or molecule in the material, results in the local field (E_L) modification and it differs from point to point as the dielectric material is not homogeneous. It is the response of the atoms and molecules in the dielectric material to the applied field which serve an important concept of linking observable bulk behaviour to microscopic material properties [30] [31].

2.4 **Charge injection and transport**

Charge injection and transport depends on the nature of material interfaces such as electrode-insulator or insulator-insulator contacts. Lewis (1989), reviewed the nature of these interfaces and of charge transfer between them in [32], while Ditchi et al (1989) study the influence of the composition of insulating resins and that of the electrodes at the interfaces using pressure wave propagation [33]. Ditchi et-al [33] observed that according to the chosen combinations of the resins and the electrodes, either charge transfer can occur at the interfaces, or transfer of ionisable impurities from the polymer can occur. They concluded that impurities contained in the insulating resin or diffusing from the electrodes into the insulator may be the origin of space charge build-up, or dipole orientation [33].

The two possible processes involving electron or hole injection from the electrode into the insulation at high fields are examined in details in [8, 31-32, 34] and are briefly described below as:

- Schottky injection; where electron/holes possess enough thermal energy to overcome the energy barrier and hop from one site to another. The ability to hop depends on the shape and site separation (barrier width) as well as the work function of the electrode-insulator interface.

- The Fowler-Nordheim effect; where electron/holes are able to tunnel through the barrier at high fields instead of hopping over due to reduction of the site separation (barrier width) by the applied field.

In general, it is felt that these processes are more likely at the p-n junctions in semiconductor devices than at real interfaces in the dielectric situation. Figure 2-4 shows the diagram of electron-transfer between adjacent sites separated by a potential barrier describing the charge transfer mechanisms discussed above. For tunnelling to occur, the separation between site 1 and site 2 for the approaching electron should be sufficiently thin (~ < 10 nm) otherwise it will be reflected back according to quantum mechanics [8].
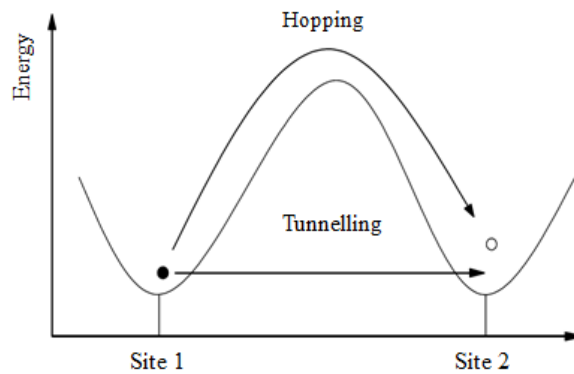
Figure 2-4: A simplified representation charge transfer mechanism [31]

2.4.1 Charge traps

The application of the band theory to solid dielectrics predicts a large energy band-gap (E_g) between the valence and the conduction band in insulators and ideally no conduction species (electrons/holes) should be present in the energy gap (i.e. in a perfect insulator). However, localised energy states for both electrons and holes called charge traps are formed within this energy gap due to the imperfect and complex nature of polymer morphology, which allow charge movement within the insulator via hopping or tunnelling effects. The depth of a trap depends on the energy required to release the charge from the trap site and is related to the affinity with which the charge is bound [35].

2.4.2 Electric conduction in polymeric insulating materials

Ideally, electrical insulating materials should prevent electrical conduction under any conditions of use. However, low-level conduction is often inevitable at high fields as no known insulator is completely free of conduction processes no matter how small

the quantity of charge carriers it may possess [30-31]. At sufficiently high fields (E_{high}), insulators may behave as semiconductors, and conduction species such as electrons (n_e), holes (p_e) or ions if present will drift, resulting in a current (J) flow as shown by equations (2.3) and (2.4) where: σ is the conductivity, and μ_n and μ_p are the respective electrons and holes mobilities [36].

$$J = \sigma \, E_{high} \qquad\qquad (2.3)$$

$$\sigma = ne\mu_n + pe\mu_p \qquad\qquad (2.4)$$

Insulators are wide band-gap materials, having energy gap (E_g) of several electron volts (eV) between the valence band and the conduction band [8]. This means that electrons must possess a lot of energy to be able to surmount this energy gap to become available for electrical conduction if present. The band theorem has been used to explain how this conduction process may be possible in insulators see [8, 31]. However, the morphology of an insulating polymers are so complex that the band theory can only be applied to it based on assumptions which many suggest may not be appropriate.

The conductivity of a practical electrical insulating material should be very low, such that the flow of current within it can be ignored completely. For this to happen, an insulating material should be able to confine the flow of current within a well-defined path (i.e. a conductor) and to prevent its leakage through the insulator [20]. At high voltages these conditions can only be met if a solid insulating material possesses the following properties [28, 30]:

- High resistivity.

- High dielectric strength and low dielectric loss.

- High mechanical strength and stiffness.

- Free of gaseous inclusions and moisture.

- Resistant to thermal, chemical deterioration.

- Resistant to water penetration.

- Ability to withstand high temperatures during service.

Inability to meet these properties could result in a current flow leading to ageing processes which will eventually compromise the reliability of the insulation.

2.5 **Ageing degradation and breakdown**

Kelen [37], defined ageing as a change to material property owing to the action of several ageing factors when exposed to the service environment. Densely [38], on the other hand, listed ageing factors under the headings *thermal*, *electrical*, *environmental* and *mechanical* as shown in Table 2-2, and stated that, the electrical insulation will fail after a period of exposure to these ageing factors when it can no longer endure them.

Table 2-2: Ageing factors which affect extruded insulations for systems for cables [38].

Thermal	Electrical	Environmental	Mechanical
Maximum T	Voltage (AC, DC, impulse)	Gasses (air, oxygen, etc)	Bending
Low, high ambient T	Frequency	Lubricants	Tension
Temperature gradient	Current	Water/humidity	Compression
Temperature cycling		Corrosive chemical	Torsion
		Radiation	Vibration

Densely [38] characterised ageing into *intrinsic* and *extrinsic* and defined intrinsic ageing as the results from the interaction of the ageing factors which when singly or in combination acted on the insulation system can induce changes to the material properties. Extrinsic ageing was defined as the degradation caused by the interaction between the ageing factors and defects such as protrusions, cavities and voids in the material bulk or at the interfaces. Figure 2-5 shows how the various intrinsic and extrinsic ageing factors could lead to insulation failure.
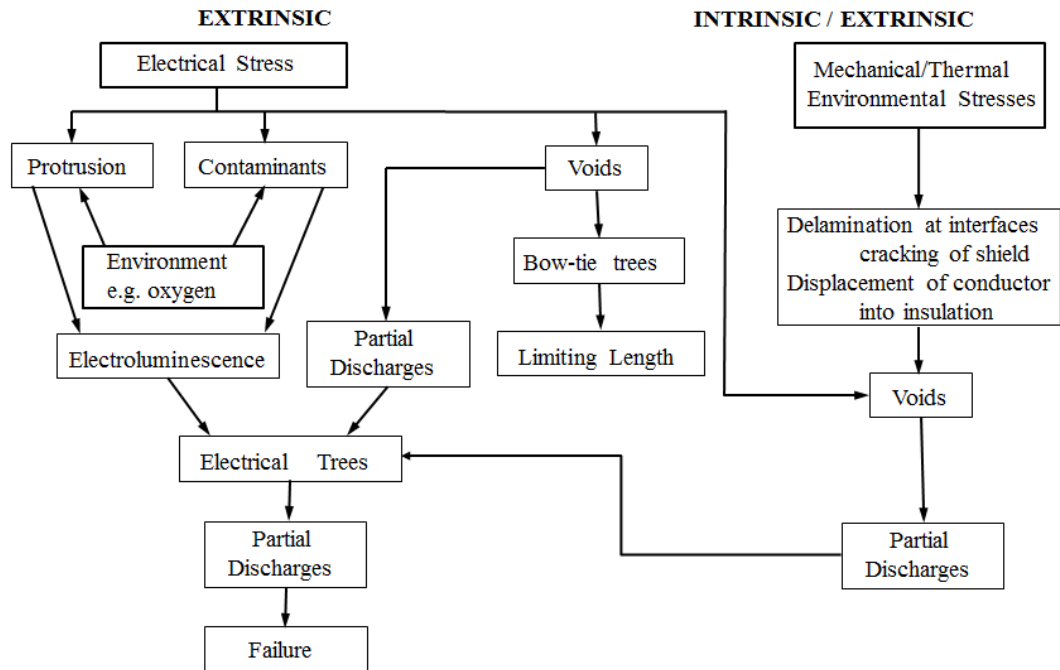
Figure 2-5: Extrinsic and intrinsic ageing factors [38].

Dissado and Fothergill [8], summarised these ageing factors into *physical, chemical* and *electrical* ageing and defined each of them as follows:

- *Physical ageing*; as time dependent changes in the polymer which arises as a result of structural relaxation of the polymer chain via segmental motion in the amorphous region due to variation in glass transition temperature [8]. It is suggested that the glass transition temperature is a critical parameter that determines the material state, and a slight change in it determines whether ageing will take place or not. Dissado et al. [8] added that, in the case of amorphous polymers, physical ageing can be associated with inefficiency of molecular packing (free-volume) which can prevent all the potential lattice sites from being occupied due to chain structure and steric hindrances.

- *Chemical ageing*; chemical ageing may change the behaviour of the insulating material due the environmental events outlined in Table 2-2, liberating electrons and ions via chain scission and bond breakage due to the action of light, UV radiation, heat or outdoor weathering. This may cause ionic conductivity leading to local joule heating at high fields resulting in current flow and thermal runaway.

45

- *Electrical ageing*; while physical and chemical ageing can occur in the absence applied electric field; the application of an electric field will accelerate the degradation process in both. The rate of material degradation depends on the type and magnitude of the applied field as well as thermal, environmental and mechanical stresses listed in Table 2-2.

Mechanical ageing may be influenced by torsional vibrations, tensions and bending stresses while thermal ageing may result from electrical ageing altogether leading to physical and chemical changes to the insulation structure such as cracks, protrusions, delamination voids or poor adhesion to interfaces; for example in cable construction. While physical ageing may be reversible by re-conditioning [39], chemical ageing is irreversible due to the morphological changes in the composition of the material produced after chemical reactions [40].

Figure 2-6 shows some of these defects in a simplified construction of a HV power cable used for AC or DC transmission. These defects may be formed during extrusion processes and others as a result of exposure to service conditions and together they lead to long-term irreversible ageing with eventual reduction of cable life. The discussions above show how multi-factor ageing processes are linked together. How these multi-factor ageing processes lead to the actual breakdown of the solid dielectrics is a subject of intense research activity due to the uncertainty surrounding ageing and degradation [41-42].
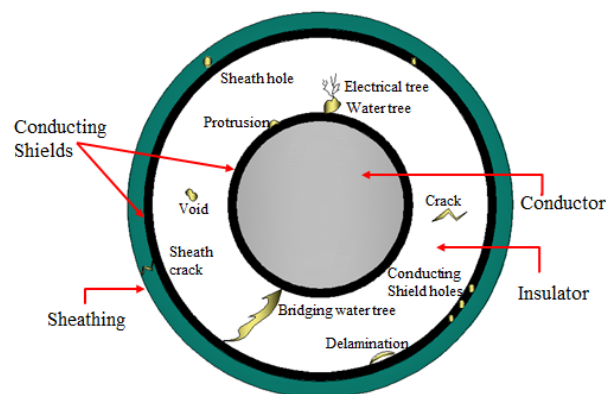
Figure 2-6: Power cable structure showing possible defects encountered in service.

Experiments have shown that time to breakdown decreases with increasing electric field [39] and also deviation from Ohm's law in conduction current and thermo-electrical ageing [43-45] suggest that both thermal and electrical effects may induce ageing which will finally lead to breakdown.

2.6 Breakdown processes of solid dielectrics

Research activity into physical processes involved in breakdown of gaseous, liquids and solids dielectrics lead to several breakdown theories with that of the solid emerging in 1922 by Wagner [46] which was based purely on local joule heating leading to thermal breakdown. Some of the early proposed theories of solid breakdown can be found in [8, 31, 47] and are listed as:

- Electronic breakdown.

- Electromechanical breakdown.

- Thermal breakdown.

- Breakdown due to discharges.

The breakdown processes listed above, usually occur in combination rather than singly on voltage application. The breakdown processes can be classified into either short-time or long-time breakdown. The former is used in determining the strength of a material, whereby a continuous rising voltage is applied to the material under test sandwiched between two electrodes at a constant rate or in steps within a short time period [48-49]. The latter is usually used in determining a material's life time and its resistance to various applied voltages through laboratory treeing tests [24, 50].

Thermal breakdown; when a high electric field of high intensity is applied to a test specimen, cumulative joule heating and temperature rise can occur more quickly in the material than the material can dissipate it. This increases the conductivity of the material further leading to thermal instability and eventual breakdown.

Mizutani [51] studied pre-breakdown currents in polyimide (PI) films of about 25 μm thick sandwiched between brass electrodes at 150°C. He observed a steep increase in pre-breakdown current with increasing temperature from about 10 ms. He attributed this to thermal run-away which resulted in filamentary thermal breakdown path in the PI samples. Nagao et al [52], also detected joule heating points prior to breakdown on thin films of Polyethylene of about 25-30 μm but at room temperature under dc fields. It was noticed that when one side of the samples under test was covered with epoxy resin, used as heat sink, the voltages at which the joule heating point appeared and electrical breakdown occurred were higher than the sample

without the heat sink suggesting that heat accumulation is strongly linked to lower breakdown field.

Intrinsic breakdown; is the maximum breakdown strength that can be attained from a solid insulating material by optimizing all test conditions [53]. This type of breakdown is solely dependent on the material property and can occur in the absence of discharges and thermal breakdown [49]. This breakdown type can reach electric fields in the excess of 100 MV/m [31]. However this intrinsic value is difficult to attain due to non-homogeneous nature of the insulating material and the imperfect testing environment.

In the intrinsic breakdown process, it is assumed that the inherent electrons in the material gain energy through collisions under the influence of the high electric field from which *electronic* or *avalanche* breakdown may occur. This theory is based on the understanding of avalanche processes in gasses which had been extended to solids. Von Hippel [54] captured electron multiplication by impact ionisation in liquid nitrogen which led to avalanches as shown in Figure 2-7.
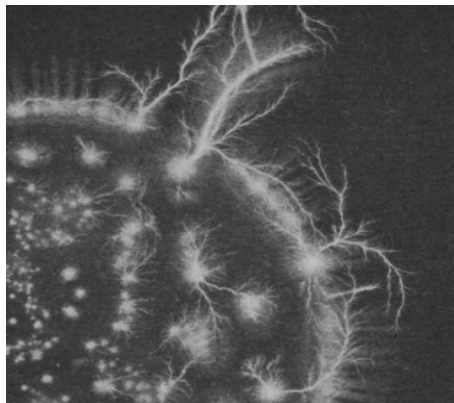
Figure 2-7: Transient discharges in nitrogen showing how the electrons multiply as in an avalanche [54]

Electromechanical breakdown; This is a dielectric failure resulting from electrostatic compressive forces which exceed the mechanical compressive strength when a high electric field is applied to solid dielectrics usually sandwiched between two electrodes. If the initial thickness of the dielectric is d_o and d is the compressed thickness after voltage V is applied, then an equilibrium exists prior to breakdown where the electrostatic compressive force and mechanical compressive strength are equal which according to Stark and Garton [55] is given by equation (2.5), where

Y and $\varepsilon_r\varepsilon_o$ are the Young modulus and dielectric constant of the material. This model predicts instability when the thickness is reduced to 40% of the original thickness. This model leads to prediction of breakdown fields much higher than seen in real solids.

$$\varepsilon_r\varepsilon_o \frac{1}{2}\cdot\frac{V^2}{d^2} = Y\ln\left(\frac{d_o}{d}\right)$$
(2.5)

Breakdown due to discharges; discharges can occur externally or internally to the material during short-term or long-term testing. External discharges occur in the medium surrounding test specimen and can cause failure to occur beyond electrode edges [47]. Internal discharges on the other hand occur within the material as a result of defects such as voids or bubbles causing partial discharges (PD) which then lead to deposition of space charge and subsequent local erosion (treeing) leading to final breakdown [38, 56]. The physical evidence of long term electrical degradation and breakdown (treeing) in solids is linked to partial discharges as well as space charge injection and formation in the dielectrics. Thus space charge measurement [57-58], partial discharge monitoring [59-61] and electrical treeing [24, 50, 53] become important tools in monitoring the health state of the material and are discussed in the sections that follows.

2.7 **Partial discharges**

IEC 60270 [62], defines partial discharge "as localised electrical discharge that only bridges the insulation between conductors and which can or cannot occur adjacent to a conductor". Partial discharge can occur at operating voltages in electrical trees, voids, cuts, cracks, fillers and contaminants with poor adhesion to the insulation and delamination at interfaces [59]. Inception of partial discharge is a sign of ageing and degradation in solid insulating systems of power plants and can be detected in an external circuit as electrical current pulses related to individual discharges in the material [63]. These discharges depend on the availability of a free electron in the gas filled cavity which may come from cosmic radiation which ionises atoms on solid surfaces or gas in the void [64] or charge injection from electrodes at high field [56, 64]. Degradation due to partial discharges is localised and minute in magnitude,

nonetheless it can cause progressive damage which overtime, leads to equipment failure [65].

The availability of wide bandwidth (800 kHz to 1 GHz) equipment, has allowed detection of short pulses of rise times in the regions of 1 to 2ns [66], which are usually companied by emission of sound, light, heat, chemical reaction and electromagnetic radiation [62-63]. Partial discharge can be detected by various techniques: electrical [65, 67] and non-electrical [62, 63]. The electrical means of partial discharge detection can be classified into detection for *internal, surface* and *corona* discharges. Surface and corona discharges are accompanied by large discharge magnitudes and usually occur at the insulation surfaces or at sharp points around conductors [65]. Surface and corona discharges are generally less harmful as compared to internal discharges which are triggered in cavities internal to the insulation with low discharge amplitudes and are often hidden or mistaken for disturbances. This could lead to data misinterpretation inducing excess or lack of equipment maintenance [68].

A common method of interpretation of partial discharges is the phase-resolved partial discharge analysis (PRPDA). PRPDA allows extracted discharge quantities, their magnitudes, time and phase of occurrence with respect to the applied voltage to be described [63]. These quantities can provide information about the nature of a defect, its size, location and the extent of damage it may cause within the insulating material [63,67, 69] where:

- q_{max} - is the maximum discharge magnitude; which is indicative of the defect site and size.
- N/n_q - discharge pulse repetition rate/number; indicative of the severity of defect, where periods of continuous discharge activity are considered more damaging as compared to the periods of intermittent discharge activity.
- $\phi_i\,(t)$ - discharge phase angle; indicative of the defect's ignition condition.

For example the energy at discharge site which may cause degradation of the dielectrics can be determined by the product of the apparent charge (q_i) and the instantaneous voltage (v_i) given by; PD $_{Energy}$ = ($q_i * v_i$) [67].

2.8 Space charge measurement

The net charges present in the bulk of an insulating material at any point in time are referred to as space charges. Space charge modifies the Laplacian electric field according to Poisson's equation given by equation (2.6):

$$\frac{d}{dx}E(x) = \frac{\rho}{\varepsilon_o \varepsilon_r}(x)$$
(2.6)

Where E(x) is the electric field as a function of position in space (x); ρ(x) is the local space charge density and $\varepsilon_o \varepsilon_r$ are the permittivity of free space and the relative permittivity respectively. The use of the *x* coordinate only implies uniformity in the yz plane.

These charges may come from electrode (anode and cathode) injection where charges travel across the bulk of the insulation and get blocked at the opposite electrodes, or may be dissociated from the material bulk in the form of ions and get attracted by the opposite electrodes [70-71]. Charge injection and transport processes are highly dependent on the conditions at the electrode-material interfaces as well as the work function of the electrode material [8]. Typical charge injection threshold was estimated in [43-44] to be about 10 to 20 kV/mm for polyethylene based materials. The work function of a material is defined as the minimum energy in eV required to remove an electron from the surface of that material. Thus the higher the work function of an electrode material, the lower the injection rate of that electrode. See Chapter 9 of [8] for detailed treatment of this subject by Dissado and Fothergill.

Chen et al [2001] investigated the effect of electrode materials on space charge formation in [72] using aluminium, gold and carbon loaded XLPE (semicon). In their experiment, they used these electrode materials as either anode or cathode and measured charge injection in each case alternately. They found the following trend for both electron and hole injection from the materials as; the semicon material injects more electrons/holes than the aluminium electrode and the aluminium electrode also injects more electrons/holes than gold (i.e. electron/hole injection; SC > Al > Au). Their result is in agreement with the work of Fukunaga et al [73] on

measurement of space charge behaviour of the charge transport layer coated on a polyester film. From the table of measured work functions of materials of their work in [73], gold's work function; Au (4.7 ± 0.02) is higher than that of aluminium; Al (4.08 ± 0.05). Thus gold is expected to inject less charge than aluminium as observed by Chen et al [72].

2.8.1   Space charge characterisation

Space charge can be characterised as either homo-charge or hetero-charge depending on the polarity of the net charge that accumulates next to the electrodes. Accumulated space charges next to an electrode and having the same polarity as that of the electrode are termed as homo-charge, while hetero-charges are accumulated space charges next to an electrode and having a polarity opposite to that of that electrode [70]. Both homo-charges and hetero-charges are field and temperature dependant. While homo-charges are generated as a result of charge injection at the electrode-insulator interfaces, hetero-charges are generated due to ionic dissociation of additives such as cross-linking agents used in improving the electrical properties of an insulator [33, 70-71]. The homo-charge and hetero-charge will modify the electric field distribution at the interfaces, as well as in the bulk of the insulating material and provides a mechanism by which electrical energy is transformed into potentially destructive mechanical energy leading to failure [8].

2.8.2   Electric field modification due to space charge

Figure 2-8 (b) and (d) show homo-charge and hetero-charge accumulation at the electrode-dielectric interfaces, while Figure 2-8 (a) and (c) show the electric field modification due to their effect. The average electric field is $E_0 = V_0/d$; given by the ratio of the applied potential difference V_0 to that of the material thickness d sandwiched by the electrodes assuming the material is homogeneous.

Figure 2-8 (a) shows the reduction of electric field below the average field E_0 at the electrode-dielectric interfaces and electric field enhancement in the material bulk due to homo-charge injection from the electrodes as shown in Figure 2-8 (b).
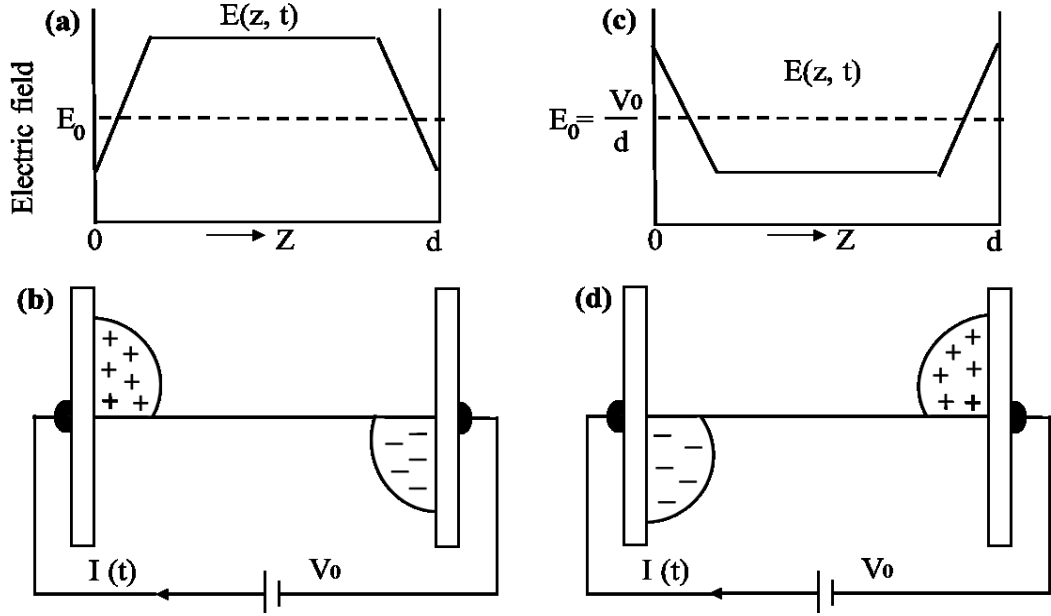
Figure 2-8: Electric field medication caused by the presence of homocharge injection [(a) and (b)] and hetero-charge distribution [(c) and (d)] in the bulk of an insulation material [12].

Hetero-charge accumulation results from polarization and dissociated impurities in the material bulk which is attracted by the opposite electrodes but is not easily extracted at the electrode-dielectric interface. This results in field enhancement above the uniform field E_0 at the interfaces and reduction in field in the bulk of the material below the uniform electric field E_0 as shown in Figure 2-8 (c). Thus the total field in the presence of space charge is given by equation (2.7);

$$E_T = E_0 \pm E_{sc} \tag{2.7}$$

Where; E_0 is applied average field and E_{SC} is the field due to space charge.

Thus the total field within the material may differ from location to location across the material by external voltage application.

2.9 Space charge measurement techniques

Space charge measurement is now a common method use to characterise the properties of solid dielectrics. Several techniques have been developed over the years for measurement on sample plaques [7, 57, 74-76] as well as for full-size cables [77-80]. Among these techniques, the pulsed electro-acoustic (PEA) technique is the most widely used because it allows the profile and charge distribution in stressed solid dielectrics to be observed non-destructively [71, 76, 81].

The quest for realisation of space charge free cables for HVDC application has led to the development of a facility for ageing HVDC cable at Alstom Grid now General Electrics in Stafford UK [82]. The facility is the world's only ageing laboratory for XLPE cables capable of monitoring cable insulation using either the PEA [80] or thermal step method (TSM) [83-84] techniques of space charge measurement. The photograph of the laboratory set up is shown in Figure 2-9.

Figure 2-9: Alstom HVDC cable ageing facility, Stafford UK [82].

2.9.1 The PEA measurement technique for plague of samples

Space charge measurement on sample plaques and in cables is based on the same principles the only difference is the sample geometries. Figure 2-10 shows the schematic diagram of the measurement principle of space charge measurement for plaque samples using the PEA method [76].
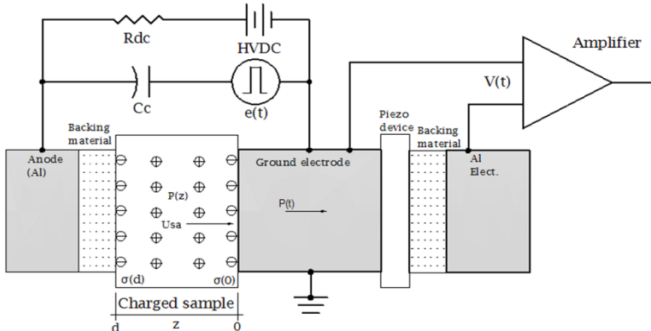
Figure 2-10: Schematic diagram of the PEA technique [76].

In this method, a short pulsed voltage coupled via a charging capacitor is used to perturb the internal charges in a sample sandwiched between two electrodes, which cause the charges to vibrate. The vibration of the charges launches an acoustic wave proportional to the charge distribution. A piezoelectric sensor (PVDF) which is essentially a microphone is used to detect the acoustic sound waves and transform it into an electrical signal which is then amplified and viewed with an oscilloscope. An oscilloscope with a high signal averaging rate of at least 2GS/s is enough to record and improve the sensitivity of the output signal which is then passed to a computer program (for example LabView) for processing. Details of signal processing technique can be found in [85-87].

The application of a DC electric field polarises the sample between the electrodes which results in a large surface charge accumulation on the electrodes seen as two peaks on the oscilloscope. If this field exceeds the threshold for charge injection (between 10 and 20 kV/mm in XLPE) [43-44, 88], charges are injected from the electrodes into the material bulk. The injection rate depends on the work function of the electrode material as shown in [72].

2.10   Electrical treeing

Electrical trees are micrometre scale defects which developed in high voltage solid polymeric insulating materials, and are precursor to long term failure. Treeing degradation is one of the most important physical evidence of internal damage to cable insulation caused by high electrical stress [24, 89-90]. Electrical treeing phenomena have been studied for many years, under both AC and DC conditions with the earliest publications reported to have emerged in 1912 [24].

Figure 2-11 outlines three distinct stages of tree growth model proposed by Dissado and Fothergill [8]. The initiation stage is define by a finite inception time which is the waiting time required for generation of a visible tree of about 10 μm in length after voltage application. The propagation stage is the second phase of tree growth marked by initial fast growth reported to be intermittent in form with bursts of growth decaying to a standstill and then followed by a region of slow fractal propagation and finally the runaway stage leading to breakdown as can be seen from the Figure.
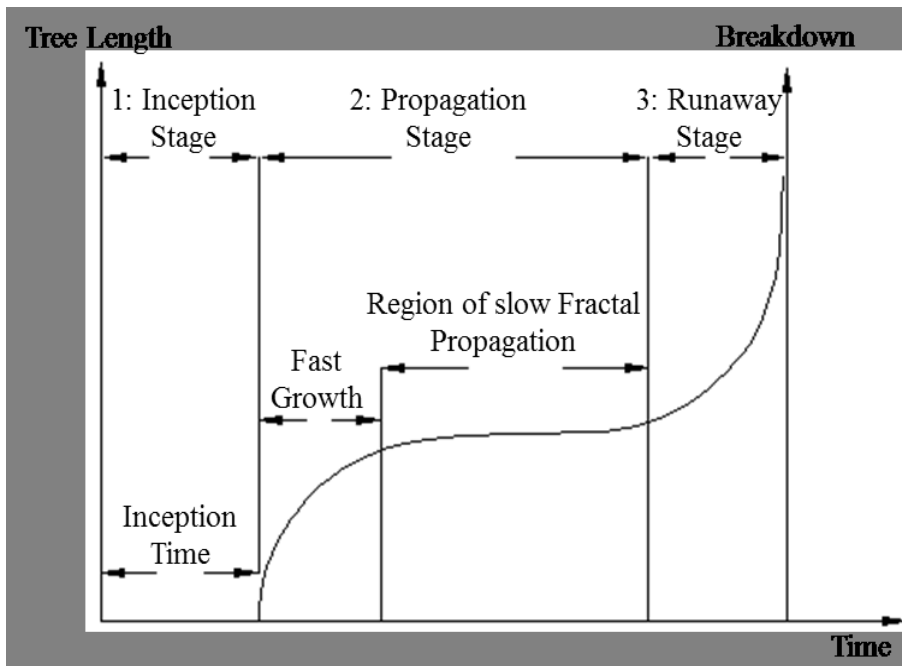
Figure 2-11: Schematic representation of typical electrical tree growth [8].

2.11 Electrical tree initiation stage

Several ageing mechanisms/models have been proposed to take place prior to the sighting of the first tree artefact (initial tree). Typical examples for dry ageing proposed by Densley [38] are shown in Figure 2-5.

Shimuzu [90] reviewed mechanisms of electrical tree initiation and the process occurring prior to electrical tree inception. He considered two scenarios for tree initiation as:

- Long-term tree initiation define with timescale >> 1s under low voltage application where; cumulative degradation under AC or repetitive pulsed voltages and other kind of stresses could lead to formation of gas-filled voids or defects leading to local field enhancement.

- Short-term tree initiation defined by time scale < 1s under high voltage; where AC, DC or impulse voltage application could lead to local breakdown involving electron avalanches in the solid.

Dissado et al. [8], on the other hand considered detection of small current pulses of about 0.04 -0.30 pC magnitudes to be the true onset of tree initiation. Tree initiation and propagation under AC, is proposed by some researchers to be induced by space charge [56, 91] coupled with frequency-dependent ageing (fatigue) [92-94] causing

56

Maxwell compressive stress which result in the formation of crazes, cracks or voids. While others are of the view that repeated electron injection and extraction to and from the polymer from the electrode each half cycle as a more viable process through which electrons gain enough kinetic energy of about 3–4 eV [95] under the influence of high field causing bond scission and physical damage to the polymer on collisions resulting in partial discharges and channel formation seen as tree [90, 96-98]. Under DC however, the initiation and propagation is proposed to be due to electrons injection and extraction during ramped DC voltage resulting in a sustained sequence of avalanche erosions creating channel in one direction only, with each new channel tip acting as possible branch point [8, 96, 99-100].

Tanaka [101], presented a typical waiting time for tree initiation under various applied voltages as shown in Figure 2-12. As can be seen from the Figure, for impulse and ramped DC voltages (monopolar voltages), the waiting time for tree initiation lies in the regions of nano-seconds to milli-seconds, while for an AC 50/60 Hz voltages, the waiting time is divided into three regions depending on the magnitude of the applied voltage. For low voltages; indicated by 5 units or less on the applied voltage axis, it can be seen that, the waiting times for tree inception in the third region is in days to years.
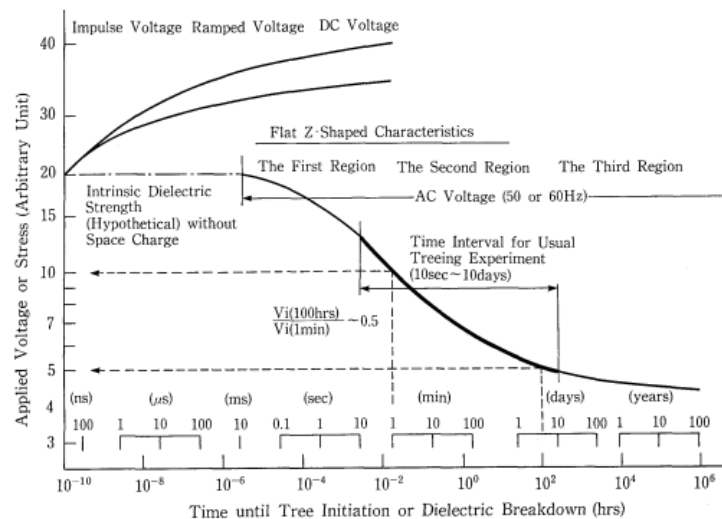
Figure 2-12: Schematic V-t characteristic for thick dielectrics in divergent field over wide range of time [101].

Tanaka [101] emphasised that material degradation in this region is not solely due to electrical, mechanical or thermal stresses but the combined effect of these stresses

and together with wet environmental condition can lead to water trees. Water and electro-chemical trees are the other types of trees observed in cable insulation [24]. Figure 2-13 (a), (b) and (c) show images of electrical water and electrochemical trees. While electrical trees are caused by electrical stress in the absence of water, water and electrochemical trees are caused by the combined effects of water, chemicals solution (ions) as well as electrical stress [102-105].
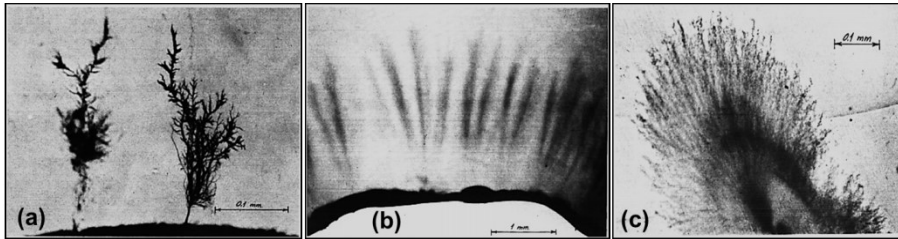
Figure 2-13: Tree types. (a) electrical tree, (b) water tree and (c) electrochemical tree [24].

Examination of electrical trees using scanning electron microscopy has shown that each branch consists of a permanent channel believed to emanate from material decomposition due to repeated periodic partial discharges [24]. Water trees, on the other hand, are found to compose of very fine diffused paths along which moisture has penetrated under the action of a voltage gradient. These paths disappear on drying or when the source of water and electrical stress is removed [24, 104]. Figure 2-5 shows that partial discharges and water trees may occur before an electrical tree is initiated. Thus partial discharge measurement is routinely used as on-line and off-line diagnostic tool for monitoring on-going degradation in insulation systems [106-107]. Prior to tree initiation, light emission is reported to have been observed and confirmed to be not partial discharges but rather electroluminescence; an indication of on-going ageing processes prior to measurable PD event [108-110].

2.11.1 Electroluminescence

Electroluminescence (EL) is a light detection associated with space charge injection into the body of a stressed polymer at high fields. The threshold for detection both space charge and EL is reported to be about ~ 100 kV/mm [90, 111]. EL has been detected under both AC and DC stresses as reported in [112]. Two possible mechanisms reported to be responsible for the observation of EL are:

58

- Impact of hot electrons resulting in excitation or ionisation of polymer molecules; the mechanism is reported to be due to electron injection from the embedded electrode or extraction from the polymer during negative and positive half cycle of applied AC voltage. These electrons are accelerated under the influence of the applied field and on collision excite a polymer molecule. When the molecule returns to its ground state it emits light detected as EL [89-90].

- Recombination between carriers of opposite charges; in this case, it is believed that during the negative half cycle of the AC waveform, negative electrons are injected into shallow and deep traps in the polymer structure, and on the positive half cycle of the waveform, most of the shallow-trapped electrons return to the electrode and the deep trapped electrons still remain trapped which then recombine with the injected holes emitting light through the processes [89-90].

Thus electroluminescence can be used to detect ageing processes prior to tree initiation. Bamji et al. [108-109] investigated tree initiation in low density polyethylene by simultaneously monitoring light (EL) and partial discharges. The sensitivity of their PD detector was about 0.04 pC, whilst the light detector can detect light of PD down to about 0.0005 pC using photomultiplier tube. The samples in their investigations were held at test voltages ranging from 10 – 42 kV and emission of light intensity were monitored at different wavelengths.

They found that the detected light in the visible range was more intense than that in ultraviolet (UV) light at all voltage levels and the UV light is only detected above the light inception voltage which corresponds to about 3645 Å and 3000 Å for two different samples respectively [108]. According to Bamji et al. [108-109], electrical trees did not develop when the samples were held below the light inception level for hundreds of hours and no PD is detected even at a very low PD detection sensitivity of about 0.04 pC [109]. However when the voltage is held above the light inception level, electrical tree always developed, with appearance of intense light and the time to treeing was observed to depend on magnitude of the applied voltage to the polymer under test [108-109]. Bamji et al. attributed the formation of the tree to photo degradation of the polymer caused by UV radiation and that the light inception

voltage at which the samples were held for long time without treeing is the threshold at which the polymer starts to degrade [108-109], and suggested that the inception voltage for light emission is probably higher than that for charge injection [108].

2.12   Electrical tree inception techniques

Treeing may take years to form under service conditions as shown in the low voltage region of Figure 2-12 (Third region). Thus, under laboratory conditions various field enhancing geometries and techniques which simulate structural defects are employed in order to initiate and propagate electrical tree within a short time period.

Some of the stresses enhancing techniques employed by researchers are:

- Wire-plane geometry attached to semi-conducting tab and moulded into the dielectric material [113].

- Leaf-like specimen configuration [114]

- Point-to-plane configurations [115-119].

The point to plane sample geometry is the most commonly used technique to generate high field. The geometric field enhancement, ignoring space charge effects can be determined using Mason's equations (2.8).

$$E_{tip} = \frac{2V}{r \ln\left[1 + (4d/r)\right]} \tag{2.8}$$

Where; V is the applied voltage, r is the radius of the needle tip, d is the gap distance between the needle tip and the ground and E_{tip} is the calculated electric field at the needle tip due to electrode system geometry in the absence of space charge.

2.13   Electrical tree propagation under DC

The main culprit causing initiation and propagation under DC is believed to be space charge. The relationship between space charge and tree imitation has been observed by many researchers in experiments involving application of ramped DC voltage, DC polarity reversal test, grounding DC after period of DC pre-stress or DC pre-stress followed impulses of different polarity [113, 115-118, 120-124]. These techniques are employed due to the difficulty of growing trees under pure DC.

For example, Ying and Xiaolong [122] investigated behaviour of tree initiation in XLPE cable insulation under various DC voltages. They initiated trees under impulse

60

voltage of 35 kV. However, with continuous application of +70 kV and -60 kV DC stress for up to about 11 hours they could not initiated DC tree. Wang [113] et al. on the other hand showed that negative DC pre-stress followed by positive impulses produced repeatable results in tree initiation and propagation. Wang [113] et al's observation is explained by many in the literature to be due to high inverse fields set up by space charge during application of the impulse voltage after initial field relief during DC pre-stress. Ieda and Nawata [118], investigated various circumstances under which DC tree can grow including temperature dependence of tree extension length. They showed by flight distance calculation that the observed tree length during a short circuit after a period of negative DC pre-stress can be taken as a measure of spatial distribution of space charge at the instant of short circuit which they calculated to be ~50 μm.

2.14 Electrical tree propagation under AC

Tree initiation and propagation under AC is strongly linked with partial discharge activity as mentioned in section 2.11. In order to determine tree growth characteristics, simultaneous measurement of partial discharge and electrical tree imaging have been carried out by many researchers [77, 125-129]. Partial discharges have been observed to behave differently during such experiments with the evolution of tree branches.

Hozumi et al [77], observed positive pulses of 0.05 to 0.1pC at the instant of tree initiation first before continuous positive and negative pulses were observed when an initial tree appeared, which then grew rapidly to about 10 μm. The growth rate dropped when the tree branched, followed by disappearance of negative pulses leaving only positive pulses which were concentrated at about 90° from the peak of the applied voltage waveform [77]. Vogelsang et al [127] also used image capture and PD measurement to monitored tree growth characteristics and identified three stages of tree growth characteristics as in [8]. At the initiation stage, no detectable PDs were observed. In the second stage they observed PDs of about 5 − 30 pC with accompanying tree channels of about 10 μm and 1 μm diameters at the tree trunk and at the tips respectively. The trees propagated to the counter electrode but did not result in immediate breakdown, and they assumed that, the trees have low conductivity [127]. In the third stage however, they observed widening of the tree

channels to diameters of about 60 – 150 μm which was accompanied by fluctuating discharges of about 50 – 220 pC reaching 2500 pC occasionally which then lead to breakdown [127]. Chen et al [125] and Wu et al [128] have observed a period during tree growth and PD measurement when the tree ceases to grow, and was accompanied by drop in observed PD magnitudes. During this period, pine braches (small fine side branches) were observed to extend from the stagnant branches in [125]. The response of partial discharges to internal degradation has allowed partial discharge measurement to be used for monitoring on-going degradation where imaging cannot be employed especially in filled materials [130].

Trees observed during such experiments have been named by their visual physical appearances. The most commonly observed tree shapes are; branch-type, bush-type and bush-branch-type [8, 96, 131-133] as shown in Figure 2-14 . Other tree shapes such as; bow tie tree, broccoli-type tree, delta, strings, dendrites, plume, spikes and fans, have been observed on cables removed from service [134]. Recently, laboratory grown trees have revealed shapes such as; branch-pine shape [125, 135-136] bine-branch shape [135, 137], stagnated tree [125] or monkey puzzle [135, 138], with each shape determining growth rate and subsequent time to breakdown. While time to breakdown in bush-type tree is longer due to slow growth rate of highly dense network of tree channels, in branch-type trees time to breakdown is shorter. Time to breakdown in bush-branch-type trees is intermediate between bush-type and branch-type tree.

| Branch | Bush | Bush branch |
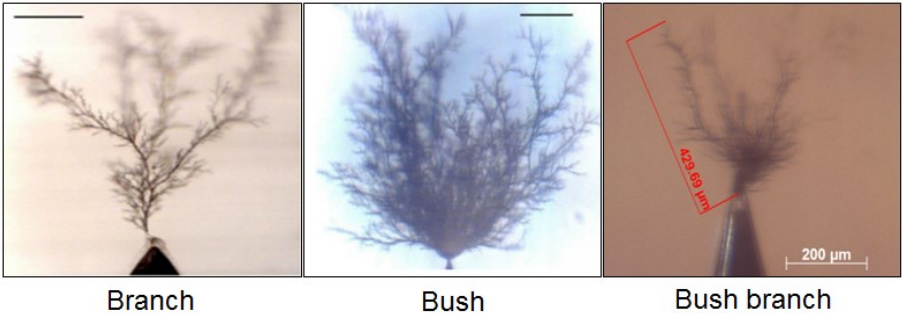
Figure 2-14: Common shapes of electrical trees captured at the University of Manchester.

Generally, bush-type trees were observed at relatively higher voltages than branch-type and bush-branch type trees [8, 96, 131]. Electrical tree shape and growth rate is also known to be influenced by voltage type (AC or DC), magnitude as well as frequency [53, 139-142]. Electrical trees can be categorised as conducting or non-

conducting depending on whether the material (epoxy) is above or below its glass transition temperature [22-23]. Confocal Raman microprobe spectroscopy has shown that conducting tree channels contain graphitic carbon whereas for non-conducting tree the channels contain only fluorescent decomposition residues, reflecting differences in their visual structure as very dark channels (conducting) and less dark channels (non-conducting) [143]. Tree growth experiments with partial discharge and light detection also showed that for non-conducting trees, the detected light and partial discharges were large and confined mainly within the tree channels and close to the point electrode, whereas for conducting trees the partial discharge activities and light were detected at the ends of the growing tree tips [23, 143-145].

2.15   Electrical tree imaging techniques

Electrical trees grow as 3-dimensional structures in solid insulation; see [146-148] for example. However captured 2D images are often used to characterise the tree growth characteristics. Usually parameters such as tree length [125-126, 131, 135, 137, 149-150], tree growth rate [125, 137, 140, 149], the expansion co-efficient of the tree [135], fractal dimension [125, 135, 140, 149-151], or accumulated damage zone as a function of zone radius [131] are used to characterise the tree growth characteristics. Fractal dimension or accumulated damage zone technique depend primarily on the area covered by the tree structure in pixels (damage zone) after image processing (conversion from grey scale to black/white) to characterise the extent of damage. However, fractal dimension is reported by Zheng et al (2008), to have limitations when identifying mixed tree structures [135]. For example, Figure 2-15 shows an attempt in this PhD work to binarise a fully grown electrical tree image with mixed (dark and fine) tree structures. As can be seen in Figure 2-15 (b) all the fine tree structure is lost during this process.
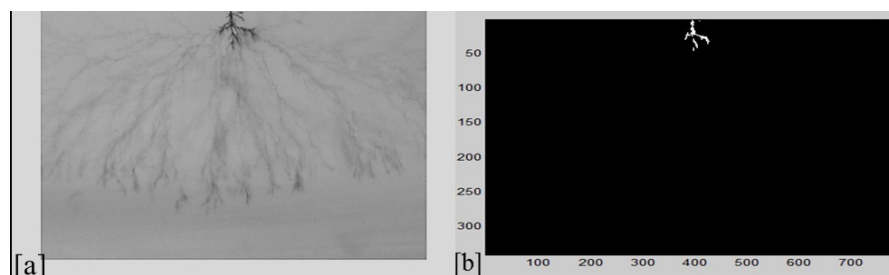
Figure 2-15: Digitizing fine tree structure; [a] before, [b] after.

Thus where fractal dimension or accumulated damage zone cannot be used to characterised degraded regions occupied by trees, measured tree length and width from projected 2D images together with propagation time are used for characterising the tree growth characteristics. These parameters are defined as:

- Tree length ; the longest distance from the needle tip to the furthest end of the tree tip or tips in the direction of the electric field (y-axis plane) in the 2D projected image which is limited by the gap distance between the two electrodes (in this study 2mm) as depicted by the schematic drawing in Figure 2-16

- Width: defined as the extent of spread of the tree channels as they grow away from the tip towards the ground electrode in 2D projected image in the x-axis plane. In this study, the maximum tree width that can be viewed is 6 mm (limited by the field of view of the lens employed).

- Growth rate (dL/dt): defined as the average rate of change of the tree length.

- Expansion co-efficient (D/L): defined as the ratio of absolute tree width (W) to the absolute length (L) from the captured tree images.

Figure 2-16 depicts the schematic representation of maximum image dimension that can be obtained by the optics employed in this study at the propagation stage which is 6 x 5 mm. This corresponds to 2452 x 2056 numbers of pixels representing width and height of the captured 2D projected images.
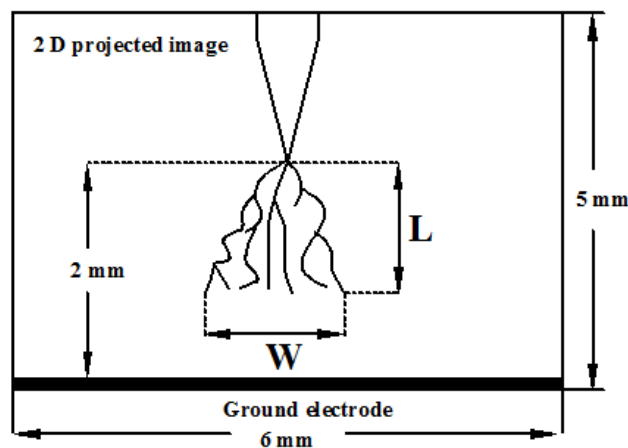
Figure 2-16: Schematic representation of 2D projected tree image from test sample.

With the known ratio (mm/pixel) between the accurate size and pixel numbers of the recorded series of 2D projected images, the tree length and width can be manually measured and calculated as the use of software becomes impossible due to the fine nature of the tree channels as illustrated in Figure 2-15. For example, if the electrical tree traversed the 2 mm gap distance, then maximum number of pixels representing its length would be 822 pixels (i.e. 2/5*2056) approximately. Although for each test the distance between camera lens and the needle tip is fixed in order to maintain a constant calibration ratio, errors can be introduced in the measurements due to the following limitations:

- The tree channel may grow out of focus of the camera lens (i.e. in a direction away or near the camera lens out of the camera depth of field) resulting in image blurring. In this case, out of focus tree channels may reach the counter electrode without being seen leading to error in the maximum measured tree length.

- For the same reason mention above, breakdown can occur before a visible tree channel is seen to have traversed the gap distance.

- Using one camera for capturing 3D images of electrical tree visually limits the accuracy in determining the general direction of the absolute length and width of the furthest tree channels.

- The intensity of the illuminating back light can also lead to a very fine tree channel not being very visible leading to human error in measured length and width.

2.16 Summary and areas identified for investigation

Polymeric insulations have been successfully used in low, medium and high voltage application due to their excellent properties. Their reliability at higher voltages is a subject of intense research activity due their vulnerability to charge injection and subsequent treeing which cause their limitation for use, especially under high DC voltage regimes. It is clear from this literature review that electrical treeing is one the major cause of insulation failure and has been studied for many years under both AC and DC conditions. The link between charge injection and material ageing,

degradation and breakdown; through mechanisms such as electroluminescence, partial discharges and electrical tree initiation and propagation have been reviewed. Whilst retained charges under AC stress is minimal resulting in the success of using polymeric insulation at higher voltages (500 kV), such success is limited under DC due to the ability polymeric insulation to retained injected charges which modify local field and reduce the breakdown strength of DC insulation. This limits the rating of polymeric cables to 320 kV under DC although 500 kV DC cables have been type-tested with modified insulation.

The current trend in bulk power transfer is to use HVDC technology as discussed in sections 1.3 and 1.4. However the complexity of such technology is beyond cable systems as shown in Figure 1.1. Converters are employed at both sides of the cable systems, and in recognition of harmonics introduced by such converters (VSC or LCC) filters are employed to mitigate the effect of harmonics. The un-answered question here; "is how harmonics will impact the cable insulation system". Literature showed that higher frequencies propagate electrical trees faster under AC. Switching (impulses, grounding and polarity reversal) experiments under DC has shown vulnerability of DC insulation to tree initiation in such circumstances. However in general, very little work has been done under DC especially using pure DC for tree initiation and propagation.

The subject of tree initiation and propagation is still one of the extensively researched areas due to incomplete understanding of the treeing phenomena. Treeing is better understood in AC insulation, allowing design criteria for cables and HV insulation system to be established. However, the knowledge of tree growth under DC is still at an infant stage and a subject of on-going research activity.

The literature survey presented in this chapter has shown a strong link between space charge injection and material ageing causing degradation, tree inception and propagation and subsequent failure. Considering this, the following areas are identified for research in this study:

- Short term breakdown strength of epoxy resin samples under AC and DC.

- Material vulnerability to charge injection through space charge measurement under DC.

- Electrical treeing under "Pure DC" and "pure AC" voltages.

66

- Electrical treeing on AC superimposed on either positive or negative DC voltages.

3. Sample preparation

3.1 **Introduction**

In this chapter, the material selected and the methods of sample fabrication for the entire study are described. Some of the challenges encountered and how those challenges were overcome is also highlighted. In a study designed to observe the electrical properties of a material, it is important to ensure that the observed behaviour is from the material property and not dominated by way the material is prepared [152-154]. Factors such as mixing, de-gassing and moulding/de-moulding techniques employed as well contact pressures applied to the samples may affect material characteristics if not well controlled. In order to achieve reproducibility of test results, a lot of effort has been made to standardise the method employed in material preparation and fabrication in this study.

Two samples types were fabricated using epoxy resin in this study. For the study of electric strength of the material and its susceptibility to charge injection, thin films up to about 250 μm were fabricated. Epoxy resin blocks cast into acrylic tubes, with an embedded needle to simulate structural defects generating high divergent fields [119], were employed for study of electrical treeing.

3.2 **Material for this study**

The material employed for this study is a low viscosity epoxy resin Araldite® LY 5052 and the corresponding hardener Aradur ® HY 5052 both supplied by Huntsman. This mixture is a cold-curing epoxy system, and from the manufacturer's data sheet, the material has the following properties:

- Low viscosity, providing easy impregnation of reinforcement materials.

- Long pot-life (2 hours for 100 ml at ambient) giving ample processing time.

- High temperature resistance (glass transition temperature after ambient cure is 60°C, and after post-cure is 100-120°C).

- Excellent mechanical and dynamic properties after ambient cure with improved properties after post-cure at elevated temperatures.

Epoxy resin is used in many engineering applications and also as dielectric material in high voltage equipment as mentioned in section 2.2.1. Thus investigations on

various types of epoxy resins [154] have been conducted by many researchers. This epoxy resin system was selected for this study because of the previous experience at the University of Manchester [155-156]. To date, the experience with this epoxy resin system at the University of Manchester is limited to point-to-plain configurations of sample fabrication [157-158]. In this study, the use of this epoxy resin system has been extended to fabricating thin films up to about 250 μm thicknesses. To ensure the observed behavior reflects the intrinsic material characteristics, a standardised preparation scheme shown in Figure 3-1 and described below is followed each time samples are prepared.
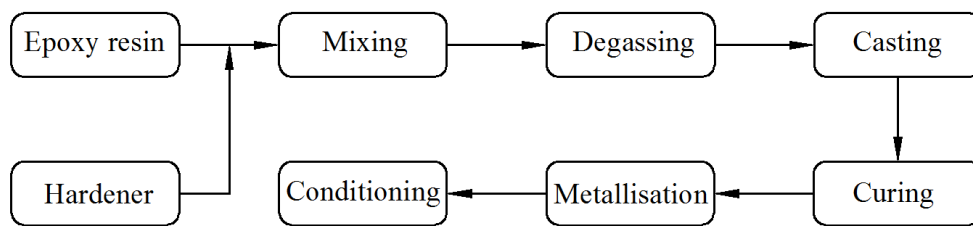
Figure 3-1: Standardised sample preparation scheme.

3.3 Mixing

To obtain the optimal properties from the material, it is ensured that the material is accurately weighed in a beaker using 100:38 (parts by weight) mixing ratio indicated by the manufacturer to obtain the required volume. The required volume of the components (Araldite LY 5052 and Aradur HY5052) is hand-mixed for about a minute, followed by magnetic stirring for 5 minutes. The mixing process results in trapped air bubbles which need to be removed through the next stage of the process by degassing.

3.4 Degassing

The pot life of this epoxy resin system is about 120 minutes, meaning it must be applied to the intended application (casting) within this time period otherwise it will become too viscous to be useful. Thus the epoxy resin mixture is degassed in a vacuum chamber for about 60 minutes (determined by experience as the optimum time of degassing) before it is removed from the vacuum chamber. A two-stage degassing procedure is adopted to enable efficient removal of air bubbles in the mixture:

- In the first stage, the vacuum chamber's vent is closed and the air inlet/outlet lever of the vacuum is turned to an open position and the pump switched on to allow the air in the vacuum chamber to be removed to until a high vacuum is attained (usually below 1mbar) on the vacuum chamber's gauge. This results in an upsurge of bubbles, from the mixture when very low pressure is attained. The inlet/outlet lever of the vacuum chamber is then turned to a closed position and the bubbles allow to settle down for 30 minutes under low pressure.

- In the second stage of degassing, the vacuum's lever is turned to an open position and the pump is switched on again, but this time degassed continuously for another 30 minutes, as before. This is to ensure that all bubbles trapped in the bulk of the material are brought up to the surface. After the 30 minutes, the pump is switched off and vacuum chamber's vent opened. This allows air back into vacuum chamber and material returns to atmospheric pressure again. This results in any remaining bubbles on the surfaces to burst. This completes the degassing process and the material is now ready for casting.

3.5 **Casting of thin film samples**

Mould plates made from 10 mm thick flat mild steel of dimensions (160 x 280) mm shown in Figure 3-2 were designed for fabricating thin sheet samples for electric breakdown strength and space charge measurements. The internal surfaces of the plates were machined to prevent major roughness on the surfaces of the samples to be prepared. The measured internal surface roughness of the plates with a Carl Zeiss (S/N: 3518000952) microscope gave an average roughness Ra: of 8.84μm to 12.0μm. Prior to casting, the following steps were followed:

1. Plates were cleaned with acetone and a thin layer of moisture curable silicone sealant (Polycoat™) release agent was uniformly applied to the plates with fine microfiber cloth.

2. A Mylar™ spacer gasket of thickness 100 μm or 200 μm was placed on the plates depending on the thickness of the sheet required.

3. The degassed material in the beaker was then poured onto the middle of the bottom plate. The top plate was then positioned in place and quickly fastened with bolts and nuts.

4. The material now sandwiched between the plates with the gasket was allowed to cure for 24 hours at room temperature after which the samples were removed from the moulds.

5. The removed samples were laser cut into discs of 55 mm diameter, bagged in re-sealable polyethylene sample bags and kept in a desiccator ready for post curing and testing. The desiccator was kept at room temperature and at $47\pm5\%$ relative humidity (RH), using Silica gel.

6. If double layer samples are required then laminates are formed by first curing a single plaque of epoxy and then forming a second layer of epoxy by doubling the gasket thickness. With this process, following the same curing regime, an epoxy-epoxy interface region with identical material properties is created.

3.5.1 The development of thin film casting process

One of the good qualities of epoxy resin is its remarkable adhesion to metals [26]. With the exception of Teflon [159], epoxy resin sticks to almost all solid materials and in most cases, the use of release agent is not recommended because the release agent may penetrate the epoxy and alter its properties. This is what makes it difficult to fabricate thin films of epoxy resin sheets, especially if the mould is made out of metal. The choice of a metal mould is to ensure uniform contact pressure is achieved on the entire surface of the sample during fastening and to control the thickness of the fabricated samples.

Several unsuccessful attempts to de-mould the thin sheets from the mould plates with Silicone oil and Teflon spray used as release agents were experienced. Figure 3-2 shows one such attempt with the cured epoxy resin stuck to the plates. Although Teflon is known to be a good release agent, the spray form was not found to be helpful on this occasion. On removal of the samples, stains are observed on the samples thus defeating the purpose as the sample is now contaminated with Teflon and processing fluids.

After several unsuccessful attempts, a few modifications were made to improve de-moulding of the samples which proved to be successful. These improvements are; the use of release agent, employing a permanent coating of Teflon on the mould plates and casting the material between transparent Mylar films as detailed below.

Figure 3-2: Unsuccessful attempt; showing sample stuck to the mould plate.

3.5.2 Release agent

Although the use of release agent is not ideal, because of its potential to influence the material being moulded, PolyCoat™, a release agent supplied by Mouldlife was employed and this proved to be successful. This release agent is one-part moisture-curable silicone sealant which when applied to the mould plates serves as semi-permanent coating on the plate which does not stick to the sample. Reading et al, [154] used similar release agent called QZ 13 in a study on epoxy resin which also proved to be effective at aiding to de-mould the samples.

3.5.3 Teflon coated plates

The Second improvement attempt was to send the mould plates out (Impreglon UK limited) to be permanently coated with about 10 μm thick Teflon. The second attempt proved to be the easiest way of de-moulding the sample from the plates. However the finish of the coating is not very smooth as expected resulting in rougher samples compared to the ones obtained using the PolyCoat™ release agent.

3.5.4 Casting between transparent Mylar films

In this method, transparent Mylar films cut to the same dimensions as the mould plates, and with holes at the same locations as on the mould plates were used. The Myler films were first placed and taped to both the top and bottom of the mould plates followed by placing a gasket having a thickness of the sample sheet to be fabricated. The required volume of the epoxy material is then poured onto the Mylar sheet on the bottom plate, followed by the top plate together with the Mylar sheet and fastened quickly. The material is allowed to cure between the Mylar films. The mould plate is unfastened after the curing time with the epoxy sheet sandwiched between the Mylar films. The epoxy sheet is removed by peeling off the Mylar sheets from both sides. This procedure is very successful resulting in much smoother epoxy resin sheets than from the Teflon coated plates. However extra care is required during peeling off of the Mylar films as the cured epoxy sheet is fragile and can result in damage of epoxy resin sheet. The epoxy resin sheets were laser cut to 65 mm diameter discs, labelled and kept in a desiccator ready for testing.

Figure 3-3 shows the Teflon coated plates and epoxy resin samples cut to sizes and labelled ready for testing. Steps 1 to 5 of section 3.5 above were used for producing both single and double-layer samples of about 100 μm to 230 μm. Double layer laminates are formed by first curing a single plaque of epoxy and then forming a second layer of epoxy by doubling the gasket thickness. With this process, following the same curing regime, an epoxy-epoxy interface region with identical material properties is created.
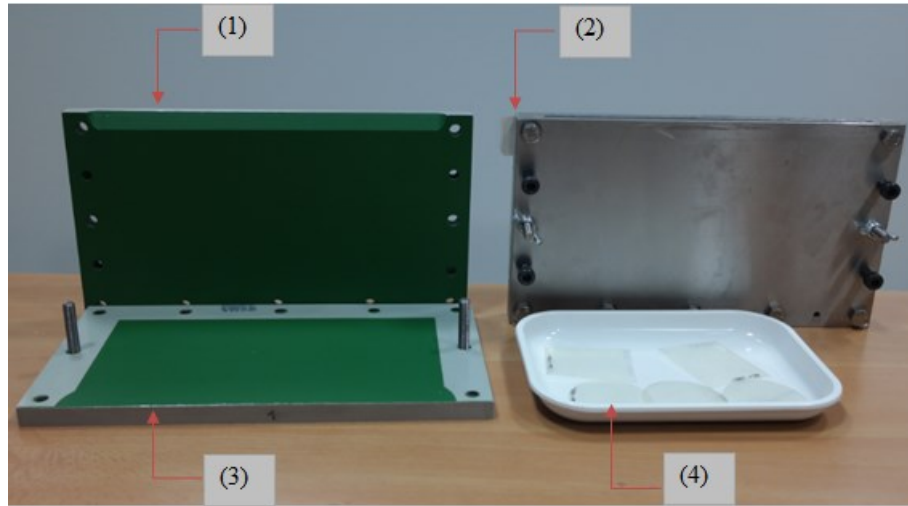
Figure 3-3: Improved sample preparation method; (1) - Top Teflon coated plate, (2) – Uncoated plate with samples cast between transparent Mylar film, (3) – Bottom Teflon coated plate showing spacer gasket and (4) – De-moulded sample cut to size and labelled ready for testing.

3.6 Casting the treeing sample

The point-to-plane method of sample preparation has been adopted at the University of Manchester [155-158] for many years. Both hypodermic (tip radius = 3 µm, thickness 1.1 = mm) and Ogura (tip radius = 3 µm, thickness 1 = mm) needles have been employed for sample preparation using acrylic cubes moulds of dimensions (25 x 25 x 25) mm as shown in Figure 3-4.
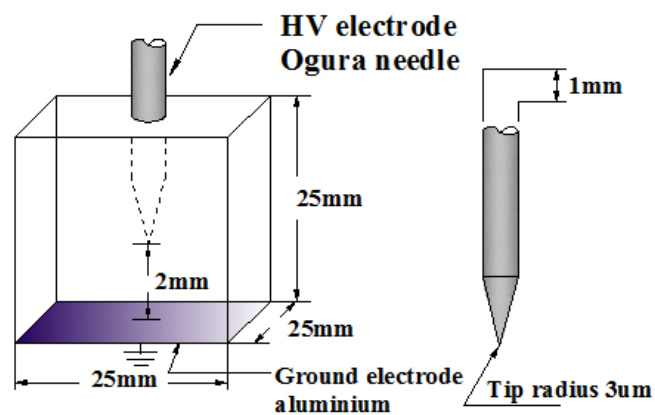
Figure 3-4 Point-to-Plane sample configuration.

3.6.1   Ogura Vs Hypodermic needles

Whilst the Ogura needle is symmetrical with a well-defined rounded tip, the Hypodermic needle has a hollow shank sliced at the tip and coated with transparent lubricant for medicinal use [160]. Whilst the Hypodermic needle cleaning is laborious due to the silicone coating supplied on it (see cleaning details in [157]) the Ogura needle is easy to clean. The Ogura needle is cleaned by dipping the tip of the needle in a bottle of acetone and removing it immediately ensuring that the tip does not touch anything to prevent damage to the tip. It is then wiped dry with a fine fibre-free cloth by carefully stroking it once from the middle of the shank toward the tip. Figure 3-5 shows the images of the two needles. With the hypodermic needle, sharp points are often encountered along the sliced edges of the hollow tip, and tree initiation is often observed along this area instead of the tip see section 7.1.1.
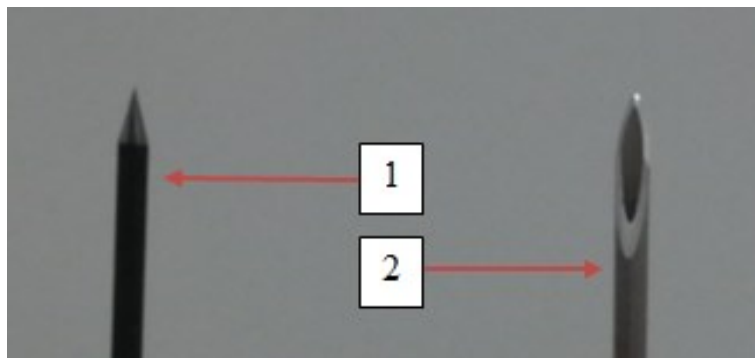
Figure 3-5: [1] Ogura needle, [2] Hypodermic needle.

3.6.2   Preparation of the acrylic cubes and sample casting

Previous studies [155, 157] adopted the use of polytetrafluoroethylene (PTFE) tape to seal off the bottom the acrylic cubes and secure it in a recessed PTFE slab to prevent permanent bonding of epoxy to the rig. However this procedure does not always result in a completely flat bottom sample and filing of the sample's bottom is needed to achieve flatness, which leads to reduction in the gap distance.

In this study the acrylic cubes were cut to the dimensions shown in section 3.6 and bottoms were sealed off with 1 mm thick PET films which were easy to remove after curing and ensured the bottoms of the samples were flat. The needles were set 2±0.2mm from the plannar surface using 2 mm thick soft rubber slab as gauge for

gap distance, and the needles were secured with the needle cap holder as shown Figure 3-6
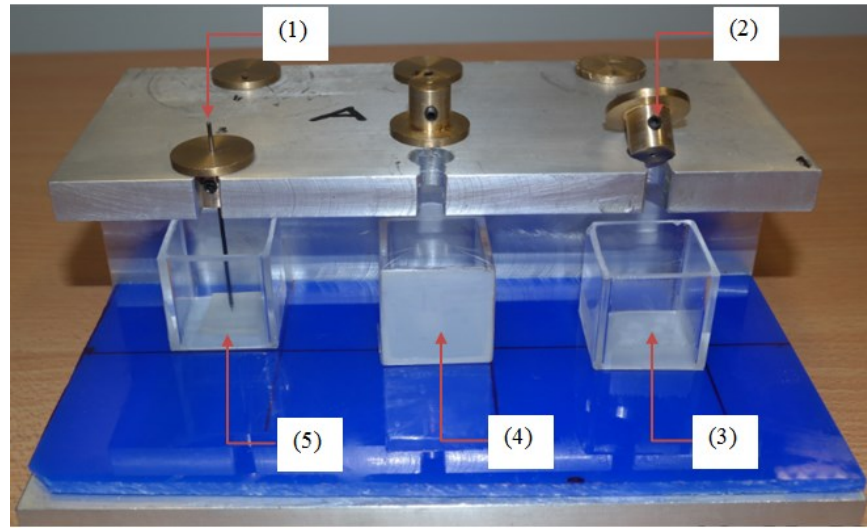
Figure 3-6: Point-to-plane sample preparation rig showing: (1)-Needle, (2) - Needle cap holder, (3) – Sealed acrylic cube, (4)- 1 mm PET Film sealant (5)- 2 mm gap slab.

The de-gassed epoxy resin mixture is then carefully poured into the acrylic cubes placed on a pre-marked position on a flat 3 mm thick acrylic sheet secured on the sample preparation rig. Each rig has a maximum capacity of six samples and with two rigs, twelve samples can be prepared in a batch. The samples were allowed to cure at room temperature for 24 hours, followed by a further 4 hours of post curing at 100 °C to achieve optimal sample characteristics [154]. Samples were removed from the acrylic tube by cutting the exposed edge of the tube (away from the epoxy) with hacksaw and using a flat head screw driver to crack it open the tube.

3.7 **Sample metallisation**

In a point-to-plain sample configuration, the sample's bottom is usually painted with sliver paint [118, 124] or with a carbon based conductive substance Aquadag [53, 157] to ensure sound electrical contact of the sample to the ground plate. Many of these substances are water based liquids, and can result in water absorption by the samples under test, especially when epoxy resins are used since they are hygroscopic. Initial investigations in this study also show that carbon painted on samples as electrodes using aquadag dissolves when the sample under test is immersed in oil. This also reduces the insulation properties of the oil for later tests.

Thus the bottoms of the samples in this study were metallised by vacuum evaporation with aluminium.

3.7.1 VCM 600 V2 Vacuum evaporation system

The samples' bottom surfaces were metallised using a compact desk-top thermal vacuum evaporation system (VCM 600 V2) which can create a highly uniform thin film of metals on substrate. The system incorporates; a thermal source, high power turbo pump and rough pump (external to the unit), high power supply unit up to 150 A current, a glass bell jar, a glass mesh guard, a vent valve and safety interlocks for turbo and filament protection. The unit operates from the mains supply with power rating of 2000W. Figure 3-7 shows the system in operation.

Figure 3-7: VCM 600 V2 thermal vacuum evaporation system.

3.7.2 Metallisation procedure

The metallisation process takes about an hour to complete. Prior to metallisation, the system is disassembled as shown in Figure 3-8.
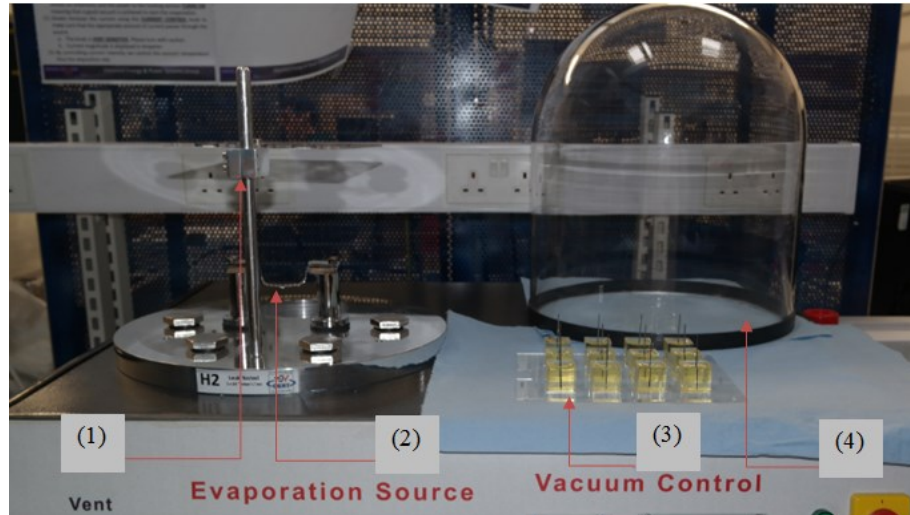
Figure 3-8: Disassemble parts of evaporation unit prior to sample metallisation; (1); Sample holder, (2); Tungsten filament, (3); Samples to be metallised and (4); Glass bell jar.

The metal (aluminium) to be vaporised is wound around a tungsten filament heat source. A U-boat heat source can also be used but this requires higher current and longer time to vaporise the metal, which may damage the sample surface. The post-cured samples are secured on a sample holder designed to hold 12 samples and the system re-assembled. Metallisation of the samples were made following the vaporisation procedure below:

- Close the vent valve (clockwise) and power the system by turning on the main power switch followed by that of the rough pump to initiate vacuum process.

- Monitor the reduction in pressure on the vacuum control indictor until the pressure falls below 1 mbar, then start the turbo pump on to accelerate vacuum attainment.

- When a high vacuum is achieved, the power to the heat source engages automatically, and the red light on the front panel turns on indicating evaporation can be started.

- The rate of current increase (temperature control) determines the evaporation/deposition rate. This is achieved by carefully turning the sensitive current knob on the current controls. 25A through a tungsten filament was found to be the optimal current for achieving good evaporation on the samples within one minute.

- On completion the current is minimised and the turbo pump turned off to allow the filament to cool for about 35 minutes.

- The vent valve is opened slowly until atmospheric pressure is reached. The power to the system is then switched off, and the bell jar slowly lifted and kept aside safely.

The samples are removed and kept in a desiccator (at 47±5% RH) to prevent water absorption. The glass jar is thoroughly cleaned using propanol with soft tissue or cloth. Vinyl gloves are worn throughout this process to avoid contamination.

3.7.3 Sample conditioning

Fabricated samples for this study and the oil in which they immersed are pre-conditioned, conditioned and kept in a desiccator and oven at room temperature prior to testing. The pre-conditioning stage of the samples produced for this study is the post-curing (4 hours at 100 °C) process outlined in 3.6.2. Afterwards, the samples are allowed to cool to room temperature and then kept in a desiccator (conditioning) before testing. For tests carried out in oil, the silicone oil is dried at 85 °C for 24 hours in a vacuum chamber and the temperature reduced to 23 °C and left under vacuum for a further 72 hours before any experiment is commenced.

The temperature and relative humidity of the testing environment and that in the desiccating chamber is always measured. Thus the pre-conditioning, conditioning and testing (M) codes [161] for samples in this study is summarised as:

24h/85°C/0%+72h/23±2°C/0%+4h/100°C+24h/23±2°C/47%±5;M/23±2°C/47±%

| Oil pre-conditioning and conditioning | Sample pre-conditioning and conditioning | Testing condition |

Figure 3-9 shows comparisons of fabricated samples' bases prior to metallisation, after metallisation and a sample with the base painted with Aquadag. It can be seen that the metallised sample appears more uniform than the Aquadag painted sample.
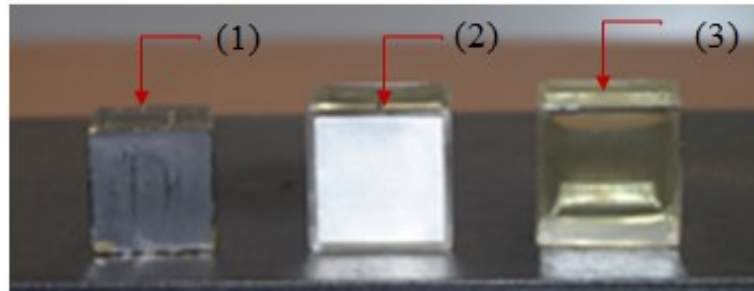
Figure 3-9: Fabricated point-to-plane sample - (1); un-metallised sample, (2); metallised sample, (3); sample painted with Aquadag.

The samples were labelled using the nomenclature shown in Figure 3-10, where:

- Bn: stands for batch number.

- Sn; stands for sample number.

- n; is an integer. Numbering starts from 1.
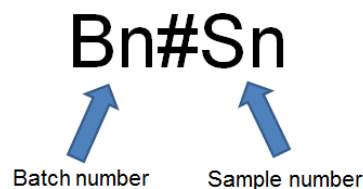
Figure 3-10: Sample nomenclature for easy identification.

For example, samples number 2 and 3 fabricated from the same batch say batch 1 will have identification as B1#S2, and B1#S3, and samples 5 and 7 fabricated from say batch 2 will be identified as B2#S5 and B2#S7 respectively. This way any trend or anomaly during testing coming from the same batch of samples can be easily tracked as samples were randomly selected for testing.

3.8 **Summary**

The growth of electrical trees and short term breakdown measurement is very dependent on sample preparation. This chapter has highlighted the methods developed to ensure consistent and well controlled sample fabrication for testing, both in thin planar and needle to plane sample geometries. The challenges of demoulding cast epoxy film on metal plates and from acrylic cubes have been resolved.

For thin films, the use of permanent coated PTFE on the metal plates requires little effort and saves time. Also casting the epoxy between transparent PET films was

successful, but the challenges here lie in the peeling of the PET films off the cast material. This stage requires care and can be time consuming due to the fragile nature of the thin epoxy cast between the PET films. Samples used for short term breakdown tests and space charge measurements in this study were those cast on transparent PET films because of the smoother finishing compared to those from the Teflon coated plates.

Needles for treeing samples are fragile and should be handled with utmost care. In case a dropped needle is to be used for any reason, the tip should be examined under microscope for damage before use.

4. Electric strength of a dielectric material

4.1 Introduction

In chapter 3, the care taken to prepare samples in a reproducible way has been described in detail. Similarly composite dielectrics need careful blending, and the importance of this is the subject of on-going work.

In this chapter the electric strength of the thin films of fabricated epoxy resin samples tested under DC (positive and negative) voltages as well as AC voltages is described. The electric breakdown strength of epoxy resin is quoted to lie between 25 – 45 kV/mm [162-163]. In reality, the breakdown strength of such a material is dependent on its intrinsic properties and other factors such the rate of voltage rise, surrounding medium, electrode configuration, contact pressure and environmental conditions during test [48]. Thus care has been taken to design a test cell to facilitate such a measurement following the guidance in IEC 60243 parts 1 and 2 [48, 164]. The developed system is described in the sections below.

4.2 The Test Cell Design

The designed test cell consists of 3 main parts, namely; the electrode system, the sample holder, and the oil bath. The test cell is designed such that the whole system is stable and no movement of either the electrode system or the cable attached to them is possible during experiments. The individual parts of the test cell are described below.

4.2.1 The electrode system

The electrode system consists of ground and top electrodes made of brass spheres of equal diameters (20 mm). It is ensured that the surfaces of the spheres are made smooth and free of any defect in order to prevent local field enhancement on the electrodes due to irregularities. The ground electrode is designed in a mushroom shape so that it can be easily secured in place in the sample holder as described in section 4.2.2. The top and the ground electrodes are provided with 4 mm screw (M4) tapped holes such that the HV cable and the ground (earthing) cables can be easily attached to the electrodes. The system is designed such that the arrangements of the electrodes are in common axis which is normal to the plane of the test sample as shown in Figure 4-1
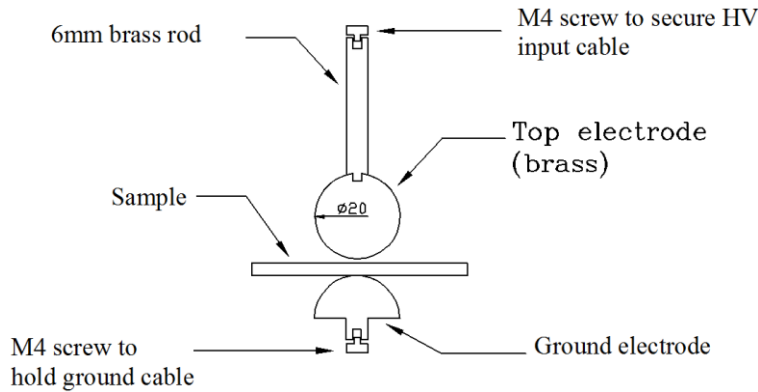
Figure 4-1: The electrode system configuration

4.2.2 The sample holder

The sample holder is carefully designed with the fragility of the samples to be tested in mind. It incorporates sample platforms which are aligned to the top of the ground electrode such that they are all in the same horizontal plane. This allows the sample under test to be placed on the sample platforms under no mechanical stress whilst being supported by both the sample holders and the ground electrode. Figure 4-2 shows the arrangement of the sample holder and its dimensions. A clearance stand and perforated holes for oil entry are provided underneath the sample holder to ensure that the sample holder can be lowered easily into and out of the oil bath with the ground cable attached to the ground electrode without disturbing the system.
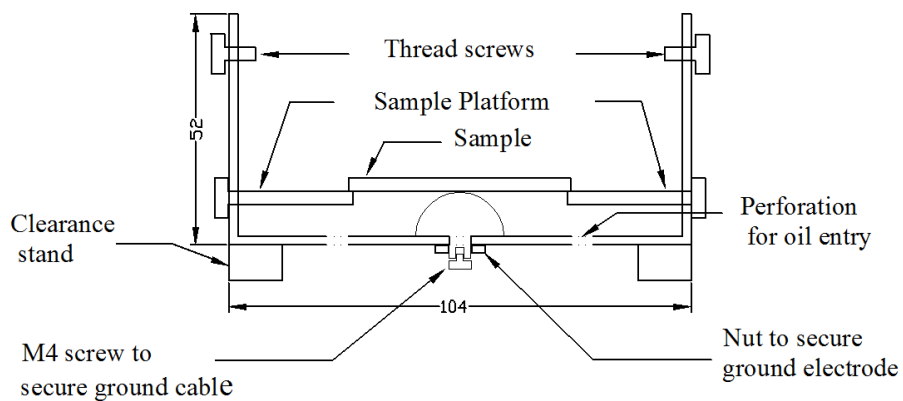
Figure 4-2: Sample holder design showing sample and sample platform.

4.2.3 The Oil Bath

The oil bath is made of a container of dimensions (164 x 122) mm and consists of two main features. One the feature is a 4 mm thick step made all around its inner base to secure the sample holder in position. The other feature is the HV rod holder made of nylon which is also centrally positioned on the oil bath lid. These two features are designed in such a way that when the sample holder is lowered into position, and the lid of the oil bath closed, the top and the ground electrodes will be axially aligned perpendicular to each other. The HV rod holder is made of nylon, with a central hole to allow the HV rod to freely slide in a perpendicular plane which allows the top electrode to sit on the sample under a uniform pressure. Also two nylon screws attached to the HV rod holder are used to secure the HV rod in position once it is lowered on to the sample. A weight attached to the HV rod is provided to ensure a uniform pressure on the sample. Figure 4-3 (a) and (b) show a schematic drawing of the whole test cell and a photograph, showing the sample holder lowered into the oil bath. It can be seen from the photograph that the HV input cable and the ground cable are attached to the electrodes ready for necessary connection.
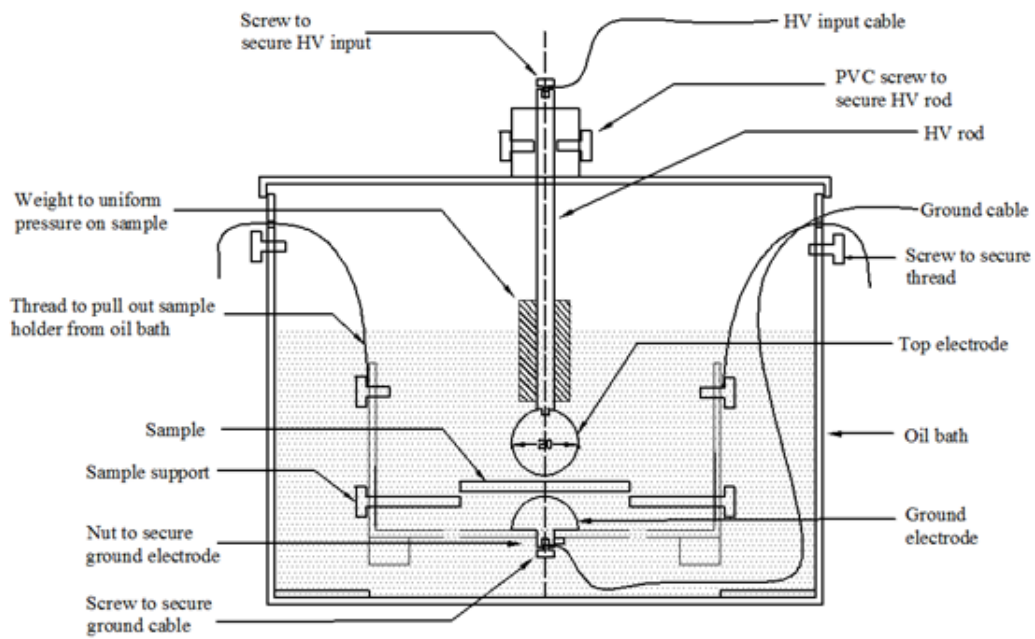
(a)
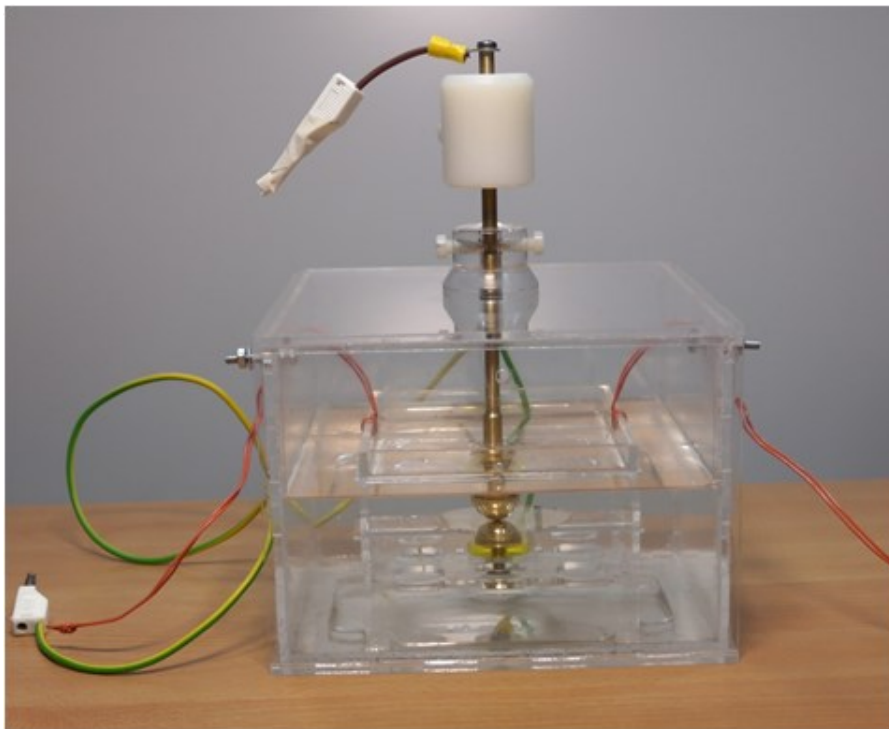
(b)

Figure 4-3: The schematic drawing and picture of the test cell system. Dimensions are given the main text.

4.3 Experimental details and test procedure

4.3.1 Test circuit

Figure 4-4 shows the test circuit employed for AC and DC breakdown tests. For the AC breakdown test, an 80 kV AC transformer was used, while for the DC breakdown test, a Brandenburg 100 kV reversible desk top DC power supply was used. A 10 MΩ current limiting resistor is connected at the output of the HV supply(s) to protect the HV supplies from damage during sample breakdown. The output voltages of the HV power supplies were monitored and measured via a 10,000:1 North Star voltage divider (VD100) and a digital oscilloscope.
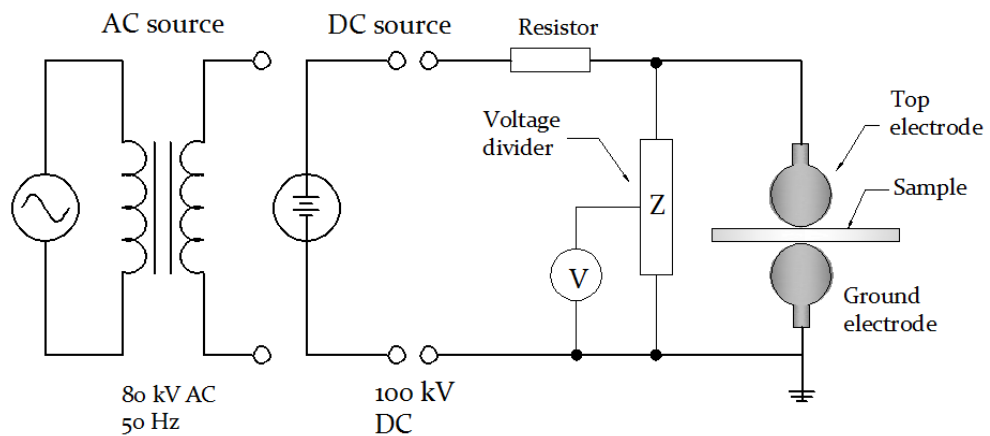
Figure 4-4: Schematics circuit diagram for AC and DC breakdown tests.

4.3.2 Sample configuration and test types

Figure 4-5 shows the configurations of the test samples for this investigation. The thicknesses of the samples range from about 100 μm to 250 μm. Details of sample fabrication method have been described in section 3.5.
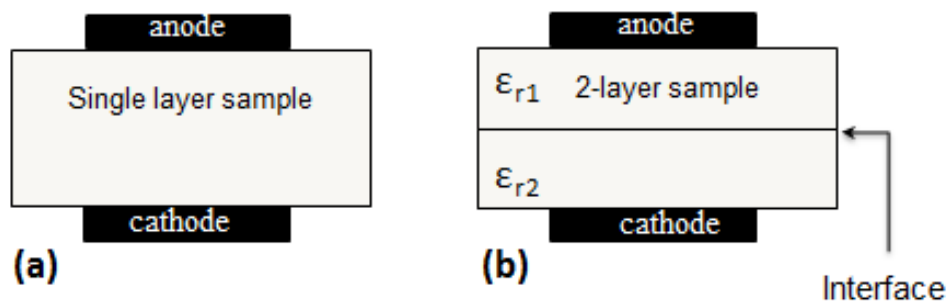
Figure 4-5: Sample configuration (a) single layer (b) double layer.

To obtain the optimal properties from the samples, the samples were preconditioned, followed by conditioning prior to any test as described in section 3.7.3. Single and double layer (epoxy-epoxy) samples were tested for three test types namely:

I.   DC breakdown tests in air.

II.   DC breakdown tests in oil.

III. AC breakdown tests in oil.

For each test type, four samples were tested for 40 breakdown sites (10 sites per sample). For DC tests, both positive and negative voltage polarity tests were carried out. A preliminary test (DC breakdown test in air) was carried out using commercially obtained Mylar (PET) films of 100 μm thicknesses used as reference samples and fabricated epoxy resin samples of about the same 100 μm thicknesses to compare the breakdown strength of the in-house fabricated samples. All tests were carried out at room temperature and the sample conditioning code for each test type is as follows [161] according to the nomenclature of section 3.7.3:

For breakdown test in Air;

- 4h/100°C + 24h/23±2°C/47%±5; M/23°C±2/47%±5

For breakdown test in Oil:

- 24h/85°C/0% + 72h/23±2°C/0%+4h/100°C + 24h/23±2°C/47%±5; M/23±2°C/47±5%

Figure 4-6 shows the test cell and bottles filled with silicone oil in an oven where they are kept at room temperature after conditioning prior to testing.

Figure 4-6: Oven where samples and test cell containing oil bath are kept at room temperature prior to testing after conditioning.

4.3.3   Voltage application

The test equipment shown in circuit diagram of Figure 4-4 is enclosed in a HV interlocked cage. Prior to voltage application, it is ensured that safety measures covered by the risk assessment for the experiment are strictly followed.

For either AC or DC tests, a continuously rising voltage is applied to the samples until the sample under test breaks down. The rate of voltage application is at about 1kV/s (manually controlled).

The sample under test is sandwiched between the HV and the ground electrodes as shown in Figure 4-1. The use of a digital oscilloscope allows the breakdown voltage to be accurately determined by recording the applied waveform after breakdown, and using the cursors to determine the peak voltage at which the breakdown occurred, as shown in Figure 4-7 by the dotted lines. After each test, the equipment is de-energised, and the system earthed by attaching earth stick on the output of the HV supply to ensure residual charges are taken to ground before any contact is made to the test equipment. The breakdown field is then determined as the ratio of the breakdown voltage and the thickness of the sample between the electrodes. Test results were then tabulated, and statistically analysed.
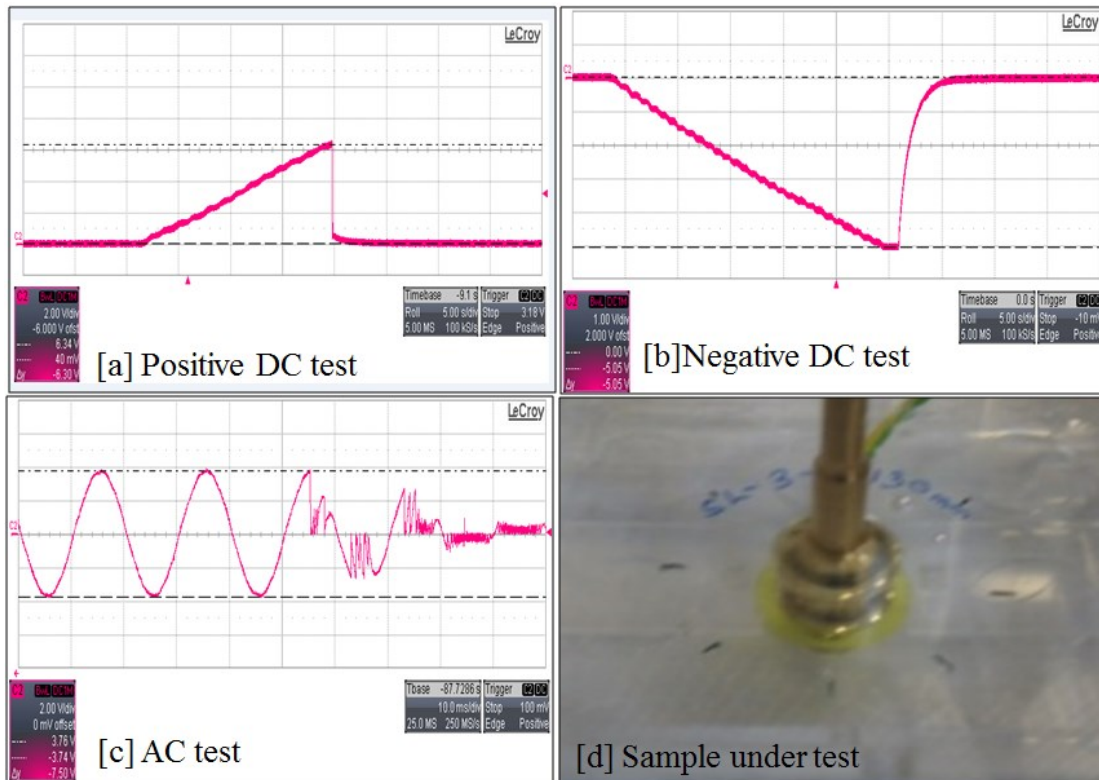
Figure 4-7: Captured waveforms during breakdown and a sandwiched sample between electrodes during test. Dotted lines on waveforms show peak voltages at breakdown.

4.4 Data representation and analysis

Data interpretation is the most important part of presentation and analysis of test results. Three statistical methods namely; Box and Whisker plots, Weibull plot and Student's "t-Statistics" are used in this study. Each method has its own merits and is briefly described below.

4.4.1 Box and Whisker plot

Box and whisker provides basic information about the data distribution, and allows visual comparison of two or more data set. The information that can be extracted from box plot is:

- The lower quartile (Q_L) representing 25% of the data set
- The upper quartile (Q_U) representing 75% of the data set
- The Median representing 50% of the data set
- The Mean of the distribution.

The height of the box represents about 50% of the data set which is the difference between the upper and lower quartile called the inter-quartile range. Whiskers are lines extending from the lower and upper quartile to the minimum and maximum value of the data set considered which indicates the spread of data outside the box, hence the name box-and-whisker plot.

Figure 4-8 shows a representation of a box chart with a normal distribution curve overlaid on the data set. In Figure 4-8 (a) all the data set are considered whereas in Figure 4-8 (b) the outliers are not considered thus reducing the length of the whisker in the lower quartile. Also a distribution with a negative skew would have a longer whisker in the negative direction than in the positive direction. This is also indicated by a smaller mean than the median as shown in Figure 4-8 (a) and (b).
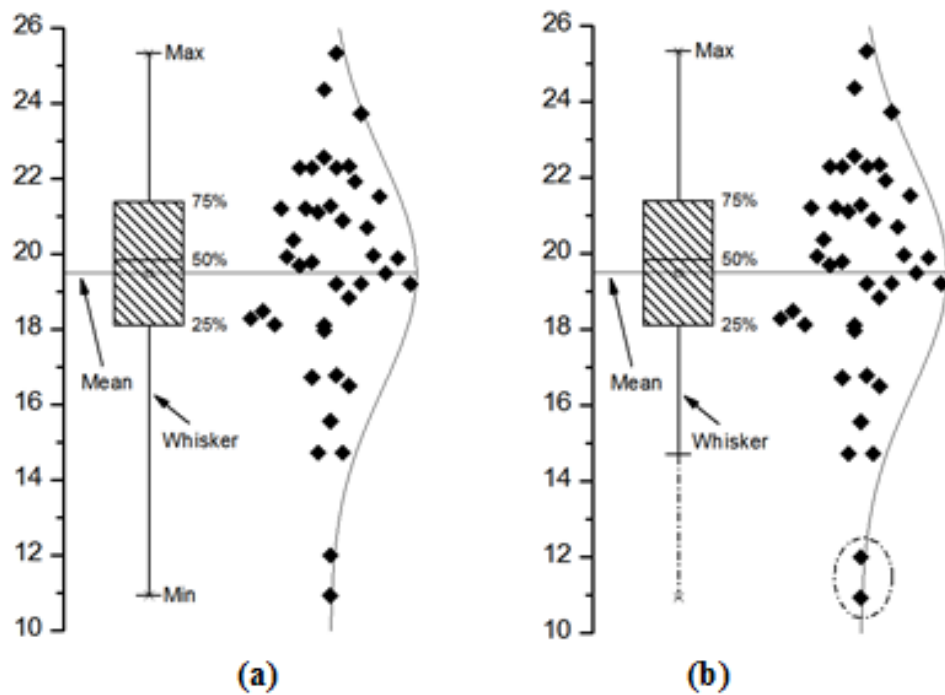
Figure 4-8: Box and Whisker plot description.

4.4.2 Weibull distribution

In engineering systems such as HV power cable design, it is inappropriate to expect high failure rates as cables are design to last in service for at least 50 years or more. Also negative values of failure times cannot occur. In such systems, the smallest extreme sample statistics such as Weibull is best used to model the failure modes

[165]. The Weibull expression for the cumulative density functions for two-parameters given by equation (4.1) is used for analysis:

$$P(t) = 1 - \exp\left\{-\left(\frac{t}{\alpha}\right)^{\beta}\right\}$$

(4.1)

Where P(t) is the probability of failure at a voltage or time less than or equal to t.

Equation (4.1) can be transformed into equation (4.2) given by:

$$\ln\ln[(1/(1-P(t))] = \beta \ln(t) - \beta \ln(\alpha)$$

(4.2)

Comparing equation (4-2) with straight line equation; y = mx + c, this gives:

$y = \ln\ln[(1/(1-P(t))]$; is the vertical scale, a highly non-linear function of the probability of occurrence of event representing the cumulative distribution function (CDF) describing the percentage of the test specimens that will fail at any time.

$m = \beta$; is the slope (shape parameter) of the line representing a measure of the spread of the distribution and may provide a clue of the failure mechanism [166]. Higher values of β, represent smaller variation across the data set (i.e. more deterministic).

$x = \ln(t)$; is the horizontal scale representing the logarithm of the measure of ageing or time to failure.

$c = -\beta \ln(\alpha)$; is the intercept, where α represents the characteristic value (scale parameter) which corresponds to age at 63.2% of the sample under test will have failed, and is often used as a key reference time for a data set rather than the mean.

From equation (4.2), a plot of y against x should produce a straight line from the data being analysed for a data set which fits the Weibull distribution. Figure 4-9 shows a typical plot from a measurement result on breakdown test on epoxy resin sample in this study. Where "B1", "B10" and "B63.2" are percentage life prediction at which 1%, 10% and 63.2% of the samples will have failed [166]. For example "B1", "B10" and "B63.2" correspond to 157 kV/mm, 200 kV/mm and 237.4 kV/mm breakdown fields respectively on the x-axis of the plot of Figure 4-9.
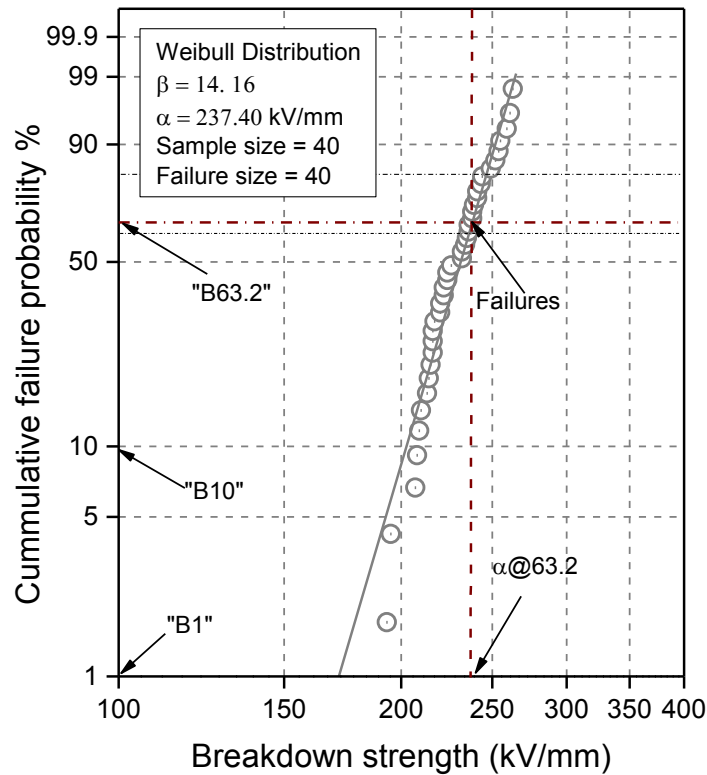
Figure 4-9: Weibull plot description.

4.4.3 Advantages of Weibull distribution

Weibull analysis provides a simple graphical solution from which life prediction and forecast can be made from small sample sizes. In engineering this is very important for cost effective component testing [166]. The slope (β) of the Weibull plot for constant stress tests indicates the mechanism of failure is present [166], where:

- (β) < 1.0 indicates infant mortality
- (β) = 1.0 means random failures (independent of age)
- (β) > 1.0 indicates wear out failure

The relationship between various values of the slope and the typical failure modes is shown in Figure 4-10.

1. Infant mortality
   - Inadequate burn-in, green run
   - Misassembly
   - Some quality problems
2. Random failures
   - Independent of time
   - Maintenance errors
   - Electronics
   - Mixtures of problems
3. Early wearout
   - Surprise!
   - Low cycle fatigue
4. Old age wearout (rapid)
   - Bearings
   - Corrosion
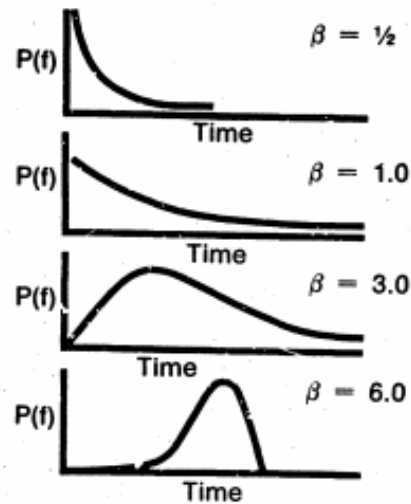
Figure 4-10: Typical failure modes plots, and suggested failure mechanisms responsible for each associated with different Weibull shape parameter values [166].

4.4.4 Student's t-Statistics

Student's "t-Statistics" allows comparison of the difference between the actual means of two data set in relation to the variability of the data set expressed as the standard deviation of the difference between the means given by equation (4.3) where; $\bar{x}$ is the mean given by equation (4.4), Sd is standard deviation of the difference between the means given by equation (4.5) and S^2 is the standard deviation of the data set given by equation (4.6).

$$t = \frac{\bar{x}_1 - \bar{x}_2}{Sd}$$ (4.3)

$$\bar{x} = \frac{\sum x}{n}$$ (4.4)

$$Sd = \sqrt{\frac{S_1^2}{n_1} + \frac{S_2^2}{n_2}}$$ (4.5)

94

$$S^2 = \frac{\sum x^2 - \left(\sum x\right)^2 / n}{(n-1)} \qquad (4.6)$$

It is worth noting here that; the student's t-test is really restricted to a Gaussian distribution. But the test results from such statistics will reasonably conform to a Weibull distribution, where the shape parameter of the Weibull is $\gg 1$ resulting in a highly peaked and narrow curve. See for example $\beta = 6$ in Figure 4-10.

Formulation of "t-Statistics" test: A null hypothesis is constructed based on the assertion that there is no difference between the means of the two data sets. The outcome of the t-test allows a statistical statement to be made with some level of confidence whether the assertion is true or not. It is calculated following below procedure [167].

1. List the data set for each test type to be investigated.
2. Record the number (n) of each test type (n_1 and n_2).
3. Calculate the degree of freedom [$(n_1 + n_2) - 2$].
4. Calculate the difference between the means of each data set ($\bar{x}_1 - \bar{x}_2$).
5. Calculate the standard deviation (S^2) of each data set as S_1^2 and S_2^2.
6. Calculate t-statistic value using equation (4-3).
7. Enter the t-table at [$(n_1 + n_2) - 2$] degree of freedoms at the appropraite column of a chosen level of significance (usually p = 0.05) and read the tabulated t value.
8. If the calculated *t- value* exceeds the tabulated value (*t-critical*) we say that the means are *significantly different* at that level of probability.
9. If the calculated t-value is less than or equal to the probability at p = 0.05, this means that the null hypothesis is correct.

A conclusion can be drawn with about 95% level of confidence based on this level of probability. But still there is about 5% chance of being wrong in reaching such a conclusion. Using t-statistic will allow a statistical statement to be made with a degree of accuracy, but cannot actually **prove** or **disprove** anything. For two tail test, the criteria for acceptance is that, the *calculated t- value* should be less or equal to the *t-critical value.* That is (-$t_{critical}$ < $t_{statistics}$ < $t_{critical}$), where t-critical is the highest t-value that when exceeded the hypothesis should be rejected. The critical value can be extracted from t-table at an appropriate degree of freedom for a chosen level of

probability (0.1% to 10%) considered for the study. Table 4-1 shows a typical t-test probability table.

Table 4-1: T-test probability table [168].

Degree of Freedom	Probability, P						
	0.1	0.05	0.02	0.01	0.005	0.002	0.001
1	6.3138	12.7065	31.8193	63.655	127.3447	318.493	636.045
2	2.92	4.3026	6.9646	9.9247	14.0887	22.3276	31.5989
3	2.3534	3.1824	4.5407	5.8408	7.4534	10.2145	12.9242
4	2.1319	2.7764	3.747	4.6041	5.5976	7.1732	8.6103
5	2.015	2.5706	3.365	4.0322	4.7734	5.8934	6.8688
6	1.9432	2.4469	3.1426	3.7074	4.3168	5.2076	5.9589
7	1.8946	2.3646	2.998	3.4995	4.0294	4.7852	5.4079
8	1.8595	2.306	2.8965	3.3554	3.8325	4.5008	5.0414
–	–	–	–	–	–	–	–
–	–	–	–	–	–	–	–
71	1.6666	1.9939	2.38	2.6468	2.8974	3.209	3.4329
72	1.6663	1.9935	2.3793	2.6459	2.8961	3.2073	3.4308
74	1.6657	1.9925	2.3778	2.6439	2.8936	3.204	3.4269
75	1.6654	1.9921	2.3771	2.643	2.8925	3.2025	3.425
76	1.6652	1.9917	2.3764	2.6421	2.8913	3.201	3.4232
77	1.6649	1.9913	2.3758	2.6412	2.8902	3.1995	3.4214
78	1.6646	1.9909	2.3751	2.6404	2.8891	3.198	3.4197
79	1.6644	1.9904	2.3745	2.6395	2.888	3.1966	3.418
80	1.6641	1.9901	2.3739	2.6387	2.887	3.1953	3.4164

Software packages such as Excel or OriginLab can be used to compute t-statistics and gives statistical parameters such as; the mean, standard deviation, variance, and the critical value etc. without using t-tables (manual calculation). Computation using these software(s) were validated with reference data from a test in this study.

A generated report from Excel at *p = 0.05* is shown in Table 4-2. It can be seen from Table 4-1, in the first column, that at degree of freedom of *78* the critical value at p = 0.05 is *1.9909*. The same value is generated in the Excel see Table 4-2 together with other statistical parameters required to either accept or reject the hypothesis at 5% level of probability. Since, the generated "t-Statistics" lies within the Critical t-value, i.e. *(-1.99 <0.80<1.99),* it can be infered with 95% level of cofidence that there is no significant difference between the means of positive negative DC polarity tests on the PET films (reference samples).

Table 4-2: Excel generated t-statistic parameters.

t-Test: Two-Sample Assuming Equal Variances		
Sample ID and statistical parameters	*PET Film SL-100 um DC test in air*	*PET Film SL-100 um DC test in air*
	Positive polarity test	*Negative polarity test*
Mean	232.545	229.225
Variance	373.226641	313.8711538
Observations	40	40
Pooled Variance	343.5488974	
Hypothesized Mean Difference	0	
df	**78**	
t Stat	**0.801048482**	
P(T<=t) one-tail	0.21276849	
t Critical one-tail	1.664624645	
P(T<=t) two-tail	**0.425536981**	
t Critical two-tail	**1.990847069**	

Also since the generated two-tail probability from Table 4-2 is **0.4255 (42.55%)** and is greater than 0.05 (5%), this implies that, the sample *mean* is within 1-Standard deviation of the mean **(μ-σ and μ+σ)** which is part of the 95% non-rejection region of the bell shape normal distribution curve [168] as shown in Figure 4-11. Thus the hypothesis cannot be rejected.
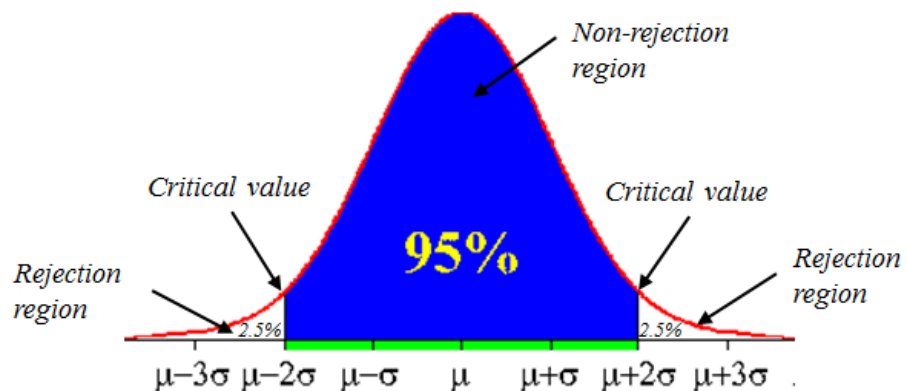
Figure 4-11: Rejection and no-rejection regions of t-statistics probability function [168].

The statistical methods introduced in this section are used for graphical representation of test results and data analysis in the section that follows. Test results

4.4.5 Single layer (SL) samples (reference and epoxy) of about ~100 μm thicknesses: AC and DC breakdown test in air and in oil

Figure 4-12 shows a box chart plots for breakdown strength of about 100 μm thick samples in air and in oil for AC and DC tests.
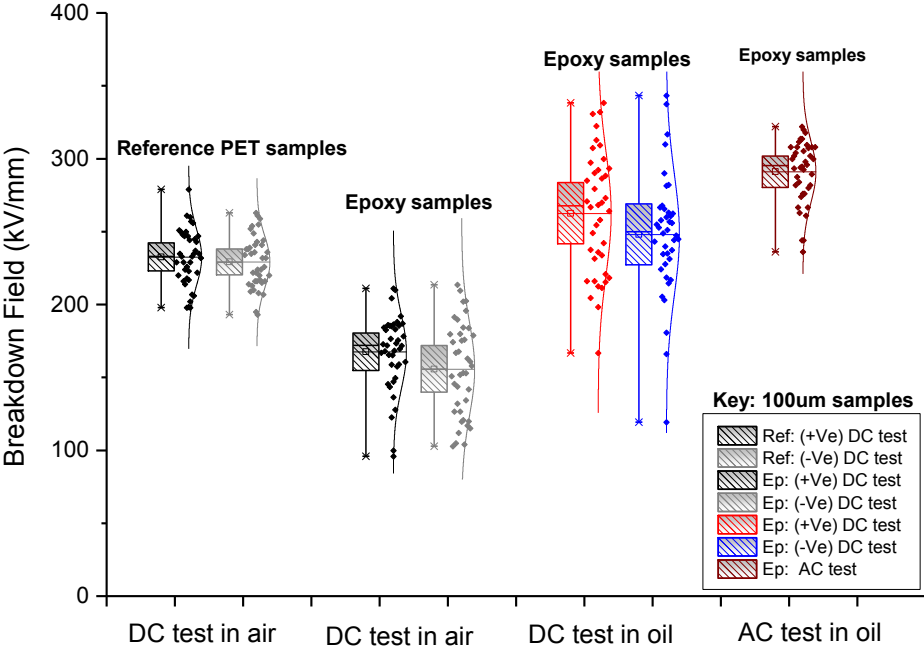
Figure 4-12: Box chart comparing average breakdown strength of single layer ref. and epoxy resin samples of ~100 μm thicknesses for AC and DC tests in air and oil.

DC test in air: This test compares the strength of the fabricated epoxy resin samples and that of the reference (PET) samples. It can be seen from Figure 4-12, that the breakdown strength of the reference samples of ~100 μm is higher than that of the fabricated epoxy resin samples of ~100 μm. The difference in average breakdown strength for positive and negative breakdown test is about 1.4% in the reference samples, where as in the Epoxy resin samples this difference is about 7%. Table 4-3 for tabulated averages of breakdown voltages and fields and Appendix A-1 to 6 for the tables of collated breakdown data for the entire tests. On average, the breakdown strength of the reference samples of ~100 μm is about 30% higher than that of the epoxy resin samples of about the same thicknesses for both positive and negative polarity tests.

AC and DC test in oil: This test compares the strength of epoxy resin samples of about 100 μm thicknesses for AC and DC tests. The strength of the epoxy resin

samples increases to about 9.5% on average for positive and negative polarity tests when the test was carried out in oil compared to the test in air. The positive polarity test value is about 5.5% higher than the negative polarity test value. On average however, AC tests in oil give mean values 45% and 12% higher than DC tests in air and in oil for both positive and negative polarity tests as shown in Figure 4-12.

Table 4-3: Collated average for breakdown voltages and fields for each test type.

Test type (I): DC Breakdown in Air				
Sample ID	Positive polarity test		Negative polarity test	
	BD Voltage (kV)	BD Field (kV/mm)	BD Voltage (kV)	BD Field (kV/mm)
SL-Pet-100μm	23.25	232.55	22.92	229.23
SL-Epoxy~100μm	19.48	167.52	16.97	155.78
Test type (II): DC Breakdown in Oil				
Sample ID	Positive polarity test		Negative polarity test	
	BD Voltage	BD Field	BD Voltage	BD Field
SL-Epoxy~100μm	31.34	262.58	31.9	248.05
SL-Epoxy~200μm	58.65	291.37	59.97	295.82
DL-Epoxy~200μm	58.63	272.82	57.38	280.26
Test type (III): AC test in Oil				
Sample ID	BD Voltage (kV)		BD Field (kV/mm)	
SL-Epoxy~100μm	29.06		291.05	
SL-Epoxy~200μm	37.03		182.83	
DL-Epoxy~200μm	37.87		181.49	

4.4.6 Single and Double layer (SL & DL) epoxy resin samples of ~200 μm thickness: AC and DC breakdown test in oil

Figure 4-13 shows the box chart plot of the results obtained for single and double layer epoxy resin samples of about 200 μm thicknesses for AC and DC tests in oil.

DC test: A difference of about 5.8% less in average breakdown strength is observed for double layer samples of ~200 μm compared with single layer samples of about the same thicknesses. However, the difference between positive and negative polarity tests for single and double layer samples of about 200 μm are 1.5% and 2.7% respectively with negative polarity test being higher in both cases.

AC tests: There is no significant difference in average breakdown strength between single and double layer samples of ~200 μm under AC test. However comparing the average strength of single and double layer samples of ~200 μm for AC and DC tests, it is observed that the average strength for AC test is about 38% and 34% lower than for DC test for positive and negative polarity tests respectively as shown in Figure 4-13.
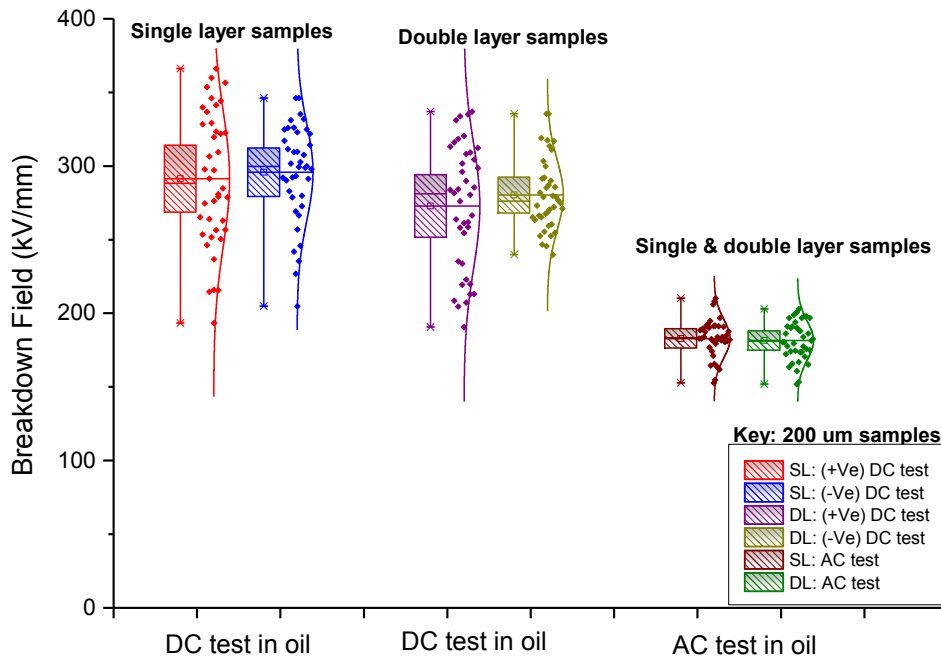
Figure 4-13: Box chart comparing average breakdown strength of single and double layer epoxy resins samples of ~200 μm thicknesses for AC and DC tests in oil.

4.5 Observed phenomena during breakdown tests

4.5.1 Nature of breakdown event

Figure 4-14 (a) and (b) show the electrodes-sample arrangements for tests in atmospheric air and in silicone oil. For test in atmospheric air, frequent sporadic discharge of arcs were observed in the region marked (*x*) in Figure 4-14 (a) prior to breakdown leaving a wide puncture and carbonisation at the edges of the puncture.
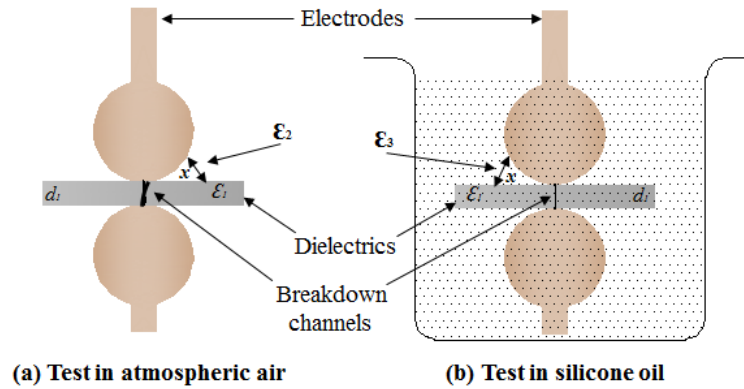
Figure 4-14: Influence of surrounding medium on breakdown channel on test samples. ε_1; is the permittivity of the test samples, ε_2; is the permittivity of air, and ε_3; the permittivity of silicone oil.

However when the test was carried out in oil, these discharges were occasional and in most cases, left a fine puncture as shown in Figure 4-14 (b) compared to the observation in Figure 4-14 (a). The explanation for this observation is that, the permittivity of air ($\varepsilon_2 = \sim 1$) is lower than that of the epoxy resin which is in the range of $2.5 < \varepsilon_1 < 4$ [169]. This results in a highly stressed region marked (*x*) in Figure 4-14 (a) and because air has a low breakdown strength, this is accompanied by many partial discharges in that region leading to the observed bigger puncture.

In Figure 4-14 (b) on the other hand, the permittivity of silicone oil is in the range $2.7 < \varepsilon_3 < 3.0$ which is slightly lower than that of the epoxy resin, and also the oil supresses partial discharges at the epoxy surfaces. Thus most of the surface discharges were eliminated in the region marked (*x*) in silicone oil leading to a fine puncture and higher breakdown field compared to the test in atmospheric air.

4.5.2 Apparent self-healing of test samples

Another observed phenomenon is the ability of the test sample to recover after initial breakdown and sustain the applied electric field for few seconds, followed by another breakdown event and so on as shown in Figure 4-15. This phenomenon is observed in both the test in air and in oil for single and double layer samples.
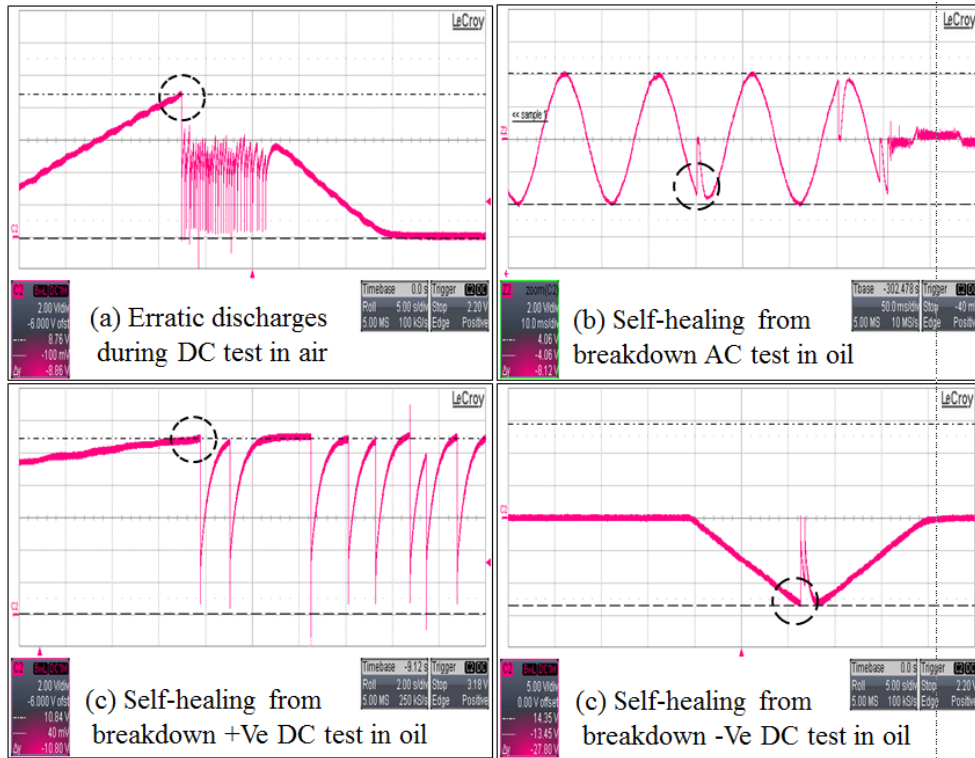
Figure 4-15: Captured waveforms showing erratic discharges (test in air) and self-healing events (test in oil) prior to complete breakdown of test samples.

For test in air, a continues sporadic discharges was observed after the initial attained peak breakdown voltage due to the lower breakdown strength of air surrounding the epoxy sample. After these sporadic discharges, the initial peak breakdown voltage is not attained again as shown in Figure 4-15 (a), and complete breakdown ensued afterwards. However, when the test was carried out in oil, after initial breakdown event, the sample recover for few seconds and sustained the initial peak breakdown voltage for few seconds followed by subsequent breakdown events as shown in Figure 4-15 (b), (c) and (d). The ability of the sample to recover the initial peak breakdown voltage is believed to be due to the fact that, the silicone oil surrounding the sample filled in the breakdown channel immediately after the initial breakdown and sustain the peak breakdown voltage only for few seconds before another breakdown ensued because the silicone oil less stronger than the epoxy sample.

It is the interaction of these surrounding media with the test sample that resulted in the differences observed in the recorded waveforms shown in Figure 4-14. The observed phenomenon during breakdown test in air is herein dubbed as "erratic discharges" while that during breakdown test in oil dubbed as "apparent self-healing"

of the test sample as the initial peak breakdown voltage is attained repeatedly before a complete breakdown ensued as shown in Figure 4-15 (b), (c) and (d).

4.6 **Weibull plots for breakdown strength test**

4.6.1 Test in air and oil for100 μm single layer (SL) samples
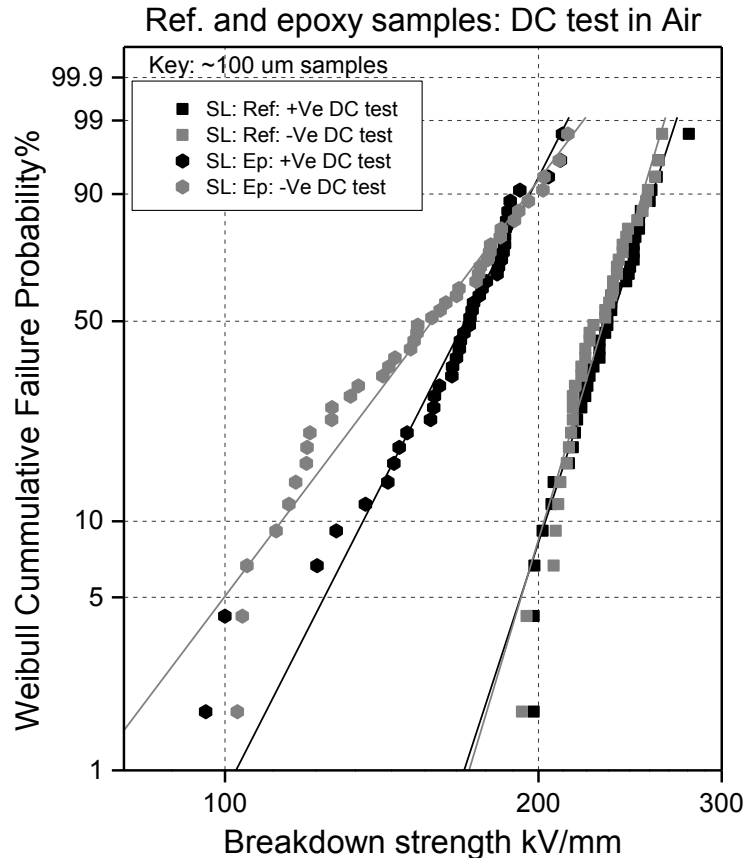
Figure 4-16: Weibull plots of short term breakdown strength of reference and fabricated epoxy resin samples for AC and DC field samples under AC/DC field.

Test in air: Figure 4-16 and Table 4-4 show the Weibull plots of 100 μm samples and the extracted Weibull parameters, where $\alpha_{E@63.2\%}$; is the breakdown strength corresponding to the cumulative failure probability at 63.2%, and β; is the shape parameter depicting the measure of deviation from the straight line of the plots. The β values are related to the material property as described in section 4.4.2. As can be seen from Table 4-4 the β values for the reference sample for DC test in air are 13.07 and 14.16; and the $\alpha_{E@63.2\%}$ values are 241.32 kV/mm and 237.4 kV/mm for positive and negative polarity tests respectively. The β values for the epoxy resin samples are 8.68 (+'Ve) and 5.66 (−'Ve) while the $\alpha_{E@63.2\%}$ values are 177.68 kV/mm (+'Ve)

and 168.66 kV/mm (–'Ve) which correspond to 26.4% and 29% lower breakdown strengths respectively compared with the reference samples. Comparing test in air and in oil between epoxy samples from Table 4-4, an average of about 37% is observed when the test was carried out in oil.

Table 4-4: Extracted Weibull parameters of Figure 4-16 and Figure 4-18.

Test type: AC and DC Breakdown strength in Air and in Oil for 100 μm samples				
DC test	Positive polarity test		Negative polarity test	
	α (kV/mm)	β	α (kV/mm)	β
Single Layer PET film 100 μm (air)	241.32	13.07	237.4	14.16
Single Layer Epoxy film ~100 μm (air)	177.68	8.68	168.66	5.66
Single Layer Epoxy film ~100 μm (oil)	280.26	7.23	265.04	6.56
AC test	α (kV/mm)		β	
Single Layer Epoxy film ~100 μm (oil)	300.22		18.1	

The lower values of β in the epoxy samples compared to that in the reference samples are indicative of defects or variations in the samples which are observed as deviation from the straight line on the Weibull plots. This observation may be due to the fact that the fabricated samples may contain some defects as the laboratory condition is not super clean. Figure 4-17 shows an in inspected fabricated epoxy sample under microscopic revealing void and some inclusions.
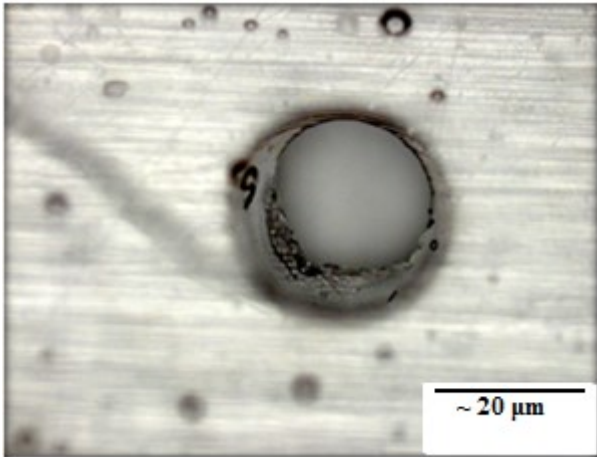
Figure 4-17: Inspection of fabricated epoxy sample under a microscope showing voids and other defects.

Breakdown tests in oil: Even though there is an increase in breakdown strength ($\alpha_{E@63.2\%}$) of about 37% for both positive and negative polarity tests when the test was carried out in oil compared to that in air, no improvement was observed in the

recorded values of β. This further indicates the fact that the fabricated samples are less clean compared to the commercially obtained reference samples.

AC tests in oil shows an improvement of 6.6% and 11.7% in $\alpha_{E@63.2\%}$ values for positive and negative polarity tests compared with DC tests in oil and the β values also show an improvement as shown in Table 4-4. Figure 4-18 below shows the Weibull plots for AC and DC tests in oil. Less deviation is observed from the plot for AC test compared to positive and negative DC polarity tests.
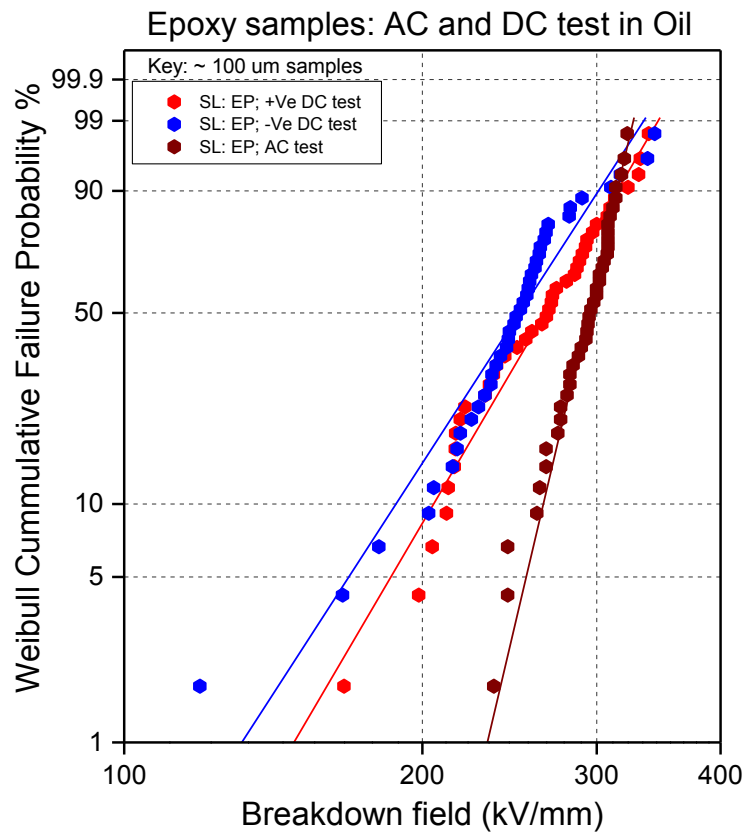
Figure 4-18: Weibull plots of short term breakdown strength of epoxy resin samples of about 100 μm thicknesses in oil under AC/DC field.

4.6.2 Test in oil for 200 μm single and double layer samples

DC breakdown tests on single and double samples: Table 4-5 below shows the extracted Weibull parameters from Figure 4-19. Polarity dependence on breakdown strength is insignificant between single and double layer samples under DC test. However, there is about 6% reduction in breakdown strength in the double layer samples when compared with the single layer samples. This value is similar to the

5.8% obtained in section 4.4.6 when computation is based on mean breakdown strengths, using box chart plot.

AC breakdown tests on single and double layer samples: AC tests on single and double layer samples followed similar trend as those in DC test showing no significant difference in the obtained $\alpha_{E@63.2\%}$ and β values. But comparison between AC and DC tests on this occasion show a significant reduction of about 39% and 35% in breakdown strength for AC test compared with DC for positive and negative polarity tests. This trend is opposite to what was observed in similar test with 100 μm thick samples where an increase in breakdown strength was observed see Figure 4-18.
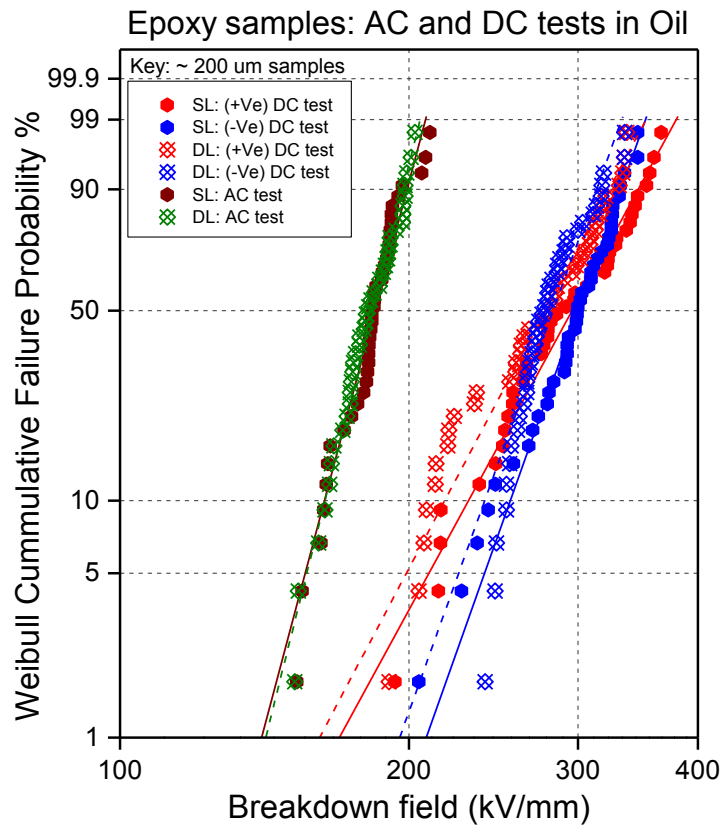
Figure 4-19: Weibull plots of short term breakdown strength of 200 μm epoxy resin samples under AC/DC field.

Table 4-5: Extracted Weibull parameters of Figure 4-19.

Test type: AC and DC Breakdown strenght in Oil for 200 μm				
DC test	Positive polarity test		Negative polarity test	
	α (kV/mm)	β	α (kV/mm)	β
Single Layer Epoxy film ~200 μm	310.49	7.58	309.52	11.64
Double Layer Epoxy film ~200 μm	290.62	7.82	291.7	11.5
AC test	α (kV/mm)		β	
Single Layer Epoxy film ~200 μm	188.72		15.57	
Double Layer Epoxy film ~200 μm	187.39		16.48	

4.7 Summary of test results

This chapter has presented test results for electrical strength of thin films of fabricated epoxy resin samples for short term AC and DC voltage stresses. Single and double layer samples were tested in air and in oil. Positive and negative polarity tests were carried out for DC and the effect of surrounding medium on breakdown event during the test was explained in section 4.5. Observed differences in breakdown strength using average values from box chart plots and cumulative breakdown strength at 63.2% using Weibull plots was discussed in section 4.6 and 4.7 respectively.

In this section statistical analysis using Student's "t-test" is used to summarised and draw conclusions for this study. Table 4-6, shows the summary of the "t-test" at 95% confidence level, comparing the difference between the means ($\bar{x}$) of positive and negative polarity test for each test type carried out in this study.

Table 4-6: Student's t-statistics test results on all test types.

t-Test: Two-Sample Assuming Equal Variances			
Samples ID and Statistical parameters	PET Film SL-100 um DC test in air		Epoxy Film SL- 100 um DC test in air	
	Positive test	*Negative test*	*Positive test*	*Negative test*
Mean	232.55	229.23	167.52	155.78
Variance	373.23	313.87	656.48	1013.21
Observations	40.00	40.00	40.00	40.00
Pooled Variance	343.55		834.85	
Hypothesized Mean Difference	0.00		0.00	
df	78.00		78.00	
t Stat	**0.80**		**1.82**	
P(T<=t) two-tail	**0.43**		**0.07**	
t Critical two-tail	**1.99**		**1.99**	
Samples ID and Statistical parameters	Epoxy Film SL 100 um DC test in oil		Epoxy Film 200 um DC test in oil	
	Positive test	*Negative test*	*Positive test*	*Negative test*
Mean	262.58	248.05	291.37	295.82
Variance	1767.12	1750.22	2064.82	1084.44
Observations	40.00	40.00	40.00	40.00
Pooled Variance	1758.67		1574.63	
Hypothesized Mean Difference	0.00		0.00	
df	78.00		78.00	
t Stat	**1.55**		**-0.50**	
P(T<=t) two-tail	**0.13**		**0.62**	
t Critical two-tail	**1.99**		**1.99**	
Samples ID and Statistical parameters	Epoxy Film DL-200 um DC test in oil		Epoxy Film 200 um AC test in oil	
	Positive test	*Negative test*	*SL- sample*	*DL- sample*
Mean	272.87	280.26	182.83	181.49
Variance	1800.46	588.25	171.23	171.98
Observations	40.00	40.00	40.00	40.00
Pooled Variance	1194.35		171.61	
Hypothesized Mean Difference	0.00		0.00	
df	78.00		78.00	
t Stat	**-0.96**		**0.46**	
P(T<=t) two-tail	**0.34**		**0.65**	
t Critical two-tail	**1.99**		**1.99**	

As can be seen in Table 4-6, all the computed "**t-Statistic values**" are less than the "**t-Critical values**" meaning the means ($\bar{x}$) of all the tests carried out are within the non-rejection region of the normal distribution curve for the test data of each test. The calculated probabilities also show how closer or far away each test is from the rejection region. For example, comparing the means ($\bar{x}$) of positive and negative polarity tests for the reference and the fabricated epoxy resin samples of about 100 µm thicknesses using the "t-test" when the test was carried out in air, yielded these

probabilities **0.43 (43%)** for reference samples and **0.07 (7%)** for the fabricated epoxy resin samples (Table 4-6). These results suggest that, the means ($\bar{x}$) of the reference samples are within 1-standard deviation of the normal distribution curve, while the means ($\bar{x}$) of epoxy samples are within 2-satandard deviation of the curve as shown by Figure 4-11. This suggests that the reference sample's data is more centred (smaller deviation) than the epoxy resin samples. See box chart plots for visual clarification.

The primary aim of this study is to compare the strength of fabricated layered epoxy-epoxy (double layer) to that of un-layered (single layer) of about the same thicknesses i.e. 200 μm. Student's t-test results (Table 4-6) on single and double layer of about 200 μm shows that there is no difference between the means of positive and negative polarity test for DC test in oil as well as that of the AC test in oil.

However, when the averages of the combined positive and negative polarity test for single layer (SL) samples and that of double layer (DL) samples were compared, the Student's t-test results shows that there is difference between their means ($\bar{x}$) as shown in Table 4-7.

Table 4-7: Student t-test results for averages of positive and negative polarity test on 200 μm Single and Double Layer samples.

t-Test: Two-Sample Assuming Equal Variances		
Sample ID and Statistical parameters	Single layer samples	Double layer samples
	Average of positive and negative polarity tests	*Average of positive and negative polarity tests*
Mean	293.59	276.56
Variance	983.80	650.38
Observations	40.00	40.00
Pooled Variance	817.09	
Hypothesized Mean Difference	0.00	
df	78.00	
t Stat	2.66	
P(T<=t) two-tail	0.01	
t Critical two-tail	1.99	

From Table 4-7, the calculated means ($\bar{x}$) for SL and DL samples are 293.59 kV/mm and 276.56 kV/mm respectively while the **"t-Stat"** value is **2.66** and the

"two-tail" probability is **0.01 (1%).** The "t-Stat" value **(2.66)** is greater than the "t-Critical" value of 1.99 at 95% confidence level. Meaning that, the null hypothesis can be rejected. Also the 1% two-tail calculated probability is within 3-standard deviation of the mean shown in by red colour at the tail ends of Figure 4-20 which is the rejection region and thus the null hypothesis can be rejected.
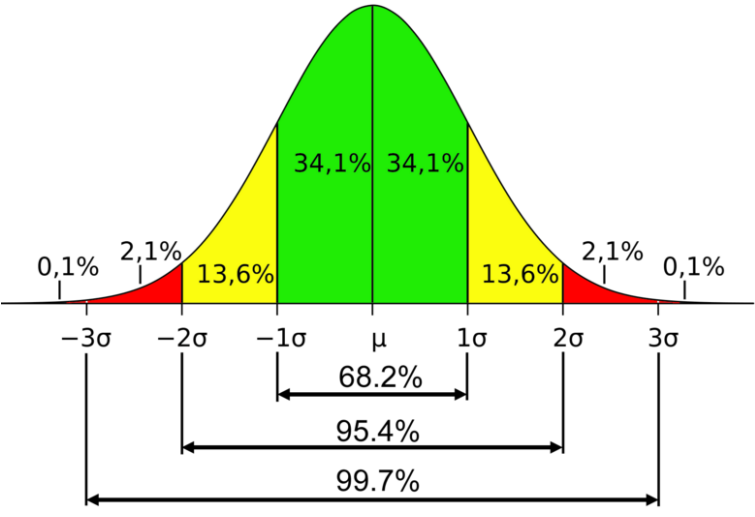
Figure 4-20: Normal distribution curve, rejection region within 3-standard deviation of the mean, non-rejection region within 2-standard deviation of the mean [168].

4.7.1 Conclusions

- The use of the three statistical methods described in section 4.4 was used to present data and analyse the test results. Data analysed from box chart plot and Weibull plot suggest that there is about 5.8% and 6% difference in breakdown strength between the single layer and double epoxy samples.

- Student's "t-Statistics" shows that there is no difference in breakdown strength between the means of positive and negative polarity tests for each test type (Table 4-6).

- Student's "t-Statistics" test shows that, there is difference in breakdown strength between single layer (SL) and double layer (DL) epoxy samples when the combined means of positive and negative polarity test for SL and DL samples were compared see Table 4-7.

This study shows that double layer sample are about 6% less strong compared to single layer samples. This 6% may be associated with defects (see Figure 4-17) in the

fabricated epoxy resin sample. Also many studies suggests that interfaces are regions were space charge are trapped [170-172], and could lead to modification and enhancement of local field which could result in the observed reduction in strength in the double layer samples. However this 6% difference is not big enough to suggest major difference between the single and double layer samples in this study. This study shows that layered material (interfaces) can prove to be strong when tailored properly and the assertion that interfaces are weak points needs to be investigated properly. In chapter 5, space charge dynamics in epoxy resin samples of similar configurations as in this Chapter are investigated to further clarify the impact of space charge at the interface in relation to the results obtained in this Chapter.

5. Space charge measurements

5.1 Introduction

In this chapter, space charge measurements are reported on plaque samples of about the same configuration and thickness as in Figure 4-5. The main aim here is to investigate the difference between charge dynamics in single and double layer samples and find out if the presence of interfaces in the double layer samples has an influence in the recorded lower DC breakdown strength obtained for double layer samples in the study carried out in Chapter 4.

The need to characterise the internal electrical properties of solid dielectrics resulted in the development of several space charge detection techniques [7, 74-75] as mentioned in section 2.9. Among these techniques, the Pulse-Electro Acoustic (PEA) method is the most widely used as it allows the charge distribution in the stressed solid dielectrics to be observed non-destructively [71, 76].

A report by CIGRE WG D1.24 on dielectric properties of XLPE/SiO$_2$ Nanocomposites [173], shows work on high field material characterisation was radically enhanced by the use of space charge measurement. This work shows cooperative test results from research institutions all over the world where the space charge measurement was used as one of the important tool for material characterisation.

Although this technique has been used for many years, the results obtained from such measurement differs from one institution to the other depending on the resolution of measurement system and the measuring procedure adopted as reported in [173]. For this reason, a standard was published in 2012 for the PEA measurement technique in order to standardised measurement procedures [174].

In this study, a PEA system has been designed and developed under the guidance of Dr. Antonois Tzimas as one of the tools for material characterisation. The hardware part of the system was designed and constructed at the University of Manchester while the software for signal processing was originally developed in LabView by Dr. M. Fu at the University of Leicester. The system is briefly described in sections that follow.

5.2 Description of a PEA system

Figure 5-1 shows the schematic representation of the PEA system for measuring plaque samples. The system developed in this study is based on the published works of Alison [71] and Maeno et al [175]. The system consists of three main parts:

1. The top electrode unit which houses the high voltage circuitry consists of a coupling capacitor (Cc = 220pF), series resistor (R_{dc} = 1MΩ) and a cylindrical electrode. The coupling capacitor prevents the applied DC from flowing towards the pulse generator while the series resistor prevents the pulse energy flowing towards the DC supply. Thus both the pulse energy and the DC are applied to the sample when energised.

2. The ground electrode is made of 10 mm thick polished aluminium plate which serves as the acoustic guide and a delay line for acoustic wave propagation.

3. The sensor unit which houses a piezoelectric transducer is made of polyvinylidene fluoride (PVDF) for detecting the generated acoustic pressure wave.
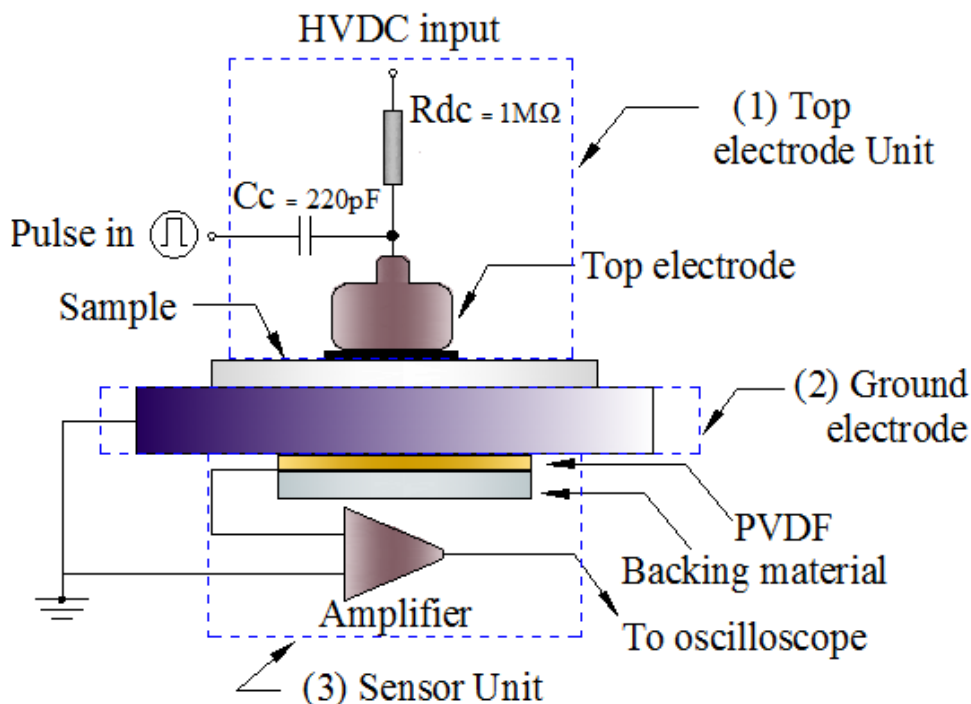
Figure 5-1 : Schematic representation of the PEA measurement system.

Even though the PEA system is easier and safer to set up compared to the other techniques [85], careful selection of components and equipment is necessary for the proper functioning of the system.

The main equipment and components required for setting up a functioning PEA system are: A high voltage DC supply, a pulse generator, a high voltage capacitor and resistor, through which the pulse and DC voltage are applied, a transducer for detecting the generated pressure wave signal, a wide-band amplifier for signal amplification, a wide band digital oscilloscope and a PC for signal recording and processing. Theories regarding system performance and components selection are extracted from [57, 76], and are described below.

5.3 **Functions of equipment and components of a PEA system**

HVDC supply: The main functions of the HVDC source in the PEA system is for polling the sample under test to induce surface charges σ(0) at the ground electrode, σ(d) on the top electrode seen as two peaks on the output signal [57, 85], and to induce space charge ρ(z) in the sample if the field exceeds the threshold for charge injection between 10 kV/mm and 20 kV/mm in PE based materials [43-44, 88].

Pulse generator: The purpose of the pulse generator is to launch a perturbation force on the charges in the sample. This is achieved by applying a short and narrow HV electric pulse $ep(t)$ through the coupling capacitor, to the sample. The internal charges then react to the pulsed voltage to produce a mechanical force $F = qE$. This mechanical force causes an acoustic wave $p(t)$ related to the charge distribution $\rho(z)$ to propagate through the ground electrode to the detection unit.

Takada reported in [85] that, the first condition for obtaining the approximate space charge distribution is that, the width of the HV pulse generated ΔT_p should be much shorter than the transient time ΔT_s given by equation (5.1):

$$\Delta T_p << \Delta T_s = \frac{d}{u_{sa}} \tag{5.1}$$

Where d is the sample thickness and u_{sa} is the acoustic velocity in the sample. It is assumed in this case that, the applied electric pulse $e_p(t)$ is a delta function which

acts as a probe, and thus the detected voltage signal $v_s(t)$ at the transducer is directly proportional to the charge distribution across the sample.

Coupling capacitance: The need for the coupling capacitance is to ensure that most of the applied pulse voltage appears across the sample. The value of the coupling capacitance C_c can be calculated from the knowledge of the sample capacitance C_{sa} from equation (5.2). The design requirement as indicated in [57] suggests that, the coupling capacitance C_c shown by (5.3) should be much larger than the value of the sample capacitance given by equation (5.2).

$$C_{sa} = \frac{\varepsilon_0 \varepsilon_r A}{d} \tag{5.2}$$

$$C_c \geq 100 \times C_{sa} \tag{5.3}$$

Thus for example, the sample capacitance C_{sa} of epoxy specimen of $\varepsilon_r = 3.5$, $\varepsilon_0 = 8.854 * 10^{-12}$ and of thickness 1 mm can be calculated using equation (5.2) to be 2.43 pF, where A is the area of the top electrode of diameter 10 mm in contact with the sample. Therefore, $C_c \approx 243$ pF using (5.3). Thus a 220 pF capacitor is selected for this system.

Series resistor Rdc: As shown in Figure 5-1, the current coming from pulse generator can flow in the direction of the DC source or towards the top electrode to the test sample. The current that contributes to the space charge measurement is the current that flows to the test sample. As such, the value of the series resistor should be large enough to allow most of the current to flow into the test sample rather than DC source.

It is reported in [57], that the value of the series resistor R_{dc} (5.4) should be about 500 times larger than the impedance of the sample capacitance C_{sa}, where f_p given by equation (5.5) is the main frequency component of the pulse voltage and ΔT_p is the pulse duration.

$$R_{dc} >> 500 * \frac{1}{2\pi f_p C_{sa}} \tag{5.4}$$

$$f_p = \frac{1}{2\Delta T_p} \tag{5.5}$$

The duration of the pulse generator employed in this system is 10 ns. Thus the minimum value of the series resistor to be selected is calculated to be 0.65MΩ. Thus a 1MΩ series resistor was selected for this design.

Transducer (PVDF) thickness: The condition for selecting the thickness b of the transducer is given by equation (5.6) where ΔT_p is the duration of the pulse voltage and u_b is the velocity of sound in the transducer. From the manufacture's data sheet [176], the acoustic velocity in PVDF is 2250 m/s. Thus using equation (5.6) the value b is calculated as 22.5 μm and so 9 μm thick PVDF is selected.

$$b \leq \Delta T_p u_b \tag{5.6}$$

The PVDF device is essentially a microphone which detects the acoustic pressure wave and transforms it into an electrical signal $q(t)$. This signal is amplified and recorded by an oscilloscope for further processing required because of signal reflections and attenuations in the system.

Amplifier and oscilloscope: Usually the electric signal $v_s(t)$ detected at the transducer is very small, in the region of 10-100 μV [57]. Thus a high gain wideband amplifier is required for signal amplification. In this system, a high gain (40dB) wide band (500 MHz) amplifier supplied by Miteq, is used for signal amplification and a Lecroy LC 334 Am 500 MHz with a sampling rate of 2GS/s is used for signal recording.

5.4 System resolution

The resolution of a PEA system is highly dependent on the duration of the electric pulse ΔT_p and is defined by equation (5.7) as:

$$\Delta l = u_{sa}\Delta T_p$$
$$\tag{5.7}$$

Where Δl is the spatial resolution and u_{sa} is the velocity of the acoustic wave in the sample [76]. The duration ΔT_p of the pulse generator employed in this system is

10 ns. Thus for example if a sample in which the acoustic velocity of 2000 m/s (LDPE) [76], is used in the system, then theoretically the resolution of the system is about ~20 μm.

In practice however, the system resolution can be reduced by several microns due to dispersion and attenuation of the acoustic signal during propagation towards the transducer, and thus signal processing (deconvolution) is required to recover the real space charge profile [76].

5.4.1 Deconvolution

As mentioned above, the electrical signal $v_s(t)$ detected at the transducer is very small, as such a wide band amplifier is employed to boost signal before it is recorded by the oscilloscope. The frequency response of the transducer and the amplifier can act as a high pass filter resulting in signal distortion and can be misinterpreted as space charge [177]. The PEA system can be viewed as linear time invariant system (LTI) [86-87], where the response of each sub-system (HV equipment and detecting equipment) is cascaded together into one system and the output response is recovered by de-convolution from a known input signal. Detailed mathematical treatments and procedures for signal deconvolution can be found in [57, 76, 85-87].

5.5 Assembly of the developed PEA system

Figure 5-2 (a) and (b) show the assemply of the PEA system in this study. As mentioned in section 5.2, the system comprises of the top electrode unit, the ground electrode, and the sensor unit. The assembly is breifly described below.

5.5.1 The top electrode unit

The top electrode unit is cylindrically designed with aluminium of internal and external diameters of 65 mm and 72 mm respectively and of height 52 mm. The internal diameter of 65 mm allows samples of diameters up to 60 mm to be used in this system with an applied DC voltage up to 10 kV without flashover between the top electrode and the ground. The HV circuitry consisting of capacitor and resistor are connected up with the top electrode within the unit as shown in Figure 5-2.

The diameter of the top electrode is 10 mm and is designed to have rounded edge to prevent discharges at high applied voltage. This 10 mm diameter is the effective area

of the top electrode that is in contact with the sample, and could be used to calculate the sample capacitance. The top electrode is insulated and held in position using polytetrafluoroethylene (PTFE). The high voltage DC input connection point is provided at the top of the unit, and the connection for the electric pulse is provided on the side of the unit via 50Ω BNC connector as shown in Figure 5-2 [(a) and (b)].

5.5.2   The sensor unit

The sensor unit is also cylindrically designed using 6 mm thick aluminium and houses the piezoelectric transducer (PVDF). The sensor is one of the most important parts of the signal detection in the PEA system. The PVDF is an electret having poled positive and negative charges on each side and can be easily shorted if not carefully handled during cutting and assembling. Details of how to handle the PVDF employed in this system can be found in [176]. The PVDF is carefully cut to 10 mm diameter and assembled in a 25 mm cylindrical aluminium casing as shown in Figure 5-2 (a).

To reduce signal reflection and match acoustic impedance, a 10 mm PMMA rod evaporated with aluminium having similar characteristics as the PVDF [57] is used as backing material and for continuity of signal transmission to the amplifier. The whole assembly is secured with two screws at the back of the ground plate directly opposite, and in-line with, the HV top electrode as shown in Figure 5-2 (a). The whole system (coaxial cable connecting the amplifier and the sensor together with other connecting cables) is well-shielded to reduce high frequency electromagnetic noise arising from the energised system. The system is shown in Figure 5-2 below.
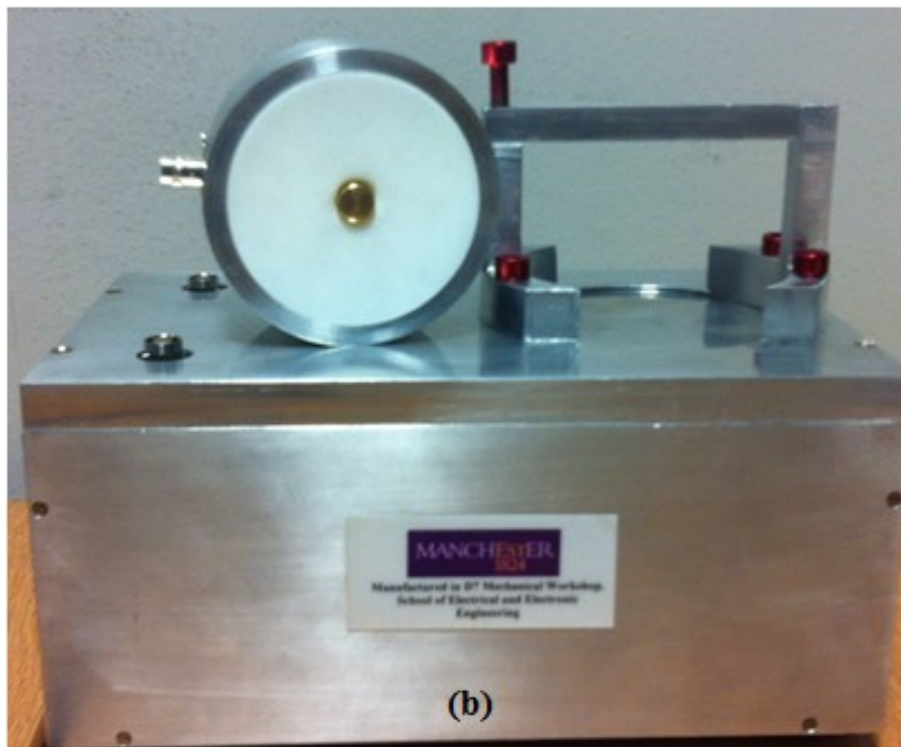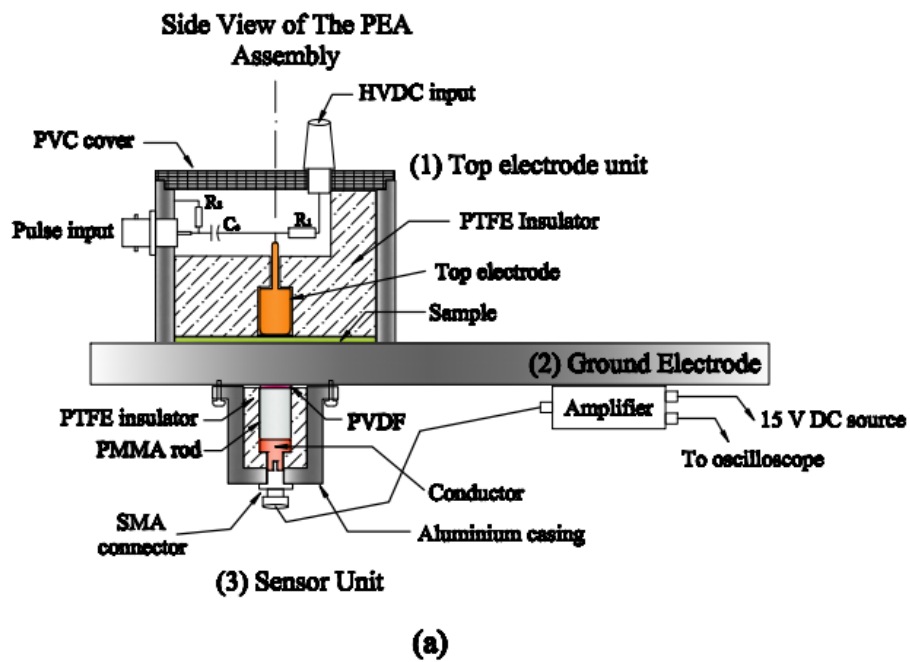
Figure 5-2: (a) and (b): Schematic side view and finished design of the PEA system.

5.6 Experimental details and test procedure

5.6.1 Test procedure

Single layer (SL) and double layer (DL) epoxy-epoxy interface samples of thicknesses 219 µm and 212 µm respectively were used in this study. Prior to the test, the samples were conditioned as outlined in section 3.7.3, wiped clean and then placed between the upper and the ground electrodes. A drop of silicone oil was applied between the ground electrode and the test sample in order to aid propagation of pressure wave signal at interfaces between electrodes and sample. The electrode-sample arrangement is shown in Figure 5-1. The top electrode unit is placed on the sample using adequate force to keep the sample tight and in contact with the electrodes using the clamping bracket shown in Figure 5-2 (b).

Measurements were taken with a voltage ramp rate of 1 kV/min in the first 8 minutes, on each sample, and the voltage was kept at 8 kV for 12 hours in each case. The voltage was switched off, and charge decay measurements taken. The semicon plaque was used as the anode and aluminium bottom electrode as the cathode. The calibration voltage was 1.5 kV DC. A de-convolution technique in LabView was used to process the data and recover the original signal. Figure 5-3 shows the complete set up for the experiments.
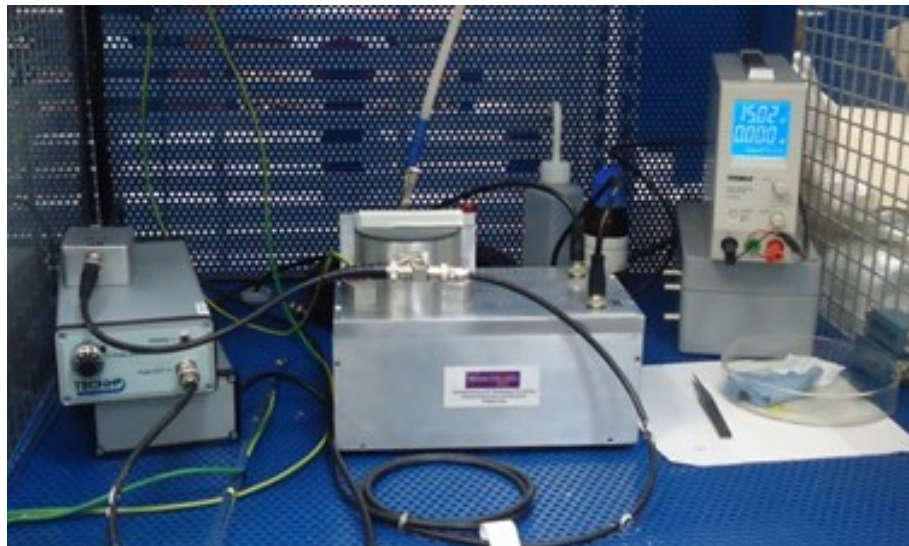
Figure 5-3: Experimental set up for space charge measurement.

5.7 **Test results**

5.7.1   **Single layer sample**

Figure 5-4 (a), (b) and (c) show the profiles of charge distribution obtained for the single layer epoxy sample under poling field of 37 kV/mm.
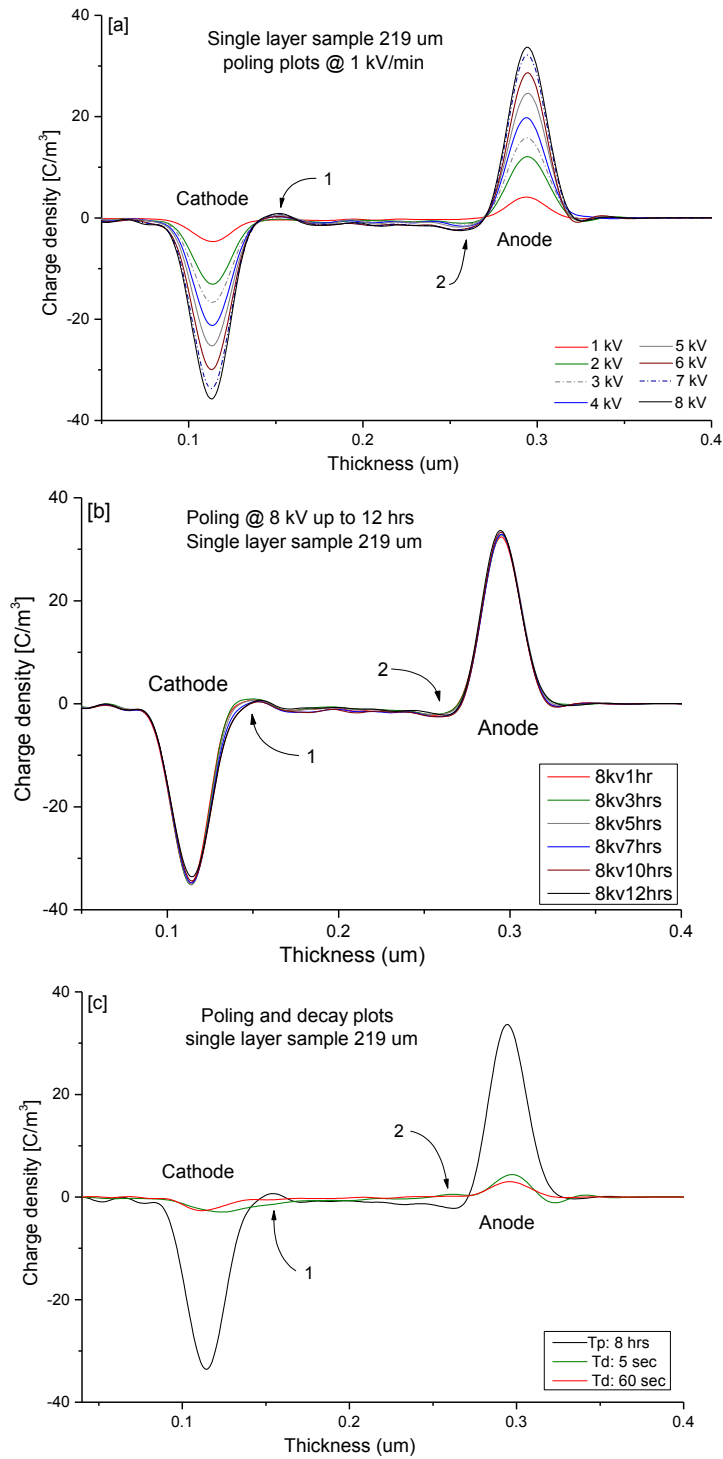
Figure 5-4: Space charge profile for single layer sample poling and decay plots.

In Figure 5-4 (a), a proportional increase of surface charge in response to increasing applied voltage is observed from 1 kV to 8 kV. Also a gradual accumulation of hetero-charges can be seen next to the electrodes as the poling voltage is increases as shown by arrows 1 and 2 in Figure 5-4 (a).

One hypothesis of the observed space charge behaviour is associated with homo-charge injection at the anode and cathode where bipolar charges travel across the bulk of the sample and get blocked at the opposite electrodes. The second one is the draft of ionised species in the sample. They could also accumulate due to different charge injection and extraction rates at the electrode-material interface.

Figure 5-4 (b) shows the plots when a DC field of 37 kV/mm was maintained across the sample for 12 hrs and measurements taken at few hours intervals. No charge accumulation is observed in the material bulk except a little increase in hetero-charge next to the cathode shown by arrow 1, and a reduction in what appeared to be hetero-charge next to the anode shown by arrow 2. Charge draft by ionisation is not considered as the reason for the observed in Figures (a) and (b) but rather a bipolar injection where a charge of opposite polarity get blocked at the electrode and accumulate as shown by arrows 1 and 2 in figure 5-4 (a) and by arrow 1 in figure 5-4 (b).

Figure 5-4 (c) shows poling (Tp) and decay (Td) plots. In the poling plot, an applied voltage of 8 kV (37 kV/mm) is maintained for 12 hours, followed by a charge decay measurement at 5 and 60 sec when the poling field is removed. It can be seen that the accumulated hetero-charges decay quickly suggesting that these charges reside in shallow trap depths.

5.7.2   2-layer sample

Figure 5-5 (a) (b) and (c) show the profiles of charge distribution obtained from 2-layer epoxy-epoxy sample of thickness 212 μm.
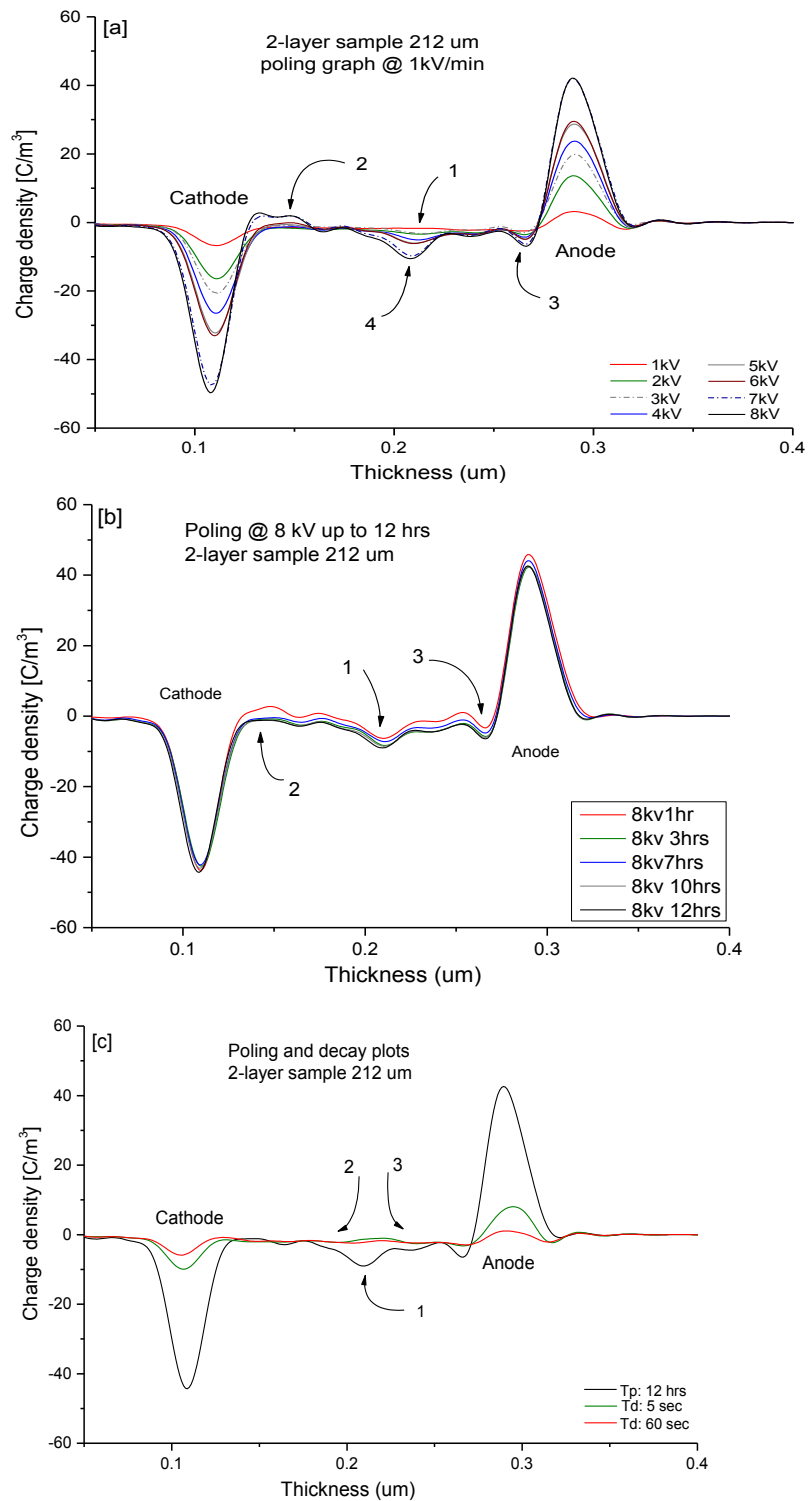
Figure 5-5: Space charge profile for 2-layer sample poling and decay plots.

124

In Figure 5-5 (a), only capacitive charges are observed at the electrodes at 1 kV. However beyond 2 kV, negative space charge is observed to be trapped at the layer interface as the poling voltage was increased from 2 kV up to 8 kV shown by arrows 1 and 4. It appears that the anode attracts negative charges while the cathode attracts positive charges which accumulate at their vicinities as hetero-charges shown by arrows 2 and 3.

Figure 5-5 (b) shows the plots when the poling field of 38 kV/mm was maintained for 12 hrs and measurements taken at few hours intervals. In contrast to what was observed in Figure 5-4 (b), in Figure 5-5 (b), hetero-charge formed next to the anode are maintained (arrow 3) and those formed next to the cathode (arrow 2) drift towards the anode where most of the them are trapped at the layer interface shown by arrow 1.

Figure 5-5 (c) shows a plot of poling (Tp) for 12 hrs followed by subsequent charge decay (Td) measurement at 5 sec and 60 sec when the voltage is switched off. Again as observed in Figure 5-4 (c), trapped negative space charges at the layer interface shown by arrow 1, have substantially decayed and diminished after only 60 sec. These negative charges are attracted away from the layer interface towards the electrodes shown by arrows 2 and 3 and may be neutralised by positive charge species during this process via recombination.

5.8 **Summary**

In this chapter space charge dynamics in single and double layer epoxy samples were presented. In single layer sample Figure 5-4 (a), only capacitive charges were observed at the electrode-dielectric interface which increases in magnitude with increasing voltage up to 8 kV, and also a gradual accumulation of hetero-charges next to the electrode and explained as bi-polar injection process [178]. Space charge is not observed in the material bulk, when the material was stressed for 12 hrs at 37 kV/mm as shown in Figure 5-4(b). However, an increase and decrease in hetero-charge next to the cathode and anode shown by arrows 1 and 2 Figure 5-4(b) was observed. When the poling field was removed the observed charge decay quickly within 60 seconds Figure 5-4(c) suggesting that injected charge were in shallow trap sites.

In Figure 5-5 (a), the effect of interface charging is clearly seen as net negative space

charge as the voltage is being increased from 2 kV and above. Increase in the net negative space charge was not observed at the interface even though the poling field of 38 kV/mm was maintained for 12 hours. However charge dynamics towards the anode was observed resulting in hetero-charge accumulation next to the anode shown by arrow 3 Figure 5-5(b), and subsequent decrease in negative net charge accumulation at the layer interface as shown by arrow 1 Figure 5-5 (b). Figure 5-5 (c) also show a fast decay of the accumulated charges at the layer interface when the field was removed confirming that the charges were in shallow depth traps.

5.8.1 Conclusion

Evidence of charge trapping at the layer interface was observed in Figure 5-5 (a) and (b) which was not observed in Figure 5-4 (a) and (b), suggesting that layer interface provides location for charge traps. This phenomenon was observed by many researchers in layered materials [170-172, 179-180]. However, care should be taken not misinterpret, acoustic reflection at the interface as charge traps [181-182]. In this case with matched materials this is not an issue.

Depending on the trap depth, these charges can remain trapped at the interface for long or short time depending on conditions such as field magnitude and temperature, and will eventually control the conductivity of the material. In the presence of defects such as voids and protrusions, higher local fields are generated due to difference in permittivity and conductivity under AC and DC conditions, which can results in other ageing mechanisms such PD activity and electrical treeing which may reduce the breakdown strength of the material. This study suggests that, the 6% reduction in DC breakdown strength for double layer samples in chapter 4 may result from space charge accumulation at the layer interface.

Space charge is also thought to be key to electrical tree growth rates in solid polymeric insulating materials. In chapter 6, electrical tree degradation in solid polymeric materials using point to plane sample geometries is investigated under various voltage stress conditions.

6. Long term electrical breakdown of insulating materials through treeing: Development of experimental methods

In Chapter 3, the method by which samples were prepared for electrical tree experiments has been described. This chapter describes the system developed for monitoring long-term treeing degradation and breakdown in solid insulating material.

6.1 Development of experimental methods

Developing a high voltage testing experiment requires careful choice of equipment with regard technical details and system requirement. Such a system must be capable of satisfying the intended experimental needs. For electrical treeing, the system must be capable of integrating both the high voltage and monitoring (imaging and PD detection) equipment without influencing experimental results.

6.2 Test equipment

For the study of electrical treeing using AC, DC and AC superimposed on steady DC voltages, the use of an Arbitrary Waveform Generator (AWG) integrated with an HV amplifier was found to be the most appropriate due to the flexibility of signal generation and control. The choice of imaging system must be such that it is capable of detecting the smallest possible electrical tree (initial tree growth of about ~10 μm) while the PD detection system should be sensitive enough to be able to detect PD levels of about (0.1-to-0.7) pC [134].

A similar system had been previously built at the University of Manchester [157]. The system developed in this study is an improvement of the previous system, providing better sensitivity of discharge measurement. Table 6-1 shows the summary of equipment specifications which are briefly described below.

Table 6-1: Summary of equipment specifications.

Equipment specification		
AWG: NI PCI 5421	Dimension	(L: 342 x W: 107 x D: 20) mm
	Bandwidth	43MHz
	Slew rate	(1620V/µs)**
	Output Voltage range	0 to ± 6 Vpk
	Gain	
Pre-amplifier: AD811	Dimension	(L: 9.91 x W: 7.87) mm
	Bandwidth	120MHz
	Slew rate	2500 V/µs
	Output Voltage range	
	Gain	plus 2
	Input voltage range	
HV amp: Trek® PD 06035	Dimension	(H: 914 x W: 430 x D: 870) mm
	Bandwidth	DC to greater than 4.0 kHz
	Slew rate	Greater than 725 V/µs (753.6 V/µs)**
	Output Voltage range	0 to ± 30 kV DC or peak AC
	Gain	3000V/V
	Input voltage range	0 to ± 10 V DC or peak AC
**Calculated Slew rate: Sr = 2πfVpk ; where f = equipment bandwidth and Vpk = peak output voltage		

6.2.1 Low voltage waveform generation

A PCI-based arbitrary waveform generator (AWG) NI 5421 [183] supplied by National Instruments was used for waveform generation. This AWG features 8 MB on-board memory, with a sampling rate of 100 MS/s (Million Sample per seconds) coupled with 16-bit ($2^{16} = 65536$) resolution with a maximum output voltage of ±6 V peak. These features allow a wide range of waveforms (periodic and non-periodic) to be generated or created and downloaded on to the on-board memory (8Mb) of the AWG. The AWG came with Soft Front Panel (SFP) software which allows flexible and interactive controls of generated waveforms. Also the NI PCI 5421 can be programmed via LabView platform for more flexible control.

6.2.2 Voltage amplification

The PD06035 HV amplifier supplied by Trek® [184], was selected for voltage amplification. This HV amplifier is a DC-stable, high voltage power amplifier with a high slew rate (725V/µs) designed to provide precise control of output voltages and currents over ranges specified in Table 6-1. The amplifier is configured as non-inverting with a fixed gain of 3 kV/V, which requires maximum input voltage of ±10 V peak to generate the maximum 30 kV peak at the HV amplifier output.

6.2.3　Pre-amplification

The maximum output from the NI PCI 5421 is ±6 V peak while the maximum input to the HV amplifier is ±10 V peak see Table 6-1. To obtain the maximum input to the HV amplifier, a non-inverting pre-amplifier was designed to have a gain of 2 using AD811 [185] capable of accurately reproducing the waveforms generated by the AWG (NI PCI 5421) was implemented. The bandwidth and the slew rate of the pre-amplifier are adequate for accurate reproduction of the waveforms generated by the AWG without distortion as shown in Table 6-1. Figure 6-1 shows the photograph of the implemented pre-amplifier circuit. Details of components specification and circuit diagram can be obtained from [185].
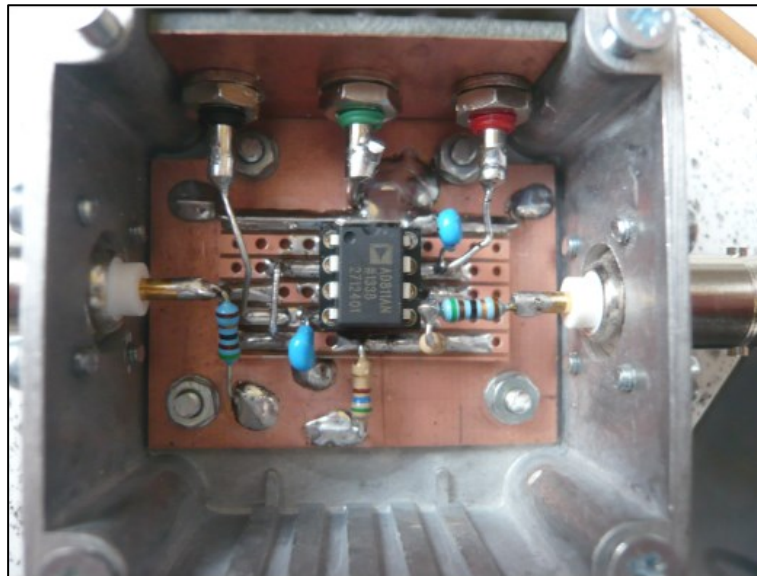
Figure 6-1: Photograph of the designed and implemented pre-amplifier.

6.2.4　Purpose built PC

The physical dimensions of the AWG detailed in Table 6-1 does not fit into a normal desk top or tower PC. Thus a purpose built PC was assembled for this test facility. The PC is loaded with LabView, Soft Front Panel (SFP) and Common Vision Blox (CVB) software from which both the HV amplifier and the image grabbing capability of the CCD camera can be controlled.

6.2.5　Imaging equipment

Capturing an electrical tree image in the initial stages of its growth (tree length of about 10 μm), requires very good and sensitive imaging equipment. Usually, cameras incorporating a highly sensitive Charge-Coupled Device (CCD) and an image

capture interface known as frame grabber are employed [127, 149, 157, 186]. For this research, an Allied Vision Technology (AVT) CCD camera, Manta G-504B monochrome progressive area scan was selected [187]. This camera is Gigabit Ethernet (GigE) vision compliant which can acquire Power over the Ethernet (PoE) and uses Common Vision Blox (CVB) camera suite for image acquisition. LabView platform can also be used to provide functionality as the CVB. The camera has the following specification:

- 2/3" Progressive scan CCD sensor

- Resolution; 2452 (W) x 2056 (H) pixel with 3.45 μm pixel size

- Active sensor size: 8.5 mm x 7.1 mm

- Frame rate: 9 frames/s (at full resolution)

- Digital output via GigE Vision Standard

- Output formats: Mono 8/16

- Lens mount for C-Mount (optional CS-Mount)

C-mount Qioptiq Macro CCD lenses 8x and 6x magnifications [188] supplied by Stemmer Imaging with a working distance of 75 mm having a (1.0 x 0.8 and 1.4 x 1) mm maximum field of view were employed. The choice of these lenses is to provide a detailed view of the needle tip and to enable detection and capture of a shortest possible tree length during experimentation. Also a telecentric C-mount lens with 6(W) x 5(H) mm dimension was employed to capture the whole tree growth event i.e. from initiation to breakdown. The camera was mounted on an X-Y mechanical stage to allow easy focussing on the needle tip in both X and Y direction.

6.2.6   Lighting

A DC light capable of providing intense and diffuse illumination was employed in order to eliminate image flickering, and have a clear view of the needle tip. A makeshift filter of white paper was attached to the light screen to achieve uniform illumination.

Figure 6-2 shows the schematic of the experimental set up and the integration of the equipment necessary for electrical treeing test. The part drawn enclosed in the solid line is the low voltage and monitoring side. This part is equipped with an

oscilloscope, a preamplifier and purpose built PC for monitoring and equipment control. The equipment drawn enclosed in the dotted line is in an HV interlocked cage and consists of a Trek HV amplifier, the test cell, and the CCD camera.
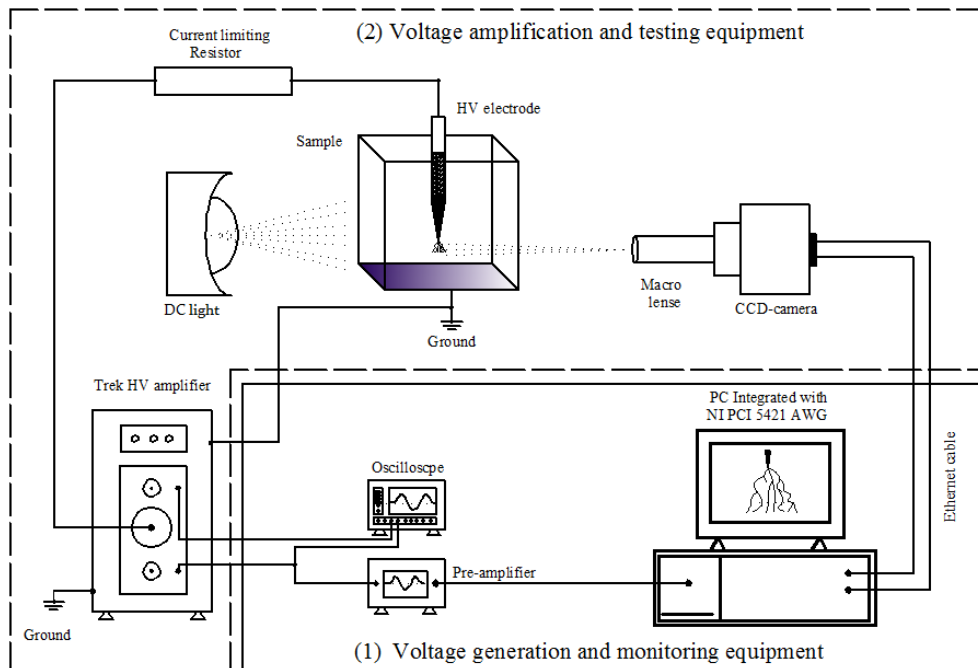
Figure 6-2: Electrical tree set-up; (1) - Low voltage side, (2) - High voltage side. Equipment is within interlocked high voltage enclosure.

6.3 **Partial discharge detection**

The two main methods of partial discharge detection are the straight and balanced circuit techniques [65]. The balanced technique has the benefit of mitigating noise levels and providing increased sensitivity compared to the 'straight' detection method. But the balanced detection technique is considerably more complicated. Researchers have used either the balanced [134, 157, 158], or the straight [77, 144, 189] detection techniques with varied levels of sensitivity depending on the experimental conditions (i.e. whether the equipment is housed in a shielded room/Faraday cage or not). A balanced circuit according to the IEC 60270 standard [62] shown in Figure 6-3, was employed for this study as in the previous studies [157, 158] at the University of Manchester due to the high level of recorded background noise (25 pC ≤ noise ≤ 30 pC) when the straight detection method was employed. This was mitigated to (10 pC ≤ noise ≤ 11 pC) using the balanced circuit approach and further reduced to ±5.5 pC by increasing the amplification gain to 50 pC in the designed amplifier filter circuit after the balanced circuit [157].
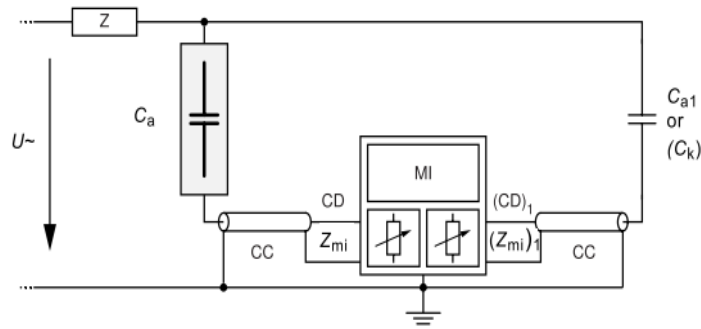
Figure 6-3: The balanced detection circuit IEC 60270 [62].

The components of the balanced circuit are:

- (U~); the high voltage supply.

- (Z); a filter at the high voltage side to mitigate background noise.

- (C_a and C_{a1}); are the test and dummy samples, having similar capacitance.

- ($Z_{mi,}$); are the input impedances of the measuring system.

- (CD); the coupling device which is part of the balance circuit.

- (CC); are the connecting cables.

- (MI); is the measuring instrument.

The balanced circuit designed by a previous PhD student in [157] is shown in Figure 6-4. In his system, the detected signal from the balanced circuit is fed to an amplifier and a filter before using NI card (5112 PCI) to acquire the PD data for processing via LabView and Matlab for phase resolved partial discharge (PRPD) plots.
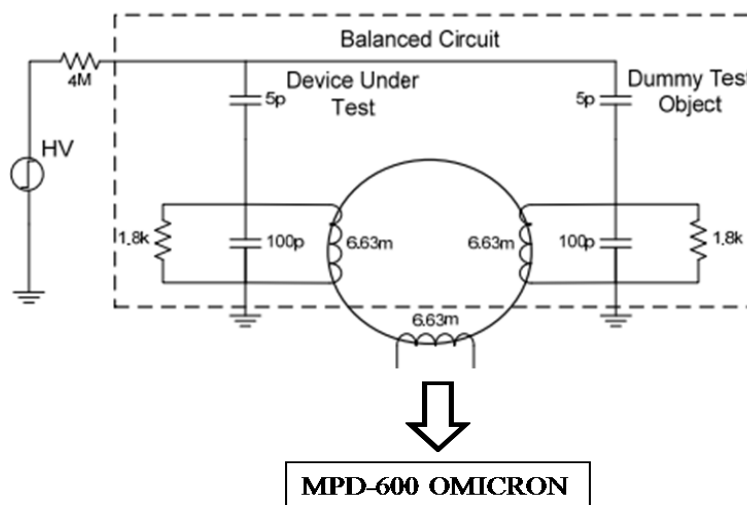
Figure 6-4: The implemented balanced circuit and the amplifier-filter stages [157].

In this study, the balancing circuit shown in Figure 6-4 was used, but the measuring instrument (MI) was replaced by a digital measurement device MPD 600 acquired from Omicron electronics GmbH for PD data acquisition and analysis [190]. The Omicron is a robust wideband (9 kHz to 3MHz) system that offers recording and post-processing analysis of the PD stream. Measurement is carried out at a centre frequency of 250 kHz and 300 kHz bandwidth for compliance with IEC 60270 [190].

The schematic of the measurement system developed in this study is shown in Figure 6-5. The test and dummy sample have similar capacitance as they are essentially the same. The test sample has a point needle in it to generate a divergent high field and encourage tree growth, while the dummy sample is cast with needle having a semi-spherical ending designed to provide a more uniform field in order to prevent electrical tree growth or partial discharges within the sample. The low voltage sides of the test and dummy sample are connected to the input of the balanced circuit.

On energising the system, the discharges (current pulses) in the sample, which have been separately shown to be coming from the test sample alone, are detected by the measuring impedance of the balance circuit, the output of which is then connected to the detection system (MPD 600) at the BNC input marked "(PD)" in Figure 6-5. The BNC marked "(V)" is connected to the output of the voltage divider for voltage reference. The output of the detector is connected to a USB controller via a fibre optic cable which connects PC loaded with Omicron software for PD data storage, visualisation and post-process analysis.
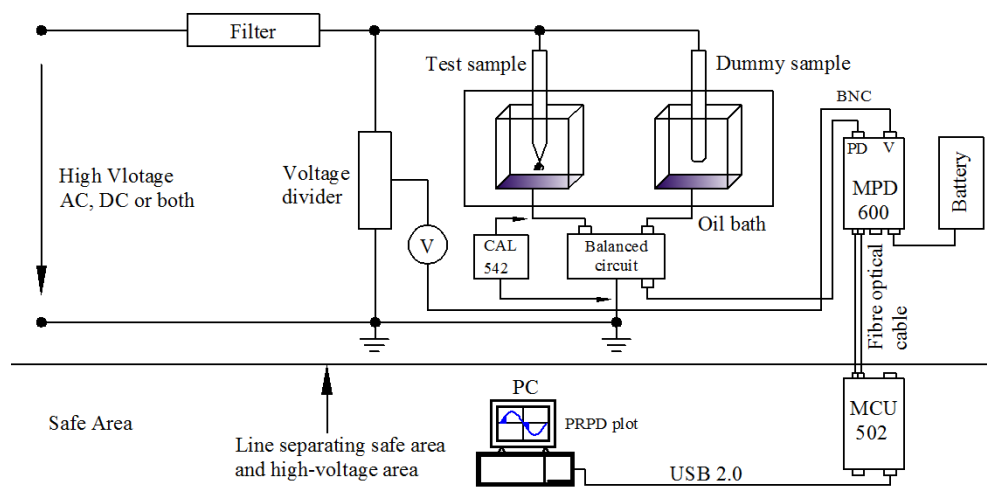
Figure 6-5: Measurement system developed in this study.

6.3.1 System limitation and background noise mitigation

Even though a balanced circuit was implemented, the peak level of background noise lies in the range of 2.0 pC ≤ noise ≤ 5.0 pC when the overall system is connected up with the high voltage amplifier energised at zero voltage. The main aim of partial discharge measurement is to monitor the ageing of an insulation construction non-destructively [65]. In such circumstances, the accuracy of the detection system and evaluation of a measured discharge magnitude is an important parameter in revealing any latent defect.

The minimum magnitude of partial discharge quantity which can be measured in a particular test is in general limited by background noise (disturbances). IEC 60270 standards [62] stipulate that, the level of background noise be less than 50 % of partial discharge magnitude under investigation. Thus in any measurement system, steps should be taken to reduce the background noise as low as possible to permit a sufficiently sensitive and accurate measurement in order to unmask any harmful discharges from the background noise.

In this study, the following steps were taken in order to further mitigate the recorded background noise:

- Copper tubes were used as connecting rails from the high voltage source to the test sample in order to achieve corona free connection.

- A 10MΩ resistor was used as filter to suppress any discharges that may be coming from the high voltage source and interference from the electrical mains.

- A crocodile clip previously used for connecting the high voltage source to the sample was eliminated.

- A cylindrical solid copper rod with diameter equal to the internal diameter of the connecting copper rail which ends in a spherical dome with a groove screw for securing the needle from the sample was designed specifically to ensure good electrical connection and to ensure corona free measurement in the set-up as shown in Figure 6-6

- Finally the whole equipment is grounded with the lighting system wrapped with a grounded chicken wire to shield it against electromagnetic interference.

These changes resulted in a reduction from the earlier recorded background noise of 2.0 pC ≤ noise ≤ 5.0 pC to between 0.25 pC ≤ noise ≤ 0.35 pC.
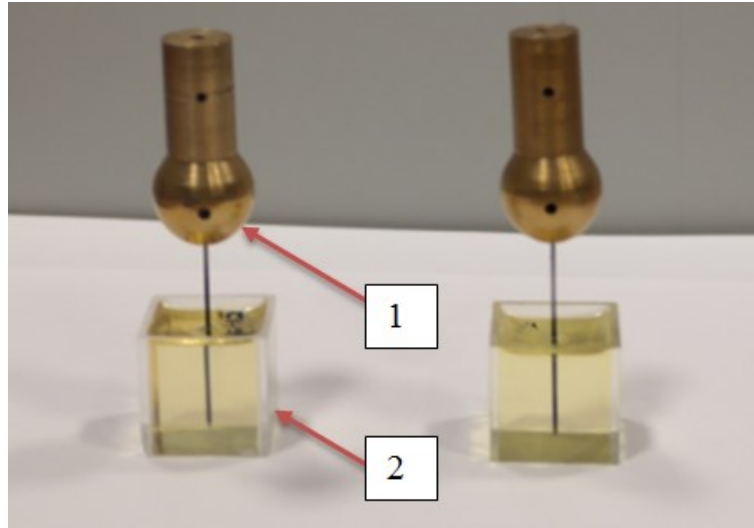
Figure 6-6: Designed system for ensuring corona-free electrical contact with the sample. [1] HV-needle connection point [2] Cured epoxy resin sample.

Kreuger stated in [65], that unwanted discharges can emanate from wires, sharp points, or even from unclean laboratory floors when testing at high voltages. The reduction of background noise achieved due to the changes implemented in section 6.3.1 above re-enforces Kreuger's point.

6.4 Integration of system's hardware and software

6.4.1   Hardware Integration

Figure 6-7 shows the photograph of the experimental set up showing all the hardware employed. This equipment is enclosed in safety high voltage interlocked cage and consists of the following:

1. A current limiting resistor which also serves as filter for noise suppression.

2. Connecting copper rails which connect the sample under test and a North Star voltage divider VD-100 (not shown) with standard ratio of 10,000:1 for voltage monitoring via an oscilloscope.

3. The high voltage amplifier with the output cable plumbed into 20 mm diameter PVC conduit to provider mechanical support which is terminated onto the resistor via copper tube.

4. Monochrome AVT CCD camera fitted with telecentric lens mounted on adjustable scissor platform.

5. The knob of the X-Y mechanical stage attached to the camera which allows manual focussing of image in X-Y direction.

6. Both the Qioptiq macro and Telecentric lens employed for image capture during tree initiation and propagation.

7. Test cell/oil bath incorporating both the test and dummy samples immersed in silicone oil to prevent surface discharges and flash over during testing.

8. Partial discharge detection instrument (MPD 600 and battery) showing fibre optic cable through which the measured data is transferred to the computer for processing and storage.

9. DC light for illuminating the sample under test and the test cell.

10. In-cage monitor to aid focussing of the needle tip from inside the cage.
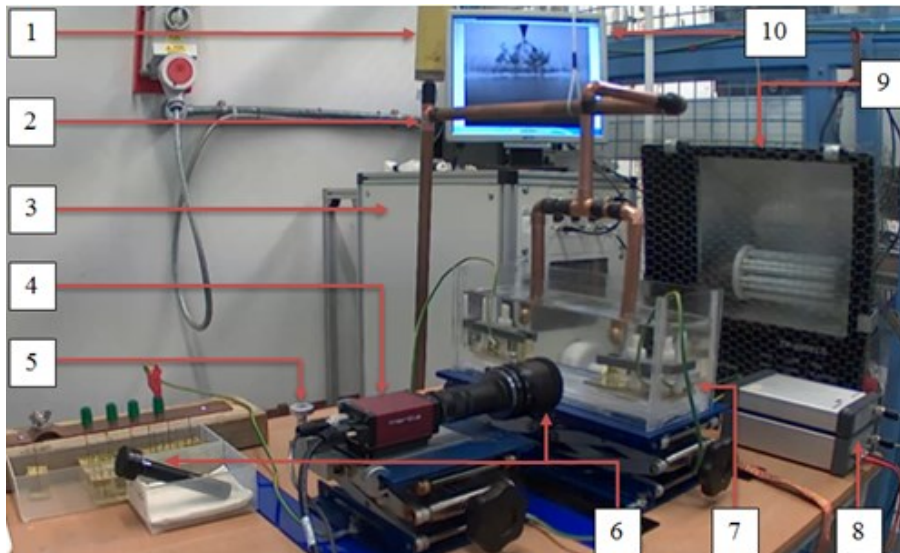
Figure 6-7: Photograph of integrated hardware assembly. Items are detailed in the main text.

6.4.2 Software integration

Figure 6-8 shows the screen shots of integrated software. The waveform generation is managed via a LabView platform, while the image capture is managed through

136

common vision blox (CVB) software. The phase resolved partial discharge (PRPD) data capture is managed via Omicron software which offers real-time visualisation of the measurement stream and post-processing capability. These software(s) were installed on a purpose built PC from which the entire test facility shown in Figure 6-7 is controlled. The screen shots were captured during acceptance test of the experimental setup.
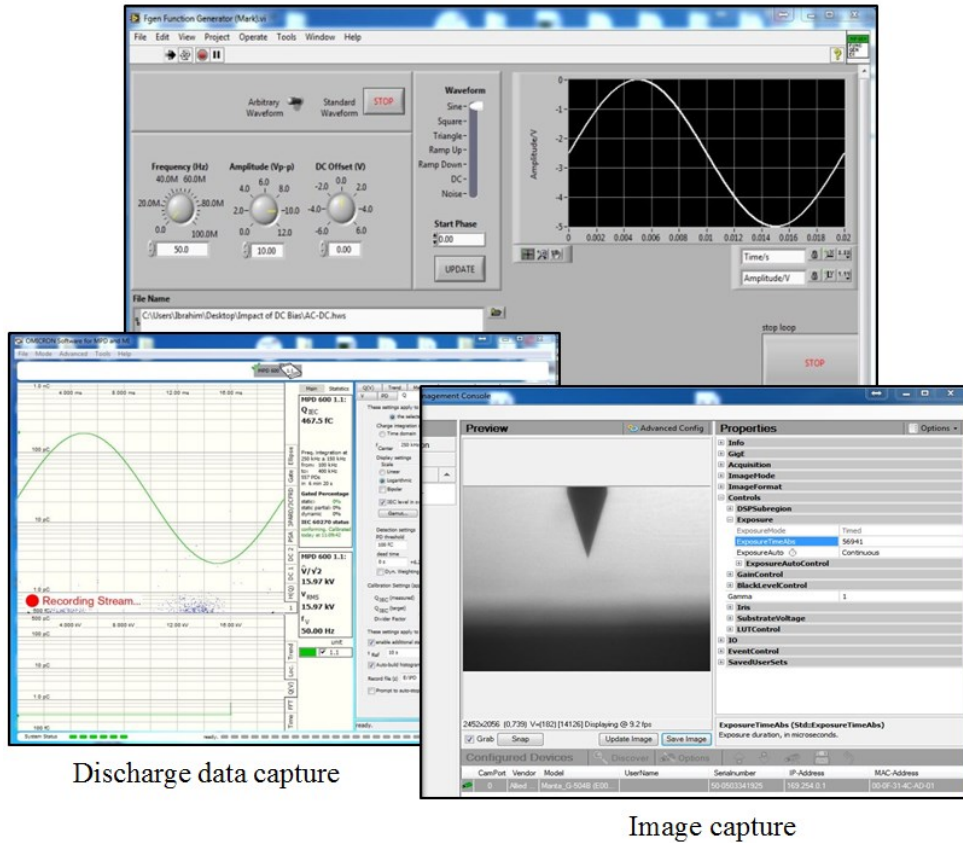
Figure 6-8: Screen shots of integrated software.

Energisation of the high voltage amplifier, the image capture and the PD stream recording are manually synchronised by enabling the remote control switch which connects the high voltage amplifier via coaxial cable with BNC cap from the control desk. The image capture and the PD "record stream button" are also enabled at the same time from their respective software control panels. With this procedure, image capture and PD measurement are acquired within five seconds of each other. This allows the measured PD data and the captured images to be correlated for any distinctive features during post-process analysis.

6.5 Assessment of the measurement system and validation tests

6.5.1 Acceptance test

The sensitivity of the partial discharge detection system during high voltage testing is very important in revealing any on-going degradation activity on insulation under investigation. IEC 60270 specifies that, the uncertainty of measuring system should be within ±10%. With a recorded background of 0.25 pC to 0.35 pC, which is possibly coming from the internal switching of solid state elements in the power supplies and the HV amplifier, the minimum detection on the measuring instrument was set to 0.4 pC after calibration to clear the background so that any discharge magnitude above this value can be viewed as genuinely coming from within the sample under test. But the threshold setting is left as default (zero) so that any repetitive discharges below the background are detected and computed by the measurement system.

6.5.2 Calibration procedure

The test setup is calibrated before any PD measurement begins. The calibration procedure involves both voltage and charge calibration. The voltage calibration ensures that the displayed voltage is matched up with the actual voltage being applied, and charge calibration determines the scale factor "k" for the measurement of the apparent charge in the measuring system.

Figure 6-9 shows the screen shot of the Omicron software during calibration. The screen is basically divided into two main parts:

- **[1] The control panel;** from which all the necessary control tabs (V, PD, Q, Q(V) etc.) for setting up the measurement instrument can be found.

- **[2] The visualisation area;** which contains the *large scope area* at the top where the PRPD plot overlaid with the monitored voltage are displayed and the *small scope area* at the bottom where various curves such as the Q(V) curve, Trend curve etc. are displayed.

Also at the visualisation area is the display statistics tab from which measured quantities according to IEC 60270 such as Q_{IEC}, Q_{peak}, Q_{ave}, n, $I_{Dis.}$ P_{Dis} etc. are displayed when enabled, where:

- Q_{peak}; is the largest absolute charge of any PD event seen during the evaluation interval

- Q_{IEC}; is the apparent charge defined according to IEC 60270 standard

- Q_{ave}; is the average charge value detected during evaluation internal

- n; is the pulse repetition rate, averaged over the evaluation interval

- I_{Dis}; the average discharge current over the evaluation interval

- P_{Dis}: the average discharge power (discharge current times instantaneous AC voltage) over the evaluation period.

- D: the quadratic rate over the evaluation interval.
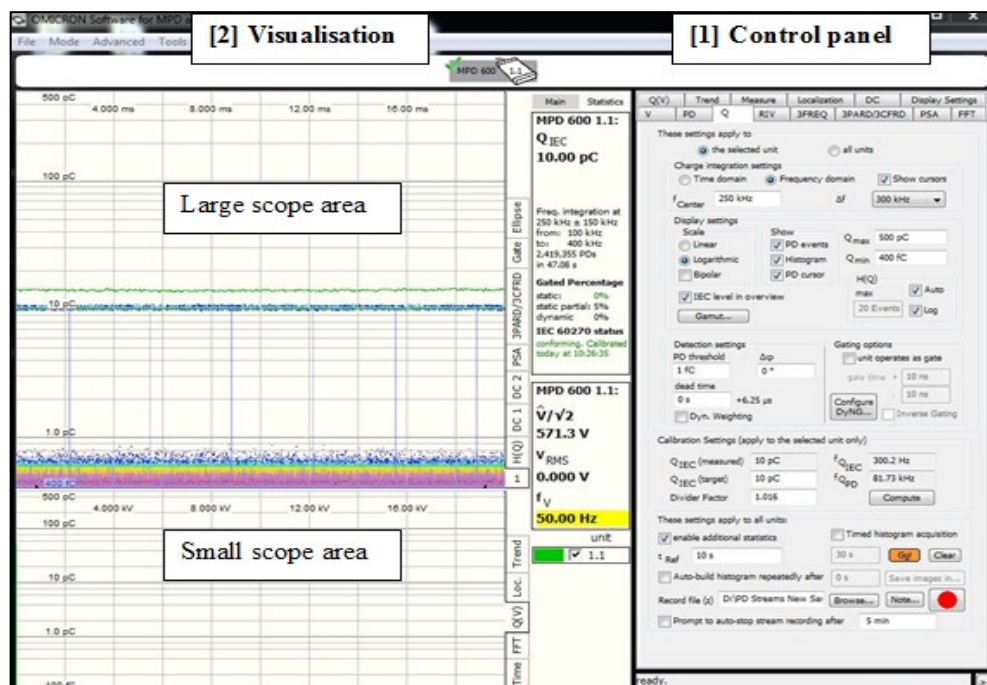
Figure 6-9: Calibration screen shot.

In this study, the charge calibration is carried out by injecting 10 pC charge pulses into the terminals of the test sample by directly connecting the calibrator to the low voltage terminals of the test sample and the ground as shown by Cal 542 in Figure 6-5 when the system is not energised. It is removed before the system is energised. The injected charge pulses are shown as blue spikes in Figure 6-9

6.5.3 System validation

PD measurement is used for monitoring the ageing state of electrical equipment such as transformer busings and cable insulation. For example, in monitoring a cable system, it is important to ascertain if the detected discharges are coming from the insulation bulk or at the joints/terminations to enable an informed decission about the health or state of the equipment to be made. Similarly in this experimental setup, it is important to establish if the detected discharges are of internal (eg. electrical tree growth), external (corona) or surface discharges. Two tests were carried out in order to validate the capability of both the Optical and PD detection system and also to investigate the sources of partial discharge in the test setup.

Firstly, corona inception voltage (CIV) was investigated using two identical dummy samples and secondly, partial discharge inception voltage (PDIV) was investigated by replacing one of the dummy samples with test samples (samples with an embedded pointed needle). The geometries of the imaged needle tips of the dummy and test samples are shown in Figure 6-10.
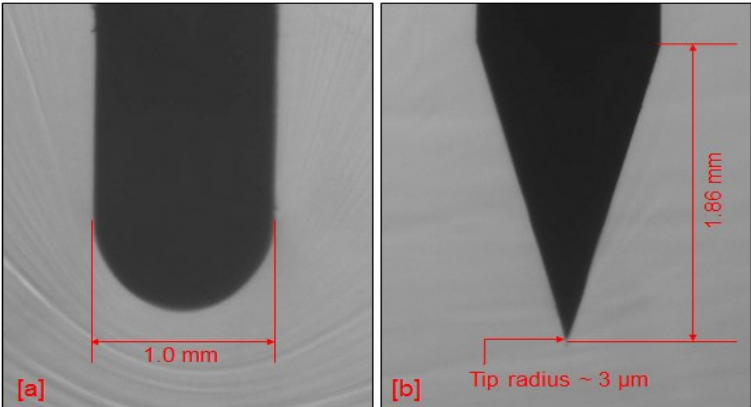
Figure 6-10: Dimensions of needle tips; [a] dummy sample [b] test sample.

Both tests were carried out in air. For tests in air, the experimental set-up is similar to the one described in section 6.4.1 Figure 6-7, except that in this case the samples were not immersed in oil bath as shown in Figure 6-11 below. The samples were clamped between sample holders as shown in Figure 6-11.
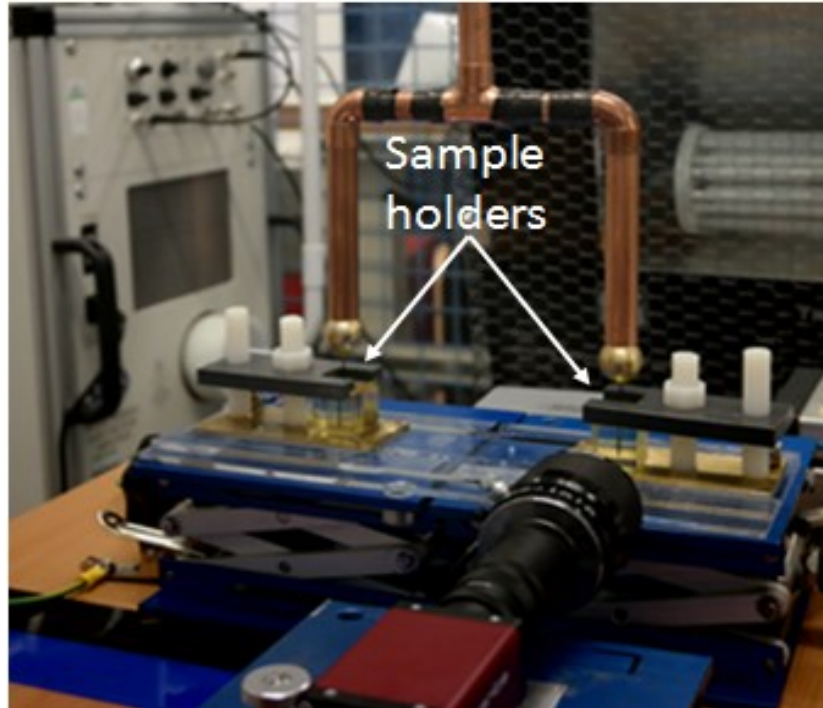
Figure 6-11: Experimental set up for test in air.

The base of the sample holders are made of brass to provide sound electrical contact between the sample bottom and the brass plate after securing samples in the holders.

In the first test, i.e. corona inception voltage (CIV) it is expected that on voltage application:

- An electrical tree should not be detected within the dummy samples due to the samples' geometry.

- That if discharge activity is observed which is not accompanied by tree growth, this discharge activity is assumed to be corona or surface discharge and the voltage at which it starts to occur is noted as the possible corona inception voltage.

- That if discharge activity is observed with tree growth in the dummy samples, the test setup is deemed unsatisfactory as the dummy samples are designed not to grow trees nor have PD in them.

However, in the second test, i.e. partial discharge inception voltage (PDIV), it is expected that on voltage application:

- Any discharge activity observed below the corona inception voltage noted earlier, which is accompanied by optically visible tree growth should be noted as possible partial discharge inception voltage as well as tree inception voltage.

- That if continuous discharge activity is observed for more than 5 minutes without visible tree growth, the test should be allowed to continue for at least 20 minutes and still if no tree is observed the sample should be removed and observed under microscope.

- That if under microscope no tree is observed, the test circuit should be deemed unsatisfactory as the source of the PD could not be ascertained.

6.5.4 Corona inception voltage

The test set up in Figure 6-11 is used in this investigation. The test voltage was increased in steps of 2 kVrms up to 14 kVrms. Figure 6-12 shows the screen shot of the recorded stream during the test showing the voltage curve and the positions at which discharge activity occurred in response to the increasing voltages. It can be seen from the screen shot that discharges were not detecteted from 2 kVrms to 12 kVrms. However, when the voltage was increased to 14 kVrms, discharges were observed. When the voltage was reduced to 13 kVrms, this discharges disappeared, and re-appeared again when the voltage was increased again from 13 kVrms to 13.4 kVrms in steps of 0.2 kV at 13.2 kVrms and 13.4 kVrms. These are shown by the arrows as three peaks on the charge curve of the small scope area of the test screen shot.
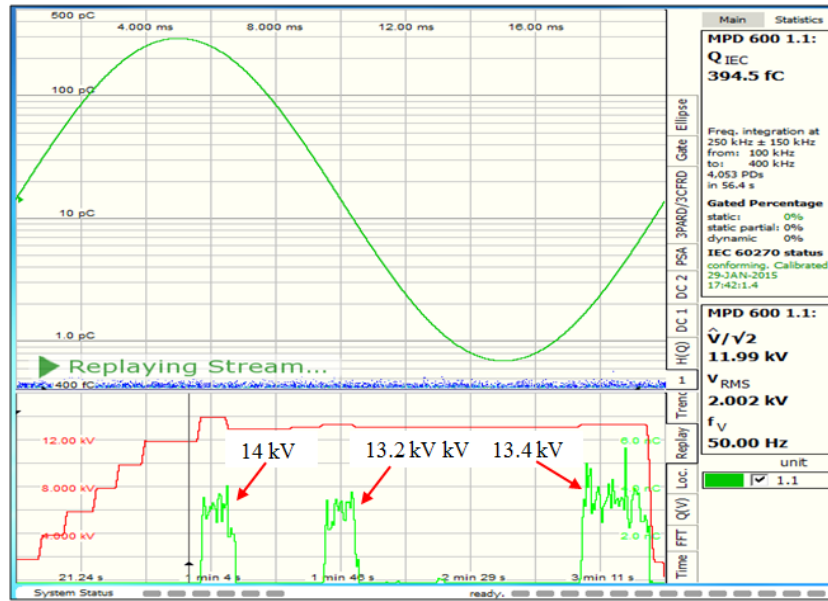
Figure 6-12: Screen shot of recorded stream during test.

The phase locations of these discharges are shown on the PRPD plots in Figure 6-13 [a], [b], [c] and [d]. Isolated discharges of magnitudes upto about 3 nC were observed in [b] and [d] which are clearly absent in [a] and [c]. However, trees were not observed in the dummy test samples used. These discharges were regarded to be of an external sources such as corona and surface discharges. This observation is confirmed to be corona in tests carried out in section 6.6.5. Also an increase in background level with time is observed in [b], [c] and [d] whereas in [a] it is constant at about 0.4 pC.
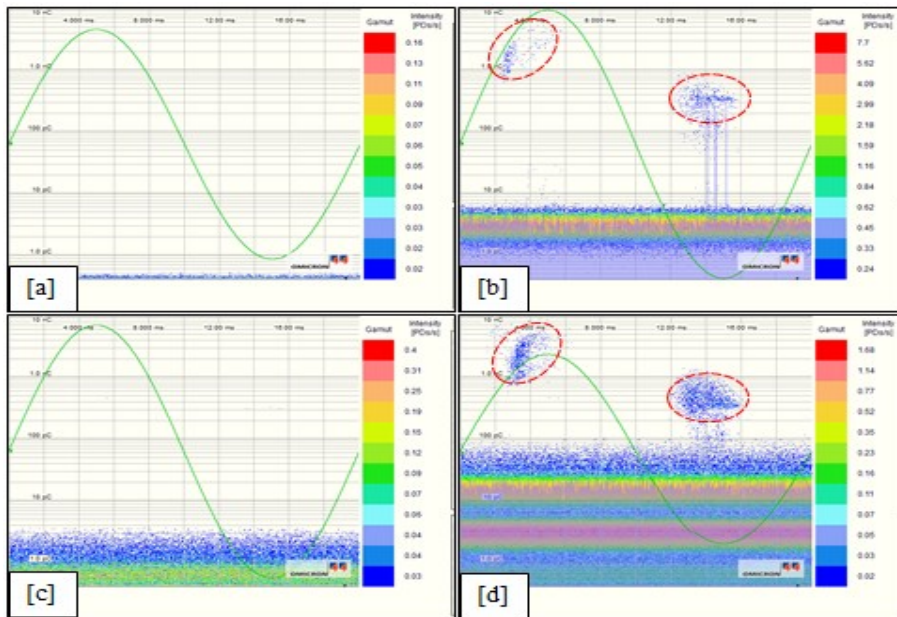
Figure 6-13: PRPD plots; [a] at 12 kVrms, [b] at 14 kVrms, [c] at 13 kVrms and [d] at 13.4 kVrms.

6.5.5 Partial discharge and tree inception voltage

In this investigation, two test samples were used, following a similar voltage application procedure as in section 6.5.4. In the first sample the voltage was increased up to 10 kVrms, and in the second sample up to 14 kVrms. In these tests, observed discharge activity during voltage application is expected to be followed by optically visible tree growth due to the samples' geometry. PRPD plot patterns above 12 kVrms were carefully inspected for any changes in discharge pattern.

First test: Figure 6-14 [a] and [b] shows the PRPD plot and Q(V) curves obtained in the first test for sample B1#S1. In both plots, and on the Q(V) curve, the black vertical lines indicates the positions of PD stream played back in that test and the horizontal red step lines indicate the magnitude of voltage applied which is 6 kVrms and 10 kVrms (not very visible from these plots) respectively. On the PRPD plot in Figure 6-14 [a], the phase of occurrence of the discharges on the positive half cycle of the applied voltage is around 5° to 90° whereas on negative half cycle is around 170° to 290° and the highest average PDs magnitude observed within the evaluation period is about 3 pC. In Figure 6-14 [b] that is at 10 kVrms, the phase of PDs occurrences increases from 0° to about 100° on the positive voltage half cycle and from about 170° to about 300° on the negative half cycle with the highest recorded average PDs magnitude of about 10 pC. The PDs were observed with emergence of

144

an electrical tree from 6 kVrms. However, isolated discharges were not observed in Figure 6-14 as they were in Figure 6-13.
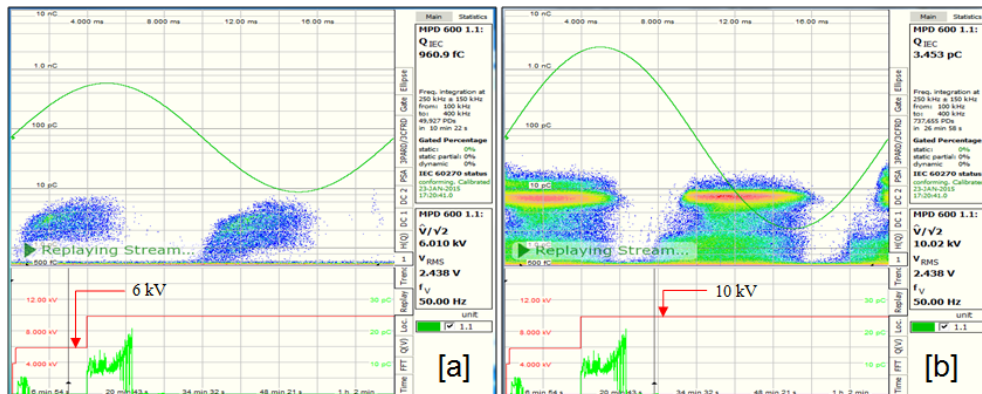
Figure 6-14: PRPD plot and Q(V) curve in test sample B1#S1.

With this observation, it is assumed the discharges were entirely due to electrical tree growth in the test sample and not from external sources. Figure 6-15 shows the electrical tree grown during this test.
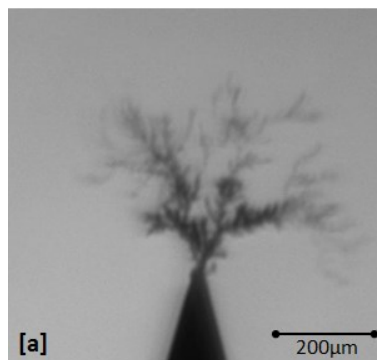
Figure 6-15: Electrical tree growth in sample B1#S1.

Second test: Figure 6-16 [a] and [b] shows the PRPD plots and Q(V) curves obtained in the second test sample B5#S1 with the black vertical and red steps horizontal lines showing the time period of voltage application and their magnitudes at 8 kVrms and 14 kVrms repectively. Although PDs were observed from 6 kVrms, and a sudden increase in PD magnitudes when the voltage was increased up to 14 kVrms at 6 min, no tree is observed until after 12 minutes after which the voltage was decreased to 12 kVrms.
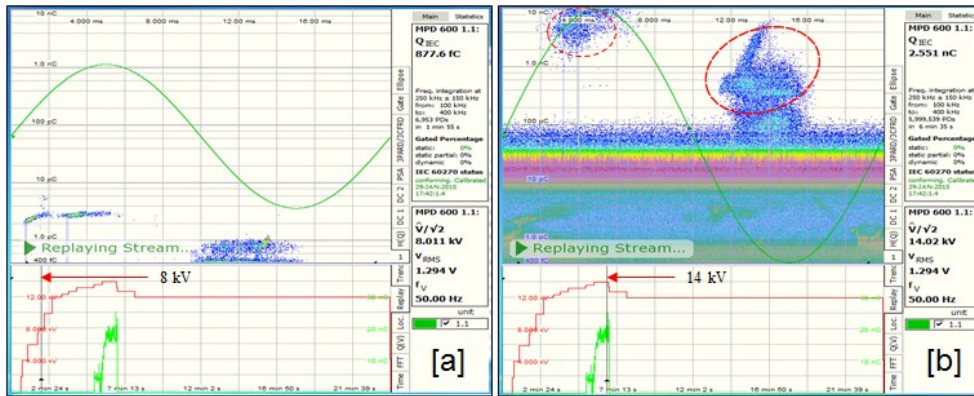
Figure 6-16: PRPD plot and Q(V) curve in test sample B5#S1.

The observed tree in this case developed suddenly and matured with recorded average PD magnitudes of about 4.5 pC which is far less than the recorded average magnitude of about 3 nC at 14 kVrms during CIV test. The recorded high values of PDs at 14 kVrms was accompanied by audible noise with a high background level. The discharges at 14 kVrms were isolated from the discharges seen ealier from 6 kV as shown in Figure 6-16 [a]. These isolated discharges are shown by the dotted ring in Figure 6-16 [b], and are located at similar positions to the ones observed in Figure 6-13 [b] and [d]. The discharges at 12 kVrms (~4.5 pC) were not visible to the eye as they were disguised by the high background level. However, the electrical tree continues to grow during this period. Figure 6-17 shows the electrical tree grown during this test. Refering back to Figure 6-14 and Figure 6-16 it is concluded that, two types of discharges occurred in Figure 6-16. One due to the electrical tree growth at voltages below 12 kVrms, and the other due to corona discharges in air at 14 kVrms as compared to Figure 6-14 where isolated discharges are not observed and hence the discharges were (assumed to be) entirely due to tree growth in that sample B1#S1.

The fact that the discharges were observed from 6 kVrms and trees were not observed until after 12 minutes, resulted in the sample being taken for further observation. Microscopic examination on the sample revealed that, the tree started growing long before it was sighted in situ. This was detected by the PD measuring instrument from 6 kVrms, however the tree was not observed optically.

This phenomena is herein dubbed as "blind spot" tree growth i.e. a growing tree from the opposite face of the focused needle which is not yet visible to the imaging equipment. Microscopic images of the inspected sample are shown in Figure 6-18 [a]

146

and [b]. Figure 6-18 [a] shows the imaged face during the experiment and Figure 6-18 [b] shows the opposite face during inspection.
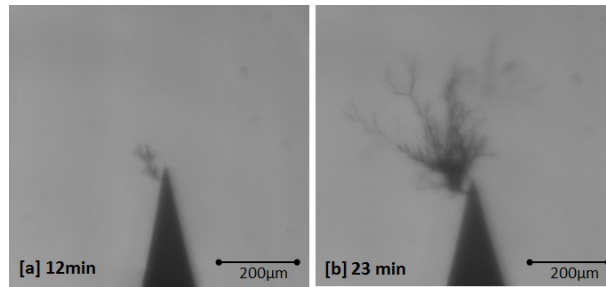
Figure 6-17: Electrical tree grown in sample B5#S1.

It can be seen from Figure 6-18 [a] that, the tree did not initiated from the needle tip but instead below the needle tip from the left side of the needle. But Figure 6-18 [b] shows that a bush-type tree started growing at the "blind spot", in what appears to be a defect on the needle, until after 12 minutes before it became visible and captured by the camera. This explains the reason why discharges were observed, long before the tree was observed.
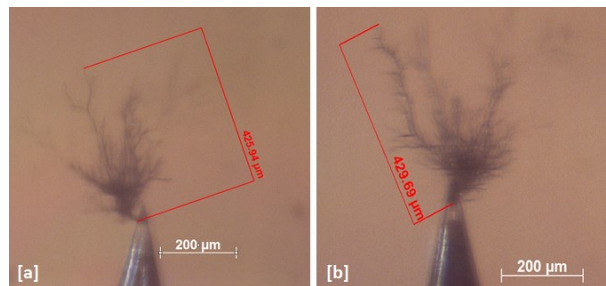
Figure 6-18: Images of microscopic inspection of sample B5#S1, [a] imaged face during experiment and [b] opposite face during inspection.

6.5.6   Summary

This chapter has presented the development of the experimental set up and equipment employed for treeing test in this study. The capability of the employed test equipment has been validated during acceptance testing and investigations on corona and partial discharge inception voltages. These investigations show that the experimenl setup can be used for:

- Detecting electrical tree growth optically and by PD means.

- Identifying external (corona) and internal (treeing) discharge activity during test.

- It is shown that partial discharge inception voltage is around 6 kVrms, and that this voltage also corresponds to tree inception voltage.

- The optical system is capable of detecting detailed images of electrical tree without the need for de-energising the system and inspects the sample under microscope as shown by Figure 6-17 (b) and Figure 6-18 [a].

- The sensitivity of the PD detection is about ~ 0.35 pC.

- It is shown that a sample tested in air at 12 kVrms and above is marked by both internal (treeing) and external (corona) discharges.

With the capabilities of the developed system, preliminary experiments were carried out, and are reported in chapter 7, from which experimental protocol developed for the remaining treeing experiment is proposed in chapter 8 that follows.

7. Preliminary investigations

In chapter 6 the experimental method developed for simultaneous imaging of electrical tree and PD measurement has been described and the capabilities of both the optical and the PD detection systems have been assessed and validated. This Chapter presents some of the preliminary experiments carried out prior to standard experimental procedure adopted for the rest of the treeing experiments.

It is worth mentioning here that, the original plan for the treeing work in this project was to establish the possibilities of growing electrical tree under steady DC or **"pure DC"** voltage stress and to investigate the impact of introduced interfaces in response to tree growth rate and time to breakdown. However, initial trials using the 30 kV DC HV amplifier described in section 6.2.2 did not result in any tree growth after several hours of continuous applied DC stress. This result is not a surprising outcome, as literature reviewed in section 2.13 already revealed the difficulty of initiating electrical trees under pure DC which results in the use of several voltage application techniques [116-118], in order to achieve initiation and subsequent growth of an electrical tree.

Recent work by Ying and Xiaolong [122] showed that applied voltages of ± (30 to 70) kV "pure DC" did not result in tree growth after up to about 11 hour in some cases. Thus for electrical tree growth under DC, a steady (ripple free) 100 kV Brandenburg HVDC power source was later employed. Having encountered these initial difficulties, a digression from the original plan was proposed. This was to investigate the impact of DC power quality on electrical tree growth by superimposing AC ripples on DC and used the resulting composite waveform for stressing the samples.

The following preliminary investigation, were carried out from which experimental protocol for the remaining tests were proposed:

1. Tree initiation from Hypodermic and Ogura needles.

2. Tree initiation by Optical and PD detection in air and in oil.

3. Determining the effect of superimposed AC ripples on DC on tree growth.

4. Determining if tree initiation can occur under "Pure DC" voltage.

The main aim of these preliminary tests was to narrow down on the set of experiments to be done and adopt the best experimental procedure for reproducible test results. Effort made to standardise sample fabrication procedure for treeing experiment has been described in section 3.6 and the comparison between samples with their flat faces painted with Aquadaq, metallised and non-metallised were explained and shown in Figure 3-9. In this preliminary tests, Aquadaq painted samples, metallised and non-metallised samples were tested in air or in oil with either Hypodermic or Ogura embedded needles as described in the sections that follow.

7.1 Tree initiation from Hypodermic and Ogura needles

In this preliminary test, samples painted with Aquadaq on their base were used. A total of 10 samples were used. 5 samples had Hypodermic needles embedded in them while the other 5 had Ogura needles embedded in them. The tests were carried out in oil to prevent flashover at 14 kVrms. Tree images were captured using CCD camera fitted with 8x magnifications Qioptiq macro lens described in section 6.2.5. The camera was set to capture images every 10 seconds, and the aim was to investigate tree initiation characteristics from these needles and to capture the emergence of the shortest possible tree image after voltage application. The results from these tests are discussed in following sections 7.1.1 and 7.1.2.

7.1.1 Tree images from Hypodermic needles

Figure 7-1 shows the captured tree images in 3 samples after 1 and 6 minutes of voltage application respectively.

H_B1#S1	H_B1#S2	H_B1#S3
[a] 1 min 100 μm	[c] 1 min	[e] 1 min
[b] 6 min	[d] 6 min	[f] 6 min
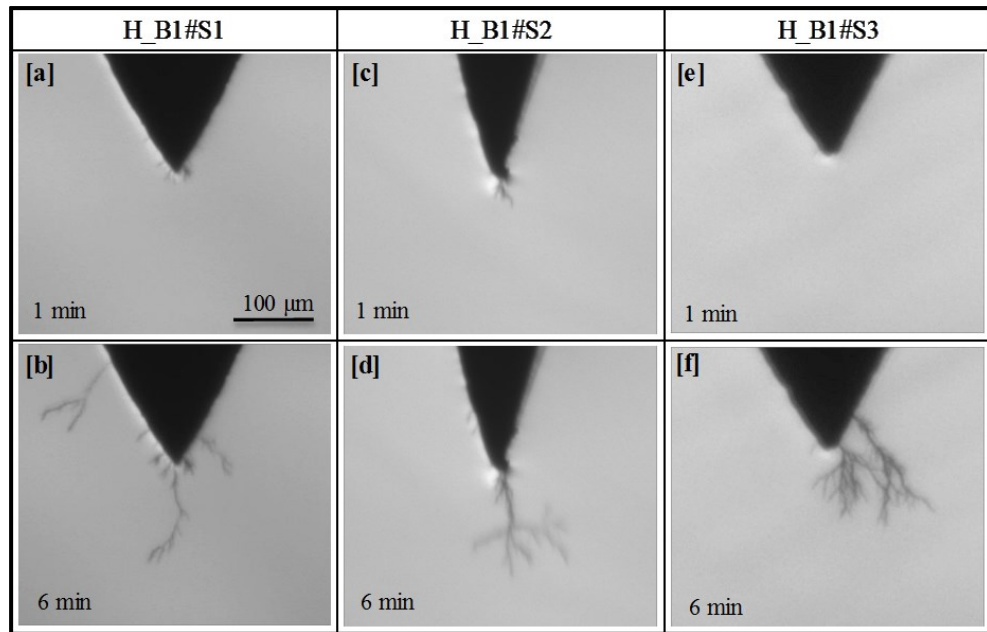
Figure 7-1: Capture tree images in Hypodermic needles. The 100 μm bar gives the scale for all images.

In section 3.6.1, the difference between the Hypodermic needle and the Ogura needle had been highlighted. The Hypodermic needle had hollow shank which is sliced at the tip. It was pointed out that, the edges of the sliced hollow shank may have sharp points along it, and that electrical trees may start from these sharp points instead of the actual tip, as these sharp points will become high stress regions when voltage is applied. Close-up images of electrical trees in all the 5 Hypodermic needle embedded samples, showed exactly this, and images from 3 samples are described here.

Images ([c] and [d]) of Figure 7-1 were imaged when the needle was focused on the side of the needle, while in images ([a] and [b]) and ([e] and [f]) the needles were focussed on the front view of the sliced hollow shanks. It can be seen from all the 6 captured images that the trees emerged either along the sliced edges or at dented spots; but not at the actual tip. It must be emphasised here that the 8x magnification macro CCD lens is an inspection lens which gives detailed observation of the needle tip if well focussed. The tip radius of both the Hypodermic and the Ogura needles are about 3 μm. Comparing the trees observed along the sliced shank in image [a] and the actual needle tip, it can be concluded that the lengths of the observed trees were less than 10 μm in lengths.

151

7.1.2 Tree images from Ogura Needles

Figure 7-2 shows the electrical tree images observed when the Ogura embedded needle samples were used. These images were selected to highlight some of the anomalies that were observed when the Ogura needles were used.

O_B1#S1	O_B1#S2	O_B1#S3
[a] 1 min — 100 μm	[c] 1 min	[e] 1 min
[b] 6 min	[d] 6 min	[f] 6 min
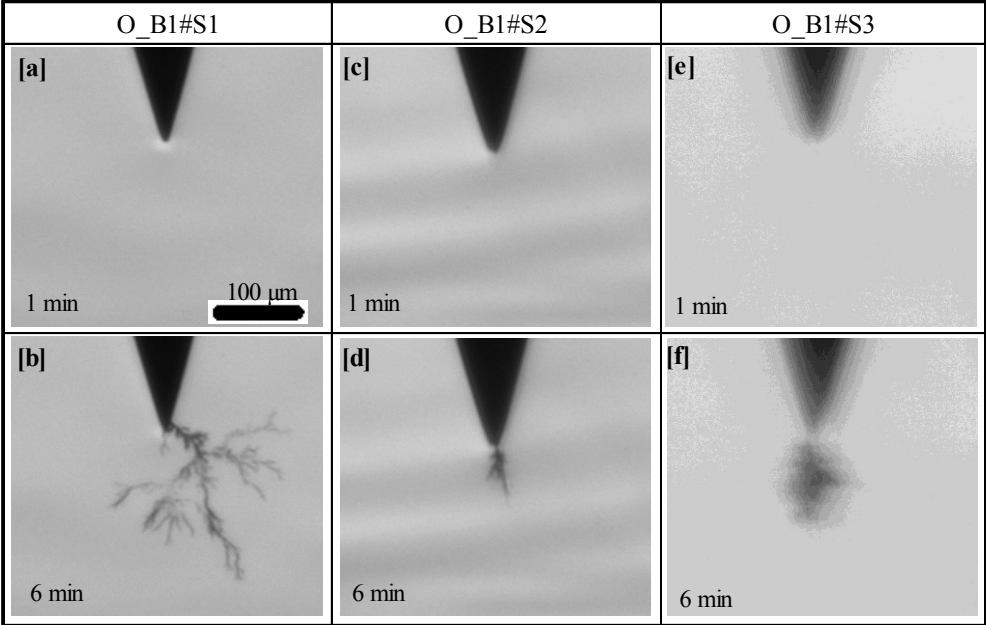
Figure 7-2: Captured tree images from Ogura needles. The 100 μm bar gives the scale for all images.

In contrast to the Hypodermic needle, the Ogura needle had smooth and rounded well defined tip. However in some cases, surface roughness around the ground end of the shank leading to the needle tip is inevitable, and in some cases resulted in treeing in the samples. Typical examples of such cases were observed during these preliminary tests in samples O-B1#S1 [b] of Figure 7-2, B4#S6 of Figure 7-3 and in sample B5#S1 of Figure 6-18 during system validation tests.

These observations are comparable to some of the real problems encountered in cables at the interfaces between conductor-semiconductor and semiconductor-insulator interfaces with respect to electrical treeing. It can also be seen from images [e] and [f] of Figure 7-2 that, the needle tips were not well focussed. This problem arises sometimes when the system is energised after initial focussing due to slight mechanical shift in the experimental set-up coming from vibrations of other equipment in other parts of the laboratory. The CCD camera in this set up is manually focussed from inside the high voltage cage and there is no means of re-

focussing externally from the control desk outside the HV cage once energised, unless the experiment is de-energised.

It is often not a good idea to stop an on-going experiment in a middle to inspect a sample or to re-focus the needle tip especially where treeing has already initiated in the sample unless it is absolutely necessary. This is because the tubules of electrical tree are normally gas-filled due to partial discharges on voltage application, and de-energising will lead to venting of the tree channel resulting in early breakdowns as reported in [53].

It was also observed that Aquadaq used to paint the bottom of the samples in these tests dissolves in the silicone oil. This leads to contamination of the oil and also reduces light transmission through the oil making it difficult to focus the needle tip. More importantly, the contamination of the oil will lead to reduced insulating characteristics of the oil for subsequent tests. As such, in the subsequent preliminary tests, aquadaq painted samples were not used.

7.2 Tree initiation by Optical and PD detection in air and in oil

7.2.1   Tree initiation in air by Optical detection only

In this preliminary test 10 samples were used. 6 of the samples were metallised using vacuum evaporation method and the remaining 4 samples were non-metallised as shown in Figure 3-9 (2) and (3). All the samples in this test had Ogura needles in them, with the aim to find out if sample metallisation has influence on tree initiation times. This test was carried out in air, and the samples were stressed with a 50 Hz voltage ranging from 2 kVrms to 21 kVrms as in section 6.5.3. The voltage was increased every 30 seconds, and immediately an initial tree image was detected, the experiment was stopped and the sample replaced with a new sample. If a tree was not observed after the applied voltage was increased up to 21 kVrms, which is the limit of the HV amplifier, after 5 minutes, the HV amplifier was switched off and the sample replaced with a new sample for the next test.

Table 7-1[A] shows the summary of the results obtained from this test. It can be seen from the Table 7-1 [A] that the tree initiation voltage for metallised and non-metallised samples ranges from about 8.4 kVrms to about 21 kVrms, and time to initiate is within 3 minutes of voltage application for these samples. For the

metallised samples, 2 out 6 samples did not initiate at 21 kVrms after 5 minutes while in the non-metallised samples, 2 samples out 4 samples did not initiate after the same time period of voltage application at 21 kVrms suggesting that metallisation has no influence in initiation times.

Table 7-1: Summary of test results.

[A] Tree initiation using metalised and non-metalised samples						
Sample No.	Sample ID	Test condition	Sample condition	Initiation voltage (kVrms)	Time to initiate (min)	Observation and comments
1	B2#S3	Optical detection only	Metalised	21.0	-	no tree after 5min
2	B2#S4	Test in air	Metalised	16.6	3	tree was observed
3	B2#S5			16.6	2.5	tree was observed
4	B2#S6			21.0	-	no tree after 5min
5	B3#S1			19.0	3	tree was observed
6	B3#S2			16.6	2	tree was observed
7	B3#S3		Non-metalised	21.0	-	no tree after 5min
8	B3#S4			12.6	2	tree was observed
9	B3#S5			8.4	1	tree was observed
10	B3#S6			21.0	-	no tree after 5min
[B] Tree initiation by Optical and PD detection on metalised samples						
Sample No.	Sample ID	Test condition	Sample condition	Initiation voltage (kVrms)	Time to initiate (min)	Observation and comments
1	B4#S1	Optical and PD detection	Test in air	Metalised	6	1	tree initiated with PD
2	B5#S6			8	2	tree initiated with PD
3	B4#S5			8	2	tree initiated with PD
4	B5#S1			12	12	tree initiated with PD
5	B4#S4			12	3	tree initiated with PD
6	B4#S3		Test in oil	Metalised	8	2	tree initiated with PD
7	B5#S3			12	2.5	tree initiated with PD
8	B5#S2			8	1.5	tree initiated with PD
9	B4#S6			18	18	tree initiated with PD
10	B4#S2			6	2.5	tree initiated with PD

7.2.2 Electrical tree initiation by Optical and PD detection

This test is similar to the test in section 7.2.1 except that here half of the samples were tested in air and the other half in oil. All the samples in these tests were metallised and the aim here is to investigate if any differences do exist between the tests carried out in air and in oil in relation to initiation times and PD patterns. Voltage application procedure during this test is similar to that in section 7.2.1 except that in this case, the voltage is left on at 21 kVrms for 20 minutes.

Table 7-1 [B] shows the summary of results from this test. It can be seen from the Table that, the tree initiation voltage in all the tested samples ranges from 6 kVrms to

18 kVrms and time to initiate also ranges from 1 to 3 minutes, except in sample B5#S1 and B4#S6 where trees were observed after 12 and 18 minutes respectively.

Sample B5#S1 had already been examined in section 6.5.5 during system validation test which is also part of the series of initial tests carried out. Examination of sample B4#S6 under a microscope revealed the "blind spot" tree growth characteristics observed in sample B5#S1. Figure 7-3 [a] shows the captured tree image during the test which became visible only after 18 minutes, while [b] shows the examined image from the microscope which is the opposite side of Figure 7-3 [a].
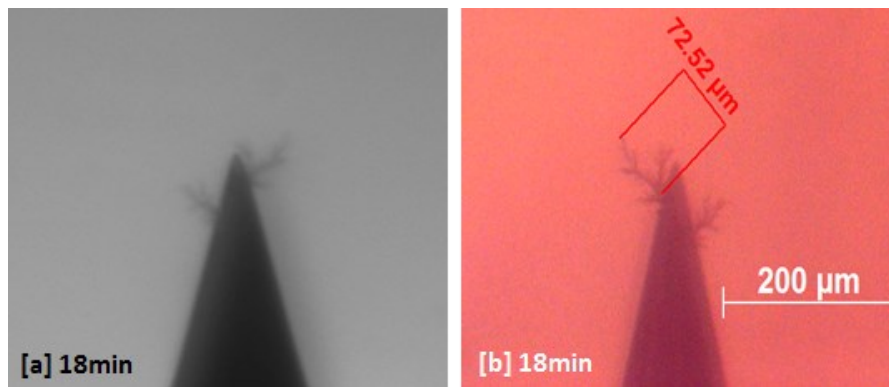
Figure 7-3: Sample B4#S6 [a] captured image during test, [b] examined image under a microscope. The 200 μm bar gives the scale for all images.

The emergence of the tree is a rapid growth of branches from a side of the needle from an existing tree which became visible only after 18 minutes as observed before in sample B5#S1 suggesting that the tree was growing long before it was optically observed. This behaviour was picked up by the PD measurement system from 6 kVrms with the occurrence of continuous discharge activity as the voltage magnitude was increased.

Even though the tree growth characteristics observed in sample B5#S1 and sample B4#S6 were similar, comparisons of the PRPD plots of the two samples revealed differences in the discharge patterns as shown in Figure 7-4. From the plot of the PRPD patterns of sample B4#S6 below, no isolated discharges can be seen even though the applied voltage was 18 kVrms compared to the 14 kVrms in sample B5#S1 where the isolated discharges were obvious as shown by the dotted red rings in Figure 7-4.
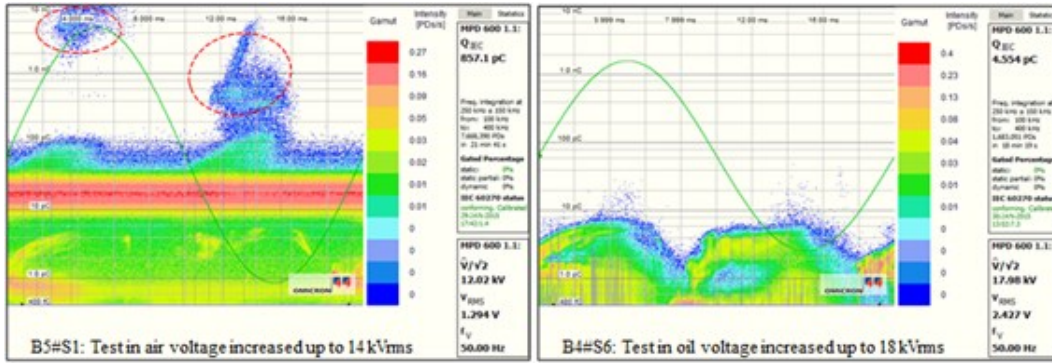
Figure 7-4: Comparisons of discharge patterns from PRPD plots of samples B5#S1 and B4#S6.

Detailed discussions of observations from sample B5#S1 has been presented in section 6.5.5 and it was concluded that the isolated discharges were due to corona discharges in air. The absence of isolated discharges in the PRPD plot of sample B4#S6 even though 18 kVrms was employed is due to the fact that the test was carried out in oil, which eliminates corona as well as surface discharges due to air traps at the interfaces between the sample and the ground plate. This observation suggests that tests above 12 kVrms in air are marked by discharges due to both electrical tree growth and corona in air or surface discharges, whereas discharges from the test in oil may be entirely due to electrical treeing internal to the test sample only.

7.3 Effect of superimposed AC ripples on DC on tree growth characteristics

The aim of this preliminary test is to simulate noise effects on steady DC and to find out if the magnitude of AC when superimposed on DC will cause tree initiation as the use of 30 kV DC stress for several hours did not result in tree initiation in the epoxy samples.

Composite waveforms were created and used for this investigation. The specifications of the HV amplifier acquired for this study and the modifications made to meet the experimental needs have been described in section 6.2. The output range of the HV amplifier is ± 30 kV DC or peak AC. 10 composite waveforms were created using waveform editor such that, the sum of the superimposed AC component on the DC component forming the composite waveform did not exceed the 30 kV peak limit of the HV amplifier as shown in Table 7-2 using equation (7.1):

$$V(t) = A + B\sin\omega t \qquad\qquad (7.1)$$

Where; **A** and **B** are the magnitudes of the DC and AC components respectively. Columns 2 and 3 of Table 7-2 show the magnitudes of AC and DC components in each composite waveforms at the low voltage side (i.e. the output of pre-amplifier section 6.2.3), which when fed to the HV amplifier, generated the values tabulated in columns 4, 5 and 6 which are the components of the DC, AC and the effective rms of the composite waveforms at the output of the HV amplifier as the gain of the HV amplifier is 3000 as described in section 6.3. A LabVIEW code was created to load and run the created waveforms from a saved folder in sequence to stress the samples for a specified time period.

Table 7-2: DC and AC components of generated composite waveforms.

Created No. of waveforms	Composite waveforms: low voltage side (V)		Composite waveforms: High voltage side (kV)		Measured rms value at HV Amp. outputin (kV)
	DC Component	AC Component	DC Component	AC Component	
1	9	1	27	3	27.1
2	8.4	1.6	25.2	4.8	25.4
3	7.6	2.4	22.8	7.2	23.5
4	7.2	2.8	21.6	8.4	23.1
5	**6.6**	**3.4**	**19.8**	**10.2**	**21.1**
6	6.2	3.8	18.6	11.4	20.3
7	5.8	4.2	17.4	12.6	19.4
8	5.6	4.4	16.8	13.2	19.2
9	5.2	4.8	15.6	14.4	18.6
10	**5**	**5**	**15**	**15**	**18.4**

In this preliminary test, 10 samples were tested. Out of these 10 samples, 3 samples had tree initiated in them when a combination of 19.8 kV DC and 10.2 peak AC was run i.e. the 5th waveform shown in the bold fonts in Table 7-2. In the remaining 7 samples, trees were observed more often when a combination of 15 kV DC and 15 kV peak AC were used.

In the previous tests in section 7.2, when AC voltages only were used, trees were initiated only from 6 kV rms (~8.5 kV peak AC) and above, and the use of 30 kV DC did not result in any tree growth. In this section when a composite waveform was used, tree initiation begins only when the AC component was 10.2 kV peak or more. This observation suggests that, tree initiation and propagation composed of AC and DC components is influenced more by the magnitude of the AC component. Figure

7-5 shows the plots of the DC and AC components of the composite waveforms, indicating the voltages at which trees were observed with round symbols.
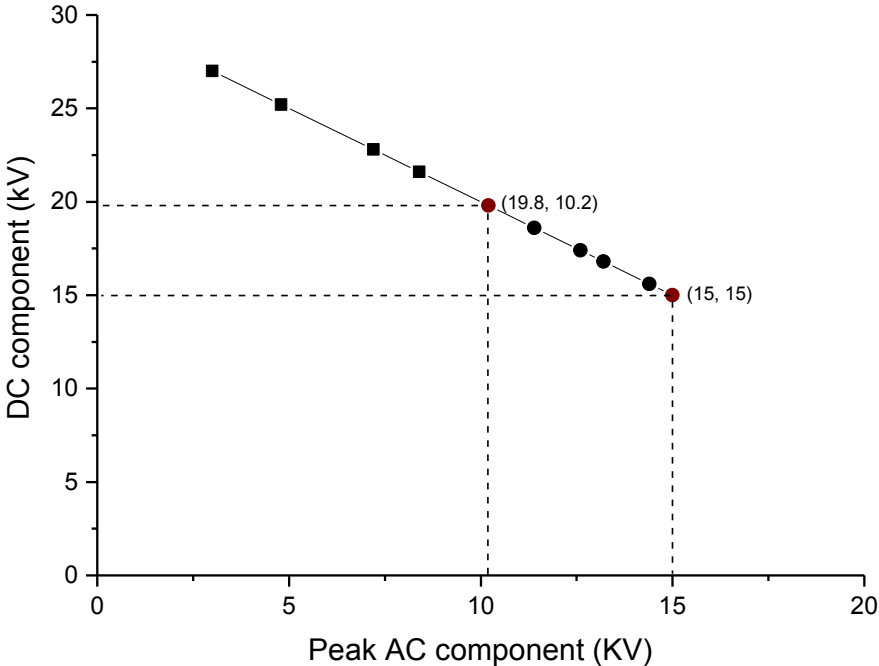
Figure 7-5: On set of tree initiation using composite waveform.

7.4 **Effect of external flashover event on tree growth under "pure DC" stress**

In this preliminary test, 3 samples were tested in silicone oil using a steady 100 kV reversible desk top DC power supply. Two of the samples were pre-initiated with AC in order to eliminate the variability of initiation time and to allow comparison of tree propagation after initiation. The third sample was not pre-initiated the aim being to initiate tree under "pure DC" voltage regime.

In the first two samples, positive or negative 60 kV DC was applied whereas in the third sample only positive 70 kV DC was used. The DC voltage was slowly increased to these specified voltages in each sample within a minute and kept at those voltages while images were captured every minute using CCD camera. The results obtained in each test are discussed below.

7.4.1   Tree propagation using -60 kV DC

First test (sample B8#S11): Figure 7-6 [a], [b] and [c] shows the images of the trees grown in sample B8#S11 after 5.5 hours of -60 kV DC stress. Image [a] shows the initial AC pre-initiated tree, while images [b] and [c] show the tree propagations after

2.5 and 5.5 hours of DC stress respectively. The initial extension of tree was observed only after 30 minutes of voltage application when flashover occurred between the HV electrode and the grounding cable causing the HVDC source to trip off.
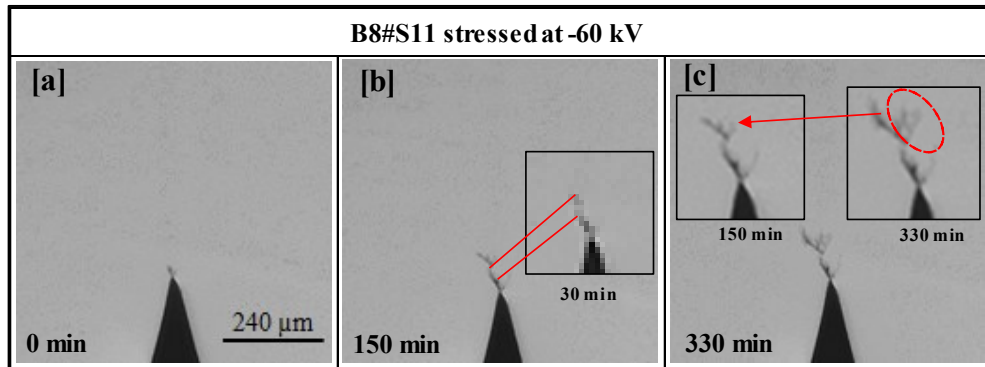
Figure 7-6: Tree growth characteristics under -60 kV DC. The 240 µm bar gives the scale for all images.

The location where the flashover occurred in the set-up is shown in Figure 7-7. The tree image inset in Figure 7-6 [b] shows the tree extension after 30 min when the flashover occurred.
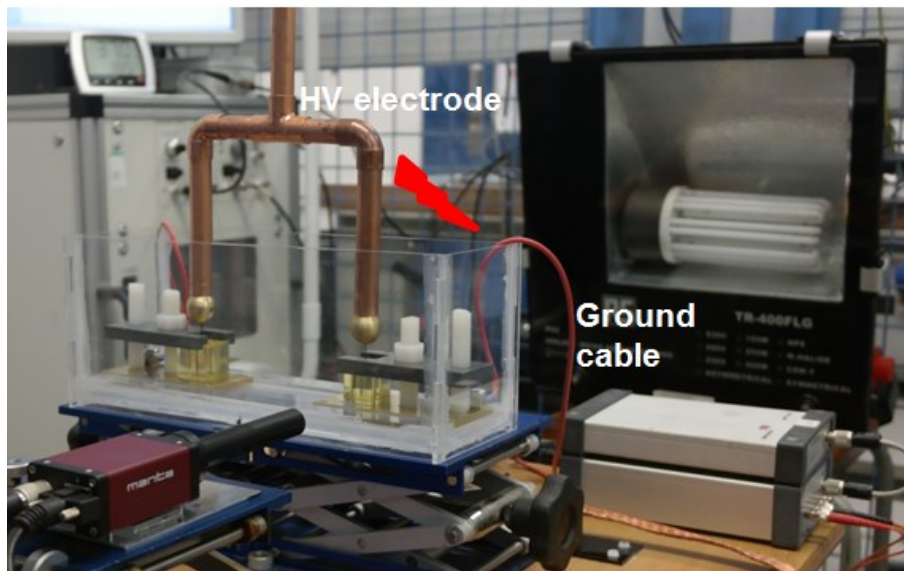
Figure 7-7: Location of flashover during test.

The HVDC source was energised again and after two hours, another flashover occurred again also causing the HVDC supply to trip off. The tree extension after this flashover event is shown in Figure 7-6 [b] after 150 minutes. To mitigate the occurrence of the flashover events, the ground cable is moved further away from the

HV electrode and more silicone oil added to the oil bath to insulate more of the grounding cable before the system was energised again and the sample stressed for further 3.0 hours. During this time period, flashovers occurred but the HVDC supply did not trip off. Figure 7-6 [c] shows the tree extension after 5.5 hours.

It can be seen from the insets of the close up images obtained after 150 minutes and 330 minutes that only little extension of side branches in the previous image pointed by the arrow and shown by the dotted ring were observed even though the time difference was 180 minutes. This observation suggests that, only disruptive flashovers that lead to short circuit between the HV electrode and the ground were responsible for significant tree extension in the test using -60 kV DC stress. This observation is further investigated in Section 7.4.2 below.

7.4.2 Tree propagation using ±60 kV DC

Second test (sample B6#S12): Investigation in section 7.4.1 revealed that tree extension is easily triggered when visible flashover which leads to short circuiting between the HV electrode and the grounding cable occurred. However when more silicone oil was added and no visible flashover events were observed as a result, little tree extension was observed as shown in Figure 7-6 [c]. This observation is further investigated using sample B6#S12. In this test also, the sample was pre-initiated with AC, and the initial tree is shown in Figure 7-8 [a].
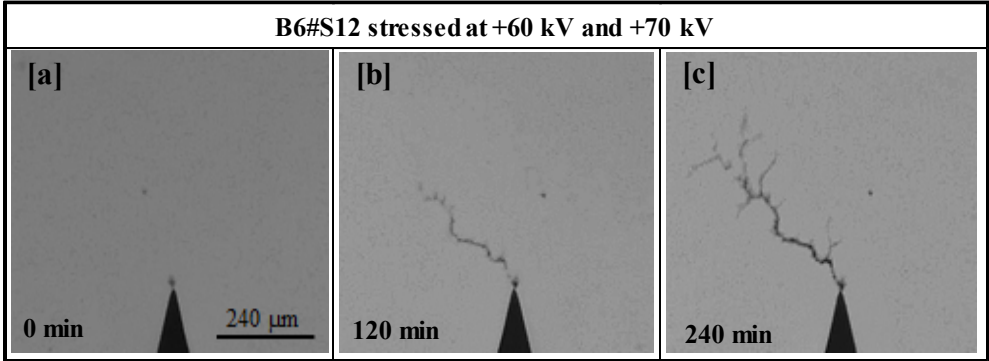
Figure 7-8: Tree growth characteristics under +60 kV DC. The 240 µm bar gives the scale for all images.

The sample was initially stressed with -60 kV DC for 8 hours. Flashover did not occur during this time, and tree extension was not observed from the initial image shown in [a]. The same sample was then stressed with +60 kV for 2 hours. During

this period, substantial tree length of about ~ 400 μm was observed as shown in Figure 7-8 [b], even though no visible flashover was observed. The voltage is further increased to +70 kV and the sample stressed for additional 2 hours. Further extensions of tree were observed with growing side branches as shown in image [c]. This test suggests that tree is more easily propagated under positive DC compared to negative DC even in the absence of visible flashover events.

7.4.3 Tree initiation and propagation under +70 kV "pure DC"

Third test (sample B6#S11): Steps taken to mitigate flashover to ground were discussed in section 7.4.2. Substantial tree propagation was observed when test was carried out on sample B6#S12 using positive DC. However, this is not case when negative DC voltage stress was used. In this section +70 kV "pure DC" is used, and the aim was to initiate and propagate trees using "pure DC". Thus the sample in this test is not pre-initiated as in the previous tests. The needle tip in the sample is shown in Figure 7-9 [a].
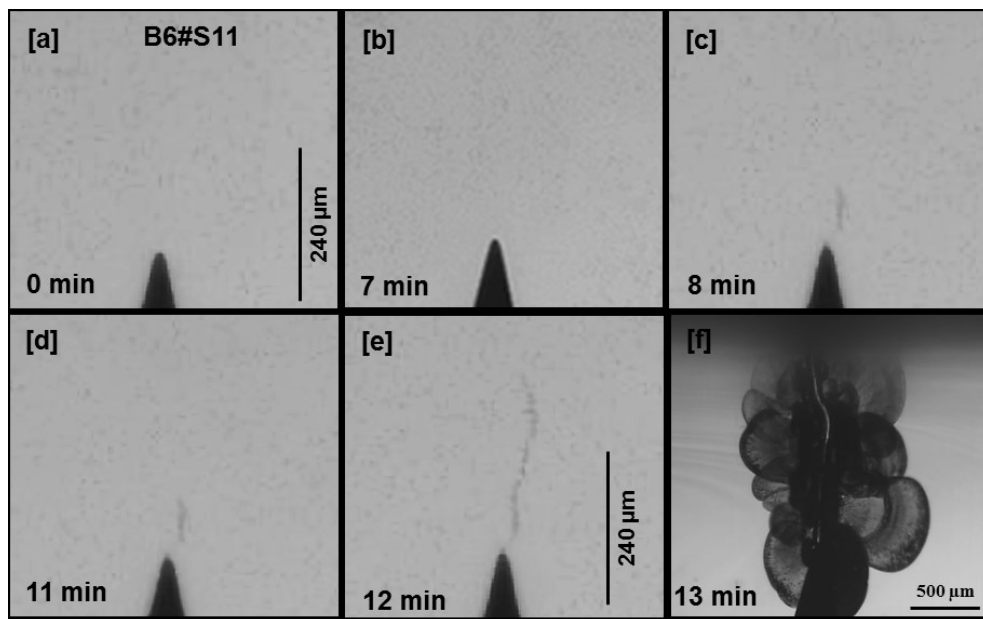
Figure 7-9: Tree growth under "Pure DC" in B6#S11.

As the applied voltage in this case is so high, care is taken in raising the voltage to 70 kV in order to prevent sudden breakdown during voltage ramp up. After 8 minutes of +70 kV DC voltage application, a tree extension of about 60 μm was observed as shown in image [c] of Figure 7-9. On inspection of the previous images, it was observed that, the tree extension occurred in the 8th minute only, as image [b]

161

of Figure 7-9 which was captured in the 7th minute has no tree in it. The next tree extension was observed in the 12th minute which then followed by breakdown in the 13th minute.

Examination and comparison of the tree images from the 8th to the 11th minute revealed that the tree extension occurred only in the 12th minutes as no tree extension was observed in the captured image from the 8th to 11th minutes until in the 12th minute as shown in images [c], [d] and [e] of Figure 7-9. Measured tree length in the 12th minute was about 250 μm, which is about 4 times longer than the tree observed in the 8th minute. Only two stages of tree extensions were involved before breakdown occurred in the 13th minute. No visible flashover was observed in the test circuit during this test.

These observations suggest that, tree propagation under DC is heavily dependent on the power quality of the DC supply and is easily triggered by flashover events. Tree propagation rate under DC is slow compared to AC voltage stress and different phenomena may be responsible in each case.

7.4.4 Summary

This chapter has presented preliminary investigation for electrical tree growth under AC, AC superimposed on DC and DC voltage stresses. Tests were either carried out in air or in oil using optical or both optical and PD means for tree detection. The sample types used in these tests are; Aquadaq painted, metallised and non-metallised with Hypodermic or Ogura needles embedded in them. Tree initiation at the vicinity of Hypodermic and Ogura needle tips were observed and compared. The findings in these preliminary tests are:

- Aquadaq (graphite water base conductive paint) dissolves in oil leading to contamination and reduced insulating strength of the oil for subsequent tests.

- Dissolved Aquadaq reduced light transmission in the oil resulting in difficulty of focussing on the needle tip and any emerging trees.

- Aquadaq is water based and can lead to water absorption by samples since epoxy is hygroscopic material.

- Magnified images of the trees initiated using Hypodermic needle samples showed that tree initiation start along the sliced hollow shank instead of at the needle tip using AC.

- In these preliminary tests only 3 out of 25 Ogura embedded needle samples had trees initiated from the rough surfaces in the vicinity of the tip using AC and composite wave form.

- Tree initiation times is independent of sample metallisation but heavily depends on the magnitude of the voltage as shown in Table 7-1.

- Tests in section 7.2 showed that corona and surfaces discharges are eliminated when the test was carried out in oil compared to what was observed in air in section 6.5.3.

- Tests in section 7.3 showed that tree initiation in composite waveforms is driven by the magnitude of the AC component instead of the DC component.

- In section 7.3, 10.2 kV peak AC/50 Hz is found to be the threshold of the AC component influencing tree initiation in composite waveform.

- Tests in section 7.4 showed that, trees can also initiate and grow under purely DC stresses at high field using extremely clean power supply.

- Tree propagates faster under positive DC stress than negative DC stress. Flashover events that results in short circuiting the supply result in bursts of tree propagation.

Findings in these preliminary tests showed that Aquadaq painted sample is not suitable for test in liquids (oil) and Ogura needle is more consistent for tree initiation from the needle tip. Even though an extremely clean DC power supply is used for tree initiation in sample B6#S11; power quality issues cannot be avoided under laboratory test conditions due to disturbances by neighbouring equipment. Based on these findings, further experiments were proposed in chapter 8.

8. Experimental design for tree growth characteristics and time to breakdown using pure DC, pure AC, and AC superimposed on DC voltages

Preliminary tests in Chapter 7 showed that trees can be initiated under AC from 6 kV rms and for the investigation on the effect of superimposed AC on DC on tree initiation, a combination of 15 kV peak AC and 15 kV DC was found to result into more frequent tree initiation. For DC tests, 60 and 70 kV DC was found to be suitable for stable electrical tree propagation and initiation respectively.

In this chapter, an experimental plan adopted after the preliminary investigation into tree growth characteristics and time to breakdown using DC, AC and AC superimposed on DC stress is described. The experiment is performed in two stages; a **quick tree initiation** process detected by optical means only and **propagation** monitored by simultaneous PD and optical detection. The quick initiation is employed to ensure all samples have a common tree inception process which results in the shortest possible tree initiated in them. In this way, the time to breakdown from the propagation stage can be equitably compared after initiation in all tests.

8.1 Test samples

Ogura needle embedded samples with the "plane" surfaces (ground) metallised with aluminium using vacuum evaporation method were used for consistency of test results and to ensure good electrical contact with the ground electrode. Figure 8-1 shows the sample configuration reproduced from section 3.6 for convenience. The samples were prepared and conditioned as outlined in section 3.7 prior to testing.
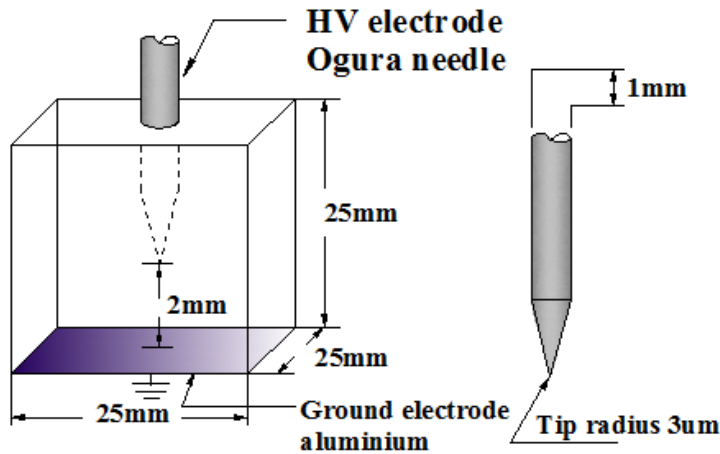
Figure 8-1: Ogura embedded metallised point to plane sample.

8.2 Quick initiation stage

In this stage of the experiment, 58 samples were initiated with an unbiased AC voltage between 12 and 16 kVrms. The aim here was to initiate a very short tree which will serve as a starting point for uniform and consistent tree propagation stage, and to eliminate initiation time as a source of variability for time to breakdown in all samples. The following protocol was adopted for the quick initiation test:

- A starting voltage of 12 kV rms was applied for the first 2 minutes.

- The voltage is then increased to 14 kVrms for further 3 minutes if no tree is observed after 2 minutes at 12 kV rms.

- The voltage is finally increased to 16 kVrms for additional 5 minutes if tree is not observed, after the previous 5 minutes time periods at 12 and 14 kV rms.

After this time period, if no tree is observed, the sample is removed and replaced with new sample. At this stage of the experiment a CCD camera fitted with a c-mount macro lens of 8x magnification with maximum field of view 1(W) x 0.8(H) mm was employed to enable detection and capture of a shortest possible electrical tree image after voltage application. All the samples were initiated in this manner from which 52 samples were randomly selected and used for the propagation stage test.

8.3 Propagation stage

In this stage, the 52 randomly selected pre-initiated samples with initial trees in them were tested using the following voltages:

a) ±60 kV DC.

b) AC test at 15 kV peak.

c) AC at 15 kV peak with +15 kV DC bias.

d) AC at 15 kV peak with -15 kV DC bias.

For DC tests, 12 out of 22 samples were stressed using +'ve DC while the other 10 samples were stressed using −'ve DC. Samples were continuously stressed for at least 10 hours. The remaining 30 samples were divided into 3 groups of 10 samples and each group continuously stressed with AC and composite voltages indicated in (b), (c) and (d) above until breakdown occurs. The schematics of the applied waveforms and calculated fields due to sample geometry only are shown in Figure 8-2 and Table 8-1.
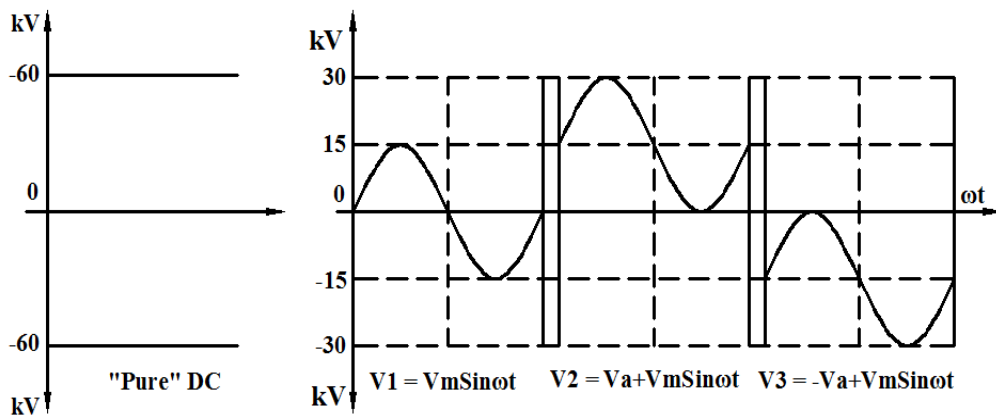
Figure 8-2: Applied waveforms.

Table 8-1: Test voltages and calculated geometrical field*.

Test type , voltages and calculated E-field	Applied voltages and calculated field at needle tip. Point = radius 3um and Gap distance = 2mm			
	Peak voltages (kV)	RMS voltages (kV)	Average field E= V/d (kV/mm)	*Field at needle tip (kV/mm)
± DC test	60	_	30	5070
AC test	15	10.6	5.3	896
(AC ± DC) test	30	18.4	9.2	1555
*E tip = 2V/rln[(1+4d/r)] (kV/mm):	*These field are associated with sample geometry only and not what is expected at the needle field			

At this stage of the experiment, the CCD camera is fitted with a c-mount telecentric lens with 6 (W) x 5 (H) mm dimensions of field of view which allows the whole tree length from the pre-initiated stage until breakdown ensued to be captured. Tests were

performed at room temperature and in silicone oil to prevent flashover. Images of the trees were captured at 1 or 60 second intervals until breakdown occurred. The results of these tests are presented in Chapter 9.

9. Experimental results and analysis for electrical treeing

9.1 Introduction

This chapter presents the test results from the outlined experimental procedure in chapter 8. The chapter contains six sections including section 9.1. The chapter starts presenting results on quick initiation of initial trees in section 9.2. Section 9.3 present results on tree propagation under ±60 kV DC while section sections 9.4 and 9.5 present results on AC and AC superimposed on DC tests. Section 9.6 finally present results on verification[2] test. A summary of test result is also presented at the end of each section.

9.2 Experimental results for quick initiation of initial trees

9.2.1 Evolution of initial trees into different tree shapes

This section presents result obtained from the quick initiation of initial trees using AC voltages. The section does not intend to critically analyse tree initiation as this is not the aim of the test but rather to highlight the influence of applied voltage on observed results during this study. Figure 9-1 shows the images of "initial tree" captured from three different samples during the quick initiation test. All the three samples initiated within 1 minute of applied 12 kV rms, but had different structures as can be seen in the Figure. While the structure of sample B8#S1 is bush-like and maintained the same structure after 2 and 5 minutes respectively, the structure of sample B6#S2 is branch-like after 1 minute and it evolved into bush and bush-branch after 2 and 5 minutes respectively. However in sample B6#S10, a single channel was observed after 1 minute, which then evolved into branch-type tree after 2 and 5 minutes respectively. The quick initiation test revealed that even with the same voltage magnitude, different types of initial tree shapes (bush-like, branch-like and bush-branch) can be obtained. See appendix B-1and 2 for compiled images of initial trees during this test.

---

[2]Verification test: is a test carried out at 30 kV peak AC to very if the reverse tree observed during test at 15 kV peaks AC in section 9.4.4 is due to the difference in applied voltage stress.
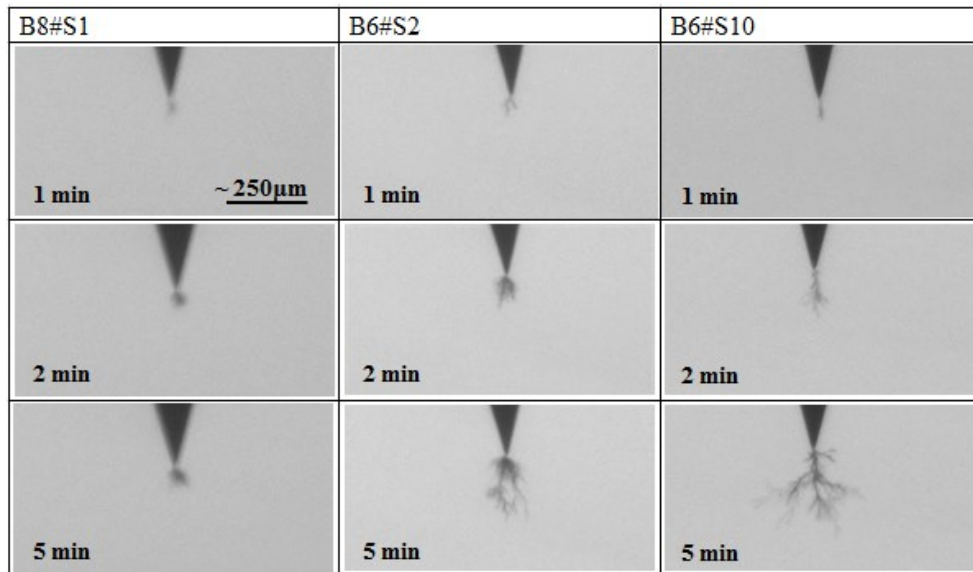
Figure 9-1: Images of typical initial trees from three different samples. The 250 μm bar gives the scale for all images.

9.2.2 Influence of applied voltage on electrical tree initiation times

Figure 9-2 shows a box chart plots of all the samples initiated in this study. The samples were fabricated in batches and each batch consists of 12 samples. During the quick initiation test 58 samples from batches 6 to 12 were initiated using 12 to 16 kV rms. Sample from batches 11/12[*], 13 and 14 comprising of 24 samples were initiated using 21 kV rms (30 kV peak) during verification testing which will be discussed in section 9.6. As can be seen in Figure 9-2, most of the samples initiated within 1 minute of voltage application i.e. including the verification test samples. But some samples in batches 11 and 12 did not initiate during the quick initiation test time slot. These samples were later used during verification testing at 21 kV rms, and are marked as batch 11/12[*] in the plot of Figure 9-2 to differentiate them from the normal batch 11/12 samples. Of these samples (8 in total), 4 samples initiated within 1 minute of voltage application at 21 kV rms, and the initiation times for the remaining 4 samples ranged from 73 minutes to 113 minutes. Also, all the samples from batch 14 initiated within 1 minutes of the applied voltage whereas for batch 13 samples, the initiation times ranges from 1 to 9 minutes at 21 kV rms.
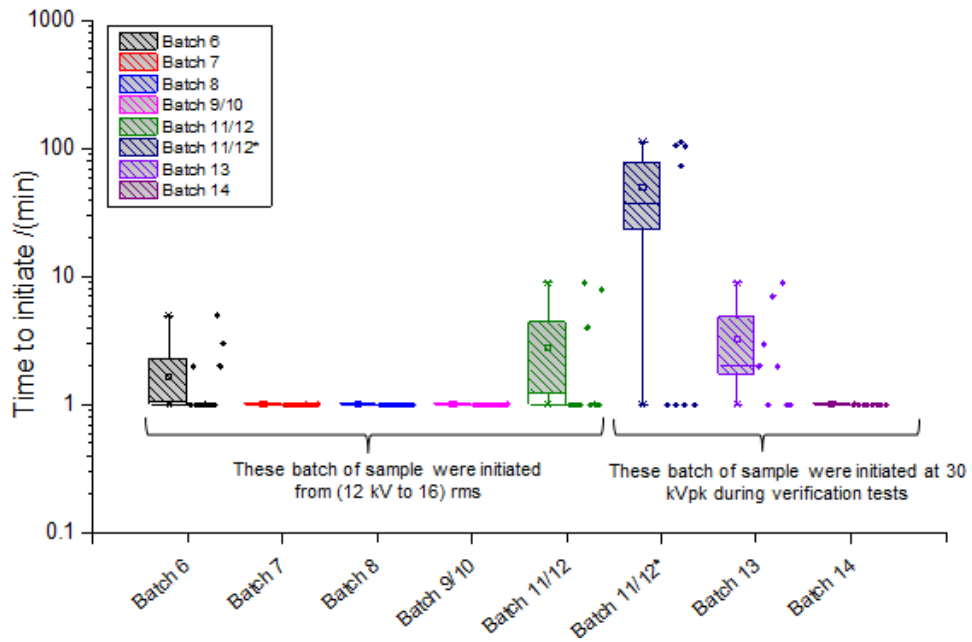
Figure 9-2: Electrical tree initiation times for batches 6-14 samples.

The pie chart shown in Figure 9-3 shows the percentage distribution of initiation time intervals of the tested samples at the applied voltages of 12 kV rms, 16 kV rms and 21 kV rms for quick initiation and verification tests respectively.

For quick initiation test 91.4% of the samples initiated within 1 minute of voltage application whereas 5.2% and 3.4% initiated after within 5 and 10 minutes of voltage application at 14 kV rms and 16 kV rms respectively. For samples initiated during verification test where 21 kV rms was used, 62.5% of the samples initiated within 1 minute of voltage application whereas 20.8% initiated within 2 to 9 minutes and 16.7% initiated within 73 to 113 minutes. This observation highlights the influence of applied voltage magnitudes on tree initiation times. It is also interesting to note that even though a high enough voltage (21 kV rms) was used for initiation during the verification test, nonetheless variable initiation times were observed.
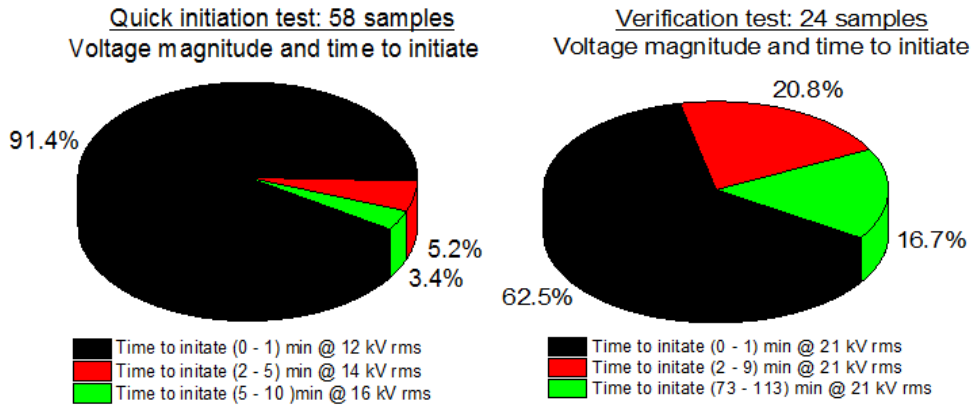
Figure 9-3: Distribution of initiation times at different test voltages

Another interesting observation was the initiation times for samples from batch 11/12[*]. These samples (7 samples) did not initiate after 10 minutes of voltage application at 12–16 kV rms during quick initiation test. However, during the verification test, 3 out of the 7 samples initiated within 1 minute and the remaining 4 samples initiated with varying times ranging from 73 to 113 minutes. This observation also highlights the importance of waiting time (ageing) for trees to initiate when using constant voltage. Perhaps the samples of batch 11/12[*] which initiated between 73 to 113 minutes could have initiated even at 12 kV rms but at much longer waiting times.

9.2.3 Influence of applied voltage magnitude on Initial tree lengths

Figure 9-4 shows a box chart plots of measured initial tree lengths of pre-initiated test samples and those initiated during verification test. The averages of the initial tree lengths for samples in batches 6, 7, 8, 9/10 and 11/12 during the quick initiation test were less than 50 μm. However, few samples had their initial length longer than 50 μm but less than 100 μm as shown in the plots.
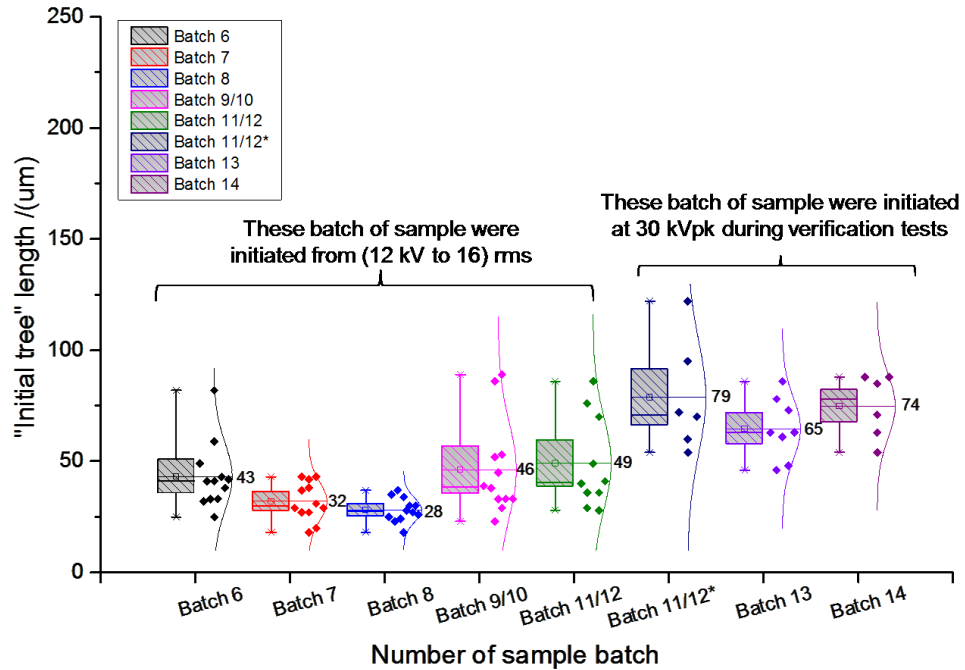
Figure 9-4: Plots the initial tree lengths of samples batches 6-14

For the samples initiated using 21 kV rms during the verification tests, generally the initial tree lengths were longer due to the higher voltage involved. As can be seen from the plots, the averages from each batch for these samples were 79 μm, 65 μm and 74 μm respectively. The plot shows samples with initial length up 113 μm only. However longer initial tree lengths were measured, but were considered as outliers and were not included in this plot. For example, in batch, 11/12[*] initial tree lengths of ~ 530 μm and ~ 576 μm were measured but were censored in the plot of Figure 9-4 as they are not representative statistically. See Appendix A–7 for collated data of initial tree lengths during the tests.

9.2.4 Summary

The findings from the results discussed in section 9.2 above showed that:

- The amplitude and duration of the applied voltage play a significant role in initiation times as well as the lengths of initial trees observed.

- Variable waiting times can exist in sample fabricated from the same batch as observed in batch 11/12 sample. However the effect is minimal here due to consistency of samples fabrication procedure adopted in Chapter 3.

- Initial trees of varying shapes can be obtained from the same magnitude of applied voltage as observed in section 9.2.1.

It is concluded that, 12 kV rms is high enough to initiate electrical tree within 1 minute of voltage application. But generally, the higher the amplitude of the applied voltage, the lower the initiation time and vice versa. Thus, for a study focussed on growing very short initial trees, voltages above 12 kV rms may result in faster and longer initial trees and should be avoided if necessary but at the expense of waiting time for tree to be initiated.

9.3 **Experimental results of electrical tree growth under ±60 kV DC**

Section 9.2 presented test results of the initiated test samples for the entire study. This section presents the test results for tree propagation and time to breakdown on the pre-initiated samples under ±60 kV DC voltage stresses. Preliminary tests in section 7.4.2 already showed that tree propagates faster under positive DC stress than under negative DC stress, and it was found that flashover events that results in short circuiting trigger tree Propagation faster under negative DC stress. The difficulty of tree initiation and growth under steady DC is suggested to be due to the effect of space charge moderation in the immediate vicinity of the needle electrode (space charge zone) by many authors [116, 123-124, 191]. It is also believed that, negative electrodes inject charges more easily than the positive electrode [116-117, 191]. It is suggested in [191] that, the observed tree length during polarity reversal can be taken as a measure of spatial distribution of space charge in the vicinity of the point electrode. The injection distance was estimated to be about ~50 μm using flight distance calculation.

From the literature then, the lack of tree growth under negative polarity test during the preliminary test is not surprising, as this may be due to the shielding effect of space charge causing field relief at the vicinity of the point electrode. This observation was further investigated for repeatability using steady DC at ±60 kV and the results are presented in this section. Table 9-1 shows the collated test results for 22 samples employed for positive and negative DC tests where:

- L_{IT} = length of initial tree.

- L_{FT} = length of final tree prior to breakdown.

- T_{TBD} = time taken for sample to reach breakdown.

- NBD = no breakdown during the test.

Table 9-1: Length of initial/final trees and time to breakdown for test samples.

DC test at +60 kV				DC test at -60 kV			
Sample ID	L_{IT} *(μm)*	L_{FT} *(μm)*	T_{TBD} *(min)*	*Sample ID*	L_{IT} *(μm)*	L_{FT} *(μm)*	*TTBD (min)*
[1] B9#S1	33	560	NBD	[1] B11#S1	28	80	NBD
[2] B10#S4	45	1435	322	[2] B11#S2	49	282	NBD
[3] B9#S4	33	333	NBD	[3] B11#S5	40	46	NBD
[4] B9#S6	29	170	NBD	[4] B11#S8	36	36	NBD
[5] B9#S5	52	1376	136	[5] B12#S1	29	54	NBD
[6] B9#S3	38	1189	272	[6] B12#S3	86	105	NBD
[7] B9#S7	23	282	NBD	[7] B12#S9	70	233	NBD
[8] B10#S6	86	1238	129	[8] B12#S5	36	80	NBD
[9] B10#S2	89	946	93	[9] B11#S7	41	54	NBD
[10] B9#S8	39	53	1	[10] B12#S4	76	418	NBD
[11] B9#S2	53	1367	612	**Averages**	**49**	**139**	
[12] B10#S5	33	958	184	NBD: = breakdown did not occur after 10 hrs			
Averages	**46**	**826**	**250**				

As can be seen from Table 9-1, for +60 kV test, 2 samples had their initial tree length much longer than 50 μm and these samples failed faster compared with the samples whose lengths are less than 50 μm. Similarly for -60 kV where breakdown did not occur in all samples, it was observed that propagation in length is more likely in samples with initial tree lengths longer than 50 μm as compared with those whose initial tree lengths were less than 50 μm at the beginning of the test. The observations during these tests are presented below.

9.3.1 Tree propagation and time to breakdown under +60 kV DC test

As shown in Table 9-1, breakdown did not occur under -60kV DC after 10 hours of voltage application for all tested samples. Thus, in this section only propagation under +60 kV is discussed. Figure 9-5 shows a column and label plot of time to breakdown for failed samples and stress times for un-failed samples extracted from Table 9-1. As can be seen from the plot, 4 out of the 12 samples did not fail after 10 hours of +60 kV DC stress shown as the shaded grey column, and 1 sample (B9#S8) failed within 1minute of voltage application out the remaining 8 samples that failed.

175
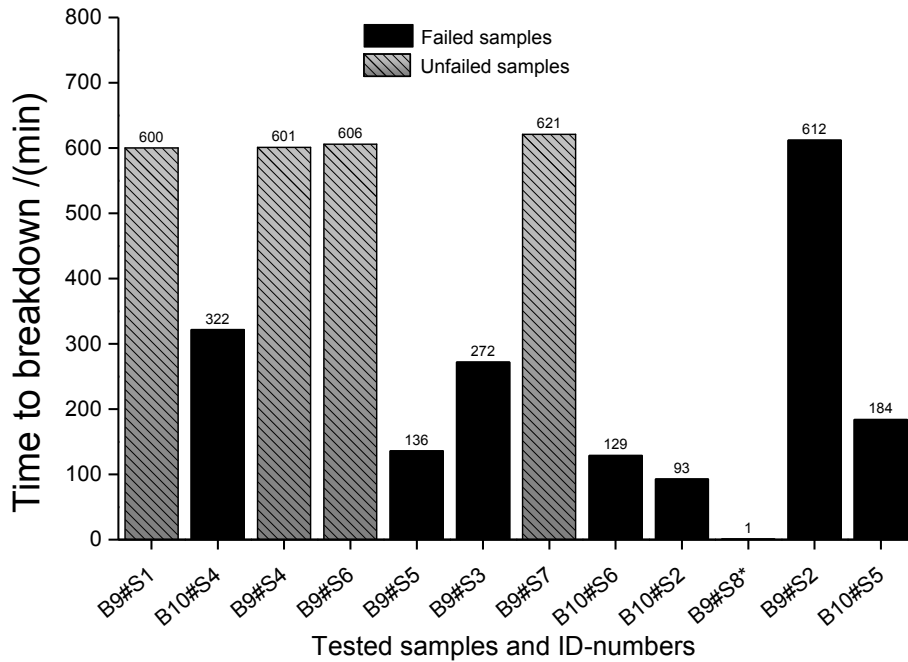
Figure 9-5: Time to breakdown for failed and un-failed samples under +60kV DC.

The plot of tree propagation as a function of time for the remaining 7 samples is shown in Figure 9-6. Although different time to breakdown was recorded for each sample, similarities in time dependent tree propagation was observed in most of the samples except for samples B9#S2 and B10#S4. Unlike for sample B9#S8, in which failure occurred within 1 minute of voltage application, in sample B9#S2, a fast tree extension was observed at the beginning of test but did not result in immediate failure, instead it stagnated at a tree length of about 0.4 mm (20% of the 2 mm gap) for about 305 minutes followed by a slow propagation until about 557 minutes, after which, a rapid acceleration was observed again before breakdown occurred at 612 minutes. Similar observation was made for sample B10#S4, but in this case the propagation continued to about 74% of the gap distance (1.48 mm) and then stagnated for about 27 minutes followed by immediate breakdown afterwards as can be seen in Figure 9-6. Considering only the failed samples and censoring sample B9#S8 which failed only after 1 minute, the average time to breakdown of the failed 7 samples was calculated to be ~250 minutes.
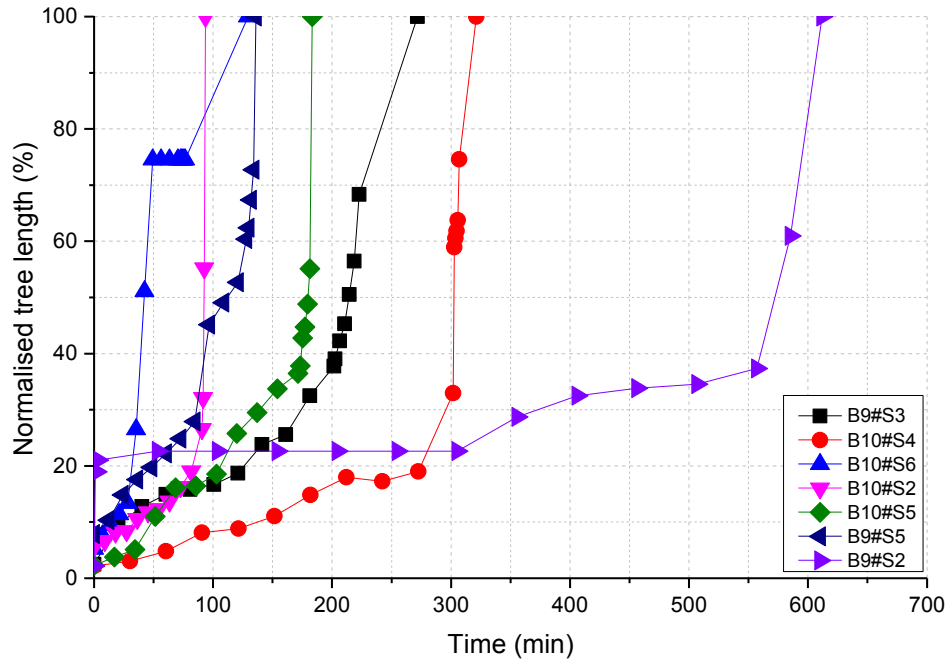
Figure 9-6: Electrical tree propagation under +60 kV until breakdown, the length of tree is normalised to the 2mm gap between the two electrodes.

9.3.2 Influence of initial tree on time to breakdown under +60 kV DC test

Figure 9-7 shows the plot of initial tree length as a function of breakdown times. It can be seen from the plot that, breakdown occurred only on samples which have an initial tree longer than approximately 33 μm. Below 33 μm, substantial growth is not observed and none of those samples fail as shown by 'x' markers with arrows on the plot. The correlation between the initial tree length and sample lifetime can be seen from Figure 9-7 showing a weak downward trend for quick failure in samples with longer initial tree lengths.
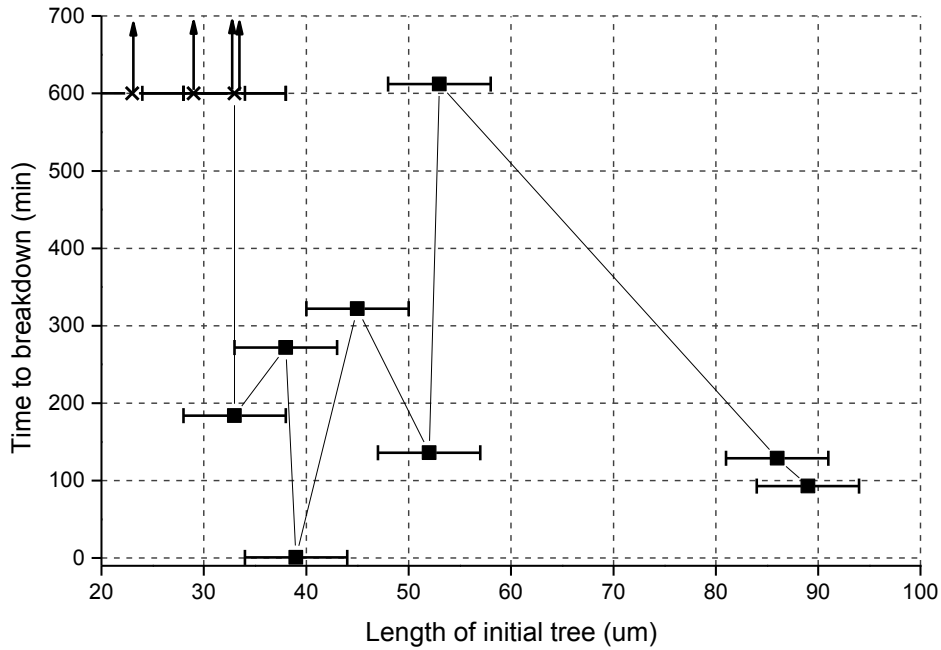
Figure 9-7: Time to breakdown under +60 kV as a function of the length of initial trees. Data with 'x' markers represents samples did not fail.

9.3.3 Influence of the initial tree on tree shape under ±60kV DC test

Figure 9-8 shows four examples of electrical trees propagated using +60 kV DC in the presence of AC pre-incepted initial trees.
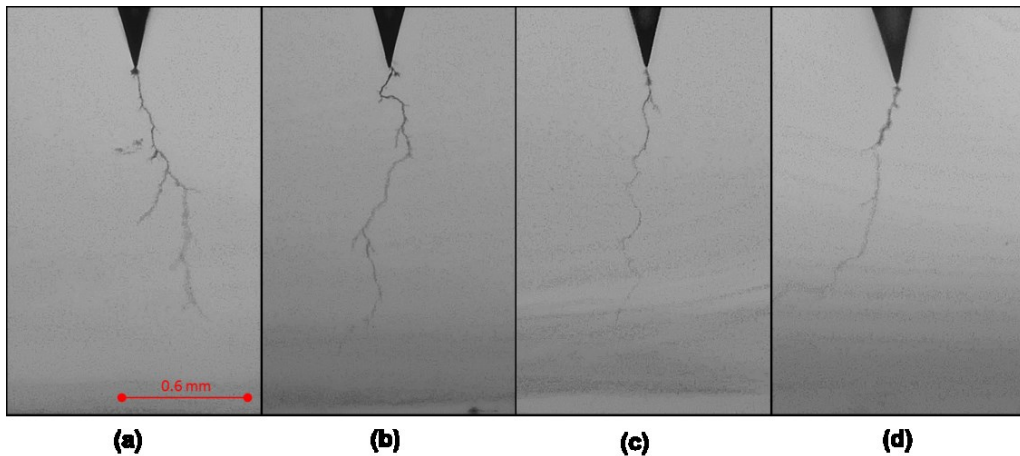
Figure 9-8: Images of DC trees showing lengths prior to breakdown. (a): sample B9#S3 (b): Sample B9#S5 (c): Sample B10#S6 and (d) Sample B10#S4. Scale bar is the same for all images.

Even though the AC pre-incepted trees had different shapes as can be seen from the images, the shapes of the DC trees propagated from the AC incepted trees were similar given that, only one main tree 'trunk' with a small quantity of short side

178

branches were observed growing towards the ground electrode but not following a straight path irrespective of the shape the initial trees.

The fact that the AC pre-incepted trees have different shapes and the DC trees propagated from them have similar shapes suggests that, similar propagation mechanism was involved in the observed +DC propagated trees, and that this mechanism may not be the same for AC propagated trees as different shapes were observed. See Appendix B–3 and 4 for compiled images of DC tree in this test.

Similarly, Figure 9-9 shows the images of initial trees prior to voltage application and the propagated final lengths after 10 hours of applied -60 kV DC voltage.
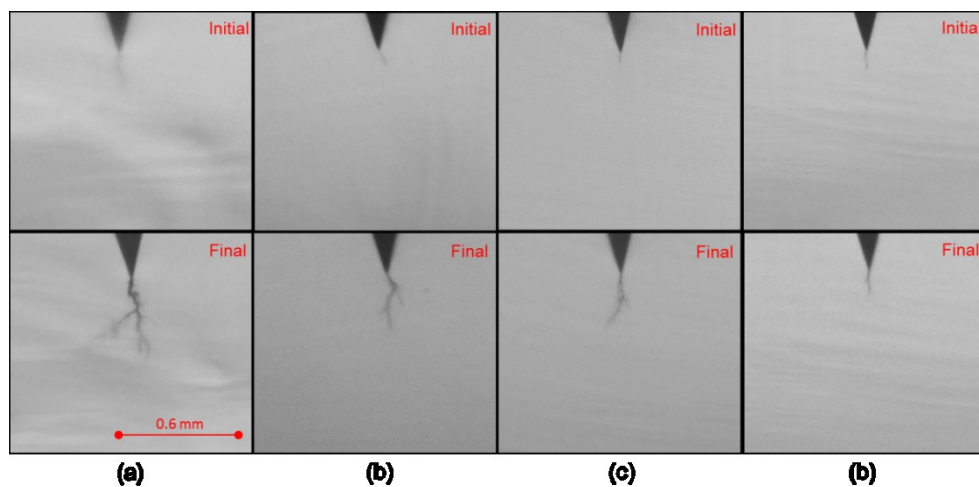
Figure 9-9: Images of -60 kV DC trees. Top images are the AC pre-incepted initial trees, and bottom images are the propagated lengths after 10 hours of -60 kV applied DC stress. Scale bar is the same for all images.

Although very little propagation was observed under -60 kV DC, the tree structures looked similar to those propagated under +60 kV DC. But under -60 kV DC test, the tree structures were thicker in comparison to the tree structures propagated under +60 kV DC. In contrast to the images of the initial AC trees shown in Figure 9-1 section 9.2.1 where branching and spreading of tree structures were observed, in this case however, no spreading was observed even though 10 hours of -60 kV DC was involved as compared with 12 kV rms applied voltage used in section 9.2.1. It is suggested therefore that similar mechanism of tree propagation is involved under both ±60 kV DC stresses but with limited propagation in length under negative polarity test.

9.3.4 Influence of the initial tree on propagation rate of tree lengths under ±60 kV DC stress

Figure 9-10 shows the propagated lengths of failed samples prior to breakdown and un-failed samples after 10 hours of applied +60 kV. Again it was observed, that, samples with initial tree lengths not longer than 33 μm had less propagation in lengths as compared to samples whose length are longer than 33 μm. As can be seen in Table 9-1, except for sample B9#S8 which failed within 1 minute of voltage application, the remaining 6 samples that failed had initial trees longer than 33 μm and higher propagation rate was observed in these samples. The average tree lengths of these samples prior to breakdown are calculated to be ~1259 μm. However, the remaining 5 samples whose initial tree lengths are not longer than 33 μm, the propagation rate was slower. The calculated average tree lengths of these samples is ~461 μm which is about 23% of the insulation gap distance at the end of those tests.
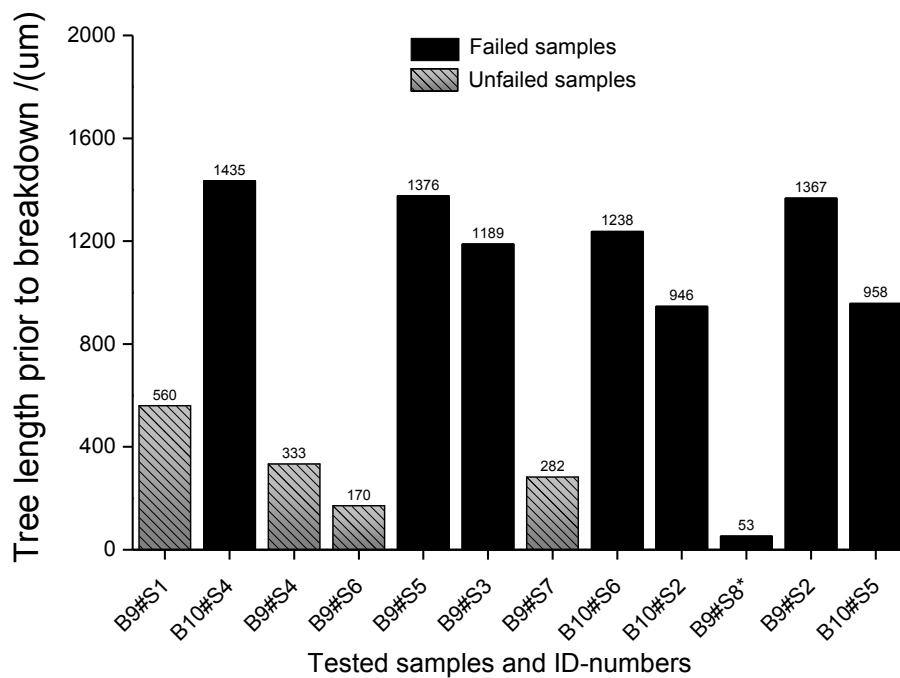
Figure 9-10: Measured tree lengths. Failed samples prior to breakdown, Un-failed samples after 10 hours.

Figure 9-11 shows the plots of the final lengths of electrical trees measured under negative 60 kV DC tests. As no breakdown occurred during the negative polarity test, only the propagated tree length in relation to the AC pre-incepted initial tree lengths is discussed. If the lengths of the initial trees were plotted against the distance

of tree propagation in each sample instead of time to breakdown as in section 9.3.2, a similar threshold around 40 μm can be roughly identified under negative DC test for which electrical treeing barely starts as depicted by Figure 9-12. Except for sample B12#S3 for which the initial tree length was 86 μm see Table 9-1 in which case, only about 19 μm growth was realised after 10 hour of -60 kV DC applied stress. If this data point is censored, then in this case, an upward trend can be seen above 40 μm for which an appreciable tree propagation is obtained.
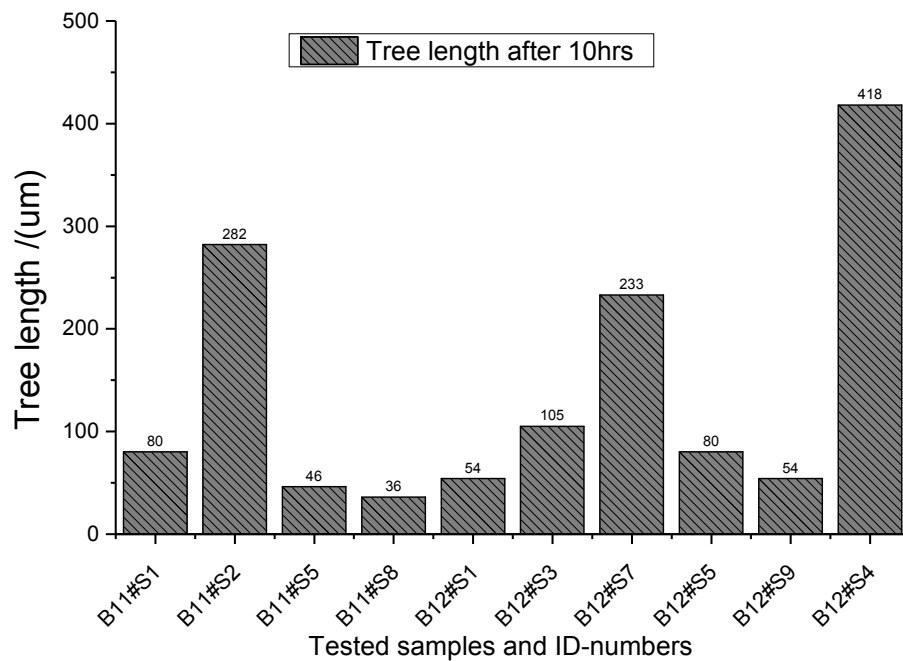
Figure 9-11: Measured final electrical tree lengths tree after 10 hours 0f -60kV DC stress.
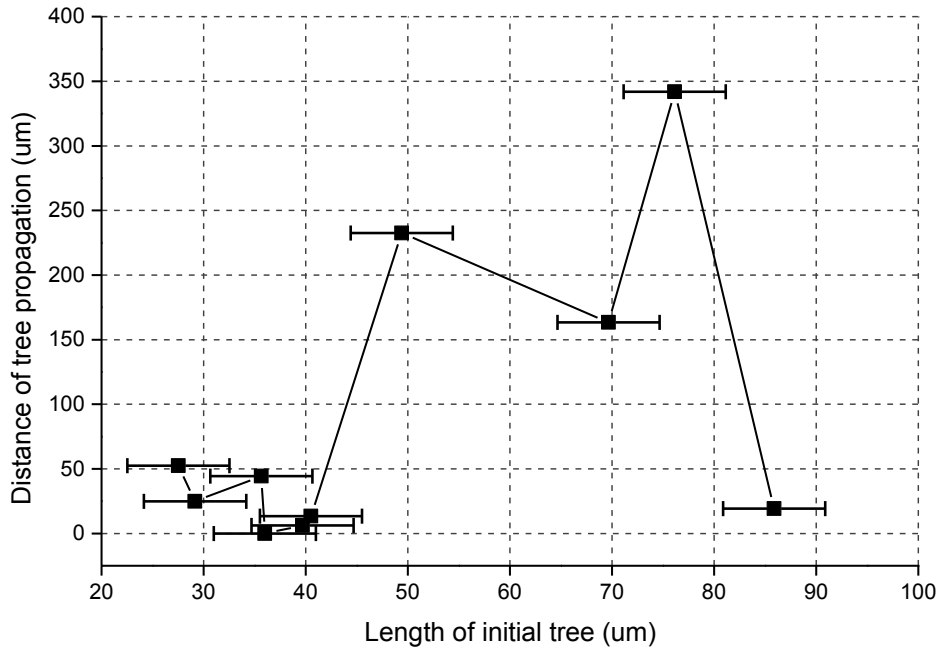
Figure 9-12: The distances of DC tree propagation under -60 kV DC plotted against the lengths of initial trees. The distance of tree propagation is the difference between the tree length at the end of 10 hours test and length of initial tree.

9.3.5 Summary

Section 9.3 presented the electrical tree growth characteristics under ± 60 kV DC stresses from which the following points can be summarised:

- The shape of the initial AC tree does not influence the shape of the propagated DC tree.

- The shorter the length of the initial AC tree, the longer the sample's life time.

- The longer the initial AC tree length short the sample's life time.

- Initial AC tree lengths of about 33 μm and 42 μm were found to be a critical length above which appreciable propagation of DC tree was obtained under positive and negative DC polarity tests respectively.

- Trees grow faster under positive DC than under negative DC as observed in the preliminary test.

9.4 Experimental results for electrical tree propagation under 15 kV peak AC

In this section, visual observation according to experimental results together with measured partial discharge behaviour of electrical tree growth characteristics is presented. Electrical treeing is widely reported to exhibit 3-stage growth characteristics in literature as; the initiation stage (stage 1) which is marked by inception time, the propagation stage (stage 2), marked by the tree growing in the direction of the applied field away from the point electrode and the run-away stage (stage 3) when a rapid growth is observed leading to the final breakdown event. In this study, monitored partial discharge behaviour during electrical tree growth exhibited 5 distinct stages of growth under 15 kV peak AC (10.6 kV rms). The results are discussed in the sections that follow.

9.4.1   Influence of 15 kV peak AC on shape of the electrical tree

The images in Figure 9-13 shows the typical tree growth characteristics observed in one sample under AC test. As can be seen from the images, the electrical tree grew in two main directions, namely:

1. The "forward tree growth" (FTG); defined as a tree growing away from the point electrode towards the ground electrode as shown in Figure 9-13 (a), and

2. The "reverse tree growth" (RTG); defined as tree growing from the counter electrode towards the point electrode as shown by Figure 9-13 (b).

In contrast to the tree shapes observed under DC testing, which had only single tree channel propagated from the AC pre-incepted initial trees, on this occasion, such phenomenon was not observed. It can be seen from images that, under AC test, the electrical trees continued from the AC pre-incepted initial trees as one structure and no clear distinction can be identified optically from the two as if only one stage experiment was involved from the start of the test. However, during the propagation phase, the visual and physical appearances of the tree structure changes having dark-widened channels, fine channels, and dense structure compared to what was observed during the DC test. The changes in tree lengths and widths were measured from the captured 2D images, from which the plots of tree lengths and widths against time were plotted for interpretation of results and growth characteristics.

(a) Forward tree growth (FTG)

(b) Reverse tree growth (RTG)
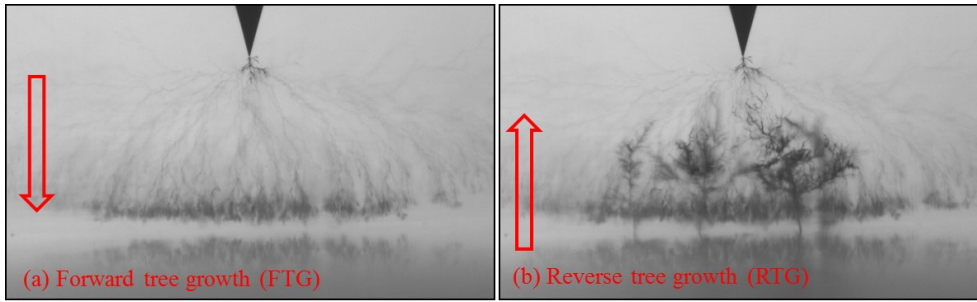
Figure 9-13: Typical example of Forward and reverse tree growth.

9.4.2 Time to breakdown under AC

Figure 9-14 shows the column and label plots for the times the samples were stressed until breakdown occurred or when the experiment was stopped for un-failed samples during the AC test.
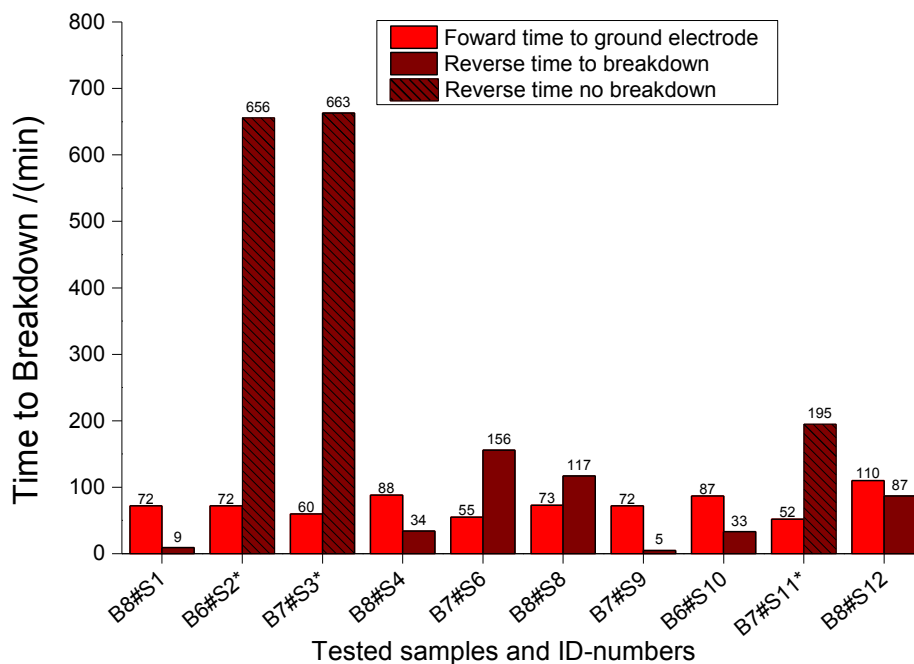
Figure 9-14: Forward and reversed stress times for tree growth under 15 kV peak AC test.

As two directions of growth were observed during this test, the tree growth times for both forward and reverse directions of growth for each sample was plotted. The sum of the forward and the reverse stress times made up the time to breakdown for the samples that failed. For the un-failed samples, the sum of forward and reverse times is the total time the sample was stressed before the experiment was stopped. The forward times in this plot are the tree growth times in the forward direction prior to the emergence of the reverse growing tree. The reverse time is the time when the first

184

branch of the backward growing tree was observed until breakdown ensued in the failed samples, or when the experiment was stopped for the un-failed samples. Thus the average growth time in the forward direction for all samples is 74.1 minutes whereas the average reversed time considering only the failed samples is 63 minutes. The average time to breakdown considering forward plus reverse time for only failed samples is 143 minutes. Comparing this with the average time to breakdown of 250 minutes recorded for the failed samples under +60 kV DC test, this is a reduction of about 43% of life time when the samples were stressed using 15 kV peak AC instead of +60 kV DC stress.

9.4.3 Electrical tree growth rate characteristics under AC

Figure 9-15 shows the plots of the measured tree lengths normalised against 2 mm insulation gap distance while Figure 9-16 shows the growth in width normalised against 6 mm maximum width of the captured images represented on the y-axis of each plots and the x-axis in each plot shows the time it took for each sample to fail.

The limitations and errors that can be introduced in such measurement were outlined in section 9.1. The 'x' markers on the plot represent the data point at which the reverse trees were observed, while the diamond '♦' markers represent the times when breakdown finally occurred in each sample. At the 'x' markers data point, most of the forward growing tree tips in the direction perpendicular to the point electrode have already reached the ground electrode, while the periphery of those spreading in the width direction were still growing. As can be seen from the plots, some of the samples failed few minutes after the tree tips touch the ground electrode shown immediately after the 'x' markers data points by the diamond marker '♦', while in some samples, it took several minutes before breakdown finally occurred as shown by the constant levelling of the curves (saturation in lengths). For example as shown in Figure 9-15, samples B6#S2, B7#S3 and B7#S11 did not breakdown, it took further 656 minutes, 663 minutes, and 195 minutes for the tree lengths and widths to saturate before the test was stopped. The curves for the plots of these samples are shown in Figure 9-15 and Figure 9-16 with arrows to indicate that breakdown did not occur when the experiment was stopped.
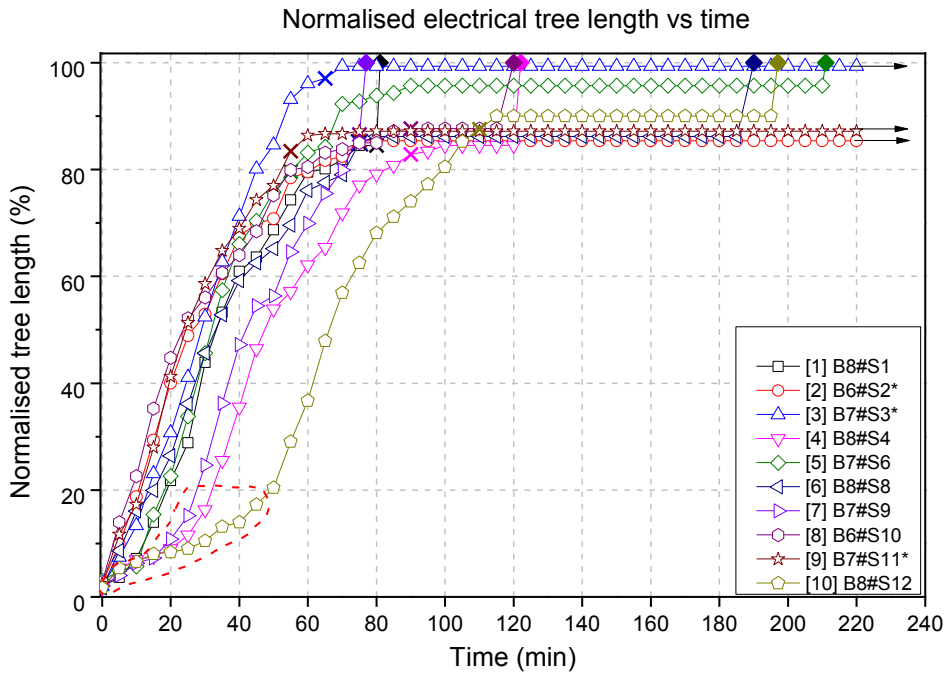
Figure 9-15: Plots of electrical tree lengths vs time of all samples normalised against 2mm insulation gap distance, 'x' markers show point when reverse tree emerges, '♦' show breakdown points and arrows show curves of un-failed samples.
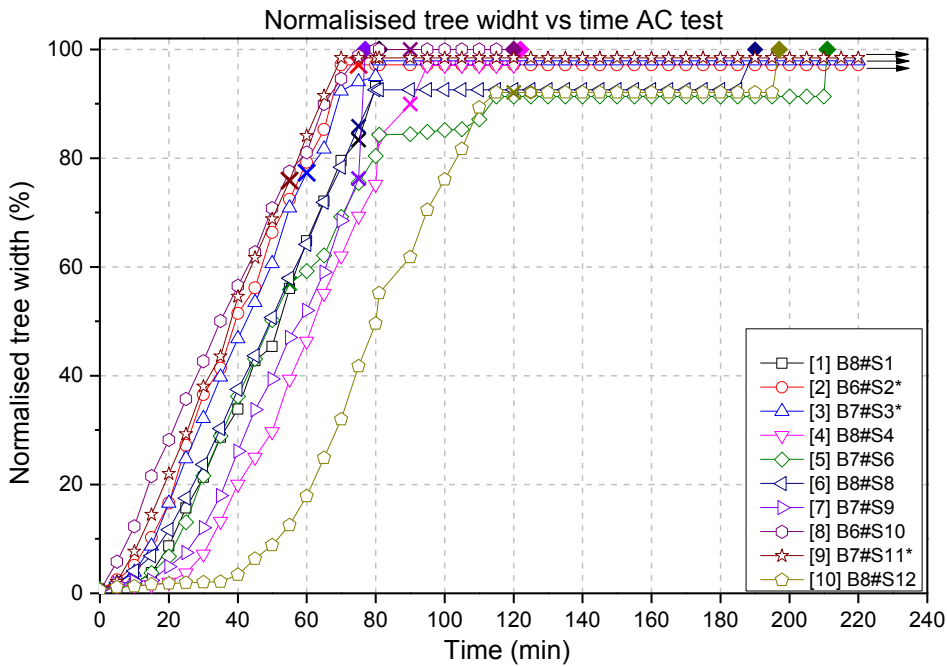
Figure 9-16: Plots of electrical tree widths vs time of all samples normalised against 6mm image width. 'x' makers the spread in width when the reverse trees emerge, '♦' when breakdown occurred and arrows show curves of un-failed samples.

It can also be seen from the plots that on average the 'x' markers of all plots lie about 85% (1.7 mm) of the normalised 2 mm insulation gap distance when no further

growth in length was observed, while in the width direction they lie about 90% (5.4 mm) of the normalised 6 mm maximum width of 2D projected images. The variations seen in the position of the 'x' markers was attributed to some of the limitations outlined in section 9.1 and deviation that can be introduced in the insulation gap distance (i.e. 2 ± 0.2) mm in each sample as outlined in chapter 3 section 3.6.2.

Generally steady growth rate in lengths and widths were observed in all samples up to about 60% (1.2 mm) and 80% (4.8 mm) of the gap distance and the width of the 2D projected images respectively, before a deceleration in growth rate were observed when the tree lengths were approaching the counter electrode from about 65% to 85% of the normalised gap distance (Figure 9-15). However, in the first 20% growth in length, the curves of three samples (B8#S4, B7#S9 and B8#S12) shown in an enclosed dotted red line in Figure 9-15 had a slow growth rate. In these samples, it was observed that the early growths of the trees maintained bush-like structures up to about 25 minutes after voltage application, which explained the slow nature of the growth rate observed as shown in Figure 9-17.
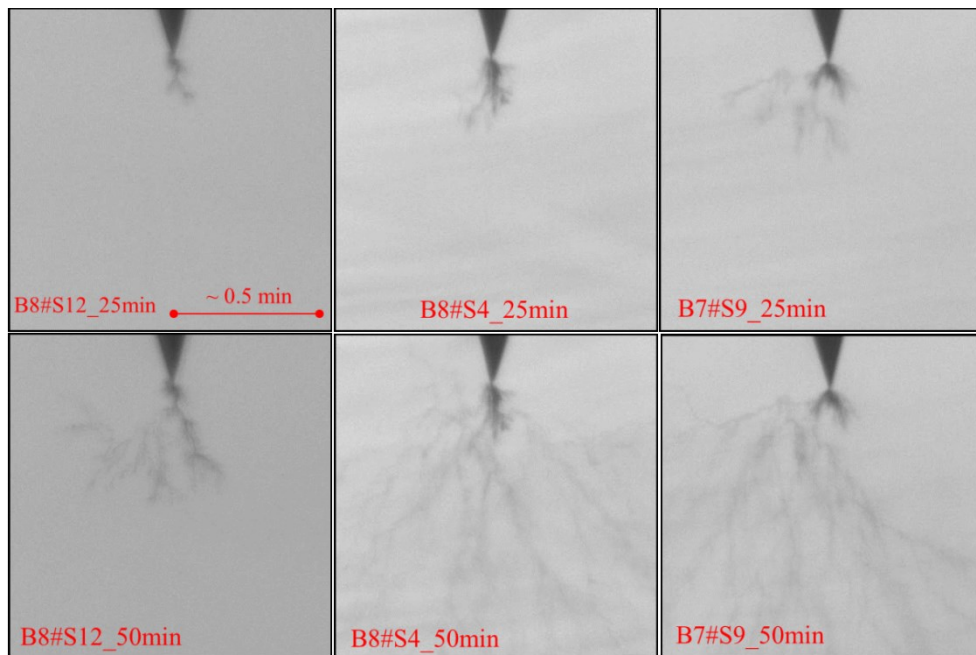
Figure 9-17: Transition of tree growth characteristics from a bush type to a fine type tree structure, exhibiting slow and fast growth during bush and fine tree structure. Scale bar is the same for all images.

They then start to grow at about the same rate when the fine tree structures started to emerge from the initial early trees which were darker in structures. This is shown in the images of Figure 9-17 in these three samples after 50 minutes of voltage application with sample B8#S4 and B7#S9 having faster growth rate than sample B8#S12.The electrical trees spread in all the samples almost at about the same rate except for sample B8#S12 as can be seen from the plots of both Figure 9-15 and Figure 9-16 and the corresponding images shown in Figure 9-17.

9.4.4   Sequence of tree growth under 15 kV peak AC with simultaneous partial discharge measurement

Figure 9-18 shows the electrical tree growth curve together with a physical measurement of partial discharge activities acquired during a test from an initial tree stage until breakdown occurred for a typical test sample plotted on 4Y-axis graph; showing the tree growth rate, the magnitudes of the average and peak values of recorded apparent charge and the discharge repetition rate with time. As can be seen from the plot of Figure 9-18, stage 1; is the inception stage which was discussed in section 9.2 as the initiation stage. The observed partial discharge characteristics together with the acquired images of tree growth which made up of 5-Stage growth characteristics is shown in Figure 9-18, and are discussed below.
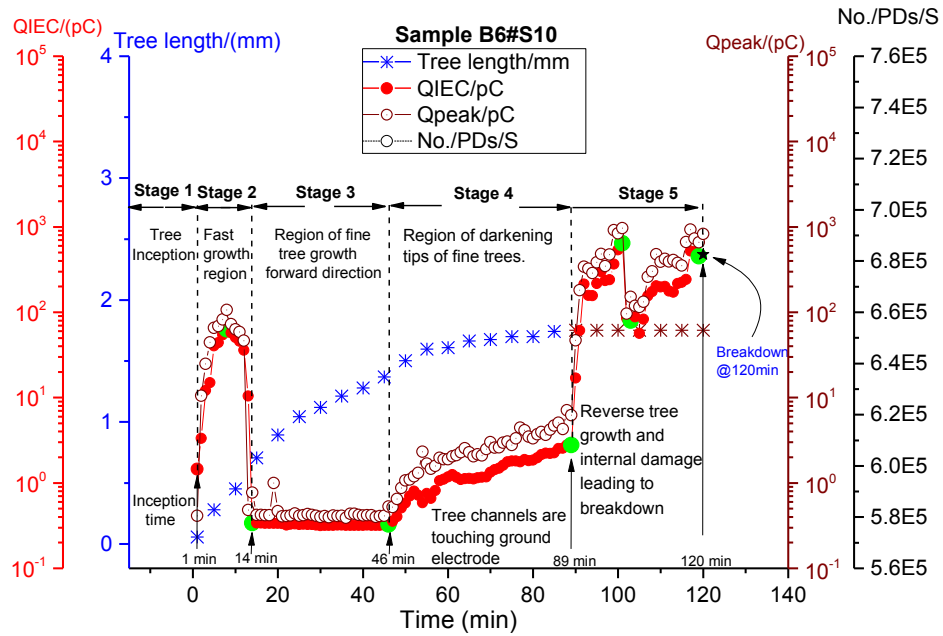
Figure 9-18: Measurement of physical tree growth and partial discharge activities allowing 4 stages of growth to be identified after pre-initiation.

Stage 1: The initiation stage; the image shown in

Figure 9-19 is the initial tree in the test sample prior to voltage application and PRPD plot shown adjacent is the plot acquired immediately after the test voltage was applied which lead to the observation in stage 2.
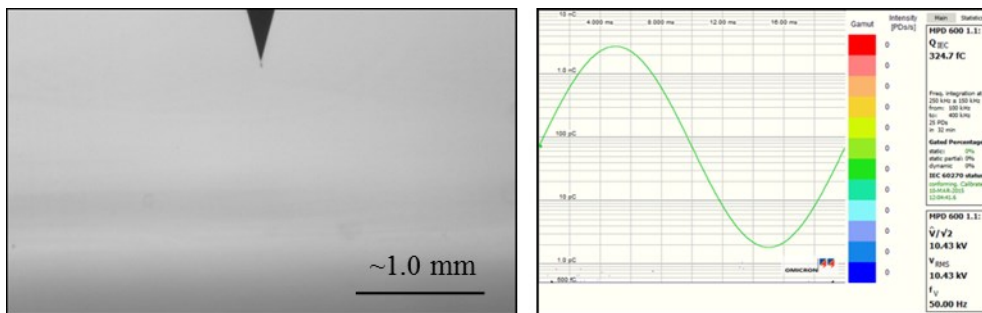
Figure 9-19: Stage 1_The initiation stage.

Tree initiation stage is usually marked by variable waiting times prior to the detection of the first visible tree artifact (ageing) as reported in [101] for example, and this can occur even in batches of samples fabricated using the same fabrication procedure as observed in section 9.2. It was for this reason that in this test all the samples were pre-initiated. In this test, samples with "initial tree" of about ~50 μm

were selected for test at the propagation stage. During the quick initiation stage partial discharge data was not collected.

Stage 2: Region of fast forward tree growth (FTG); Figure 9-20 shows the captured tree image and the corresponding measured PD activity adjacent after 14 minutes of voltage application on the pre-initiated sample shown in stage 1. The image in Figure 9-20 reveals two types of tree channels. Dark, widened branched tree channels extending from the existing "initial tree", and is marked by rising PD activities which increased sharply from an average apparent charge magnitude of about ~1.4 pC in the first minute, up to about ~80 pC in the 7th minute. This then followed by a larger array of finer tree channels propagating in length and width up to the 14th minute and is marked by decreasing value of recorded average apparent charge value of about ~80 pC in the 8th minute to about ~0.3 pC value which is the effective average discharge value computed by the measurement system in the 14th minute.
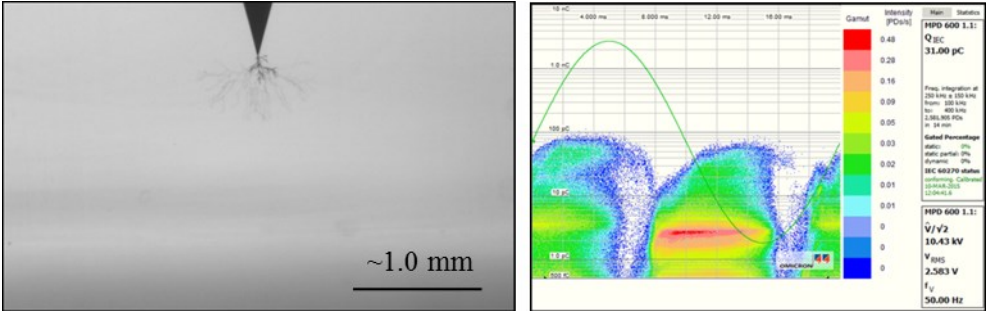
Figure 9-20: Stage 2_ (1 to 14) min. Region of combined dark and fine trees channels.

This observation is depicted in the plot of Figure 9-18 stage 2. The PRPD plot shown in Figure 9-20 shows the distribution of cumulative discharge intensity, during this stage (14 min) of growth, in which the PDs were active throughout the period.

Stage 3: Region of fine tree growth; in this region, steady tree growth rate is observed in both length and width direction. However the magnitudes of the recorded PD values are about ~ 0.3 pC throughout this period which lasted for about 30 minutes shown in Figure 9-18.
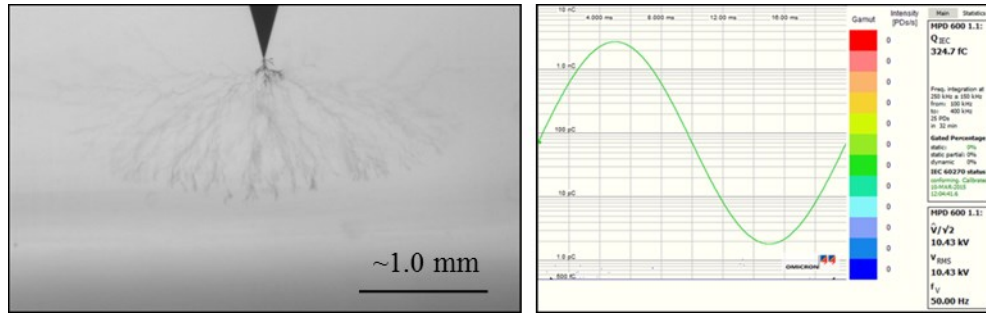
Figure 9-21: Stage 3_ (14 to 46) min. Region of fine tree growth.

The rate of tree growth in both length and width is about the same, as the boundaries of the tree tips propagate towards the counter electrode. Comparing Figure 9-20 and Figure 9-21, the initial dark tree branches observed in Figure 9-20 were not observed to grow at the heart of the fine tree channels observed in this stage throughout the 30 minutes time period. Also no obvious distinction was observed between the fine tree channels observed in stage 2, and those observed in stage 3 even though the magnitude of PD values recorded in stage 3 was only about ~0.3 pC, and those in stage 2 ranges up to 80 pC in the first 7 minutes of voltage application before declining to about ~0.3 pC in the 14th minute. This observation suggests that PDs with high magnitudes were responsible for the formation of dark tree channels, and lower magnitude PD were responsible for the finer tree growth.

Stage 4: Regional of darkening fine tree channels: At this stage, gradual increase in the magnitude of the average apparent charge was observed from about 0.3 pC to about ~ 3 pC in the 46th to 89th minutes as shown in Figure 9-18, with the tree growth curve becoming saturated at the end of that period. The image captured at the end of this period, is shown in Figure 9-22. It can be seen that most of the fine tree channels approaching the ground electrode in stage 3 (Figure 9-21), have traversed the gap between the point and the ground electrode, and the 'length' of the tree is self-limited.
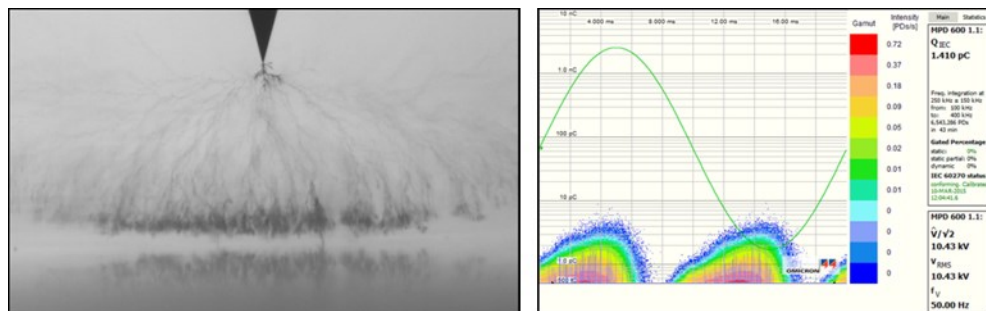
Figure 9-22: Stage 4_ (46 to 89) min. Region of darkening fine tree channels.

The trees also become optically denser as can be seen in Figure 9-22. In the example shown here; this stage lasted for 43 minutes. The shapes of the trees observed at the end of this stage are bush-like, shown as dark region along the ground electrode in the captured image in the 89th minute with the corresponding plot of the cumulative discharge activity depicted in the PRPD plot shown adjacent to the image.

Stage 5: Region of reverse tree growth (RTG); the observed features of tree growth at this stage can be further characterized into two distinct characteristics.

Firstly, a reverse tree growth process, marked by tree growing from the ground electrode (RTG) towards the point electrode. The RTG is rapid in all tested samples but does not lead to immediate failure of the samples. Figure 9-23 shows a typical image of a reverse tree in this example. The RTG started to emerge in the 89th minutes as two separate branches, with the leading branch quickly approaching the FGT from the point electrode after 1 minute as shown in Figure 9-23.
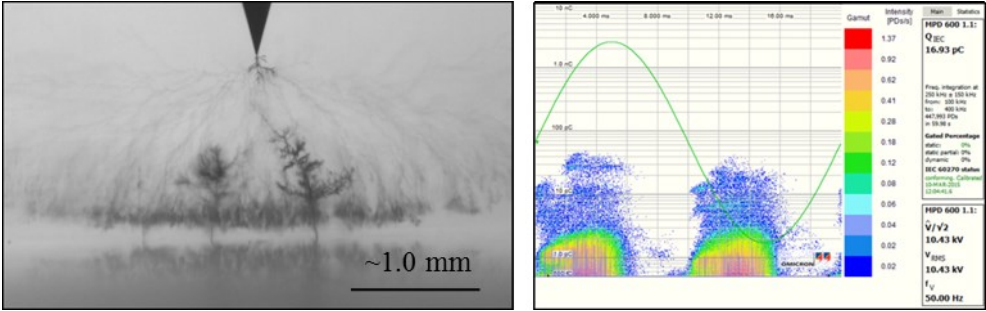
Figure 9-23: Stage 5-1_ (89 to 90) min. Region of reverse tree growth.

The reverse treeing process lasted for about 12 minutes with the leading branch already bridging the FTG in the 101 minutes as shown in Figure 9-24. During this period, a third branch also emerged as shown in the image. As can be seen in both Figure 9-23 and Figure 9-24, the reverse tree branches are darker and thicker having different structures as compared with the branch and bush-like structures observed in stages 2 and 4 repectively. The structures of the reverse tree branches observed in this study were similar to those observed in [125, 135] and were described as pine-like or bine branches. See Appendix B-5 and 6 for compiled images of the reverse tree structures. The emergence of the reverse tree was marked by sharp increase in discharge activity from average apparent charge values of about 3 pC to about 600 pC in the first 12 minutes, followed by decrease in apparent charge magnitude to about 100 pC. This was accompanied by temporary stagnation of the reverse and the onset

of more internal damage of the sample. The rapid growth of the reverse tree in Figure 9-23 in one minute (89th to 90th minutes) is the behaviour that would normally be referred to as run-away stage in the traditional 3-model of tree growth but here is shown to be a tree growth over a distinct period of time in the reverse direction i.e. from the plane electrode towards the point electrode which lasted for about 12 minutes as shown in Figure 9-24 (90th min to 101min).
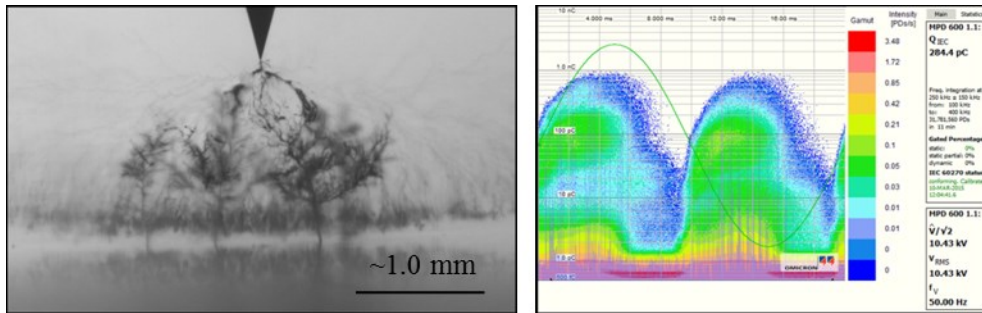
Figure 9-24: Stage 5(2) _ (90 –to 101) min. Reverse tree bridging forward tree.

Secondly, macroscopic internal damage leads to carbonization of the entire visible gap spacing between the point and the plane in the test sample with attendant fluctuating large magnitude of PD values starting from 101 minutes which lasted for further 19 minutes leading to breakdown of the test sample in 120th minute as shown in Figure 9-25 . The cumulative plot of PRPD pattern prior to breakdown during this period is shown adjacent in the Figure. It can be seen from Figure 9-25 that a huge halo surrounds the breakdown channel showing structural change of the insulation. This observation suggests that the final breakdown event generates high energy and is a distinct process from treeing. However, 2 of the tested samples did not breakdown during the reverse treeing process after 12 hours of voltage application and 1 sample after about 4 hours of voltage application though extensive damage has been inflicted on the test samples. Several visual observations were made within the body of insulation during the reverse treeing process. The reverse tree growth process can be a very pronged in some cases as observed in three test samples during this test. These observations are discussed further in section 9.4.5.
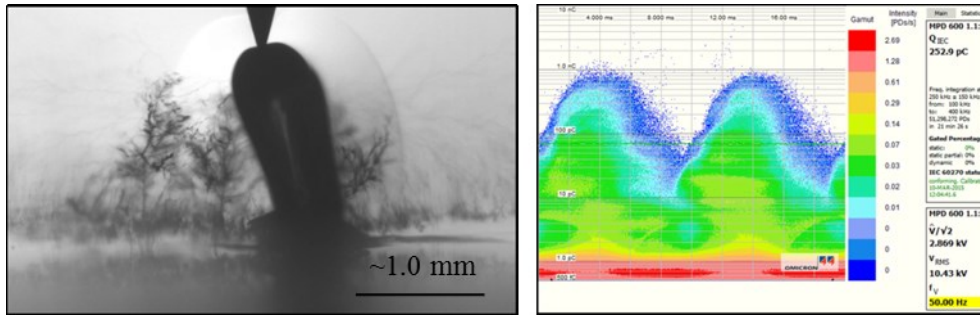
Figure 9-25: Stage 6_ Breakdown at 120 min.

9.4.5   Ageing mechanism and internal damage during reverse treeing

Section 9.4.4 discussed the general trend of electrical tree growth characteristics observed in all the 10 samples under AC test. It was shown that the forward tree growth involved three mains stages whereas the reverse tree process involved about two stages. However, the observed visual phenomena during the reverse treeing process were more complex events. Video recording of the observed behavior would have been better capturing such events so that a play back would allow post-recording analysis of captured event when required. The CCD camera used in this experiment has no recording function and thus only captured and logged images of events will be discussed here.

During the reverse treeing process the camera was set to capture images every second in some cases and 1000s of images were obtained. The developments of the reverse trees were rapid off-shoot of tree branches from the ground electrode. A process defined hereafter as 'sprouting' which was accompanied by high and rising magnitudes of apparent discharge values in the regions of 100s of pico-coulombs as shown in Figure 9-18 from 89 to 101 minutes, which then followed by internal damage as discussed above. The physical phenomena observed can be summarised into three processes namely; rapid off-shoot of tree branch from counter electrode (sprouting), crack-like propagation and whitish bursts in the body of the insulation, and finally light flashes and carbonisation of the cracked regions. These phenomena are described below.

Sprouting of tree branches: The sprouting of the tree branches starts from the ground electrode hence the name "reverse tree" but afterwards, trees sprouting from the main body of the insulation which was not visibly linked to any existing tree

194

branch was observed as shown circled in solid red line in Figure 9-26 (b) after 92 min. Note that Figure 9-26 (b) is the magnified region shown by red rectangle in Figure 9-26 (a). This sprout of bushy-like tree is not seen at 90 min in Figure 9-26 (a)
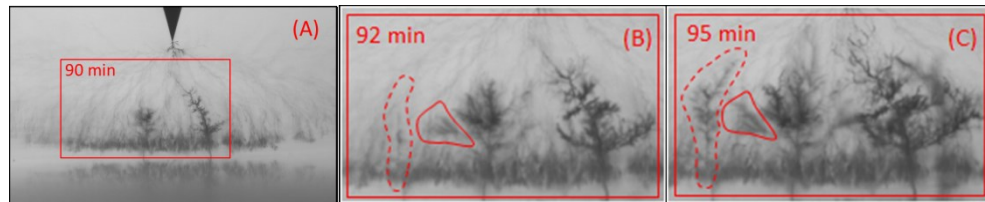
Figure 9-26: Reverse tree growth and sprouting of tree in the main body of insulation.

Crack-like propagation and whitish bursts; another observed phenomenon was the widening of the fine tree channels which appeared like crack propagation in existing fine tree channels as well as whitish bursts (cracks) in the main body of the insulation. To use the analogy of a growing flower, this phenomenon can be likened to an opening of a flower bud when it received energy from a rising morning sun which appeared as whitish bloom in the body of the insulation. Similar observation was made from existing fine tree channels which then appears as white widened channels (cracks) as shown in Figure 9-26 (b) by enclosed red dotted line. It can be seen that this widened white channel provided path for the formation of a fully grown pine-like tree after 3 minutes shown in Figure 9-26 (c) also marked by enclosed dotted line. Similar phenomenon was observed again in the 96th minute shown by marked regions in red in Figure 9-27 (a) which became darkened perhaps filled with carbonised decomposition bi-products in the 100th minute shown in Figure 9-27 (b).
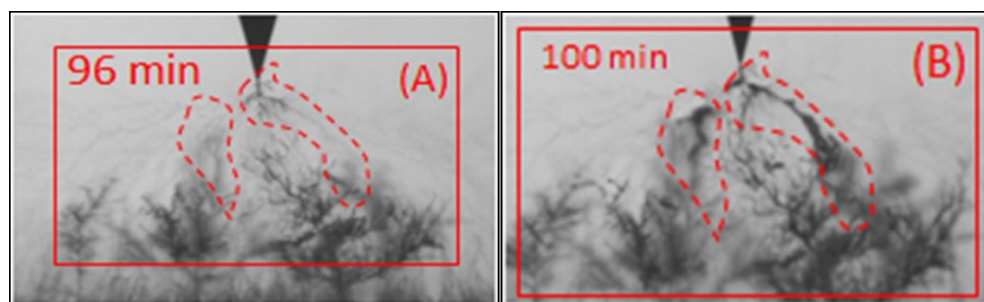
Figure 9-27: (A); crack in the body of insulation and widened fine channel, (B); regions in (A) filled with carbonised decomposition bi-product.

Light flashes and crack carbonisation: lastly, the phenomenon observed during this prolonged reverse treeing process was what appeared to be occasional ignition of light flashes in the so-called "cracked regions". This process starts by the appearance of a

whitish burst (crack), followed by a flash of light and carbonisation of the region when the light extinguished. Figure 9-28 (a) shows a typical example of such flash of light enclosed in solid red line and in Figure 9-28 (b) when the light extinguished after 1 minute.
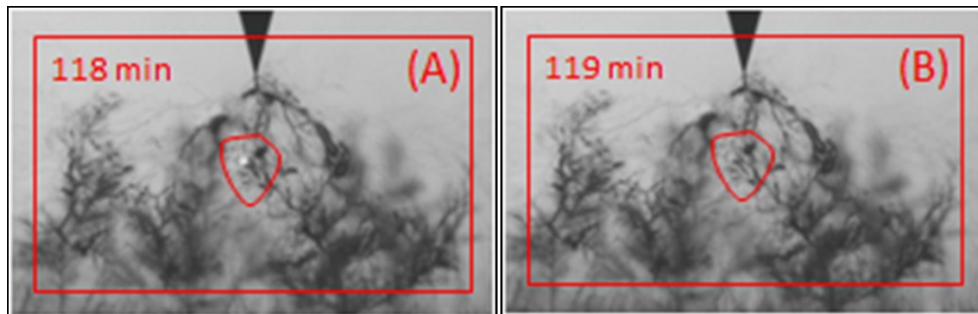
Figure 9-28: Observation of light flush in the body of the insulation.

The phenomena described above were not a one off event but occurred regularly during the reverse treeing process under AC test and was marked by fluctuating and high discharge activities. During this test (AC at 10.6 kV rms) two samples did not breakdown after 12 hours as mentioned earlier. The images shown in Figure 9-29 (A) and (B) are for these two un-failed samples while (C) was for a failed sample which lasted for 197 minutes before breakdown occurred. Comparison can be made of the extent of internal damage to the samples. Images (A_1), (B_1) and (C_1) are acquired few minutes after the reverse treeing starts, and (A_2), (B_2) and (C_2) after the time period shown on the images.
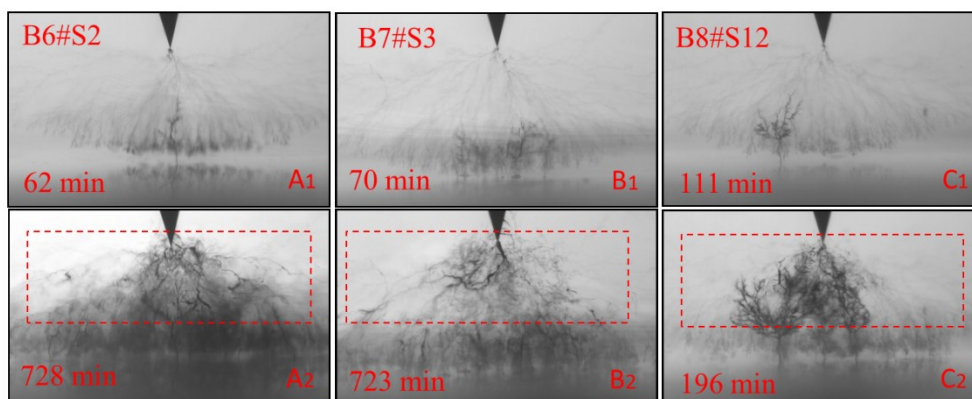
Figure 9-29: Images of reverse trees a few minutes after they appeared, A_1, B_1, C_1 and internal damage suffered by samples due to prolonged ageing in the process, A_2, B_2, C_2.

The red rectangles in these images show regions where these cracking and what appeared to be occasional light flashes were observed. Comparing images (A_1), (B_1)

and (C_1) to (A_2), (B_2) and (C_2) the contrast in background can be seen due to accumulated damage suffered by the material with time. The longer the stress time before breakdown, the more damage is accrued seen as more whitish area in A_2 and B_2 compared to (C_2) as a results of the time scale involved due to the burst of cracks described above and in combination of the illuminated background light.

Figure 9-30 shows the plot of partial discharge activity for a complete life cycle acquired for sample B8#S12. Figure 9-29 C_{1-2} were the images acquired in the final stages of that test. This plot looks more complex than the example presented in Figure 9-18 for sample B6#S10 with the 5-stage growth characteristics clearly marked. However, the stage 5 in Figure 9-30 has been further divided into stages 5.1 to 5.3 which reflect growth characteristics observed in sample B8#S12. The reverse tree shown by stage 5.1 in Figure 9-30 was followed by a period stagnation where the leading reverse tree branches stopped growing for a period lasting 22 minutes shown on the time axis of Figure 9-30 from 126 minutes to 148 minutes as stage 5.2. During this period, the magnitudes of the average apparent charge values measured fluctuate between 0.6 pC to 1.5 pC.
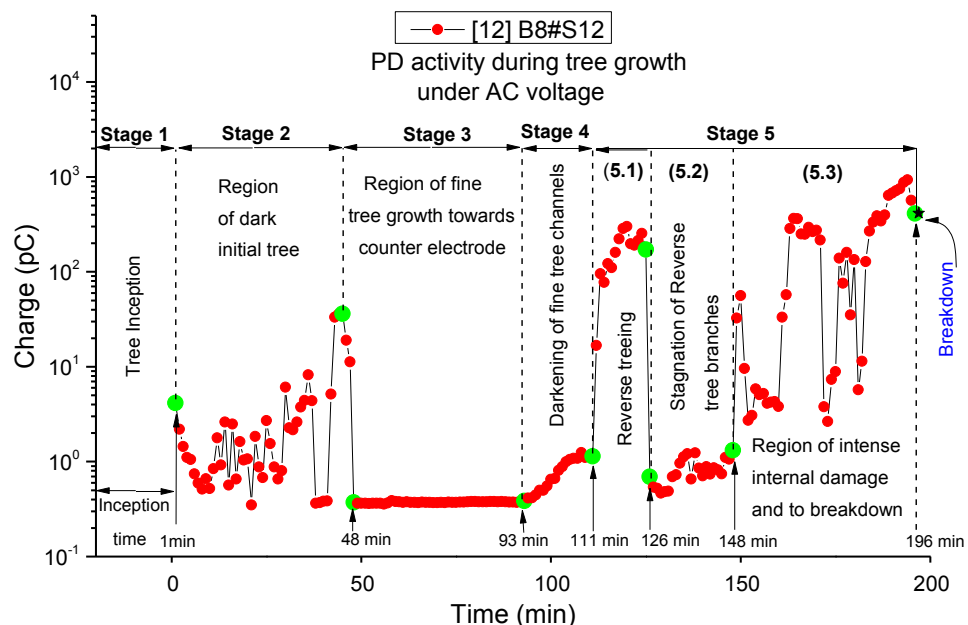
Figure 9-30: Partial discharge activity during physical tree growth characteristics in sample B8#S12.

The captured tree images during this time period are shown in Figure 9-31. As can be seen from the images, distinct differences cannot be identified between the two image due to the stagnation even though the time elapsed between the two images

197

was 22 minutes which is a long time to cause a significant damage as seen for the 15 minutes it took to generate the huge reverse trees from 111minute to 126 minutes in stage 5.1 of Figure 9-32; image is shown in Figure 9-31A. It must be emphasised here that, when the leading branches stop growing, very short spiky and sometimes fine side branches grow from the main branch. See appendix B–5 and 6 for compiled images of reverse trees under AC test.
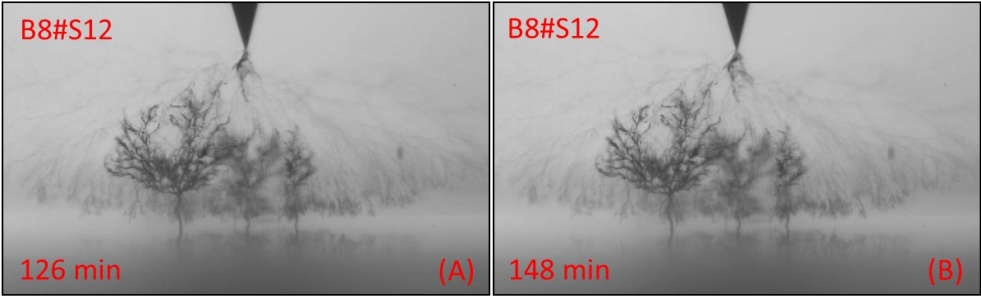
Figure 9-31: Stagnation of reverse treeing. The time difference between the two images is 22 minutes but structural differences cannot be identified from the images.

After this time period, sporadic discharges begin again in stage 5.3 the so-called "region of internal damage". As can be seen from Figure 9-31, stage 5.3 this is marked by highs and dips values of charge magnitudes which culminated into a severe damage within the sample and finally resulted in breakdown of the sample. Figure 9-32 (a) shows the captured images prior to breakdown and (b) shows the final breakdown event.
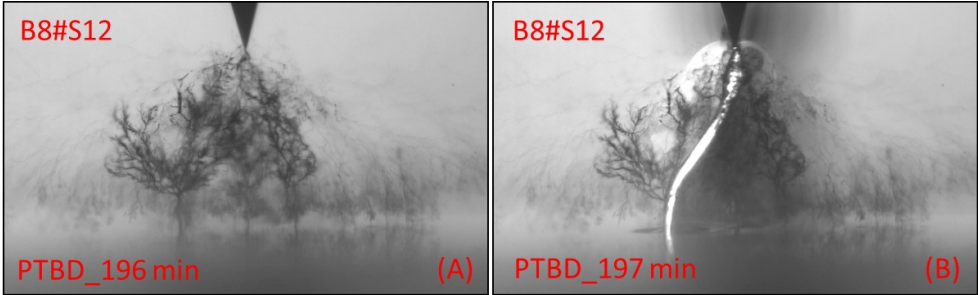
Figure 9-32 : (A); internal damage prior to breakdown and (B); breakdown channel showing light coming from the root of the reversed tree following one of the reverse tree branch and bridging the HV electrode.

Figure 9-33 shows the plot of magnified region of the partial discharge activity during internal damage process together with the recorded values of the average apparent charge magnitudes. It was this kind of unstable discharge activity that was responsible for the bursts seen as whitish cracks in the body of the insulation together with the

198

apparent light flashes observed during this prolonged internal damage activity described above.
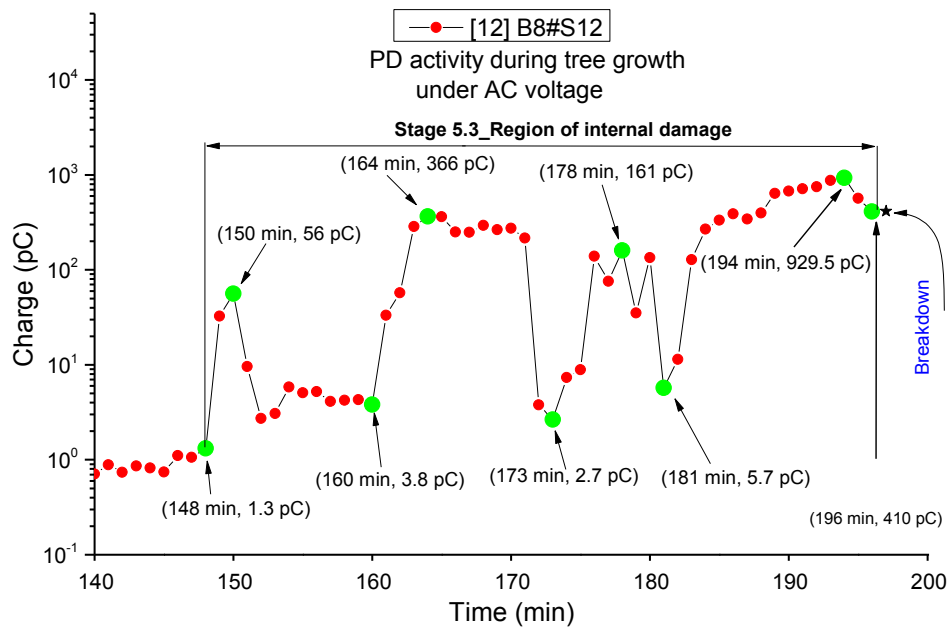
Figure 9-33: Fluctuating discharge activity which led to intense internal damage in sample B8#S12 shown in Figure 8-34.

9.4.6 Summary

The results of simultaneous imaging of electrical tree growth and partial discharge measurement which allowed 5-stages of the electrical tree growth characteristics to be identified has been presented. Tree shape, growth rate, and time to breakdown under AC test were found to be different to that of DC testing. The key findings during the AC test can be summarised as:

- **Growth characteristics;** forward and reverse growth was found in all samples stressed using 15 kV peak AC.

- **Electrical tree shape;** unlike under DC testing where a single branch tree was observed to emanate from the incepted initial trees, under AC variable shapes were observed having dark-widened channels, as well as fine and dense tree structures.

- **Time to breakdown**; the average time to breakdown for failed samples under AC test was 143 minutes. This is a reduction in lifetime of about 43% of

failed samples under DC test in which the recorded average time to breakdown was 250 minutes.

- **Growth rate characteristics;** Tree growth rate was faster than under DC test. The trees occupied very large volume of the entire sample resulting in an extensive damage before breakdown occurred.

Figure 9-34 shows the plots of apparent charge magnitudes normalised against propagation time for all failed samples under AC test. As can be seen from the plot, the time scale of discharge activities in each individual sample is different during the propagation. Fluctuations in discharge activity prior to breakdown can be observed in all samples together with the 5-stage growth process described above. Appendix C-1 shows the plot of partial discharge activity of each individual sample tested under AC test.
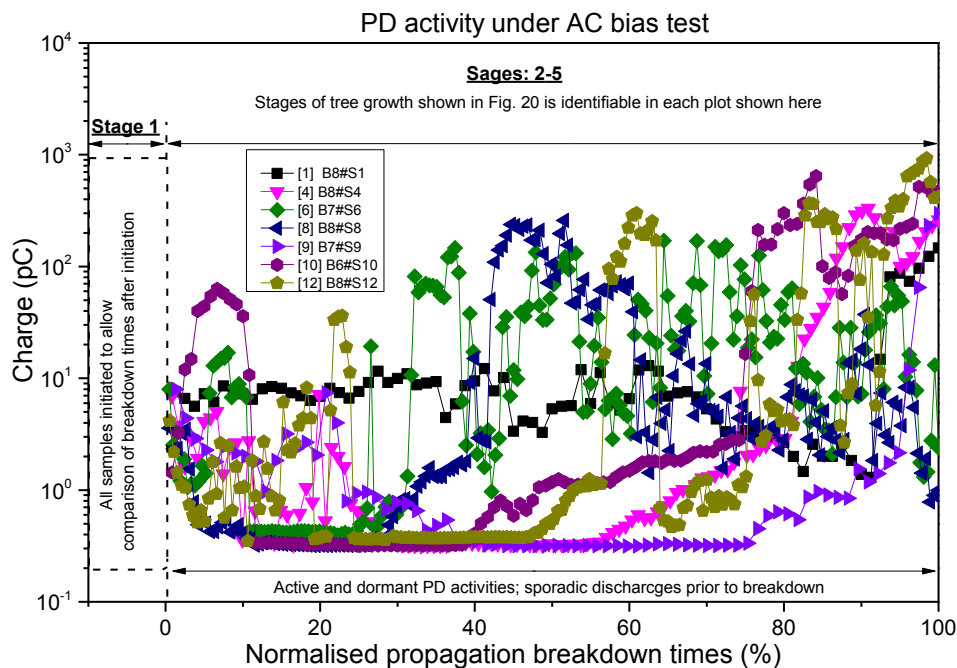
Figure 9-34: Partial discharge activity for all failed samples under AC test normalised against propagation breakdown times.

9.5 Effect of superimposed ±15kV DC on 15 kV peak AC on tree growth characteristics

In sections 9.3 and 9.4, above, the electrical tree growth characteristics and time to breakdown were found to vary significantly under AC and DC voltage regimes. In this section, the results of the effect of AC superimposed on positive DC and on negative DC (positive DC bias and negative DC bias) tests and how it influences the

electrical tree shape, growth characteristics and times to breakdown are now presented.

9.5.1 Influence of ±15kV DC bias on 15 kV peak AC on electrical tree shape

The electrical trees grown under positive and negative DC bias tests had similar shapes to those observed under AC test, with initial extension of dark bushy trees which had a slow growth rate for about 25 minutes of voltage application in some samples after which faster growth rate were observed when the fine arrays of tree structure started to grow. Unlike under AC tests where a forward and reverse propagation was observed, in this case only forward growth was observed in all samples until breakdown ensued. In the final stages of the growth when the trees were approaching the counter electrode, widening of the fine tree structures which appeared darker were observed under both positive and negative DC bias tests. These widened tree channels then facilitate paths to breakdown. This phenomenon was observed almost in all samples. But, more visible and well-defined darkened long tree channels were observed often under negative DC bias test.

Figure 9-35 and Figure 9-36 show three examples of the typical images of electrical tree shapes stressed with positive and negative biased voltages. The images at the top show tree shapes in their first 25 minutes of voltage applications and images at the bottom show the shapes prior to the occurrence of breakdown. As can be seen in the images, the first 25 minutes in both test types, the fine tree channels were not clearly visible. However, in the final stages of the experiment, the captured images the trees before the occurrences of breakdown event, became dark and widened with visible long channel via which breakdown occurred.
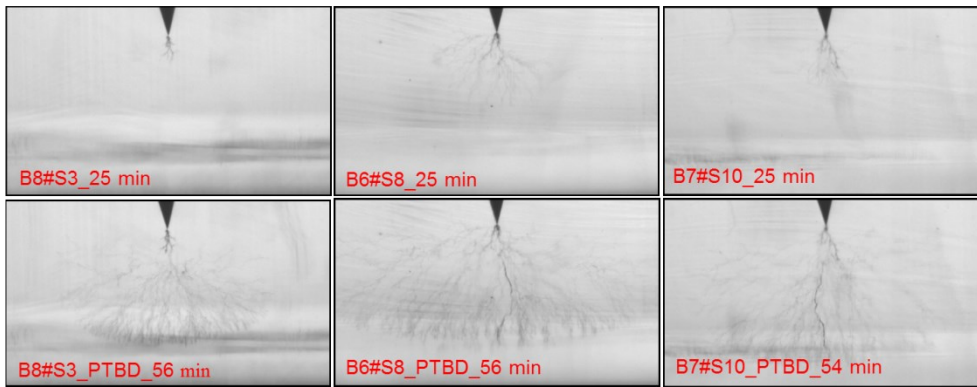
Figure 9-35: Electrical tree shape under positive DC bias test showing initial bush tree, fine tree channels and finally dark and widened long channels prior to breakdown (PTBD).
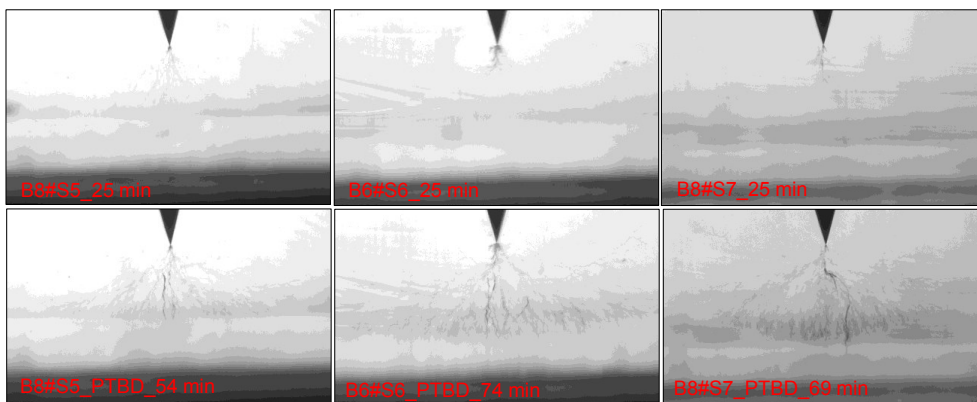
Figure 9-36: Electrical tree growth shape under negative DC bias test showing initial trees, fine tree channels and finally dark and widened long channels prior to breakdown (PTBD).

9.5.2 Influence of ±15 kV DC bias on 15 kV peak AC on time to breakdown

Figure 9-37 and Figure 9-38 show the column and label plots of breakdown times for all the samples tested under positive and negative DC bias tests. Unlike in the case of AC test where only 70% of the samples failed, in these tests all the samples failed, and the time to breakdown for each sample is shown on the columns of the plots. The average time to breakdown for the samples stressed with positive DC bias test was 54 minutes whereas for those stressed with negative DC bias test it was 78 minutes.
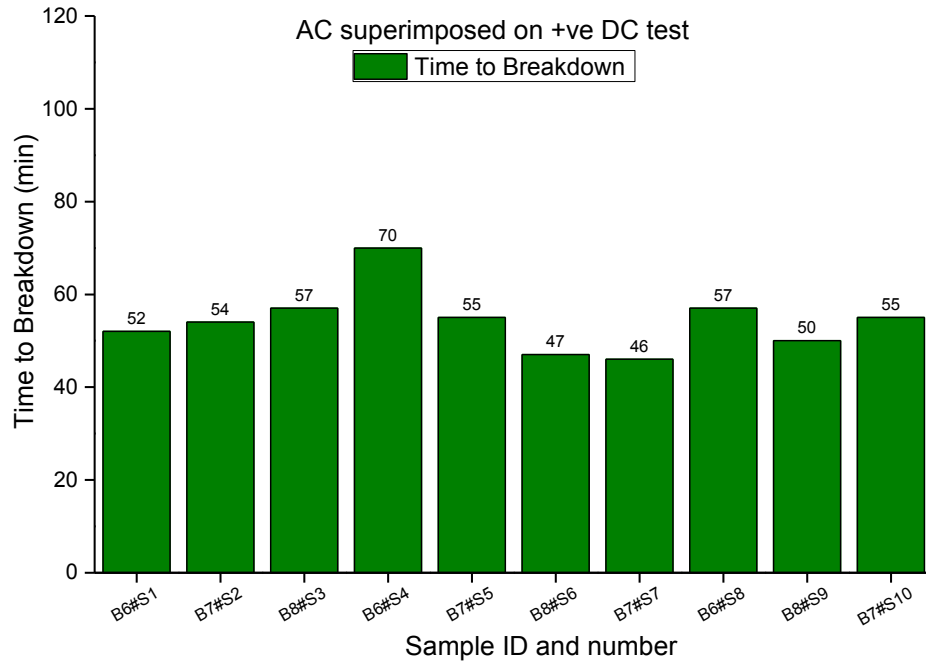
Figure 9-37: Column and label plot showing breakdown times for all samples under15 kV peak AC superimposed on +15 kV DC.
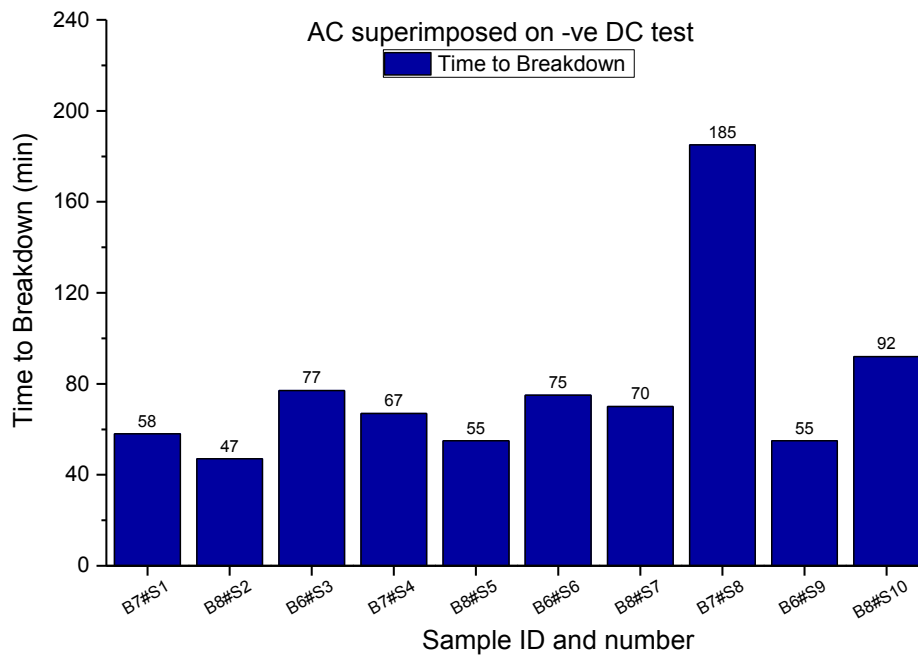
Figure 9-38: Column and label plot showing breakdown times for all samples under 15 kV peak AC superimposed on -15 kV DC.

Comparing these lifetimes to those observed under "pure DC" and "pure AC", the following trend was observed for all the test types carried out in this study:

- Negative DC test at 60 kV; higher life times no breakdown in all tested samples.

- Positive DC test at 60 kV; average life time for failed samples 250 minutes.

- AC test at 15 kV peak AC; average life time for failed samples 143 minutes.

- 15 kV peak AC superimposed on -15 kV DC test; average life time 78 minutes.

- 15 kV peak AC superimposed on +15 kV DC test; average life time 54 minutes.

From the above listed bullet points of average life times in each test type, it can be inferred that; samples stressed with negative DC stress are more reliable than those stressed with positive DC stress and those stressed with negative DC bias test are more reliable than those stressed with positive DC bias stress.

9.5.3 Influence of superimposed 15 kV peak AC on ±15 kV DC on Electrical tree growth rate/characteristics

Growth rate in length direction: Figure 9-39 and Figure 9-40 show the plots of electrical tree growth rate characteristics in lengths direction normalised against 2 mm insulation gap distance of the captured 2D images on the y-axis and their propagation times on the x-axis for both positive and negative DC bias tests. The average propagation times until breakdown occurs for each test type were 54 and 78 minutes respectively shown in section 9.5.2. These breakdown times signifies faster growth rate compared with the 143 and 250 minutes recorded during "pure AC" and "Pure DC" tests respectively. From the shapes of the time dependent plots of Figures Figure 9-39, and Figure 9-40 progressive growth rate characteristics were generally observed. However, samples B8#S3, B6#S4 and B7#S10 showed slow growth rate in the early stages of their propagation under positive DC bias test as shown in Figure 9-39.

Captured images of these samples showed that the slow growth rate were due to the formation of bushier tree structure in the early growth stages of these samples. See

Appendix B-7 to B-10 for compiled images of early and latter tree growths in all samples under these tests. Even though most of the samples had bushy initial tree structures, the time dependent growth rate for each sample was different. This difference may be associated with the internal morphology in each sample which may have high and low density regions and may either hinder or encourage tree growth rate.
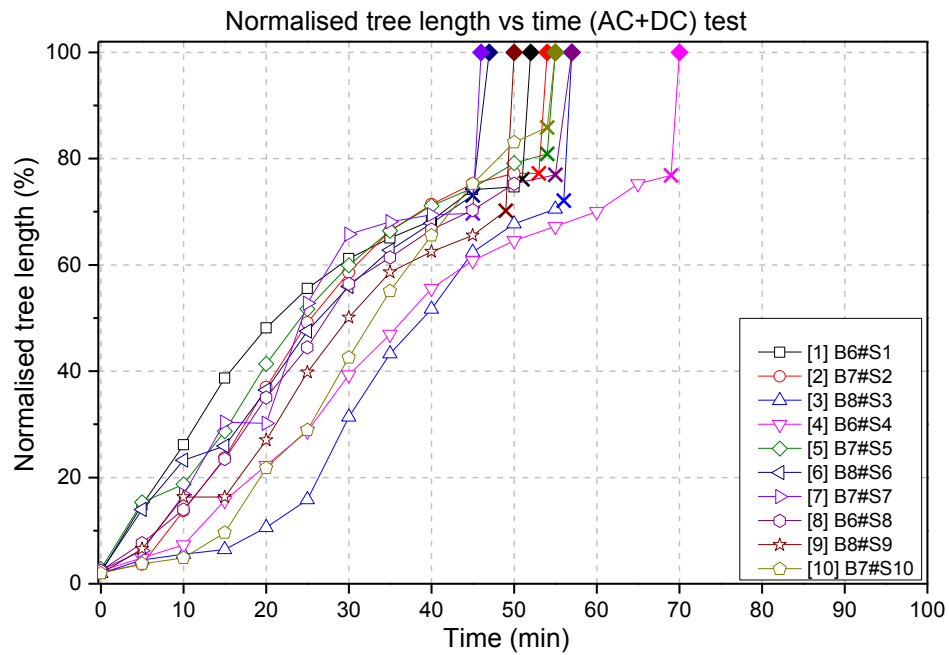
Figure 9-39: Plots of tree lengths vs time for all samples normalised against 2mm insulation gap distance for (AC+DC) test. The 'x' markers show the maximum tree length prior to sample breakdown.
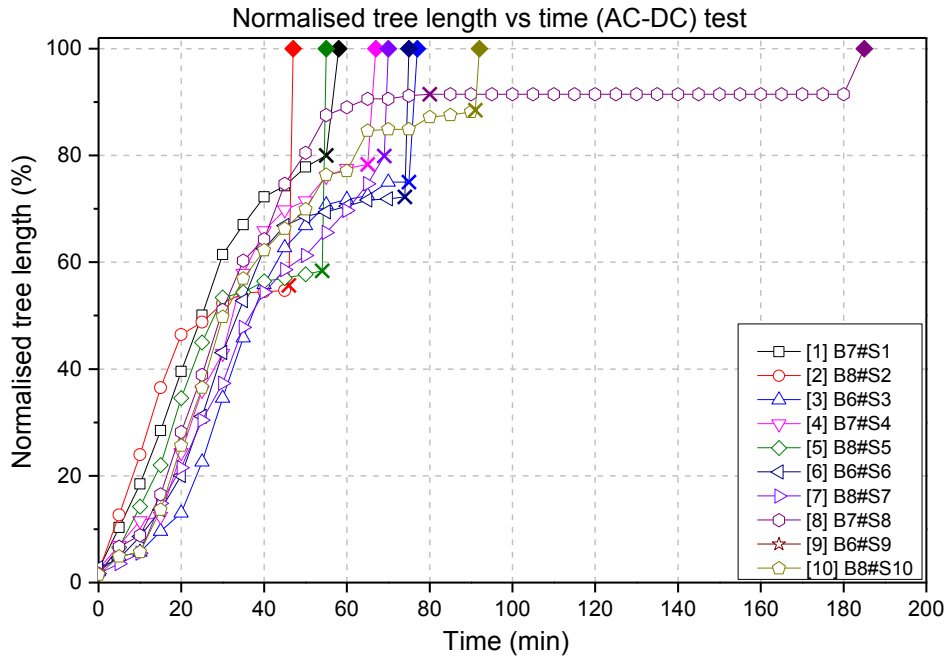
Figure 9-40: Plots of tree lengths vs time for all samples normalised against 2mm insulation gap distance for (AC-DC) test. The 'x' markers show the maximum tree lengths prior to sample breakdown.

The 'x' markers in the plots of Figure 9-39 and Figure 9-40 show the maximum measured tree lengths propagated prior to breakdown, while the solid diamond symbols '♦' show when breakdown finally occurred. It can be seen from the plot of positive DC bias test (Figure 9-39) that most of the 'x' markers cluster around 70% (1.4 mm) to 80% (1.6 mm) of the gap distance, whereas for negative DC bias test (Figure 9-40), the 'x' markers are widely distributed from about 55% (1.1 mm) to about 90% (1.8 mm) of the of the gap distance in comparison with the positive DC bias test.

In section 9.1, it was mentioned that the tree length may not be observed to have reached the maximum gap distance due to the limitation of the optical system and the variation in gap distance (2 ± 0.2) mm in each sample. However, an interesting observation was made here. It seemed that the higher the absolute value of the applied voltage for a particular test type, the rapid the acceleration to breakdown when the tree lengths were approaching the counter electrode. Similar observations were made for samples stressed with "pure DC" at +60 kV in section 9.3.1 in Figure 9-6, where the maximum measured gap distance was about 75% (1.5 mm) before breakdown occurred.

206

It can be seen from Figure 9-40 that, sample B7#S8 did not breakdown immediately until after 100 minutes even though the length had reached 90% of the gap distance in the 80th minute where it became saturated until it finally failed. This type of growth characteristics were observed in almost all samples stressed under AC test when the reverse treeing starts. However, in this case, only widening of the tree channels were observed in the whole body of the insulation showing huge level of accrued damage but reverse tree was not observed. Figure 9-41 (a) and (b) show the images of this sample prior to failure and after failure. This observation further suggests that the reverse treeing is an AC voltage stress phenomena and may be due to magnitudes of the voltages involved.

(a): B7#S8_PTBD_184 min   (b): B7#S8_BD_185 min
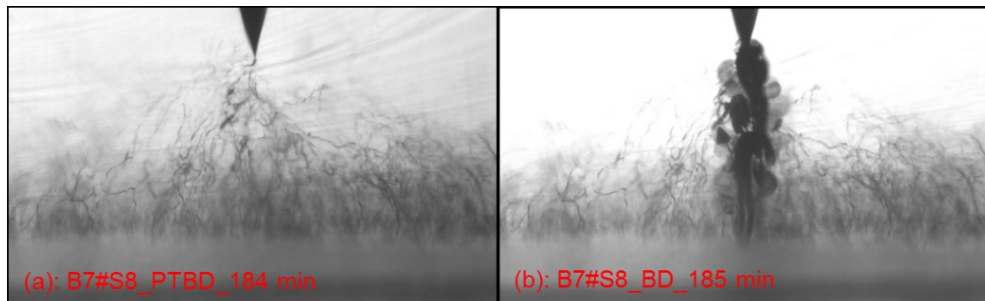
Figure 9-41: Intense internal damage in negative DC bias test, but reverse tree is not seen.

Growth rate in width direction: Figure 9-42 and Figure 9-43 show the plots of normalised tree widths against the 6 mm width of the captured 2D images on the y-axis versus tree propagation time on the x-axis for all samples tested under positive and negative DC bias tests. As can be seen from these plots, the initial stages of the growth in width up to about 20% for most of the samples were slow due to the initial bushier tree growth structures formed in the early stages which do not spread much in the width direction. But beyond 20% of the normalised plot, steady growth can be seen in both plots. The 'x' markers on the plots show the maximum measured tree width prior to breakdown.
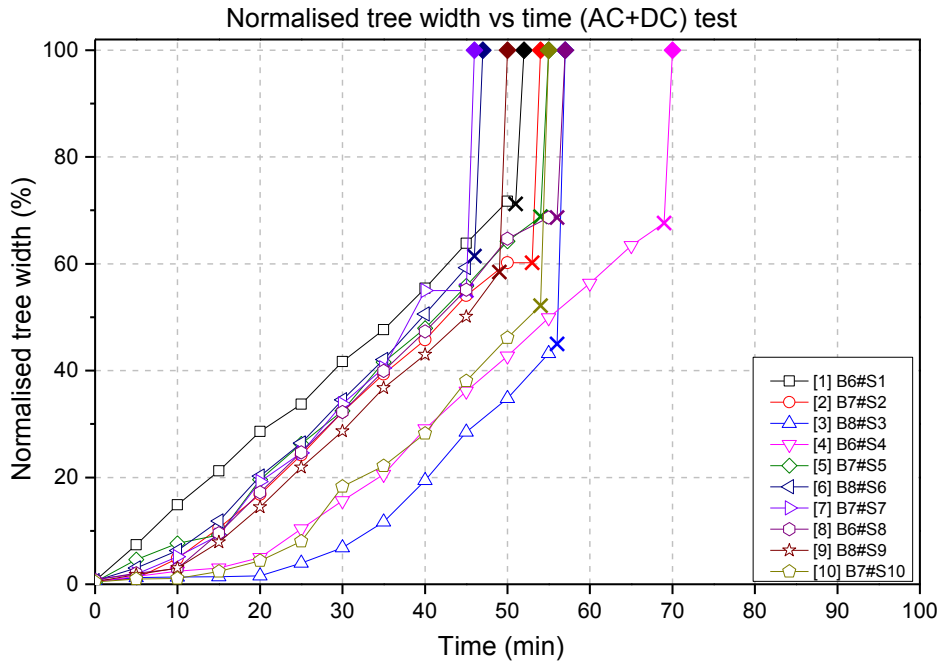
Figure 9-42: Plots of tree width vs time for all samples normalised against 6 mm width of the captured 2D images for positive DC bias test. The 'x' markers show the maximum tree width prior to sample breakdown and '♦' makers show when breakdown finally occurred.
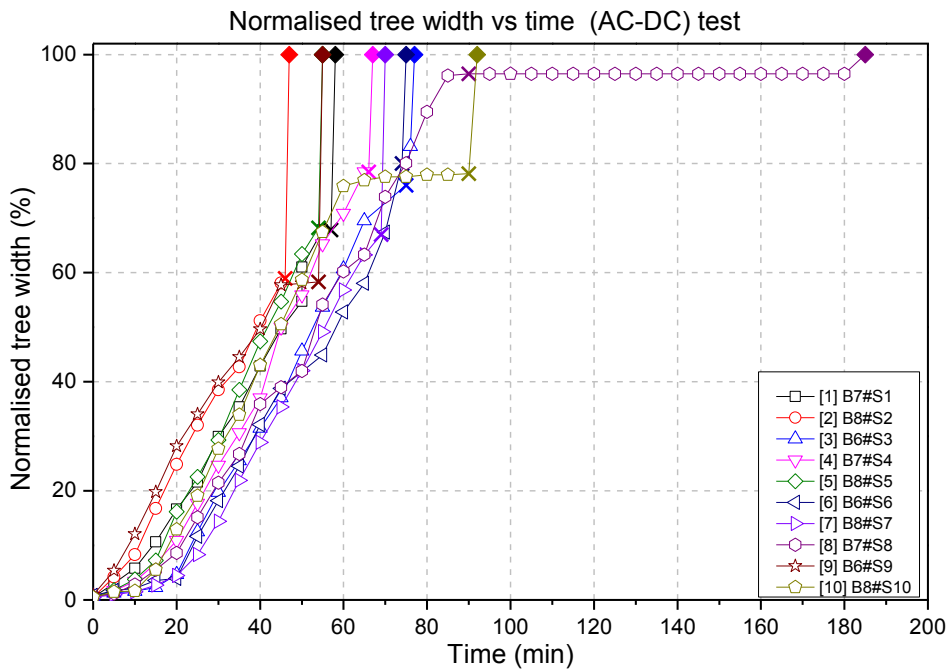
Figure 9-43: Plots of tree width vs time for all samples normalised against 6 mm width of the captured 2D images for negative DC bias test. The 'x' markers show the maximum tree width prior to sample breakdown and '♦' makers show when breakdown finally occurred.

Generally, less spread of the tree channels was observed under positive DC bias test compared with those under negative DC bias test. The 'x' markers cluster from

about 44% (2.6 mm) to about 70% (4.2 mm) of the maximum width under positive DC bias test, while under negative DC bias test, the 'x' markers cluster from about 60% (3.6 mm) to about 97% (5.8 mm).

The following trend of tree growth rate in length and width for positive and negative DC bias tests were observed:

- Electrical trees grow shorter in lengths under positive DC bias test than under negative DC bias test.

- Electrical trees spread less under positive DC bias test than under negative DC bias test.

- The reduced spread of tree width and shorter tree lengths measured under combined AC and DC test as compared to under pure AC may be related to the absolute magnitudes of the stressing voltages involved see Table 8-1.

9.5.4 Sequence of tree growth with simultaneous partial discharge measurement under 15 kV AC superimposed on ±15 kV DC

In section 9.44, the sequence of electrical tree growth together with physical measurement of partial discharge activity under AC which showed 5-stage growth characteristics has been presented. In this section, the results on the effect of superimposed 15 kV peak AC on ±15 kV DC on growth characteristics with simultaneous partial discharge measurement is presented.

Figure 9-44 and Figure 9-45 show the curves of electrical tree growth together with the observed physical measurement of partial discharge activities acquired for two samples stressed with 15 kV peak AC superimposed on +15 kV DC (positive DC bias) test and 15 kV peak superimposed on -15 kV DC (negative DC bias) test. In contrast to the 5-stage growth characteristics observed in section 9.4.4, in this section only 4-stage growth characteristics including the initiation stage were observed. The evolution of the captured images of the electrical tree structures together with the magnitudes of the discharge data acquired which showed the changes in physical structure of the electrical trees in the two tests voltage regimes are presented below.

Figure 9-46 and Figure 9-47 show the condensed stage by stage captured images and the cumulative PRPD plots at each stage of the experiments for both test types.

These plots together with those in Figure 9-44 and Figure 9-45 are used to correlate differences observed in each test type. As can be seen from Figure 9-44 and Figure 9-45, partial discharge data was not acquired at stage 1. The reason for this was discussed in section 9.4.4. The remaining 3-stages of growths in both cases are discussed below.
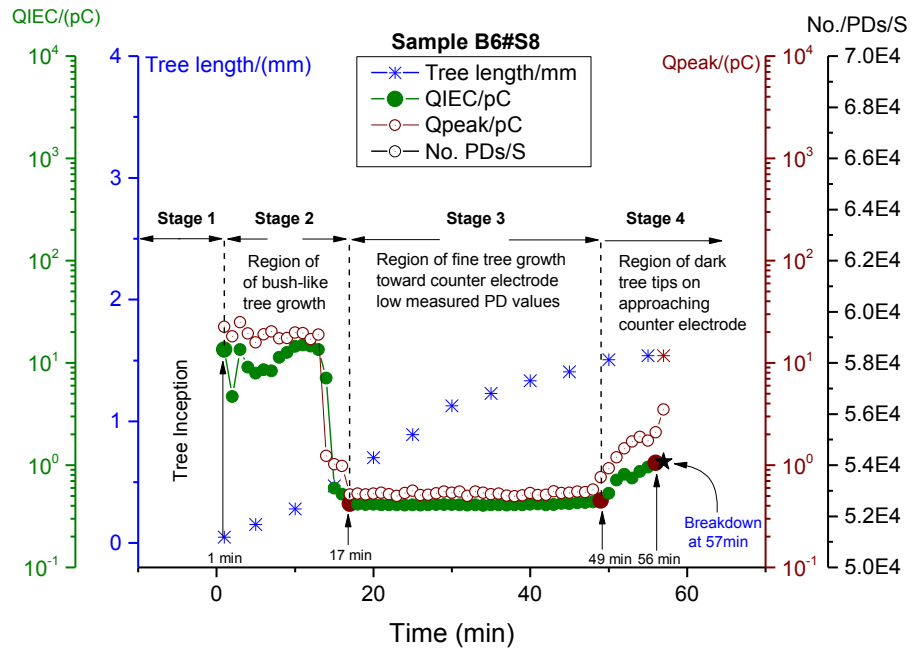
Figure 9-44: Plot of physical tree growth and partial discharge activities under combined peak 15kV AC and +15 kV DC stress showing 3-stages of growth characteristics after inception stage.
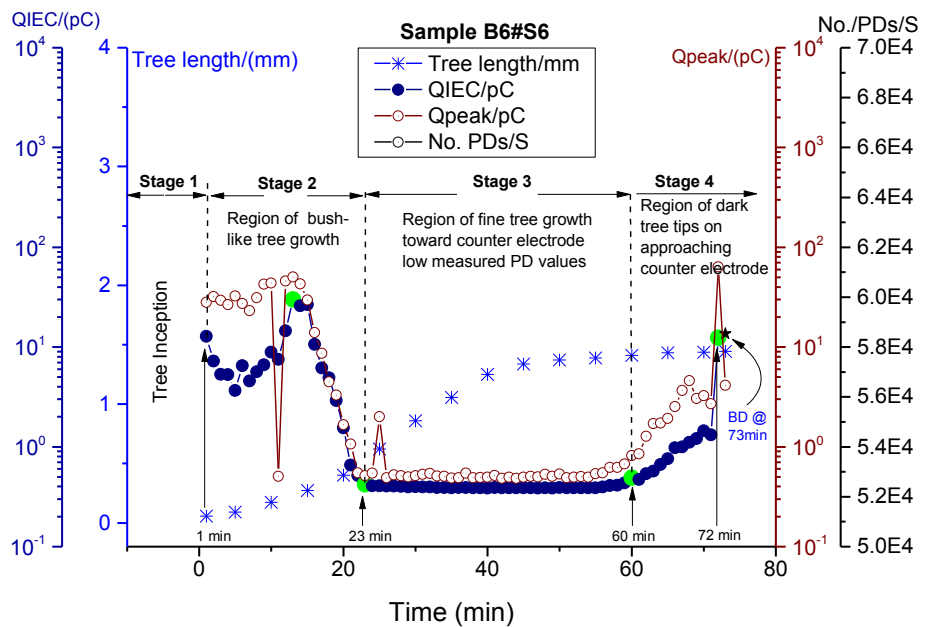
Figure 9-45: Plot of physical tree growth and partial discharge activities under combined peak 15kV AC and -15 kV DC stress showing 3-stages of growth characteristics after inception stage.

211
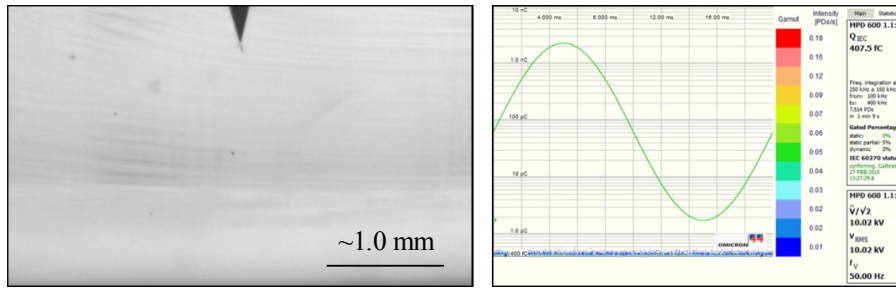
Stage 1: The initiation stage
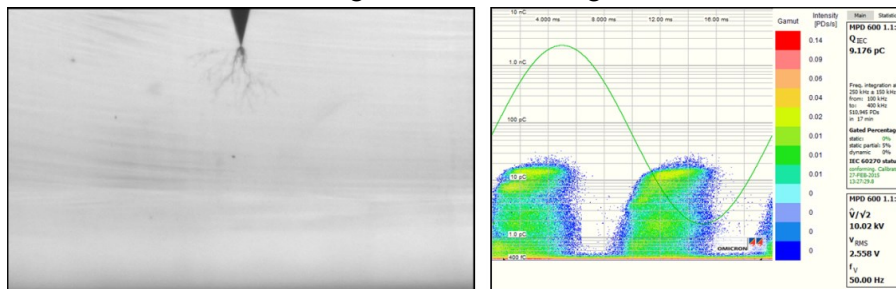
Stage 2: (1- 17) mins_Region of dark tree growth
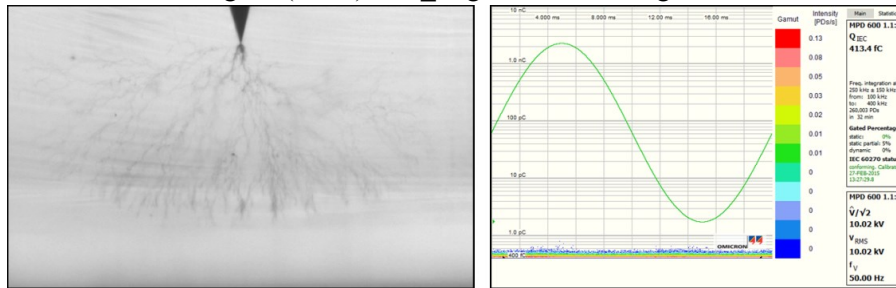
Stage 3: (17-49) mins_Region of fine tree growth
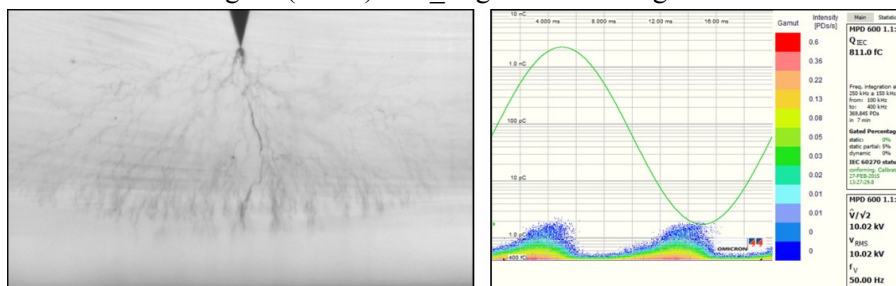
Stage 4: (49-56) mins_Region of thickening fine branches
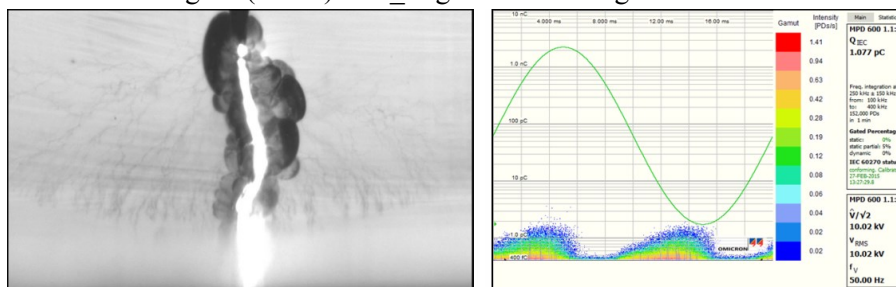
Breakdown in 57th minute

Figure 9-46: Tree imaging and corresponding PD patterns at different stages of growth until breakdown for positive DC bias test. The scale bar is the same for all pictures.
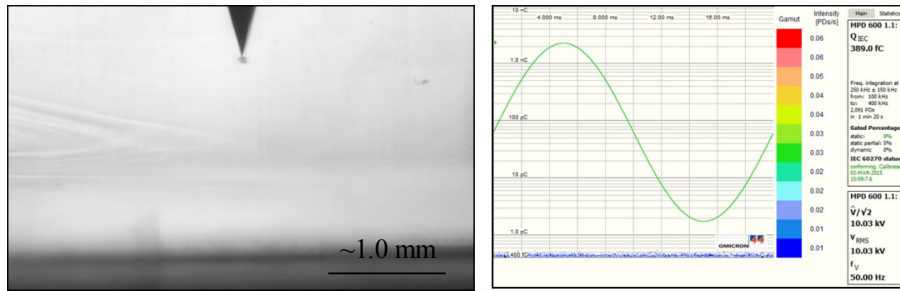
Stage 1: The initiation stage
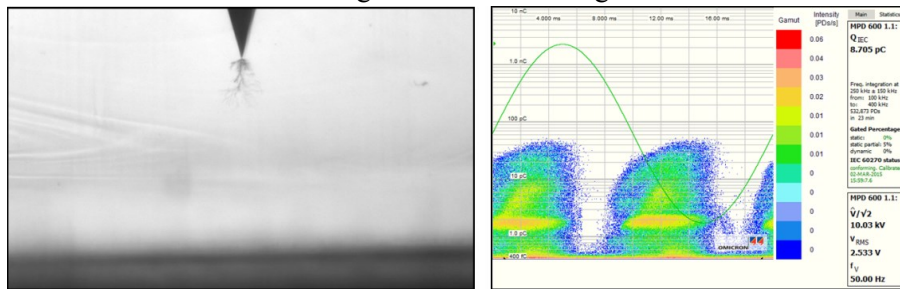
Stage 2: (1- 23) mins_Region of dark tree growth
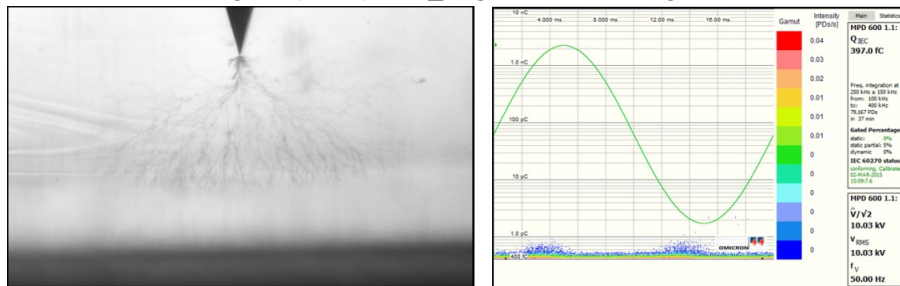
Stage 3: (23-60) mins_Region of fine tree growth
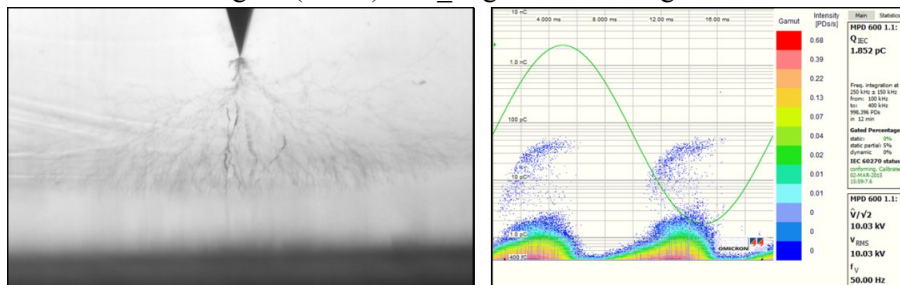
Stage 4: (60-72) mins_Region of thickening fine branches
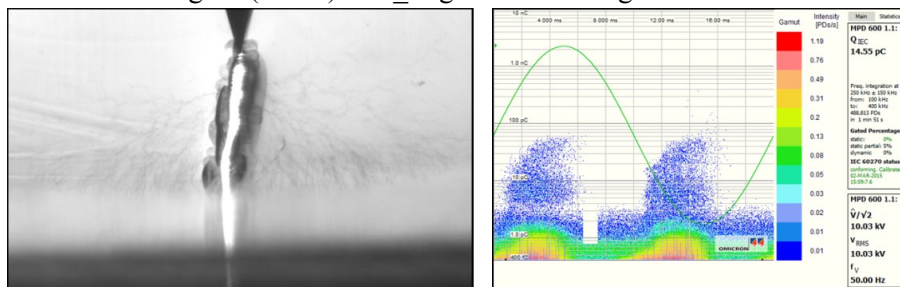
Breakdown in 73rd minute

Figure 9-47: Tree imaging and corresponding PD patterns at different stages of growth until breakdown for negative DC bias test. The scale bar is the same for all pictures.

Stage 1: **The initiation stage;** as mentioned above, partial discharge data was not collected at this stage. The images shown in Figure 9-46 and Figure 9-47 stage 1; are the AC pre-incepted initial tree images prior to voltage application, and the PRPD plots shown adjacent to them are the plots immediately the test voltages were applied. As can be seen from Figure 9-46 and Figure 9-47, both images had bush-like initial trees in them. This resulted in slow growth rate in the first 17 minutes and 23 minutes of the second stage of each test type on voltage application as shown by the tree growth rate curves in Figure 9-44 and Figure 9-45.

Stage 2 formation of bush tree: The partial discharge and tree growth characteristics in the stage 2 for both positive and negative DC bias tests bear similarities. For positive DC bias test, the magnitudes of the average charge was a fairly steady fluctuating between ~13.5 pC to ~7.2 pC in the first 14 minutes when dark bush trees were extending from the initial trees. It then decreases to ~0.4 pC in the 17th minutes when the arrays of fine trees started to extend from the dark bush trees as shown in the image of Figure 9-46 stage 2, and the plot of Figure 9-44. Similarly for negative DC bias test, the average magnitude of the apparent charge in the first 13 minutes ranged from ~ 12.8 pC to ~ 30 pC. This was marked by extension of the existing initial bush tree from stage 1, before the magnitude of the PDs decreased to about 0.4 pC in the 23rd minute, when finer tree branches started to emerge from the dense bush trees. Figure 9-45 stage 2 shows the plot of the average charge magnitudes while Figure 9-47 stage 2 shows the captured image and the cumulative PRPD plot adjacent at the end of the 23rd minutes.

It can be seen clearly from Figure 9-44 and Figure 9-45 that, for both positive and negative DC bias tests, the extensions of the bush trees were marked by relatively higher but steady average apparent charge magnitudes in the initial stages of the bush tree expansions for some time before reducing to their respective minimum values of ~ 0.3 pC and ~ 0.4 pC. In contrast to the growth of branch trees observed during the AC tests (see Figure 9-18 stage 2), the partial discharge activity started to rise sharply from ~ 1.4 pC in the first minute to ~ 80 pC in the 8th minute before it declined to ~ 0.3 pC when the finer trees started to grow. These observations show that, different PD patterns were responsible for the evolution of bush and branch type trees which were marked by different quantities of discharge magnitudes.

Stage 3 formation of fine trees: These stages were marked by continuous growth of the fine tree structures observed in stages 2 in both length and width but at a relatively higher rate compared to the growth for pure AC test at the same stage. As can be seen from the images of Figure 9-46 and Figure 9-47, the tree tips were already approaching the ground electrode with wide spread in the width direction within 32 minutes (17min to 49min) for positive DC bias test, and for negative DC bias test within 37 minutes (23min to 60min).The measured average apparent discharge magnitude during this stage is ~0.4 pC throughout in both cases which was similar to ~0.3 pC recorded during the AC test. Even though the magnitudes of the effective rms of the applied voltages under positive and negative bias test were higher in comparison to that of the AC test (see Table 8-1), the emergence of the fine tree structures for both cases were accompanied by low values of PD quantities. This suggests that, the evolution of the fine tree structures is independent of the magnitude of the applied voltages but rather on the severity of the discharge activities and their magnitudes. As can be seen on the PRPD plots in both cases, the partial discharge activities became dormant and almost no discharge pulses were registered during these periods even though the fine trees continued to grow.

Stage 4 formations of thick dark tree channels: Partial discharge activities at this stage of three growths for both positive and negative DC bias tests became active at this stage of tree growth. The magnitudes of the apparent charge increased from ~0.4 pC to ~1.1 PC for positive DC bias test and from about ~0.4 pC to ~12.4 pC for negative DC bias test as shown at stages 4 of Figure 9-44 and Figure 9-45 respectively. Subsequently, further spread of the tree structures were observed and the fine trees became darker and thicker with visible long tree channels appearing in both cases.

In AC tests, the observation at this stage was different. The recorded discharge magnitudes of ~0.3 pC to ~3 pC were measured at stage 4. This led to the formation of dense bush-like structures along the perimeter of the tree tips, and subsequently the appearance of reverse trees shown as stage 5 under AC test in Figure 9-18. In the case of positive and negative DC bias tests however, only thickening of the fine branches with the formation of long dark single tree channels were observed in both cases which resulted into the final breakdown event. It can be seen from the images in Figure 9-46 and Figure 9-47 that the breakdown event is accompanied by

generation of light within the tree channels suggesting that it is a high energy event. The partial discharge activities for both positive and negative DC bias tests behaved similarly in all tested samples except that in the negative DC bias test, the discharge activity increased slightly than under positive DC bias test before failure.

9.5.5 Summary 1

Simultaneous imaging of electrical tree growth and partial discharge measurement which showed 4-stages of the electrical tree growth characteristics under positive and negative DC bias test was carried out. Tree shapes at stages 1, 2 and 3 under positive and negative DC bias tests were similar to that of the AC test. However growth rate was faster under positive and negative DC bias test than under AC test. The key findings during the AC superimposed on positive and negative DC test can be summarised as:

- **Growth characteristics;** tree growth was in the forward direction only in all samples for the two test types.

- **Electrical tree shape;** tree structures were similar as in AC tests. But dense tree structures were not observed in stage 4 as in the AC tests, but rather thicker, dark and long widened tree channels were observed before breakdown occurred.

- **Time to breakdown**; the average time to breakdown under positive DC bias testing was 54 minutes and that under negative DC bias tests was 78 minutes respectively. This resulted in about 14% difference in life time between the two tests.

- **Growth rate characteristics;** Tree growth rate was faster under AC superimposed on DC than under only AC and DC tests respectively. The trees reach the counter electrode faster with less spread in the width direction when compared with AC test.

Figure 9-48 and Figure 9-49 show the plots of the partial discharge activities normalised against propagation time for the failed samples during these tests showing the identified stages of propagation presented above. It can be seen from the plots that almost all the samples had initial active partial discharge activity in the stage 2, followed by period of quiescent discharge activity in stage 3 and

216

finally moderate discharge activity before breakdown occurs. The individual plot of each sample can be found in Appendix C-2 and 3.
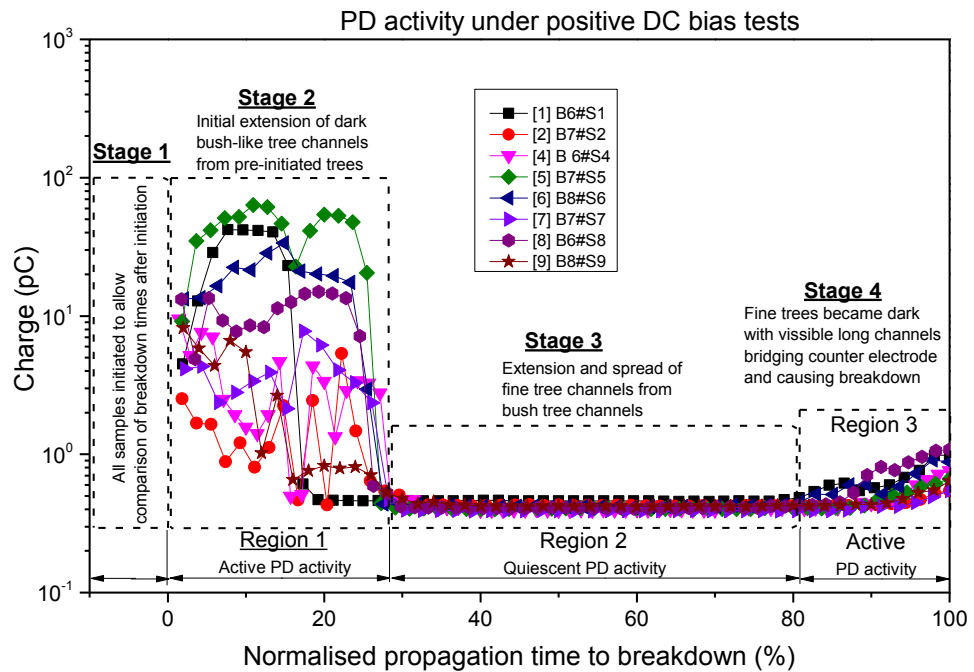
Figure 9-48: Partial discharge activity samples under positive DC bias test showing the identified 4-stages of growth.
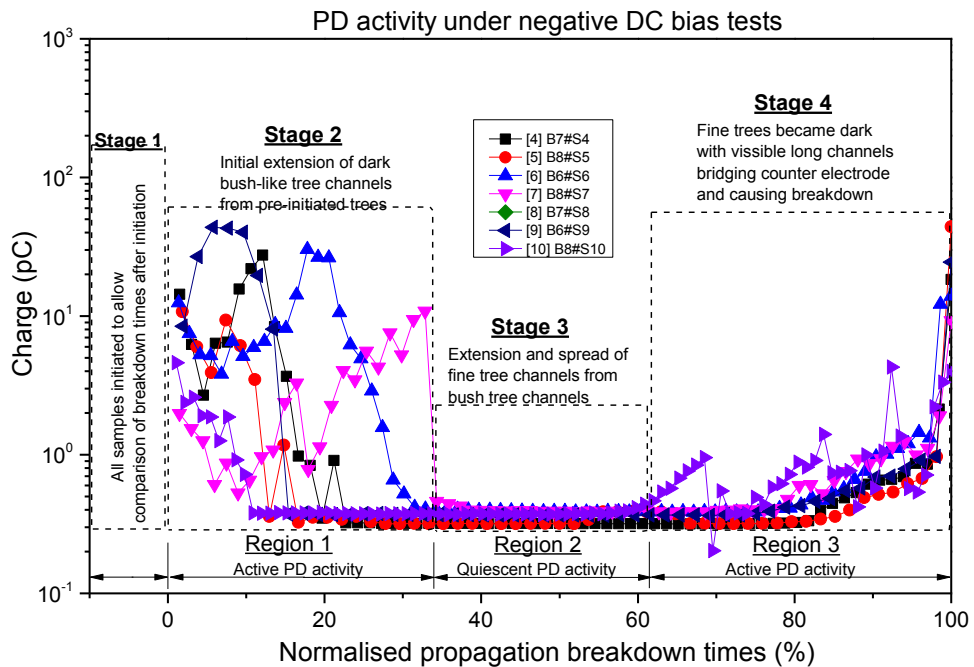
Figure 9-49: Partial discharge activity samples under negative DC bias test showing the identified 4-stages of growth.

Tests under positive and negative DC bias tests demonstrated only 4-stage growth characteristic compared to the 5-stage characteristics observed under AC. The shorter life time under combined AC and DC tests compared to either AC or DC test alone may be due to the combined effect of the AC and DC components (rms and peak values) of the applied waveforms and not only the AC components. The absence of reverse trees under both positive and negative DC bias tests also suggest that the reverse treeing process may be due to the relatively lower effective rms voltage involved, see Table 8-1. This observation led to further experiment in section 9.6 to verify if indeed the reverse treeing observed under AC is the result of the lower field involved.

9.6 **Verification test**

In this section tests were carried out to verify if the reverse treeing process observed under AC test is actually due to the relatively lower voltage magnitude compared to those under positive and negative DC bias tests. During this test, Partial discharge activity is not measured.

In this test, 24 samples were used and all were initiated using 30 kV peak AC. The influence of the applied voltage magnitude on time to initiate as well as initial tree lengths during the initiation stage was presented in sections 9.2.2 and 9.2.3. Summary of the collated test results for initiation times and initial tree lengths can be found in Appendix A–7.

In this section, experimental protocol and test results during tree propagation from these 24 samples is presented. Three different tests were carried out using the following protocol:

I.   1-stage test; in this experiment 4 samples were used. The samples were continuously stressed using 30 kV peak AC from initiation until breakdown occurs.

II. 2-stage test; in this experiment 10 samples were used. In the first stage of the experiment, the samples were initiated with 30 kV peak AC. In the second stage of the experiment, the samples were divided into 2 groups of 5 samples and each group stressed with either positive or negative DC bias (15kV pk AC ± 15 kV DC) waveforms as in section 9.5 for at least 2 hours. The experiment is stopped after 2 hours if breakdown did not occur.

III.   3-stage experiment; in this experiment, 10 samples were used following similar protocol as in 2-stage experiment. However, the trees were not allowed to breakdown. The tests were stopped when the tree were approaching the counter electrode and 15 kV peak AC is then applied as the third stage of the experiment. The experiment is stopped after 2 hours if breakdown did not occur. Captured tree images are then compared with those from pure AC test in section 9.4 for any differences in the tree structure.

9.7 Results from the verification experiment

As mentioned in section 9.6, the aim of this experiment is to verify if the reverse tree observed under 15 kV peak AC were due to the relatively low voltage under AC test compared to those under the composite waveforms. The results are presented in the sections below.

9.7.1   1-stage test at 30 kV peak AC

It is worth mentioning here that, the 4 samples used for this test, were samples that did not initiate during the quick initiation test up to 16 kV rms, but initiated at variable times during this test. The results for the initiation times were already presented in section 9.2.2 and here only the results of the tree shapes are discussed.

Figure 9-50 shows the images of trees initiated within 1 minute of voltage application. Images shown at the top in the Figure were captured 5 minutes after initiation in each sample and the images shown at the bottom were captured prior to breakdown occurred.

B11#S12*	B12#S11*
Initiated in 1 min. 5 min after inintiation	Initiated in 1 min. 5 min after inintiation
PTBD image at 28 min	PTBD image at 105 min
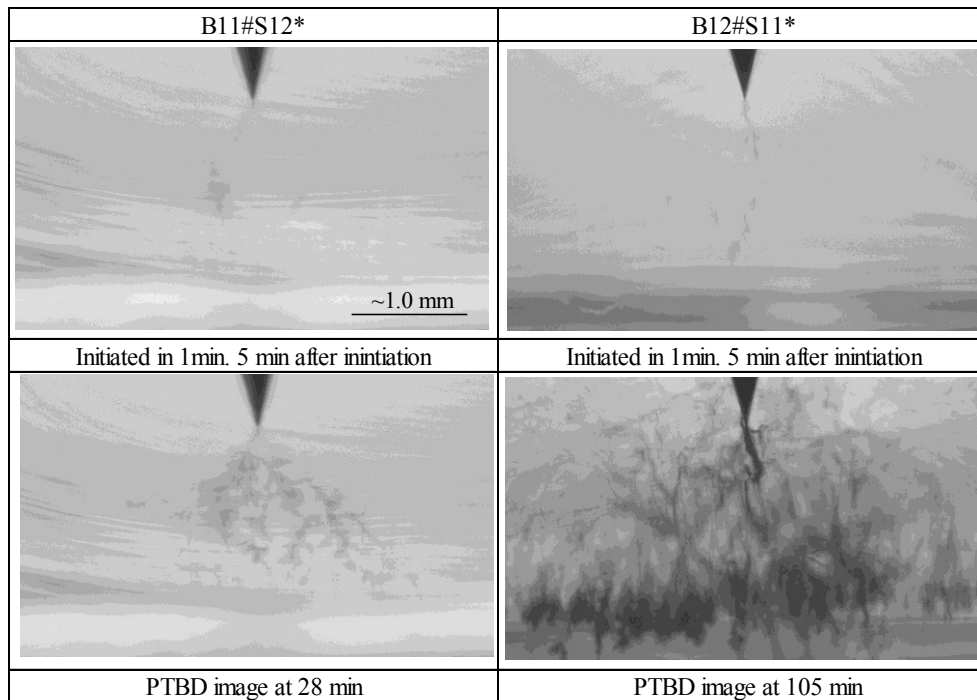
Figure 9-50: Absence of reverse tree at 30 kV pk AC.

The speed at which the trees propagates can be seen 5 minutes after initiation in the top images with sample B12#S11 already approaching the counter electrode and sample B11#S12, traversing more than 50% of the insulation gap distance (~ 2 mm). However in both cases trees growing from the counter electrode (reverse trees) were not observed as in the case of AC test at 15 kV peak even though extensive damage had been done to sample B12#S11.

Figure 9-51 also shows images of trees grown at 30 kV peak. But in these samples, the trees initiated only after 104 minutes and 113 minutes of voltage application showing very long initial trees after initiation. For example in B12#S2, the initial tree length in the image is about ~ 503 μm and in sample B11#S4 the initial tree length at initiation was 54 μm. However after 1 minute i.e. at 114th minutes the measured length was about ~ 535 μm also showing that the trees propagate faster at 30 kV peak AC. But under pure DC even at 60 kV DC, the propagation speed was slow. In this case also reverse trees were not observed as shown in the images prior to breakdown at 125 and 165 minutes respectively.

220

B12#S2*	B11#S4*
Initiated at 104 min	Initiated at 113 min, image at 114 min
B12#S2* _ PTBD at 125 min	B11#S4* _ PTBD at 165 min
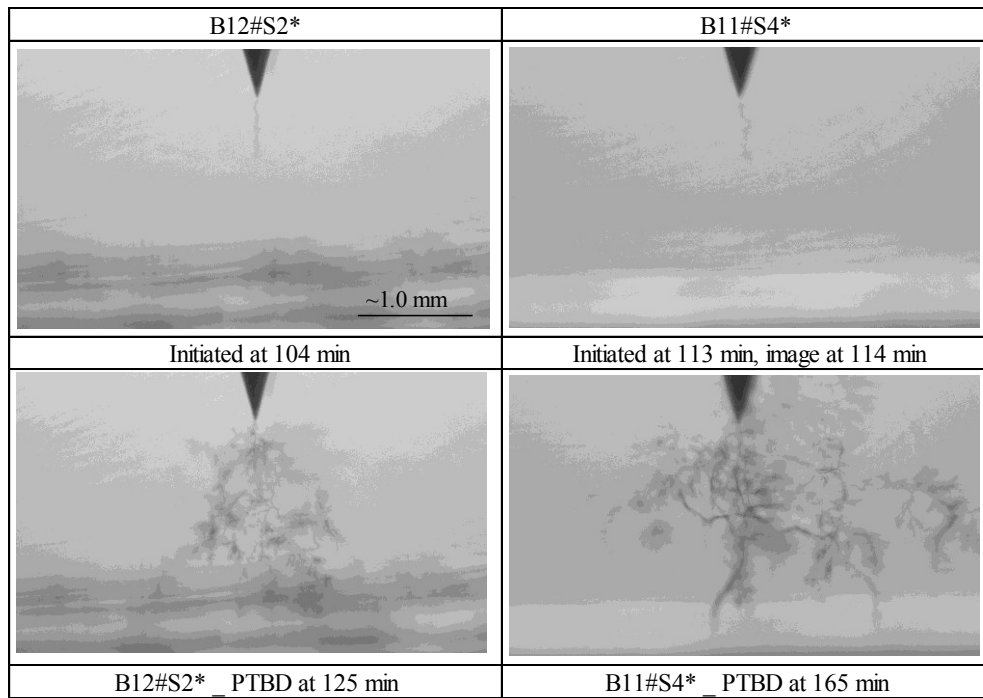
Figure 9-51: Long initial tree at 30 kV and absence of reverse trees prior to breakdown.

9.7.2   2-stage test results under positive and negative bias test

In this test 10 samples were used. 5 samples for positive DC bias test and the remaining 5 for negative DC bias test. This test is similar to the test in section 9.5, except that here the samples were initiated at 30 kV. The results from this test were also similar to those in section 9.5.

For positive DC bias test, 2 samples did not breakdown after 2 hours and the experiment was stopped following the protocol in section 9.6 for 2-stage test. The calculated average time to breakdown for the remaining 3 samples was 46 minutes. In the case of negative DC bias test, 4 out the 5 tested samples failed with average time to breakdown of 57 minutes. See Appendix A–8 for time to breakdown in each sample. This result followed the same trend as the tests in section 9.5, with test under negative DC bias generally having longer time to breakdown than that of positive DC bias test.

9.7.3   3-stage test results under positive and negative DC bias tests plus AC tests

The protocol outlined for 3-stage experiment in section 9.6 was followed in this test using 10 samples. As mentioned in section 9.6, the aim of this test was to established

221

if the reverse treeing process is due to the lower voltage involved under AC test and to find out if any differences may exist in tree shapes due to the applied voltages under this test. Figure 9-52 shows the captured tree images from 2 samples during the 3-stage experiment for positive DC bias pre-stress waveform in the second stage 2 followed by the application of AC waveform in the third stage. The images at the top were captured during the application of the composite waveforms and the images at the bottom were captured when AC voltage was applied.

B13#S1	B13#S3
Stage 2 (AC+DC) test after 42 min	Stage 2 (AC+DC) test after 40 min
Stage 3 (AC) test after 2 hours	Stage 3 (AC) test after 2 hours
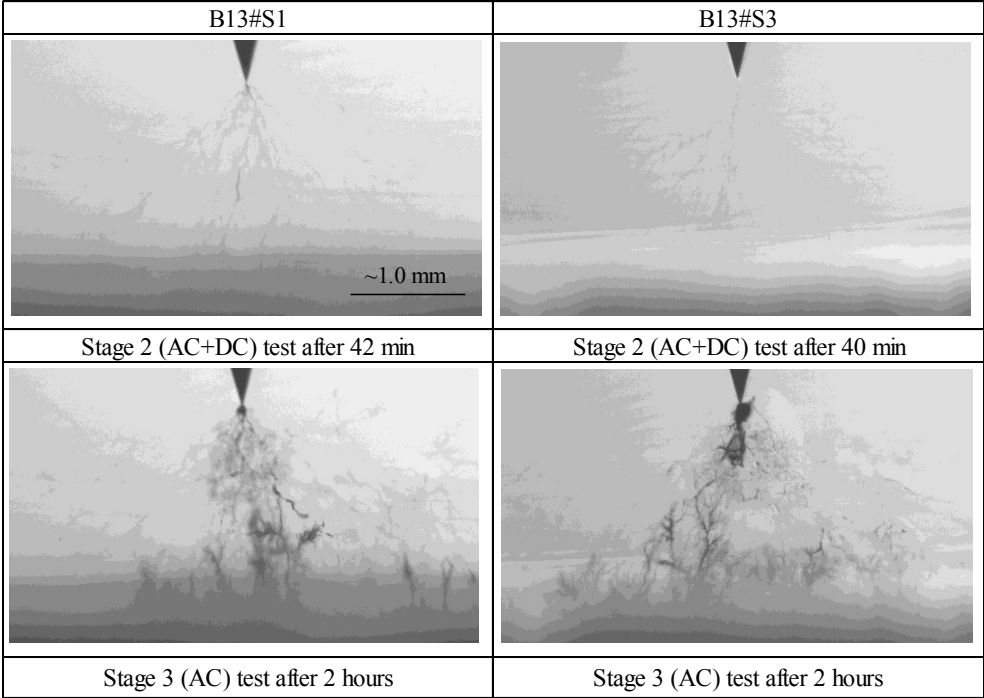
Figure 9-52: Tree images for 3-stage test. Top images were captured during positive DC bias test and the bottom images were captured during AC test.

It can be seen from the images at the top of the Figure that, the tree structures observed had the normal fine tree structures observed in the previous tests in section 9.5, whereas the images at the bottom had trees growing from the counter electrode as observed during AC test in section 9.4.1.

Figure 9-53 also shows the tree images captured when negative DC bias waveform was applied followed by AC voltage from two test samples. As can be seen from the images of Figure 9-53, the tree structures were similar to those in Figure 9-52 at the stages 2 and 3 of the applied voltages, showing distinct tree structures at each stage of the applied waveforms.

B14#S5	B14#S2
Stage 2 (AC-DC) test after 44 min	Stage 2 (AC-DC) test after 50 min
Stage 3 (AC) test after 117 min	Stage 3 (AC) test after 2 hours
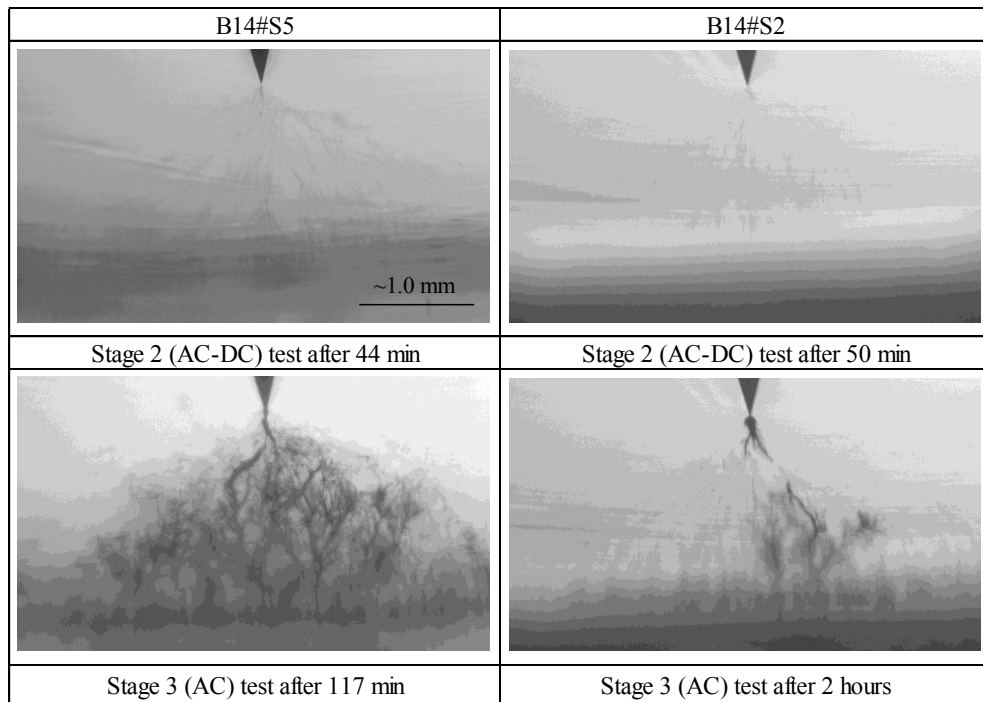
Figure 9-53: Tree images for 3-stage test. Top images were captured during Negative DC bias test and the bottom images were captured during AC test.

These observations suggest that, the application of either positive or negative DC bias waveforms prior to the AC waveform do not affect the subsequent reverse tree structures.

9.7.4   Summary 2

The verification test carried out in this section has repeated the previous tests carried out in sections 9.4 and 9.5. In addition, test was carried out 30 kV peak AC. The results showed that:

- The application of composite waveform prior to the application of AC waveform at 15 kV peak AC does not stop reverse treeing process.

- That application of only composite waveform (positive or negative DC bias) does not result in reverse treeing process.

- The application of 30 kV peak AC only does not result into reverse treeing process.

- Application of 15 kV peak AC only or after pre-stressing with composite waveform resulted into reverse treeing process in all samples tested.

223

These results confirmed that the reverse treeing process is due to the relatively lower voltage under 15 kV peak AC, as this phenomena is not observed neither at 30 kV peak AC nor when the composite waveforms were only used.

9.8 Comparison of tree growth rate and time to breakdown under DC, AC and AC superimposed on DC

Figure 9-54 shows the plots of tree growth characteristics of four selected samples with similar times to be breakdown under the four test types employed in this study. As none of the samples under negative DC test failed and no significant growth is observed, only the positive DC test is discussed here. Although each of these samples failed within 100 minutes of voltage application, the difference in tree growth characteristic between DC test and the other test types is very clear from the plots.
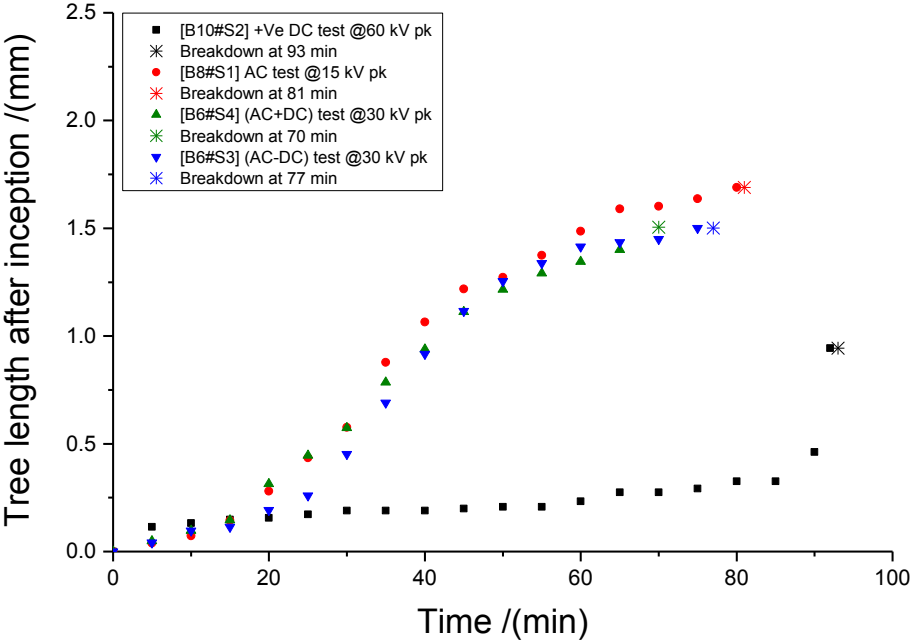
Figure 9-54: Comparison of growth rate plot of four samples from the four test types.

As can be seen from the plot, the maximum length attained after 85 minutes is ~0.25% of the insulation gap distance after which rapid failure ensued in 93minutes. Figure 9-6 shows the plots of all failed samples under DC test depicting similar characteristics.

In contrast, for AC and AC superimposed on positive and negative polarity DC tests, the individual samples that succumbed to failures have similar changes to their growth rates showing the common "lying S" shape growth characteristics observed by many in literature. But on average, lifetime for each test type is different as shown

in Figure 9-55. Even though the calculated geometrical field (see Table 8-1), at the needle tip neglecting the effect of space charge under DC test at 60 kV is about 6 and 3 times compared to that of the AC and the AC superimposed on DC tests, the average lifetime under the DC test is about 2 times that of AC test and 5 and 3 times that of positive and negative DC bias tests respectively.
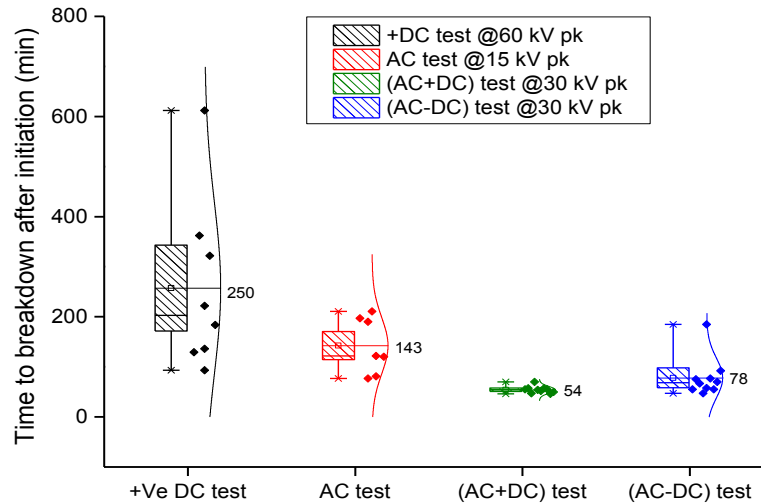
Figure 9-55: Box chart showing spread and average time to breakdown for the four test types.

The possible reason for longer lifetime under DC test, as explained section 9.3, is believed to be due to space charge reducing the field at needle tip under DC tests resulting in samples lifetime extension. The association of space charge reducing the field to cause longer lifetime can also be seen in the difference in lifetime under positive and negative DC bias test. As it is believed that the negative electrode inject more charges than the positive electrode [116-117, 191], then it is assumed that there will be more shielding effect under negative DC bias test due to space charge. Then it is consistent that the negative DC bias test had longer lifetimes compared to that of positive DC bias test and that under only negative DC test breakdown did not occur at all in all samples. The fact that time to breakdown under positive and negative DC bias tests are shorter than under AC test suggests that, the rate of propagation is driven by the combined effect of AC and DC components (effective rms value) of the applied composite waveform and not only the AC component. This observation is in agreement with the findings in [121] on tree initiation using superimposed voltages.

10.   Discussions and conclusions

10.1   Introduction

The main aim of this work is to develop understanding of the potential issues of using solid polymeric insulating materials for HVDC application. In particular, the response and performance of the material under high DC voltage stress as well as AC and AC superimposed on DC electric stresses. In this work, epoxy resin was selected as insulating material due to its excellent electrical properties which makes it find use in various medium and high voltage applications.

The initial aim of the project was to investigate the effect of space charge on short term breakdown strength, and long term breakdown through treeing in layered dielectrics so that an understanding of the link between space charge and material strength and life times can be clarified. This required setting up experiments to enable such measurements to be carried out. Thus three experiments were designed and developed as described in chapters 4, 5 and 6 during this project to enable these objectives. However time constraint did not allow treeing investigations in layered samples, and this will be considered for future projects.

Reproducibility of any experiment depends on how well the experiment is designed and samples to be tested are fabricated. In Chapter 3, the care taken to fabricate samples in a reproducible manner for this study was presented. The outcomes of this study are discussed in Section 10.2.

10.2   Sample preparation

Successful and consistent methods of fabricating both point to plane sample geometries and thin planar samples (layered and un-layered) of about ~200 to 250 μm thicknesses were developed as outlined in Chapter 3. Generally the ability of epoxy resin to bond very well with other materials and especially with metals is a challenge in sample fabrication. Whilst this property is beneficial in producing void free samples at the sample-needle interfaces in point to plane samples, the same property makes it difficult in demoulding thin planer samples. Casting material on Teflon coated metal plates and between Mylar films shown in Figure 3-3 was found to be successful without the need of using releasing agent.

Outcome: a successful and well-control method of sample preparation was developed for both planer and point to plane sample geometries.

10.3   Test facilities

Experimental measurement systems for: short-term breakdown tests and space charge on planer samples and long term breakdown via treeing tests were successfully designed developed and operated.

Short term breakdown measurement system; Figure 4-3 shows the schematic and the photograph of the developed system for short term breakdown test. The main advantage of the test cell is the way it was designed to hold the sample under test between the electrodes system without exerting undue pressure on the sample or allowing any movement during test. This is an important feature to be considered in this experiment to ensure that results are not influenced by external factors such as contact pressure or movements of connecting leads during experimentation. The use of a digital oscilloscope allows the breakdown voltage to be accurately determined by recording the applied waveform after breakdown, and using the cursors to determine the peak voltage at which the breakdown occurred, as shown in Figure 4-7.

Space charge measurement on planer samples; the pulsed electro-acoustic method of charge detection was implemented in this study. Figure 5-2 (a) and (b) show the assembly of the system. The system can accommodate samples of diameters up to 60 mm and able to withstand up to 10 kV DC long term ageing of sample under test without flashover. The system is properly grounded to shield it against external noise. The thoritical resolution of the system is about $\sim$ 20 µm and sample thicknesses of $\sim$ 500 µm can be succesfully investigated using this system.

Long term breakdown through treeing; the set up for this investigation is shown in Figure 6-7. the system is capble of simultaneously imaging electrical trees and detecting partial discharges with sensitivity of about 0.35 pC. The system enables the use of standard as well as composite waveforms for study of electrical treeing investigations. This test facility provides a platform for future dielectric research and featured:

- 100 MS/s arbitrary waveform generator capable of producing programmable non-power frequency waveforms with the ability to shield itself from

external unknown disturbances.

- A high voltage amplifier with maximum output voltage of ±30 kV, 40mA DC or peak AC and capable of driving waveforms with slew rate 725 V/μs at full load.

- A progressive area scan monochrome CCD camera with resolution of 2452 x 2056 pixels and equipped with C-mount Qioptiq and telecentric lenses capable of capturing electrical tree image of about 10 μm or less.

- A wide band (9 kHz to 3MHz) digital PD measurement device (MPD 600) that offers recording and post-processing analysis of the PD stream with detection sensitivity of about ~ 0.35 pC.

Outcomes: Three experimental measurement systems were designed, built and successfully operated which facilitate dielectric material ageing, monitoring and lifetime investigations under AC, DC and composite waveforms.

10.4 Short term breakdown strength and space charge measurement

The primary aim of this study is to compare the strength of fabricated layered epoxy-epoxy (double layer) to that of un-layered (single layer) epoxy sample of about the same thicknesses (i.e. 200 μm) in this study. The study starts by first comparing the strength of in-house fabricated epoxy resin to that of a commercially obtained PET reference samples. It was shown in section 4.4.5 that the PET reference samples were about 30% stronger than the in-house fabricated epoxy resin samples. This result is believed to be due to defects in the in-house fabricated samples. For example, as shown in Figure 4-17, which may be due to the fact that the laboratory conditions are not as clean as a commercial environment. The discussion here will be focussed on the performance of single and double layer samples of about 200 μm and how the effect of space charge injection and accumulation influenced the differences in observed results.

The observed trends in results during these investigations are as follows:

- Generally breakdown strength in air is lower than that in oil due to the effect of surrounding medium as discussed in section 4.5.1. It is concluded that testing in air cannot be considered to give intrinsic breakdown strengths.

- For layered and un-layered samples of about 200 μm Weibull statistics and computed averages from box chart showed that; single layer samples are

about ~ 6% higher in breakdown strength than the double layer samples. However, this difference is not big enough to suggest any major differences between the layered and un-layered samples.

- Generally there is no significant difference in breakdown strength between positive and negative polarity tests as confirmed from the student's t-test results in section 4.7.

- Average breakdown strength analysis using a box chart showed that; the AC test yields breakdown values about 38% and 34% lower than DC tests for samples of ~ 200 μm thickness, whereas for 100 μm thick samples the trend was different with AC tests giving about 12.3% higher breakdown strengths than DC tests. This variation is believed to be thickness dependent, but more work is required to understand this.

Results obtained from space charge measurements on single and double layer samples of about ~ 200 μm showed the following:

- No charge accumulation in the material bulk after 12 hrs at 37 kV/mm applied field, as shown in Figure 5-4 (b) for single layer sample.

- Capacitive charge build-up at the electrode-dielectric interfaces were the main feature of the single layer sample response after 12 hrs at 37 k/mm applied stress which decayed quickly after 60 seconds when the applied field was removed as shown in Figure 5-4 (c).

- For double layer samples, the effect of interface charging was observed immediately when the poling field was increased from 2 kV and which became clearly visible as net negative charge at the layer interface after 8 minutes together with the formation of hetero-charges seen next to the electrodes as shown in Figure 5-5 (a).

- When the poling field of 38 kV/mm was maintained for 12 hrs and measurements taken every hour, as shown in Figure 5-5 (b), significant charge increment is not observed at the layer interface. Charge dynamics towards the anode was observed resulting in hetero-charge formation at the anode and subsequent decrease in negative net charge accumulation at the layer interface as shown by arrow 1 Figure 5-5 (b).

- Removal of the poling field resulted in a fast decay of the accumulated charges at the layer interface after 60 seconds suggesting that charges were not

deeply trapped.

The results of space charge measurement on double layer sample showed that the interface provides a location for charge trapping. The ability of polymeric insulation to trap charges is one of the main issues that limit its use for high voltage DC application as discussed in section 1.4.1. Interfaces are often regarded as weak points especially at joints and terminations of real systems such as power cable and bushings. Space charge accumulation at interfaces is strongly linked with field modification that could lead to intensification of local field resulting in accelerated failure. Short term breakdown test on single and double layer epoxy samples showed a reduction of ~ 6% in DC breakdown strength in the double layer samples. Student's 't-statistics' test did not show difference between the means of positive and negative polarity test in each test type (single and double layer samples. See Table 4-6). However computation of the absolute average in each test type revealed that difference exists between single and double samples as shown in Table 4-7.

The 6% reduction in DC breakdown strength is therefore suggested to be due to space charge accumulation at the layer interface in this study.

Outcome: The reduction of about 6% in breakdown strength of double layer samples is thought to be associated with effect of space charge accumulation at the layer interface in double layer samples. However this 6% difference is not big enough to suggest major difference between the single and double layer samples as shown in this study. This study shows that layered material (interfaces) can prove to be strong when tailored properly and the assertion that interfaces are weak points needs further investigation.

10.5   Influence of applied voltage magnitude on tree initiation times

The influence of the applied voltage magnitude on tree initiation times was discussed in sections 9.2.2. Figure 9-3 shows the summary of the percentage distribution of tree initiation times in response to the magnitude of the applied voltages during quick initiation and verification tests. The following statistics show the dependence of tree initiation times on voltage magnitude:

- For quick initiation tests, 91.4% of the total samples (58 samples) initiated within 1 minute of voltage application at 12 kV rms whereas 5.2% and 3.4% initiated after within 5 and 10 minutes of applied voltages of 14 kV rms and

16 kV rms respectively.

- For samples initiated during verification tests, where 21 kV rms was used, 62.5% of the total samples (24 samples) initiated within 1 minute of voltage application whereas 20.8% initiated within 2 to 9 minutes and 16.7% initiated within 73 to 113 minutes respectively.

Outcome: Tree initiation times are heavily dependent on the magnitude of the applied voltage. The higher the magnitude of the applied voltage, the shorter the time to initiate a tree. Time to initiate can vary from the same sample batch as observed in batch 11/12 samples in section 9.2.2. However the effect is minimal in this study due to consistency of samples fabrication procedure adopted in Chapter 3.

10.6   Influence of applied voltage magnitude on initial tree length

Figure 9-4 shows the plots of the measured lengths of the initial trees in response to the applied voltage magnitudes. The Figure show average lengths shorter than 50 μm for samples stressed with voltages ranging from 12 to 16 kV rms whereas for samples stressed with 21 kVrms, the average lengths were longer than 50 μm.

Outcome: The higher the magnitude of the applied voltage the longer the length of the initial trees. The length of the initial tree depends on how quickly the applied voltage was de-energised after the tree was observed on voltage application.

10.7   Tree growth characteristics under ±DC stress

Effect of flashover event: Preliminary tests in section 7.4 showed that trees can readily grow under steady high DC stress (+70 kV) in samples without initial trees as shown in Figure 7-9. A faster propagation rate was observed in AC pre-initiated samples stressed under positive DC as shown in Figure 7-8 than under negative DC stress where tree propagation is only triggered by flashover events as shown in Figure 7-6 and Figure 7-7. This observation is consistent with the findings in literature where homo-charge injection during DC pre-stress period is believed to cause field relief at the electrode tip and thus preventing tree growth [116, 123-124, 191]. The inverse field set up by space charge as result of hetero-charge formation due to short circuiting can be 5 times higher than the intrinsic breakdown of the material as mentioned in [118]. This caused immediate damage seen as step-wise tree growth after each flashover event especially during negative DC test where tree propagation is hardly seen without flashover as shown in Figure 7-6.

Effect of initial tree on DC propagated trees: Further investigation on AC pre-initiated samples showed a stark difference in tree growth characteristics under positive and negative DC stress. All the 12 samples stressed with positive DC had appreciable trees grown in them with 8 (67%) samples propagating to failure. The remaining four samples that did not fail all had "initial tree lengths" shorter than 33 μm. Under negative DC none of the samples (10 samples) failed after 10 hours of – 60 kV DC stress. Only 3 samples with "initial tree lengths" longer than ~ 40 μm had an average propagation of 246 μm in length between them in comparison with the existing initial trees in the samples. Thus a threshold of about 33 μm and 40 μm are herein suggested to be the critical tree lengths under positive and negative DC tests below which tree propagation is slowed and above which higher propagation rate is observed with reduction in lifetime as shown in Figure 9-7 and Figure 9-12 respectively.

These thresholds may be related to homo-space charge formation at the vicinity of the needle electrode as believed by many [6, 116, 123-124, 191] to be caused by charge injection from the electrodes. These injected charges then form a zone of homo space charge which relieves the electrical field and therefore may decelerate the dielectric degradation e.g. the formation of electrical tree and subsequent breakdown. Since the initial tree channels incepted in the glassy epoxy resin are supposed to be conducting trees [145], they might just act as tiny wire electrodes of a diameter of around 2 μm – 4 μm [146] penetrating the zone of homo-charge and therefore reducing the positive effect of homo-charge on preventing electrical treeing.

Consequently, the thresholds found on the lengths of initial trees may correspond with the depths of injected homo-charge believed to be about 50 μm as shown by flight distance calculation in [118]. It is also believed by many [116-117, 191] that the negative electrode inject more charge than the positive electrode. This then make sense as to why limited tree growth is observed under negative DC test due to greater field relief resulting from larger zone of homo-charge under negative test as compared to that of positive test. This situation could be catastrophic in the face of single time events such as flashover, lightning or in-service switching events that result in surges and transients which will result in immediate breakdown due to a

very high inverse field that can be set-up by a sudden change of homo-charges into hetero-charges.

Effect of initial tree on DC tree shape and sample lifetime: Figure 9-8 shows the structure of pre-initiated AC trees, as either bush-like or branch-like. The fact that the AC pre-incepted trees have different shapes and the DC trees propagated from them have similar shapes suggests that, similar propagation mechanism was involved in the observed positive DC propagated trees, and that this mechanism may not be the same for AC propagated trees as different shapes were observed. The DC treeing observed in this study exhibited a runaway propagation to breakdown as shown in Figure 9-6. The tree shapes shown in Figure 9-8 are consistent with the breakdown structure predicted by Discharge-Avalanche Model in [99-100].

Outcome: Electrical trees were initiated under steady high positive DC stress. Flashover events are shown to trigger tree growth under negative DC. A critical length of initial tree of about 33 μm and 40 μm were found to be a rough limit below or above which tree will either cease to grow or will grow substantially under positive and negative tests respectively. The shape of AC pre-incepted initial tree does not affect the shape of propagated DC tree extending from them. Therefore the features of DC tree observed in this study should be representative of that obtained on samples without the initial tree.

10.8   Tree growth characteristics under AC

Tree shape and direction of growth at 15 kV peak AC: Under 15 kV peak AC voltages, two directions of tree growth were observed. Firstly, the commonly known directions of tree growth i.e. "forward tree growth" (FTG) as shown in Figure 9-13 (a), and secondly, the "reverse tree growth" (RTG) as shown by Figure 9-13 (b). The optically observed shapes of the trees during these two stages of growth are different. Three distinct changes in tree shapes namely; dark-widened channels, fine channels, and dense structure were observed during forward growth direction. The shapes of the trees growing from the counter electrode (RTG) are generally thicker and darker having spiky thick and fine side branches and are more visible than the forward growing trees. This types of shape were describe in [125, 135] as pine-like or bine branches. Appendix B-5 and 6 show the repeatability of this observation in all samples. No breakdown event was observed during the forward growth even though

the trees traversed the ground electrode. Only the reverse growing trees facilitate path to failure showing a huge halo and light through the breakdown channel due to high energy involved in the process. See Appendix B-11 for images typical breakdown channels.

Tree shape and direction of growth at 30 kV peak AC: tests at 30 kV (verification tests) were carried out to find out if the reverse treeing process will occur at 30 kV as observed at 15 kV. However none of the samples tested at 30 kV showed reverse treeing process. The tree shapes observed in this case mostly had less spread and few branches at the early stages of growth as shown in Figure 9-50 and Figure 9-51. Tree growth rate was faster than that at 15 kV pk AC.

Outcome: Repeatable forward and backward tree growths were observed at 15 kV peak AC. Only forward growing trees were observed at 30 kV peak AC. Reverse treeing process is shown to be due to relatively low voltage phenomena. This is probably because the high voltage leads to failure too quickly for reverse trees to develop.

10.9 Tree shape and direction of growth under ac superimposed on DC

Section 9.3 presented results of tree growth under ±60 kV DC. While trees readily grow under positive DC, they hardly grow under negative DC until external events associated with transients leading to flashover occurred. Also several hours of 30 kV DC did not result in tree growth during this study. However, results from section 9.5 when 15 kV peak AC was superimposed on ±15 kV DC, showed similar trees shapes as those of AC at 15 kV with growth characteristics restricted to the forward direction only. The visual physical structure of the trees for both positive and negative DC bias tests were similar, having initial dark branches followed by fine arrays of tree but no dense bush-like structures observed as in AC test at 15 kV. Instead, on approaching the counter electrode, the fine tree structures became darker with visible long widened channels appearing which then facilitate paths to breakdown. Similar tree shapes were observed in [127] using 28 kV rms. Generally the tree growth rate is faster here than under AC at 15 kV but slower than at 30 kV pk AC. See Appendix B–7 to B–10 for compiled images of tree structures under positive and negative DC bias tests.

Outcome: Only 'forward' traditional tree growth was observed with tree shapes having similar structure to those under AC at 15 kV. Growth rate was faster than under AC at 15 kV pk but slower than at 30 kV pk AC.

10.10 Partial discharge characteristics during AC and AC superimposed on DC test

The results of simultaneous imaging and partial discharge activities during physical tree growth characteristics was presented in sections 9.4 and 9.5 for AC test at 15 kV peak and 15 kV peak AC superimposed on ±15 kV DC. AC tests showed 5-stage tree growth characteristics as shown in Figure 9-18 while tests with AC superimposed on DC showed 4-stage tree growth characteristics as shown in Figure 9-44 and Figure 9-45 respectively. Figure 9-46 and Figure 9-47 showed similar tree growth characteristics as the traditional tree growth model proposed by Dissado and Fothergill shown in Figure 2-11. While Figure 9-18 and Figure 9-30 showed more complex growth characteristics depicting physical activity during AC treeing in this study. In general the monitored partial discharge can be divided into 3 regions (i.e stages; 2, 3 and 4 of Figure 9-44 and Figure 9-45) for AC superimposed on DC tests, and 4 regions (i.e. stages 2, 3, 4 and 5 of Figure 9-18 and Figure 9-30) for AC tests (without considering the initiation stage, as all the samples were pre-initiated before the tests). During pre-initiation, partial discharge measurement was not carried out. The observed discharge characteristics in stages 2 to 4 for all test types are similar and stage 5 was observed only under AC testing. The partial discharge behaviour at stages 2, 3, 4 and 5 are now discussed.

- Stage 2; partial discharge activity in stage 2 is active in all three test types with increasing discharge activity which then decrease sharply at the end of the stage. This is marked by extensions of dark tree channels from the pre-incepted initial trees as discussed in sections 9.4.4 and 9.5.4. The magnitudes of the recorded apparent charge in this stage for each sample is different from the beginning of the stage to the end of the stage depending on whether the evolving tree is branch-type tree or bush type tree. See Figure 9-48 and Figure 9-49 for examples of how each sample behave differently from the beginning of the stage to the end. Generally it was observed that, for evolving branch-type tree the discharge activity is more sporadic than that of an evolving bush-type tree which is more steady.

236

- Stage 3; this is a region of quiescent PD activity as shown in Figure 9-48 and Figure 9-49. It begins at the end of stage 2 when discharge activity decreased to about ~0.35 pC (the equipment sensitivity) and almost no PDs where measured. At this stage, the dark tree channels stop growing. However, arrays of fine tree channels extending from the dark trees observed in stage 2 continue to grow in length and spread, occupying large volumes of the insulation as shown in stages 3 of Figure 9-21, Figure 9-46 and Figure 9-47 for AC and AC superimposed on ±DC test respectively. This observation is consistent with the extinction of PD reported by Wu et al [129] and Chen et al [125]. When the PD magnitude dropped to a low level in [129], the branches stopped growing for a long time. In [125] the branches stopped growing, but the pines started to grow along the branches. In this study fine tree channels grow continuously, and the dark branches stop growing. Even though the tree structures reported in [125] and [129] were different (pine or fine branches), the response of the PD activity to change in tree structures were similar; i.e when the PD magnitude reduces to a very low magnitudes, dark thick branches stop growing and only pines or fine branch were generated and in this study fine tree channels continuous to grow. This suggests that the low PD magnitude in stage 3 corresponds to low level of damage (fine tree channels). The fact that neither the fine tree channels in stage 3 nor the previously formed dark tree channels in stage 2 produce high magnitude of PDs in stage 3 suggest that, stage 2 become non-conducting channel while the fine tree channels in stage 3 are conducting [23, 129, 145]. This observation is consistent with experimental and simulation works on conducting and non-conducting trees by Wu [129] and Dodd et al [23, 145], where the light emission of the PD changed from the main body of the tree structure to the periphery of the tree tip and is accompanied by low level of PD activity.
- Stage 4; most of the fine tree channels in all the three test types were approaching the counter electrode with those from AC test becoming dense and forming bush-like structure at the periphery, while those from AC superimposed on DC tests were having visible long widened dark channels as shown in Figure 9-22 for AC tests, and Figure 9-46 and Figure 9-47 for AC superimposed on DC tests respectively. This change in structure was

associated with high PD values as shown in Figure 9-18, Figure 9-44 and Figure 9-45 respectively. This observation further suggests that dark tree channels with high magnitude PDs are due to non-conductive tree channels, where the partial discharges are restricted to the main body of the tree channel. The energy of PD would then erode the channel wall causing widening of the channel, with subsequent deposition of conducting decomposed by-products on the tubule walls seen as the dark tree channels. The partial discharge behaviour is consistent with the imaged tree structures during the experiment as seen in stages 2, 4 and 5. In general at stage 2, the electric field near the needle tip is extremely high, resulting in high partial discharge activity in the newly formed dark tree channels. The high magnitude PDs erodes and widens the tree channel to make it more conductive. So that electric field near the needle electrode drops, while the electric field at the tree tips intensifies resulting in the observed reduction in high magnitude PDs activity in the main body of the tree as well as at tree tips. In stage 4, the electric field will intensify again due to the reduction in insulation gap distance as most of the tree channels are approaching the ground electrode. This then lead to a gradual increase in PDs magnitude resulting in long widened dark channels observed in AC superimposed on DC test which led to sample breakdown at this stage. However, none of the samples under AC tests breakdown at this stage. They rather form a bush-like tree structures near the ground electrode after which an increase in partial discharge magnitudes of several hundreds of pC were recorded leading to reverse treeing process seen in stage 5.

• Stage 5; the reverse treeing process is firstly believed to be due to the relatively low voltage (15 kV) AC test compared to that under 30 kV AC and AC superimposed on DC at 30 kV as confirmed in the verification test in section 9.6. The process leading to the formation of a reverse tree is firstly the formation of dense bush like structure at the periphery of the tree tips which prevent further propagation and is then followed by spouting of trees from the ground electrode marked by high PD activities. These trees were observed to grow independently from existing fine tree channels. However the fine tree channel became widened and darkened after touching the ground electrode

during this period. The mechanism of reverse tree growth is not fully understood and further study is on-going for better understanding in the future.

Outcome: Simultaneous imaging of electrical tree and partial discharge measurement which allow 5 stages of tree growth to be identified was successfully carried out. It is observed that high magnitudes of partial discharges are related to the formation of widened dark trees (bush-type or branch-type). Low magnitudes PDs (below the 0.35 pC sensitivity of the measurement system) are related to the formation of fine trees. Partial discharge monitoring alone cannot readily be used to detect fine tree channels and their observation in a semi-transparent material may be illusive. Reverse treeing is not observed at higher voltages. If this event is indeed associated with lower voltages, it will impact practical insulation design and requires further investigation.

10.11 Conclusions

The following conclusions were drawn from the research. These form the main contribution of this thesis to knowledge.

- This study shows that layered material (interfaces) can prove to be strong when tailored properly and the assertion that interfaces are weak points needs further investigation.

- Tree initiation times heavily depend on the magnitude of the applied voltage.

- Electrical tree initiates and grow under steady high positive DC stress.

- Electrical tree hardly grow under negative DC, however flashover events trigger growth easily.

- Space charge appears to plays a significant role in tree initiation and propagation under DC tests.

- A critical length of initial tree of about 33 μm and 40 μm related to depth of space charge injection was identified in this study to be a rough limit below which tree growth is not observed and above which substantially tree growth is observed under positive and negative tests respectively.

- It is justified to pre-incept samples prior to test as this does not affect the subsequent shape of the trees either AC or DC tree. The pre-initiation allows better comparison of sample life time.

- Simultaneous imaging of electrical tree and partial discharge measurement has allowed 5 stages of tree growth to be identified in this study under AC test.

- Reverse treeing process is shown to be a relatively low voltage phenomenon.

- Partial discharge monitoring alone cannot be used to detect fine tree channels and their observation in a semi-transparent material may be illusive. This may result in limitation of using PD detection for condition monitoring of HV equipment if the measuring system is not sensitive enough.

- Insulation lifetime is hugely reduced when AC ripples at 50Hz superimposed on DC was used to stress the samples compared to when individual AC and DC magnitudes alone were used as shown in Figure 9.55. This reinforces further the effect of power quality issues on DC insulation, and could be worse at harmonic frequencies as trees grow quicker at higher frequencies.

- Tree growth under pure DC is polarity dependent and is hugely linked with the effect of space charge injection at the electrode vicinity.

10.12 Future work

This research has developed equipment necessary for ageing and lifetime investigation of insulation material through charge detection technique, short term breakdown strength and long term breakdown through treeing. From the results of this study it can be inferred that, the tested insulation material is more reliable when subjected to DC voltage than AC voltage stress and worse when AC superimposed on DC was used as shown in Figure 9-55, suggesting that power quality will impact DC systems.

Power quality can be defined as "the measure, analysis, and improvement of the bus voltage to maintain a sinusoidal waveform at a rated voltage and frequency" [192].

Natural events such as lightning, resulting in one-off events (spikes transients or over voltages) are known to affect power quality and cannot be avoided in real systems. Literature and findings in this study showed that DC insulation is vulnerable to such events.

This thesis is an introductory work on the consequences of DC power quality. It was shown that 15 kV/ 50 Hz peak AC superimposed on ±15 kV DC accelerate tree growth resulting in shorter lifetimes. For example, 15 kV is only 3% of 500 kV and if realised as ripple on say 500 kV DC link will serve as a potential threat to reliability of such a system. Power quality is a broad subject which relates to; supply reliability, current/voltage quality and quality of power consumption [192]. Power quality can be viewed from three main areas; the utilities, the customers, and the manufactures. The coordination of these three areas is necessary for mitigating power quality problems [192].

This study proposes to further investigate the following:

- The effect of long term "pure high DC" stress on electrical tree growth characteristics.

- The effect of dielectric barriers on long term "pure DC" stress on electrical tree growth characteristics.

- The effect of non-power frequency AC voltage superimposed on DC on electrical tree growth characteristics.

- The effect of barrier and non-power frequency AC voltage superimposed on DC on electrical tree growth characteristics.

- The effect of harmonics on DC electrical tree growth characteristics.

- Further investigations to understand reverse treeing phenomenon.

- Partial discharge characteristics and characterisation under DC will be examined.

- Image detection to be improved to allow control of camera outside HV cage once experiment is energised to reduce blurring of captured images.

References:

[1] EPSRC, "Top and Tail Transformation: a grand challenge in energy network.," *Online available from:http://www.topandtail.org.uk.*

[2] K. P. Padiyar, *HVDC Power Transmission Systems: Technology and System Interactions*. New Delhi, India: John Willey & Sons, 1990.

[3] B. M. Weedy, *Electric power systems*, Third. John Wiley & Sons, 1987.

[4] E. Uhlmann, *Power Transmission by Direct Current*, 1st ed. Berlin/Heidelberg, New York: Springer-Verlag, 1975.

[5] Ensg, "Our Electricity transmission network: a vision for 2020," no. February 2012, p. 43, 2012.

[6] T. Sato, K. Muraki, N. Sato, and Y. Sekii, "Recent technical trends of 500 kV XLPE cable," *Power cables and accessories. Hitachi Cable, Ltd., Japan*, no. November, pp. 59–63, 1993.

[7] Y. Li and T. Takada, "Progress in space charge measurement of solid insulating materials in Japan," *IEEE Electr. Insul. Mag.*, vol. 10, no. 5, pp. 16–28, Sep. 1994.

[8] L. A. Dissado and J. C. Fothergill, *Electrical Degradation and Breakdown in Polymers*. London, U.K.: Peter Perengrinus Ltd., 1992.

[9] Y. Shen, "DC cable systems with extruded dielectrics," *Electr. power Res. Inst.*, p. 82, 2004.

[10] M. Salah Khalil, "International research and development trends and problems of HVDC cables with polymeric insulation," *IEEE Electr. Insul. Mag.*, vol. 13, no. 6, pp. 35–47, 1997.

[11] M. J. P. Jeroense and P. H. F. Morshuis, "Electric fields in HVDC paper-insulated cables," *IEEE Trans. Dielectr. Electr. Insul.*, vol. 5, no. 2, pp. 225–236, 1998.

[12] T. Takada, "Acoustic and optical methods for measuring electric charge distributions in dielectrics," *1999 Annu. Rep. Conf. Electr. Insul. Dielectr. Phenom. (Cat. No.99CH36319)*, vol. 6, no. 5, pp. 519–547, 1999.

[13] G. S. Eager, B. Fryszcczyn, C. Katz, H. a. Elbadaly, and a. R. Jean, "Effect of DC testing water tree deteriorated cable and a preliminary evaluation of VLF as alternative," *IEEE Trans. Power Deliv.*, vol. 7, no. 3, pp. 1582–1591, 1992.

[14] G. S. Eager, C. Katz, B. Fryszczyn, J. Densley, and B. S. Bernstein, "High voltage VLF testing of power cables," *IEEE Trans. Power Deliv.*, vol. 12, no. 2, pp. 565–570, 1997.

[15] B. Jacobson, B. Westman, and M. P. Bahrman, "500kV VSC Transmission System for lines and cables," *CIGRE Colloq. - Adv. VSC Technol. B4-6*, pp. 1–7, 2012.

[16] M. Byggeth, K. Johannesson, C. Liljegren, L. Palmqvist, U. Axelsson, J. Jonsson, and C. Tornkkvis, "The development of an extruded HVDC cable system and its first application in the Gotland HVDC light project," *Jicable,* p. 538, 1999.

[17] M. Callavik, A. Blomberg, J. Häfner, and B. Jacobson, "Break-through!: ABB's hybrid HVDC breaker, an innovation breakthrough enabling reliable HVDC grids," *ABB Rev.*, no. 2, pp. 7–13, 2013.

[18] R. Rudervall, J. P. Charpentier, and R. Sharma, "High Voltage Direct Current (HVDC) Transmission Systems Technology Review Paper," no. Ccc, pp. 1–17, 2000.

[19] S. Bahadoorsingh and S. Rowland, "A Framework Linking Knowledge of Insulation Aging to Asset Management - [Feature Article]," *IEEE Electr. Insul. Mag.*, vol. 24, no. 3, pp. 38–46, 2008.

[20] F. D. Miner, *Insulation Of Electrical Apparatus*. New York and London, 1941.

[21] M. Ieda, M., Nagao, M., Hikita, "High-field Conduction and Breakdown in Insulating Polymers," *IEEE Trans. Dielectr. Electr. Insul. Vol. 1 Oct.*, vol. 1, no. 5, pp. 934–945, 1994.

[22] S. J. Dodd, "A deterministic model for the growth of non-conducting electrical tree structures," *J. Phys. D. Appl. Phys.*, vol. 36, no. 2, pp. 129–141, 2003.

[23] J. V. Champion and S. J. Dodd, "Simulation of Partial Discharges in Conducting and Non-conducting Electrical Tree Structures," *J. Phys. D. Appl. Phys.*, vol. 34, pp. 1235–1242, 2001.

[24] R. M. Eichhorn, "Treeing in Solid Extruded Electrical Insulation," *IEEE Trans. Electr. Insul.*, vol. EI-12, no. 1, pp. 125–131, 1977.

[25] M. Ieda, "Electrical Conduction and Carrier Traps in Polymeric Materials," *IEEE Trans. Electr. Insul.*, vol. EI-19, no. 3, pp. 162–178, 1984.

[26] W. G. Potter, *Uses of Epoxy Resins*. London, U.K.: Newnes-Butterworths, 1975.

[27] A. Barlow, "The Chemistry of Polyethylene insulation," *IEEE Electrical Insulation Magazine*, vol. 7, no. 1, 1991.

[28] N. H. Malik, A. A. Al-Arainy, and M. I. Qureshi, *Electrical Insulation in Power Systems*. New York: Marcel Dekker, 1998.

[29] J. K. Nelson, "Dielectric polymer nanocomposites," *Dielectr. Polym. Nanocomposites*, pp. 1–368, 2010.

[30] C. C. Ku and R. Liepins, *Electrical Properties of Polymers : chemical principles*. Munich; New York: Hanser Publishers: Distributed in the U.S.A. By Macmillan Publishing Company, 1987.

[31] D. Blythe, T. Bloor, *Electrical properties of polymers*, Second. Cambridge, UK.: Cambridge University Press, 2005.

[32] T. John Lewis, "Electrical effects at interfaces and surfaces," *IEEE Trans. Electr. Insul.*, vol. EI-21, no. 3, pp. 289–295, 1986.

[33] T. Ditchi, C. Alquic, J. Lewiner, E. Favrie, and R. Jocteur, "Electrical properties of electrode / pol yethylene / electrode structures," *IEEE Trans. Electr. Insul. Vol. 24. No. 3, June 1989*, vol. 24, no. 3, pp. 403–408, 1989.

[34] G. Teyssedre and C. Laurent, "Charge transport modeling in insulating polymers: From molecular to macroscopic scale," *IEEE Trans. Dielectr. Electr. Insul.*, vol. 12, no. 5, pp. 857–874, 2005.

[35] W. C. Johnson, "Electronic transport in insulating films," *IEEE Trans. Nucl. Sci.*, vol. 19, no. 6, pp. 33–40, 1972.

[36] W. Bolton, *Electrical and Magnetic Properties of Materials*. London, U.K.: Longman Group Uk., 1992.

[37] A. Kelen, "Ageing of Insulating Materials and Equipment Insulation in Service and Tests," *IEEE Trans. Electr. Insul.*, vol. E1–12, no. 1, 1977.

[38] J. Densley, "Ageing and diagnostics in extruded insulations for power cables," *IEEE Int. Conf. Conduct. Break. Solid Dielectr.*, pp. 1–15, 1995.

[39] J. V Champion and S. J. Dodd, "The effect of voltage and material age on the electrical tree growth and breakdown characteristics of epoxy resins," *J. Phys. D. Appl. Phys.*, vol. 28, no. 2, pp. 398–407, 1995.

[40] L. A. Dissado, G. Mazzanti, and G. C. Montanari, "The role of trapped space charges in the electrical aging of insulating materials," *IEEE Trans. Dielectr. Electr. Insul.*, vol. 4, no. 5, pp. 496–506, 1997.

[41] J. C. Fothergill, "Ageing, space charge and nanodielectrics: Ten things we don't know about dielectrics," in *2007 International Conference on Solid Dielectrics, ICSD*, 2007, pp. 1–10.

[42] S. W. Rowe, "Electrical ageing of composites: An industrial perspective," *2007 Int. Conf. Solid Dielectr. ICSD*, pp. 401–406, 2007.

[43] G. C. Montanari, "The electrical degradation threshold of polyethylene investigated by space charge and conduction current measurements," *IEEE Trans. Dielectr. Electr. Insul.*, vol. 7, no. 3, pp. 309–315, 2000.

[44] L. A. Dissado, C. Laurent, G. C. Montanari, and P. H. F. Morshuis, "Demonstrating a threshold for trapped space charge accumulation in solid dielectrics under dc field," *IEEE Trans. Dielectr. Electr. Insul.*, vol. 12, no. 3, pp. 612–620, 2005.

[45] D. Fabiani, G. C. Montanari, C. Laurent, G. Teyssedre, P. H. F. Morshuis, R. Bodega, and L. a. Dissado, "HVDC cable design and space charge accumulation. Part 3: Effect of temperature gradient," *IEEE Electr. Insul. Mag.*, vol. 24, no. 2, pp. 5–14, Mar. 2008.

[46] K. W. Wagner, "The Physical Nature of the Electrical Breakdown of Solid Dielectrics," *Trans. Am. Inst. Electr. Eng.*, pp. 288–299, 1922.

[47] E. Kuffel, W. S. Zaengl, and J. Kuffel, *High Voltage Engineering Fundamentals*, 2nd Editio. Oxford, UK: Butterworth-Heinemann, 2000.

[48] IEC-60243-2, "Electric strength of insulating materials," (Standard), 2001.

[49] E. I. Materials and R. Bartnikas, "Standard Test Method for Dielectric Breakdown Voltage and Dielectric Strength of Solid Electrical Insulating Materials at Commercial Power," *Astm*, vol. 09, no. Reapproved, pp. 1–13, 2013.

[50] J. H. Mason, "Assessing the resistance of polymers to electrical treeing," *IEE Proc.*, vol. 128, no. No. 3, pp. 193–201, 1981.

[51] T. Mizutani, I. Kanno, M. Hikita, M. Ieda, and G. Sawa, "Pre-Breakdown Currents Due to Filamentary Thermal Breakdown in Polyimide Films," *IEEE Trans. Electr. Insul.*, vol. EI-22, no. 4, pp. 473–477, 1987.

[52] M. Nagao, T. Kimura, Y. Mizuno, M. Kosaki, and M. T. Ieda, "Detection of Joule heating before dielectric breakdown in polyethylene films," *IEEE Trans. Electr. Insul.*, vol. 25, no. 4, pp. 715–722, 1990.

[53] E. J. Mcmahon, "A Tutorial on Treeing," *IEEE Trans. Electr. Insul.*, vol. EI-13, no. 4, pp. 277–288, 1978.

[54] a. Von Hippel, "Dielectrics in Electrical Engineering," no. September, pp. 771–773, 1950.

[55] C. G. Garton and K. H. Stark, "'Electric strength of irradiated polythene,'" *Nature*, vol. 176, pp. 1225–1226, 1955.

[56] G. Bahder, T. Garrity, M. Sosnowski, R. Eaton, and C. Katz, "Physical Model of Electric Aging and Breakdown of Extruded Pplymeric Insulated Power

Cables," *IEEE Trans. Power Appar. Syst.*, vol. PAS-101, no. 6, pp. 1379–1390, 1982.

[57] T. Takeda, J. Holboell, A. Toureille, J. Densley, N. Hampton, J. Castellon, R. Hegerberg, M. Henriksen, G. C. Montanari, M. Nagao, and P. Morshuis, "Space charge measurement in dielectrics and insulating materials," *Cigre task force D1.12.01*, no. February, pp. 1–51, 2006.

[58] T. Takeda, J. Holboell, a. Toureille, J. Densley, N. Hampton, J. Castellon, R. Hegerberg, M. Henriksen, G. C. Montanari, M. Nagao, and P. Morshuis, "Guide for Space Charge Measurements in Dielectrics and Insulating Materials," *Tech. Broch. TF D1.12.1*, no. 223, pp. 1–6, 2005.

[59] J. Densley, "Ageing mechanisms and diagnostics for power cables - an overview," *IEEE Electr. Insul. Mag.*, vol. 17, no. 1, pp. 14–22, 2001.

[60] S. M. Gargari, P. A. A. F. Wouters, P. C. J. M. Van Der Wielen, and E. F. Steennis, "Practical experiences with on-line PD monitoring and interpretation for MV cable systems," *Proc. 2010 IEEE Int. Conf. Solid Dielectr. ICSD 2010*, pp. 1–4, 2010.

[61] A. N. Cuppen, E. F. Steennis, and P. C. J. M. Van Der Wielen, "Partial discharge trends in medium voltage cables measured while in-service with PDOL," *2010 IEEE PES Transm. Distrib. Conf. Expo. Smart Solut. a Chang. World*, pp. 1–5, 2010.

[62] IEC-60270:2000, "High-voltage test techniques - Partial discharge measurements," (Standard), 2000.

[63] I. J. Kemp, "Partial discharge plant-monitoring technology: present and future developments," *IEE Proc. - Sci. Meas. Technol.*, vol. 142, no. 1, p. 4, 1995.

[64] A. Cavallini, F. Ciani, G. Mazzanti, and G. C. Montanari, "First electron availability and partial discharge generation in insulation cavities: Effect of light irradiation," *IEEE Trans. Dielectr. Electr. Insul.*, vol. 12, no. 2, pp. 387–394, 2005.

[65] F. H. Kreuger, *Partial Discharge Detection in High-Voltage Equipment*. London: Butterworths, 1989.

[66] R. Bartnikas, "Partial discharges their mechanism, detection and measurement," *IEEE Trans. Dielectr. Electr. Insul.*, vol. 9, no. 5, pp. 763–808, 2002.

[67] E. Gulski and F. H. Kreuger, "Determination of discharge sources by analysis of discharge quantities as a function of time," *Conf. Rec. 1992 IEEE Int. Symp. Electr. Insul.*, pp. 397–400, 1992.

[68] G. C. Montanari, a. Cavallini, and F. Puletti, "A new approach to partial discharge testing of HV cable systems," *IEEE Electr. Insul. Mag.*, vol. 22, no. 1, pp. 14–23, 2006.

[69] S. M. Strachan, S. D. J. McArthur, M. D. Judd, and J. R. McDonald, "Incremental Knowledge-Based Partial Discharge Diagnosis in Oil-Filled Power Transformers," in *Intelligent Systems Application to Power Systems, 2005. Proceedings of the 13th International Conference on*, 2005, pp. 181–186.

[70] J. Zhang, Y., Lewiner, C. Alquie, and N. Hampton, "Evidence of strong correlation between space-charge buildup and breakdown in cable insulation," *IEEE Trans. Dielectr. Electr. Insul.*, vol. 3, no. 6, pp. 778–783, 1996.

[71] J. M. Alison, "A high field pulsed electro-acoustic apparatus for space charge and external circuit current measurement within solid insulators," *Meas. Sci. Technol.*, vol. 9, pp. 1737–1750, 1999.

[72] G. Chen, T. Y. G. Tay, A. E. Davies, Y. Tanaka, and T. Takada, "Electrodes and Charge Injection in Low-density Polyethylene Using the Pulsed Electroacoustic Technique," *IEEE Trans. Dielectr. Electr. Insul.*, vol. 8, no. 6, pp. 867–873, 2001.

[73] K. Fukunaga, T. Maeno, Y. Hashimoto, and K. Suzuki, "Space charge formation at the interface between a charge layer and a polyester film," *IEEE Trans. Dielectr. Electr. Insul.*, vol. 5, no. 2, pp. 276–280, 1998.

[74] G. M. Sessler, "Charge distribution and transport in polymers," *IEEE Trans. Dielectr. Electr. Insul.*, vol. 4, no. 5, pp. 614–628, 1997.

[75] N. H. Ahmed and N. N. Srinivas, "Review of space charge measurements in dielectrics," *IEEE Trans. Dielectr. Electr. Insul.*, vol. 4, no. 5, pp. 644–656, 1997.

[76] Y. Li, M. Yasuda, and T. Takada, "Pulsed Electroacoustic Method For Measurement Of Charge Accumulation In Solid Dielectrics," *IEEE Trans. Dielectr. Electr. Insul.*, vol. 1, no. 2, pp. 188–195, Apr. 1994.

[77] N. Hozumi, T. Okamoto, and H. Fukagawa, "Simultaneous Measurement of Microscopic Image and Discharge Pulses at the Moment of Electrical Tree Initiation," *Jpn. J. Appl. Phys.*, vol. 27, no. Part 1, No. 4, pp. 572–576, 1988.

[78] M. Marzinotto and G. Mazzanti, "A procedure for space charge measurements in full-size HVDC extruded cables in order to access the electric field in the insulation wall," in *IEEE*, 2012, pp. 804–807.

[79] G. Mazzanti, G. Chen, J. C. Fothergill, N. Hozumi, J. Li, M. Marzinotto, F. Mauseth, P. Morshuis, C. Reed, a. Tzimas, and K. Wu, "A protocol for space charge measurements in full-size HVDC extruded cables," *IEEE Trans. Dielectr. Electr. Insul.*, vol. 22, no. 1, pp. 21–34, 2015.

[80] T. Takeda, N. Hozumi, H. Suzuki, M. Hara, Y. Murata, K. Fujii, K. Terashima, K. Watanabe, and M. Yoshida, "Space charge behavior in full-size 250 kV DC XLPE cables," *IEEE Trans. Power Deliv.*, vol. 13, no. 1, pp. 28–39, 1998.

[81] O. Gallot-Lavallée, V. Griseri, G. Teyssedre, and C. Laurent, "The pulsed electro-acoustic technique in research on dielectrics for electrical engineering. Today's achievements and perspectives for the future," *Rev. Int. génie électrique*, vol. 8, no. 5–6, pp. 749–772, 2005.

[82] R. King, C. Barker, A. Tzimas, G. Lucas, and N. Kirby, "Validation of Cable Modelling for HVDC Transient Analysis Simulation," in *CIGRE Conference Canada*, 2015, pp. 1–8.

[83] P. Notingher, A. Toureille, S. Agnel, and J. Castellon, "Determination of electric field and space charge in the insulation of power cables with the thermal step method and a new mathematical processing," *IEEE Trans. Ind. Appl.*, vol. 45, no. 1, pp. 67–74, 2009.

[84] J. Castellon, P. Notingher, S. Agnel, a. Toureille, F. Brame, P. Mirebeau, and J. Matallana, "Electric field and space charge measurements in thick power cable isulation," *IEEE Electr. Insul. Mag.*, vol. 25, no. 3, pp. 30–42, 2009.

[85] T. Takada, Y. Tanaka, N. Adachi, and X. Qin, "Comparison between the PEA method and the PWP method for space charge measurement in solid dielectrics," *IEEE Trans. Dielectr. Electr. Insul.*, vol. 5, no. 6, pp. 944–951, 1998.

[86] B. Vissouvanadin, C. Laurent, S. Le Roy, G. Teyssedre, I. Denizet, M. Mammeri, and B. Poisson, "A deconvolution technique for space charge recovery in lossy and dispersive dielectrics using PEA method," *Annu. Rep. - Conf. Electr. Insul. Dielectr. Phenomena, CEIDP*, no. 1, pp. 10–13, 2010.

[87] G. Chen, Y. L. Chong, and M. Fu, "Calibration of the pulsed electroacoustic technique in the presence of trapped charge," *Meas. Sci. Technol.*, vol. 17, no. 7, pp. 1974–1980, Jul. 2006.

[88] D. Fabiani and G. Montanari, "Polymeric HVDC cable design and space charge accumulation. Part 1: insulation/semicon interface," *Featur. Artic. IEEE Electr. Insul. Mag.*, vol. 24, no. 1, pp. 14–24, 2007.

[89] L. A. Dissado, "Understanding electrical trees in solids: From experiment to theory," *IEEE Trans. Dielectr. Electr. Insul.*, vol. 9, no. 4, pp. 483–497, 2002.

[90] N. Shimizu and C. Laurent, "Electrical tree initiation," *IEEE Trans. Dielectr. Electr. Insul.*, vol. 5, no. 5, pp. 651–659, 1998.

[91] G. Mazzanti, G. C. Montanari, and L. A. Dissado, "Electrical aging and life models: The role of space charge," *IEEE Trans. Dielectr. Electr. Insul.*, vol. 12, no. 5, pp. 876–890, Oct. 2005.

[92]   J.-P. Crine, J.-L. Parpal, and C. Dang, "Influence of fatigue on some electrical aging mechanisms of polymers," *IEE Proc. - Sci. Meas. Technol.*, vol. 143, no. 6, p. 395, 1996.

[93]   L. A. Dissado, S. V. Wolfe, J. C. Filippini, C. T. Meyer, and J. C. Fothergill, "Analysis of field-dependent water tree growth models.," *IEEE Trans. Electr. Insul.*, vol. 23, no. 3, pp. 345–356, 1988.

[94]   M. N. Arbab and D. W. Auckland, "The influence of vibration on the initiation of trees in dielectrics," *IEE Proc. A Phys. Sci. Meas. Instrumentation, Manag. Educ.*, vol. 133, no. 9, pp. 618–622, 1986.

[95]   E. Cartier and Pfluger, "Detection of hot electron-induced readiation damage in organic dielectrics by exoelectron emission from thin films," *IEEE Trans. Electr. Insul.*, vol. E1–22, no. 2, pp. 123–128, 1987.

[96]   S. Bamji, "Electrical Trees, Physical Mechanisms and Experimental Techniques," in *Wiley Encyclopedia of Electrical and Electronics*, J. Webster, Ed. John Wiley & Sons, 1999, pp. 264–275.

[97]   N. Shimizu, T. Takahashi, and S. Iemura, "Initiation mechanism of electrical tree under alternating stress-electron impact or UV photo-degradation?," *IEEE 7th Int. Conf. Solid Dielectr.*, no. 3, pp. 423–426, 2001.

[98]   T. Tanaka and A. Greenwood, "Effects of charge injection and extraction on tree initiation in polyethylene," *IEEE Trans. Power Appar. Syst.*, vol. PAS-97, no. 5, pp. 1749–1759, 1978.

[99]   L. A. Dissado and P. J. J. Sweeney, "An analytical model for discharge generated breakdown structures," in *1992 Proceedings of the 4th International Conference on Conduction and Breakdown in Solid Dielectrics*, 1992, no. 2, pp. 328–332.

[100]   L. A. Dissado, "Discharges and the formation of tree-shaped breakdown sturtures," in *Partial discharges, International Conference on*, 1993, pp. 60–63.

[101]   T. Tanaka, "Tree initiation mechanisms," *[1991] Proc. 3rd Int. Conf. Prop. Appl. Dielectr. Mater.*, pp. 18–24, 1991.

[102]   C. T. Meyer and A. Chamel, "Water And Ion Absorption By Polyethylene In Relation to Water Treeing," *IEEE Trans. Electr. Insul.*, vol. EI - 15, no. 5, pp. 389–393, 1980.

[103]   C. T. Meyer, "Water absorption during water treeing in polyethylene," *IEEE Trans. Electr. Insul.*, no. EI-18, pp. 28–31, 1983.

[104]   M. Shaw and S. Shaw, "Water Treeing in Solid Dielectrics," *IEEE Trans. Electr. Insul.*, vol. EI-19, no. 5, pp. 419–452, 1984.

[105] E. F. Steennis and F. H. Kreuger, "Water Treeing in Polyethylene Cables," *IEEE Trans. Electr. Insul.*, vol. 25, no. 5, pp. 989–1028, 1990.

[106] G. C. Montanari, "Insulation Diagnosis of High Voltage Apparatus by Partial Discharge Investigation," *Prop. Appl. Dielectr. Mater. 2006. 8th Int. Conf.*, pp. 1–11, 2006.

[107] T. Ishida and M. Nagao, "Time variation of partial discharge current waveforms with degradation of insulators," *Proc. Int. Symp. Electr. Insul. Mater.*, vol. 2, pp. 494–497, 2005.

[108] S. S. Bamji, A. T. Bulinski, and R. J. Densley, "Evidence of near-ultraviolet emission during electrical-tree initiation in polyethylene," *J. Appl. Phys.*, vol. 61, no. 2, pp. 694–699, 1987.

[109] S. S. Bamji, A. T. Bulinski, and R. J. Densley, "Threshold voltage of luminescence and electrical tree inception in low-density polyethylene," *J. Appl. Phys.*, vol. 63, no. 12, pp. 5841–5845, 1988.

[110] Y. Muramoto, S. Mizuno, T. Mito, and N. Shimizu, "Electroluminescence properties of water-treed XLPE under long time voltage application," *Proc. Int. Symp. Electr. Insul. Mater.*, pp. 456–459, 2008.

[111] J. Andrianjohaninarivo, M. R. Wertheimer, and A. Yellon, "Nucleation of Electrical Trees in Polyethylene," *IEEE Trans. Electr. Insul.*, no. 6, 1987.

[112] G. Teyssedre, G. Tardieu, D. Mary, and C. Laurent, "Ac and dc electroluminescence in insulating polymers and implication for electrical ageing," *J. Phys. D. Appl. Phys.*, vol. 34, no. 14, pp. 2220–2229, 2001.

[113] W. Le, C. Xiangrong, S. M. Hu. Libin, Gubanski, and J. Blennow, "Electrical Tree Formation as a Measure of Degradation Resistance in Polymeric Materials for HVDC Applications," *Annu. Conf. Electr. Insul. Dielectr. Phenom.*, pp. 510–513, 2013.

[114] R. Kurnianto, Y. Murakami, N. Hozumi, and M. Nagao, "Electrical tree propagation in epoxy resin under different characteristics," in *International Symposium on Electrical Insulating Materials*, 2005, vol. 3, pp. 718–721.

[115] H. Kawamura and M. Nawata, "DC Electrical Treeing Phenomena and Space Charge," *IEEE Trans. Dielectr. Electr. Insul. Vol. 5, No. 5, Oct. 1998*, vol. 5, no. 5, pp. 741–747, 1998.

[116] T. Katsuta, Ginzo, Itaya, H. Miyata, T. , Takahashi, Tohru, Niwa, and T. Electric, "DC and Impulse treeing characteristics in Insulating Material for HVDC Cable," in *IEEE International Conference on Properties and Applications of Dielectric Materials*, 1997, pp. 422–425.

[117] Y. Sekii, H. Kawanami, M. Saito, K. Sugi, and I. Komatsu, "DC tree and grounded DC tree in XLPE," *CEIDP '05. 2005 Annu. Rep. Conf. Electr. Insul. Dielectr. Phenomena, 2005.*, pp. 523–526, 2005.

[118] M. Ieda, M. Nawata, I. Ieda, and N. Nawata, "DC Treeing Breakdown Associated With Space Charge Formation in polyethylene," *IEEE Trans. Dielectr. Electr. Insul. Vol. EI-12, No. 1 February, 1977*, vol. 12, no. 1, pp. 19–25, 1977.

[119] J. H. Mason, "Breakdown of solid dielectrics in divergent fields," *Proc. IEE Part C Monogr.*, vol. 102, no. 2, p. 254, 1955.

[120] M. Selsjord and E. Ildstad, "Electrical Treeing Caused by Rapid DC-Voltage Grounding of XLPE Cable Insulation," in *IEEE International Symposium on Electrical Insulation*, 2006, pp. 502–505.

[121] Y. Saito, M. Fukuzawa, and H. Nakamura, "On the Mechanism of Tree Initiation," *Electr. Insul. IEEE Trans.*, vol. EI-12, no. 1, pp. 31–34, 1977.

[122] L. Ying and C. Xiaolong, "Electrical tree initiation in XLPE cable insulation by application of DC and impulse voltage," *IEEE Trans. Dielectr. Electr. Insul.*, vol. 20, no. 5, pp. 1691–1698, 2013.

[123] F. Noto, N. Yoshimura, and T. Ohta, "Tree initiation in polyethylene by application of DC and impulse voltage," *IEEE Trans. Electr. Insul.*, vol. E1–12, no. 1, pp. 26–30, 1977.

[124] N. Yoshimura and F. Noto, "Effect OF DC Prestressing On Tree Initiation in Polyethylene with and without Needle-shaped Void," in *IEEE Transactions on Electrical Insulation Vol. EI-19 No.2, April 1984*, 1984, no. April, pp. 135–140.

[125] X. Chen, Y. Xu, X. Cao, S. J. Dodd, and L. a. Dissado, "Effect of tree channel conductivity on electrical tree shape and breakdown in XLPE cable insulation samples," *IEEE Trans. Dielectr. Electr. Insul.*, vol. 18, no. 3, pp. 847–860, Jun. 2011.

[126] C. Laurent and C. Mayoux, "Analysis of the propagation of electrical treeing using optical and electrical methods," *IEEE Trans. Electr. Insul.*, vol. EI-15, no. 1, pp. 33–42, 1980.

[127] R. Vogelsang, B. Fruth, T. Farr, and K. Fröhlich, "Detection of electrical tree propagation by partial discharge measurements," *Eur. Trans. Electr. Power*, vol. 15, no. 3, pp. 271–284, May 2005.

[128] K. Wu, Y. Suzuoki, T. Mizutani, and H. Xie, "Model for partial discharges associated with treeing breakdown: III. PD extinction and regrowth of tree," *J. Phys. D. Appl. Phys.*, vol. 33, no. 10, pp. 1209–1218, 2000.

[129] K. Wu, Y. Suzuoki, T. Mizutani, and H. Xie, "Model for partial discharges associated with treeing breakdown: I. PDs in tree channels," *J. Phys. D. Appl. Phys.*, vol. 33, no. 10, pp. 1197–1201, 2000.

[130] R. Schurch, S. M. Rowland, R. S. Bradley, T. Hashimoto, G. E. Thompson, and P. J. Withers, "Three dimensional imaging of electrical trees in micro and nano-filled epoxy resin," *IEEE Conf. Electr. Insul. Dielectr. Phenomena, CEIDP*, pp. 39–42, 2014.

[131] J. V Champion, S. J. Dodd, and G. C. Stevens, "Analysis and modelling of electrical tree growth in synthetic resins over a wide range of stressing voltage," *J. Phys. D. Appl. Phys.*, vol. 27, no. 5, pp. 1020–1030, 1994.

[132] R. Sarathi, A. Nandini, and M. Danikas, "Understanding Electrical Treeing in XLPE Cable insulation adopting UHF Technique," *J. Electr. Eng.*, vol. 62, no. 2, pp. 73–79, Jan. 2011.

[133] R. Sarathi, A. Nandini, and T. Tanaka, "Understanding treeing phenomena and space charge effect in gamma-irradiated XLPE cable insulation," *Electr. Eng.*, vol. 93, no. 4, pp. 199–207, Apr. 2011.

[134] G. Bahder, C. Katz, J. Lawson, and W. Vahlstrom, "Electrical and Electro-Chemical Treeing Effect in Polyethylene and Crosslinked Polyethylene Cables," in *Power Apparatus and Systems, IEEE Transactions on*, 1974, vol. PAS-93, no. 3, pp. 977–989.

[135] X. Zheng and G. Chen, "Propagation mechanism of electrical tree in XLPE cable insulation by investigating a double electrical tree structure," *IEEE Trans. Dielectr. Electr. Insul.*, vol. 15, no. 3, pp. 800–807, Jun. 2008.

[136] Y. Zhou, R. Liu, F. Hou, X. Zhang, and W. Xue, "Morphology of electrical trees in silicon rubber," *J. Electrostat.*, vol. 71, no. 3, pp. 440–448, 2013.

[137] M. Bao, X. Yin, and J. He, "Structure characteristics of electrical treeing in XLPE insulation under high frequencies," *Phys. B Condens. Matter*, vol. 406, no. 14, pp. 2885–2890, 2011.

[138] B. Du, Z. Ma, Y. Gao, and T. Han, "Effect of ambient temperature on electrical treeing characteristics in silicone rubber," *IEEE Trans. Dielectr. Electr. Insul.*, vol. 18, no. 2, pp. 401–407, 2011.

[139] R. J. Densley, "An Investigation into the Growth of Electrical Trees in XLPE Cable Insulation," *IEEE Trans. Electr. Insul.*, vol. EI-14, no. 3, pp. 148–158, 1979.

[140] G. Chen and C. Tham, "Electrical treeing characteristics in XLPE power cable insulation in frequency range between 20 and 500 Hz," *IEEE Trans. Dielectr. Electr. Insul.*, vol. 16, no. 1, pp. 179–188, Feb. 2009.

[141] R. Thiamsri, N. Ruangkajonmathee, A. Oonsivilaiand, and B. Marungsri, "Effect of Applied Voltage Frequency on Electrical Treeing in 22 kV Cross-linked Polyethylene Insulated Cable," *World Acad. Sci. Eng. Technol.*, vol. 60, no. 12, pp. 376–381, 2011.

[142] J.-J. Park, "Effect of Electric Field Frequency on the AC Electrical Treeing Phenomena in an Epoxy/Reactive Diluent/ Layered Silicate Nanocomposite," *Trans. Electr. Electron. Mater.*, vol. 15, no. 2, pp. 87–90, 2014.

[143] A. Vaughan, S. Dodd, and S. Sutton, "Electrical treeing in polyethylene: analysis by confocal Raman microprobe spectroscopy," in *Conference on Electrical Insulation and Dielectric Phenomena*, 2003, pp. 534–537.

[144] J. V Champion, S. J. Dodd, and J. M. Alison, "The correlation between the partial discharge behaviour and the spatial and temporal development of electrical trees grown in an epoxy resin," *J. Phys. D. Appl. Phys.*, vol. 29, no. 10, p. 2689, 1996.

[145] S. J. Dodd, N. M. Chalashkanov, and J. C. Fothergill, "Partial discharge patterns in conducting and non-conducting electrical trees," *IEEE Int. Conf. Solid Dielectr.*, pp. 1–4, 2010.

[146] R. Schurch, S. M. Rowland, R. S. Bradley, and P. J. Withers, "Three dimensional characterisation of electrical trees," *IEEE Conf. Electr. Insul. Dielectr. Phenomena, CEIDP*, pp. 494–497, 2013.

[147] R. Schurch, S. M. Rowland, and T. Starborg, "Serial block-face scanning electron microscopy for three-dimensional imaging of electrical trees," *IEEE Int. Conf. Solid Dielectr. ICSD*, pp. 271–274, Jun. 2013.

[148] R. Schurch, S. M. Rowland, and P. J. Withers, "Techniques for electrical tree imaging," *IEEE Int. Conf. Imaging Syst. Tech. Proc.*, pp. 409–414, Jul. 2012.

[149] J. V. Champion, S. J. Dodd, Y. Zhao, a. S. Vaughan, M. Brown, a. E. Davies, S. J. Sutton, and S. G. Swingler, "Morphology and the growth of electrical trees in a propylene/ethylene copolymer," *IEEE Trans. Dielectr. Electr. Insul.*, vol. 8, no. 2, pp. 284–292, Apr. 2001.

[150] A. Xie, X. Zheng, S. Li, and G. Chen, "Investigations of electrical trees in the inner layer of XLPE cable insulation using computer-aided image recording monitoring," *IEEE Trans. Dielectr. Electr. Insul.*, vol. 17, no. 3, pp. 685–693, 2010.

[151] K. Kudo, "Fractal analysis of electrical trees," *IEEE Trans. Dielectr. Electr. Insul.*, vol. 5, no. 5, pp. 713–727, 1998.

[152] T. N. Matheson, A. S. Vaughan, J. Cooper, and A. Minigher, "Impact of sonication on the electrical properties of epoxy-clay composites," *IEEE Trans. Dielectr. Electr. Insul.*, pp. 219–222, 2008.

[153] C. Calebrese, L. Hui, L. S. Schadler, and J. K. Nelson, "A review on the importance of nanocomposite processing to enhance electrical insulation," *IEEE Trans. Dielectr. Electr. Insul.*, vol. 18, no. 4, pp. 938–945, 2011.

[154] M. Reading, Z. Xu, a S. Vaughan, and P. L. Lewin, "On sample preparation and dielectric breakdown in nanostructured epoxy resins," *J. Phys. Conf. Ser.*, vol. 310, p. 012009, Aug. 2011.

[155] H.-Z. Ding and B. R. Varlow, "Electrical treeing studies on the Araldite LY/HY 5052 epoxy resin over a wide range of stressing voltage," *IEEE Conf. Electr. Insul. Dielectr. Phenomena, CEIDP*, pp. 306–309, 2004.

[156] H.-Z. Ding and B. R. Varlow, "Effect of nano-fillers on electrical treeing in epoxy resin subjected to AC voltage," *IEEE Conf. Electr. Insul. Dielectr. Phenomena, CEIDP*, pp. 332–335, 2004.

[157] S. Bahadoorsingh, "Asset Management and the Role of Power Quality on Electrical Treeing in Epoxy Resin," PhD Thesis, The University of Manchester, Manchester United Kingdom, 2009.

[158] R. Schurch, "Three-Dimensional Imaging and Analysis of Electrical Trees," PhD Thesis, The University of Manchester, Manchester United Kingdom, 2014.

[159] D. A. Seanor, Ed., *Electrical Properties of Ploymers*. New York: Academic Press Inc., 1982.

[160] BSI, "ISO 7864: 1996 Sterile hypodermic needles for single use." (Standard),1996.

[161] BS EN-60212:2011, "Standards Publication Standard conditions for use prior to and during the testing of solid electrical insulating materials." 2011.

[162] P. Barber, S. Balasubramanian, Y. Anguchamy, S. Gong, A. Wibowo, H. Gao, H. J. Ploehn, and H. C. Zur Loye, "Polymer composite and nanocomposite dielectric materials for pulse power energy storage," *Materials (Basel).*, vol. 2, no. 4, pp. 1697–1733, Oct. 2009.

[163] R. Gorur G, *Dielectrics in Electric Field*. New York USA: Marcel Dekker Inc., 2003.

[164] IEC 60243-2 (20001) "Electric strength of insulating materials." (Standard), 2001.

[165] IEEE-930-2004 "Guide for the Statistical Analysis of Electrical Insulation Breakdown Data" (IEEE Standard), 2004.

[166] J. E. Abernethy, R. B. Breneman, C. H. Medlin, and G. L. Reinman, *Weibull analysis handbook*. Florida: Pratt & Whitney Aircraft Government Product Divission United Technologies Corporation, 1983.

[167]   J. Deacon, "The really easy statistics site." [Online]. Available: http://archive.bio.ed.ac.uk/jdeacon/statistics/tress1.html. [Accessed: 10-Jan-2016].

[168]   Google search, "Normal distribution curves." [Online]. Available: www.google.co.uk/search?q=normal+distribution+curves&espv. [Accessed: 10-Jan-2016].

[169]   C. L. Wadhawa, *High Voltage Engineering*, 2nd editio. New Delhi, India: New age international, 2007.

[170]   G. Chen, Y. Tanaka, T. Takada, and L. Zhong, "Effect of Polyethylene Interface on Space Charge Formation," *IEEE Trans. Dielectr. Electr. Insul.*, vol. 11, no. 1, pp. 113–121, Feb. 2004.

[171]   Z. Xu and G. Chen, "Interfacial characteristics of space charge in multi-layer LDPE," *Proc. 2008 Int. Conf. Cond. Monit. Diagnosis, C. 2008*, pp. 332–335, 2007.

[172]   Y. Li, T. Takada, H. Miyata, and T. Niwa, "Observation of charge behavior in multiply low-density polyethylene," *J. Appl. Phys.*, vol. 74, no. 4, p. 2725, 1993.

[173]   T. Tanaka, A. Bulinski, J. Castellon, M. Fréchette, S. Gubanski, J. Kindersberger, G. C. Montanari, M. Nagao, P. Morshuis, Y. Tanaka, S. Pélissou, A. Vaughan, Y. Ohki, C. W. Reed, S. Sutton, and S. J. Han, "Dielectric properties of XLPE/Sio2 nanocomposites based on CIGRE WG D1.24 cooperative test results," *IEEE Trans. Dielectr. Electr. Insul.*, vol. 18, no. 5, pp. 1484–1517, 2011.

[174]   PD IEC/TS 62758 : 2012 "Standards Publication Calibration of space charge measuring equipment based on pulsed electroacoustic (PEA) measurement principle"(BSI), 2012.

[175]   T. Maeno and K. Fukunaga, "High-resolution PEA charge distribution measurement system," *IEEE Trans. Dielectr. Electr. Insul.*, vol. 3, no. 6, pp. 754–757, 1996.

[176]   P. Acoustics, "Guide to Using Poled PVdF: PVDF properties and uses." [Online]. Available: www.acoustics.co.uk. [Accessed: 01-Dec-2012].

[177]   P. Morshuis and M. Jeroense, "Space charge measurements on impregnated paper: A review of the PEA method and a discussion of results," *IEEE Electr. Insul. Mag.*, vol. 13, no. 3, pp. 26–35, 1997.

[178]   J. M. Alison and R. M. Hill, "A model for bipolar charge transport in insulators," *IEEE Int. Conf. Conduct. Break. Solid Dielectr.*, pp. 319–323, 1995.

[179] H. Tanaka, Y. Ohki, K. Fukunaga, T. Maeno, and K. Okamoto, "Space charge distributions in glass fibre/epoxy resin composites under dc 10 kV/mm electric field," *J. Phys. D. Appl. Phys.*, vol. 40, no. 5, pp. 1489–1496, Mar. 2007.

[180] S. Holé, L. a Dissado, M. N. Ajour, and J. C. Fothergill, "Space charge behaviour in epoxy laminates under high constant electric field," *J. Phys. D. Appl. Phys.*, vol. 38, no. 16, pp. 2890–2898, Aug. 2005.

[181] G. C. Montanari and P. H. F. Morshuis, "Space charge phenomenology in polymeric insulating materials," *IEEE Trans. Dielectr. Electr. Insul.*, vol. 12, no. 4, pp. 754–767, 2005.

[182] R. Bodega, P. H. F. Morshuis, and J. J. Smit, "Space charge measurements on multi-dielectrics by means of the pulsed electroacoustic method," *IEEE Trans. Dielectr. Electr. Insul.*, vol. 13, no. 2, pp. 272–281, 2006.

[183] National Instrument, "NI 5421 Arbitrary waveform generator." [Online]. Available: http://www.ni.com/pdf/products/us/04-3076-305-101.pdf. [Accessed: 15-Jun-2014].

[184] Trek-Inc, "Operator, manual Trek Model 30 / 20A High-Voltage Power Amplifier", "www.trek.com", 2013.

[185] Analog Devices, "AD811 High performance video Op Amp." [Online]. Available: http://www.analog.com/en/products/amplifiers/video-amplifiers-analog-video-functions/video-op-amps/ad811.html.

[186] J. V Champion, S. J. Dodd, and G. C. Stevens, "Long-term light emission measurement and imaging during the early stages of electrical breakdown in epoxy resin," *J. Appl. Phys.*, no. 27, pp. 604–610, 1994.

[187] Allied Vision, "Manta G-504B CCD camera." [Online]. Available: https://www.alliedvision.com/en/products/cameras/detail/g-504.html. [Accessed: 15-Jun-2014].

[188] Stemmer Imaging, "Qioptiq CCD Macro lenses." [Online]. Available: http://www.stemmer-imaging.co.uk/en/products/series/qioptiq-macro-lenses. [Accessed: 15-Jun-2014].

[189] J. Bryden, I. J. Kemp, A. Nesbitt, J. V. Champion, S. Dodd, and Z. Richardson, "Correlations Among Tree Growth and the Measurable Parameters of Partial Discharge Activity," in *IEEE High voltage engineering symposium*, 1999, no. 467, pp. 79–83.

[190] Omicron, "User Manual MPD 600; Omicron electronics GmbH." 2013.

[191] M. Ieda and M. Nawata, "DC Treeing Breakdown Associated With Space Charge Formation in polyethylene," *IEEE Trans. Dielectr. Electr. Insul. Vol. EI-12, No. 1 February, 1977*, vol. 12, no. 1, pp. 19–25, 1977.

[192] F. Fuchs, Ewald and M. A. S. Masoum, *Power quality in power systems and electrical machines*. San Diego, Calfornia, London.: Elsevier academic press Ltd, 2008.

Appendix A-1: Collated test result for breakdown test in for PET reference samples of 100 μm thicknesses.

No. of breakdowns	Sample ID	Breakdown voltage (kV)	Breakdown field (kV/mm)	Sample ID	Breakdown voltage (kV)	Breakdown field (kV/mm)
	Single layer Sample: Positive polarity test in air			**Negative polarity test in air**		
1	Sample 1: 100 μm PET film	19.84	198.40	Sample 1: 100 μm PET film	22.40	224.00
2		22.30	223.00		21.60	216.00
3		22.60	226.00		21.60	216.00
4		22.90	229.00		20.80	208.00
5		21.70	217.00		24.30	243.00
6		22.40	224.00		22.20	222.00
7		21.80	218.00		24.10	241.00
8		19.80	198.00		22.00	220.00
9		20.20	202.00		19.30	193.00
10		21.40	214.00		23.60	236.00
11	Sample 2: 100 μm PET film	24.44	244.40	Sample 1: 100 μm PET film	25.50	255.00
12		19.80	198.00		22.40	224.00
13		20.70	207.00		21.00	210.00
14		23.30	233.00		22.20	222.00
15		21.60	216.00		24.90	249.00
16		22.90	229.00		21.70	217.00
17		24.70	247.00		23.20	232.00
18		23.50	235.00		21.30	213.00
19		25.70	257.00		25.90	259.00
20		23.30	233.00		25.40	254.00
21	Sample 3: 100 μm PET film	27.90	279.00	Sample 1: 100 μm PET film	24.10	241.00
22		25.00	250.00		23.50	235.00
23		25.60	256.00		25.20	252.00
24		23.70	237.00		21.50	215.00
25		23.50	235.00		20.90	209.00
26		24.70	247.00		20.70	207.00
27		24.50	245.00		22.60	226.00
28		22.20	222.00		21.40	214.00
29		22.00	220.00		23.90	239.00
30		24.80	248.00		26.10	261.00
31	Sample 4: 100 μm PET film	24.30	243.00	Sample 1: 100 μm PET film	26.30	263.00
32		23.50	235.00		23.20	232.00
33		26.10	261.00		24.40	244.00
34		25.00	250.00		23.80	238.00
35		26.00	260.00		23.60	236.00
36		24.70	247.00		23.80	238.00
37		22.90	229.00		19.50	195.00
38		20.60	206.00		22.00	220.00
39		25.10	251.00		23.40	234.00
40		23.20	232.00		21.60	216.00
Average values		**23.25**	**232.55**		**22.92**	**229.23**

Appendix A-2: Collated test result for DC breakdown test in air for epoxy resin samples of about 100 μm thicknesses.

No. of breakdowns	Sample ID	Breakdown voltage (kV)	Breakdown field (kV/mm)	Sample ID	Breakdown voltage (kV)	Breakdown field (kV/mm)
	Single layer Sample: Positive polarity test in air			**Negative polarity test in air**		
1	Sample 1: 114 μm Epoxy film	16.77	147.11	Sample 1: 110 μm Epoxy film	13.28	120.73
2		15.56	136.49		13.18	119.82
3		21.26	186.49		13.94	126.73
4		19.20	168.42		14.78	134.36
5		21.10	185.09		20.28	184.36
6		20.88	183.16		22.24	202.18
7		10.93	95.88		16.86	153.27
8		18.10	158.77		19.8	180.00
9		18.84	165.26		19.28	175.27
10		19.77	173.42		18.46	167.82
11	Sample 2: 120 μm Epoxy film	22.28	185.67	Sample 1: 100 μm Epoxy film	17.6	176.00
12		17.96	149.67		11.2	112.00
13		22.56	188.00		10.4	104.00
14		22.32	186.00		16.7	167.00
15		21.20	176.67		16.3	163.00
16		22.28	185.67		15.2	152.00
17		12.00	100.00		15.3	153.00
18		25.32	211.00		10.5	105.00
19		14.72	122.67		13.2	132.00
20		21.92	182.67		11.7	117.00
21	Sample 3: 116 μm Epoxy film	20.36	175.52	Sample 1: 105 μm Epoxy film	15.1	143.81
22		23.72	204.48		12.6	120.00
23		22.28	192.07		22	209.52
24		19.20	165.52		13.3	126.67
25		19.69	169.74		14.9	141.90
26		19.96	172.07		18.3	174.29
27		19.92	171.72		10.8	102.86
28		19.48	167.93		16.9	160.95
29		20.69	178.36		15.3	145.71
30		24.36	210.00		16.6	158.10
31	Sample 4: 115 μm Epoxy film	16.50	143.48	Sample 1: 118 μm Epoxy film	23.1	195.76
32		21.20	184.35		21.2	179.66
33		14.72	128.00		21.1	178.81
34		18.12	157.57		22.4	189.83
35		19.88	172.87		13.6	115.25
36		21.52	187.13		21.7	183.90
37		18.48	160.70		22.6	191.53
38		16.72	145.39		23.9	202.54
39		19.20	166.96		17.8	150.85
40		18.28	158.96		25.2	213.56
Average values		**19.48**	**167.52**		**16.97**	**155.78**

Appendix A-3: Collated test result for DC breakdown test in oil for epoxy resin samples of about 100 μm thicknesses.

		Single layer Sample: Positive polarity test in oil		Negative polarity test in oil		
No. of breakdowns	Sample ID	Breakdown voltage (kV)	Breakdown field (kV/mm)	Sample ID	Breakdown voltage (kV)	breakdown field (kV/mm)
1	Sample 1: 117 μm Epoxy film	30.2	258.12	Sample 1: 125 μm Epoxy film	31.4	251.20
2		31.4	268.38		30	240.00
3		34.2	292.31		32.5	260.00
4		36.2	309.40		33.2	265.60
5		32.7	279.49		29.4	235.20
6		23.2	198.29		32.1	256.80
7		36.6	312.82		32.9	263.20
8		31.6	270.09		33.5	268.00
9		19.5	166.67		31.1	248.80
10		27.6	235.90		32	256.00
11	Sample 2: 112 μm Epoxy film	23.8	212.50	Sample 2: 140 μm Epoxy film	39.4	281.43
12		37.2	332.14		40.6	290.00
13		32.5	290.18		36.1	257.86
14		29.9	266.96		30.6	218.57
15		33.6	300.00		34.2	244.29
16		32.1	286.61		35.4	252.86
17		33.3	297.32		39.5	282.14
18		28.5	254.46		36.5	260.71
19		30.6	273.21		31.9	227.86
20		24.2	216.07		32.4	231.43
21	Sample 3: 130 μm Epoxy film	27.5	211.54	Sample 3: 130 μm Epoxy film	26.4	203.08
22		26.6	204.62		27.9	214.62
23		30.1	231.54		26.7	205.38
24		28	215.38		41.2	316.92
25		35.2	270.77		40.3	310.00
26		30.4	233.85		28.2	216.92
27		30.9	237.69		23.5	180.77
28		31.5	242.31		30.5	234.62
29		28.1	216.15		21.6	166.15
30		28.4	218.46		15.5	119.23
31	Sample 4: 120 μm Epoxy film	38.7	322.50	Sample 4: 120 μm Epoxy film	29.7	247.50
32		40.6	338.33		30.6	255.00
33		29.9	249.17		32	266.67
34		39.7	330.83		28.5	237.50
35		31.7	264.17		29.4	245.00
36		34.6	288.33		26.9	224.17
37		34.2	285.00		40.5	337.50
38		36.9	307.50		41.2	343.33
39		26.5	220.83		29.2	243.33
40		35.2	293.33		31.5	262.50
Average values		**31.34**	**262.58**		**31.9**	**248.05**

Appendix A-4: Collated test result for DC breakdown test in oil for single layer epoxy resin samples of about 200 μm thicknesses.

		Single layer Sample: Positve polarity test in oil		Negative polarity test in oil		
No. of breakdowns	Sample ID	Breakdown voltage (kV)	Breakdown field (kV/mm)	Sample ID	Breakdown voltage (kV)	Breakdown field (kV/mm)
1	Sample 1: 212 μm Epoxy film	72.40	341.51	Sample 1: 195 μm Epoxy film	63.00	323.08
2		67.80	319.81		58.40	299.49
3		58.60	276.42		63.60	326.15
4		68.60	323.58		52.00	266.67
5		63.00	297.17		65.40	335.38
6		41.00	193.40		52.50	269.23
7		73.40	346.23		64.60	331.28
8		54.40	256.60		60.40	309.74
9		69.80	329.25		57.20	293.33
10		45.80	216.04		53.20	272.82
11	Sample 2: 190 μm Epoxy film	69.60	366.32	Sample 1: 200 μm Epoxy film	56.00	280.00
12		55.40	291.58		58.50	292.50
13		53.40	281.05		66.40	332.00
14		68.40	360.00		59.80	299.00
15		61.20	322.11		65.20	326.00
16		64.00	336.84		51.40	257.00
17		45.00	236.84		56.60	283.00
18		40.80	214.74		48.40	242.00
19		56.60	297.89		65.00	325.00
20		41.00	215.79		49.20	246.00
21	Sample 3: 212 μm Epoxy film	65.00	306.60	Sample 1: 208 μm Epoxy film	64.40	309.62
22		60.40	284.91		63.00	302.88
23		73.00	344.34		67.60	325.00
24		56.00	264.15		62.80	301.92
25		59.20	279.25		60.60	291.35
26		68.40	322.64		72.00	346.15
27		75.00	353.77		60.40	290.38
28		65.60	309.43		58.00	278.85
29		53.40	251.89		49.00	235.58
30		75.60	356.60		42.60	204.81
31	Sample 4: 190 μm Epoxy film	47.60	250.53	Sample 1: 208 μm Epoxy film	47.20	226.92
32		52.20	274.74		67.00	322.12
33		50.00	263.16		64.00	307.69
34		64.60	340.00		64.80	311.54
35		62.40	328.42		72.00	346.15
36		46.80	246.32		62.40	300.00
37		50.40	265.26		66.00	317.31
38		48.80	256.84		62.00	298.08
39		53.00	278.95		65.40	314.42
40		48.20	253.68		60.80	292.31
Average values		**58.65**	**291.37**		**59.97**	**295.82**

Appendix A-5: Collated test result for DC breakdown test in oil for double layer epoxy resin samples of about 200 μm thicknesses.

No. of breakdowns	Sample ID	Breakdown voltage (kV)	Breakdown field (kV/mm)	Sample ID	Breakdown voltage (kV)	Breakdown field (kV/mm)
	Double layer Sample: Positive polarity test in oil			**Negative polarity test in oil**		
i	Sample 1: 218 μm Epoxy film	69.9	320.64	Sample 1: 204 μm Epoxy film	54.8	268.63
2		48.6	222.94		64.8	317.65
3		67.2	308.26		54.6	267.65
4		57	261.47		58.6	287.25
5		51	233.94		55.2	270.59
6		72.8	333.94		58.2	285.29
7		45.2	207.34		59.2	290.20
8		65.8	301.83		61.2	300.00
9		63.2	289.91		59.6	292.16
10		60.2	276.15		64	313.73
11	Sample 2: 216 μm Epoxy film	66.8	309.26	Sample 1: 205 μm Epoxy film	57.2	279.02
12		64	296.30		57.4	280.00
13		68.8	318.52		53.2	259.51
14		72.4	335.19		59.8	291.71
15		55	254.63		62.2	303.41
16		56.6	262.04		68.8	335.61
17		60.6	280.56		53.4	260.49
18		61.4	284.26		54.4	265.37
19		55.8	258.33		50.4	245.85
20		65.8	304.63		55.8	272.20
21	Sample 3: 215 μm Epoxy film	47.2	219.53	Sample 1: 205 μm Epoxy film	63.8	311.22
22		68	316.28		65.4	319.02
23		61.4	285.58		54.6	266.34
24		55.6	258.60		57.2	279.02
25		67.2	312.56		56	273.17
26		71.2	331.16		56.8	277.07
27		45.8	213.02		51.8	252.68
28		60.6	281.86		52.4	255.61
29		41	190.70		54	263.41
30		64.2	298.60		68.8	335.61
31	Sample 4: 210 μm Epoxy film	70.8	337.14	Sample 1: 205 μm Epoxy film	58.6	285.85
32		46.2	220.00		57.8	281.95
33		55.4	263.81		49.2	240.00
34		49.4	235.24		65	317.07
35		59.6	283.81		56.4	275.12
36		43	204.76		50.6	246.83
37		56	266.67		52.2	254.63
38		44.8	213.33		54.4	265.37
39		43.8	208.57		51.8	252.68
40		65.8	313.33		55.6	271.22
Average values		**58.6275**	**272.87**		**57.38**	**280.26**

Appendix A-6: Collated test result for AC breakdown test in oil for epoxy resin samples of about 100–200 µm thicknesses.

		AC test in oil: Single layer sample ~100 µm		Single layer sample ~ 200 µm			Double layer sample ~ 200 µm		
No. of breakdowns	Sample ID	Breakdown voltage (kV)	Breakdown field (kV/mm)	Sample ID	Breakdown voltage (kV)	Breakdown field (kV/mm)	Sample ID	Breakdown voltage (kV)	Breakdown field (kV/mm)
1	Sample 1: 95 µm Epoxy film	29.00	305.26	Sample 1: 195µm Epoxy film	32.30	165.64	Sample 1: 200µm Epoxy film	37.80	189.00
2		27.80	292.63		33.40	171.28		38.00	190.00
3		29.80	313.68		37.40	191.79		37.60	188.00
4		30.20	317.89		35.00	179.49		38.80	194.00
5		29.80	313.68		34.00	174.36		39.40	197.00
6		29.40	309.47		37.30	191.28		39.80	199.00
7		29.60	311.58		35.40	181.54		40.60	203.00
8		30.40	320.00		32.00	164.10		36.80	184.00
9		29.20	307.37		35.40	181.54		33.40	167.00
10		28.00	294.74		32.10	164.62		40.20	201.00
11	Sample 2: 100 µm Epoxy film	27.60	276.00	Sample 2: 195 µm Epoxy film	40.60	208.21	Sample 2: 205 µm Epoxy film	39.20	191.22
12		29.80	298.00		40.20	206.15		40.60	198.05
13		32.20	322.00		41.00	210.26		39.00	190.24
14		29.40	294.00		35.90	184.10		40.60	198.05
15		30.80	308.00		35.60	182.56		33.00	160.98
16		30.20	302.00		31.80	163.08		40.40	197.07
17		24.40	244.00		37.30	191.28		35.60	173.66
18		30.40	304.00		38.00	194.87		38.20	186.34
19		29.60	296.00		30.20	154.87		39.20	191.22
20		30.80	308.00		38.40	196.92		40.40	197.07
21	Sample 3: 100 µm Epoxy film	24.40	244.00	Sample 3: 208 µm Epoxy film	39.60	190.38	Sample 3: 206 µm Epoxy film	36.00	174.76
22		30.20	302.00		37.80	181.73		38.40	186.41
23		30.00	300.00		40.00	192.31		35.80	173.79
24		27.40	274.00		38.30	184.13		37.00	179.61
25		30.00	300.00		36.80	176.92		37.40	181.55
26		27.60	276.00		39.90	191.83		36.60	177.67
27		28.40	284.00		31.80	152.88		37.20	180.58
28		30.80	308.00		33.70	162.02		34.20	166.02
29		28.00	280.00		39.70	190.87		37.60	182.52
30		30.80	308.00		39.00	187.50		31.60	153.40
31	Sample 4: 105 µm Epoxy film	24.80	236.19	Sample 4: 212 µm Epoxy film	38.30	180.66	Sample 4: 225µm Epoxy film	38.40	170.67
32		30.20	287.62		39.00	183.96		39.20	174.22
33		29.60	281.90		39.20	184.91		39.60	176.00
34		27.60	262.86		40.20	189.62		36.80	163.56
35		29.60	281.90		38.40	181.13		34.20	152.00
36		27.40	260.95		38.80	183.02		40.60	180.44
37		28.00	266.67		39.80	187.74		37.20	165.33
38		30.40	289.52		40.00	188.68		40.00	177.78
39		28.00	266.67		38.60	182.08		39.40	175.11
40		30.80	293.33		38.80	183.02		38.80	172.44
Average values		29.06	291.05		37.03	182.83		37.87	181.49
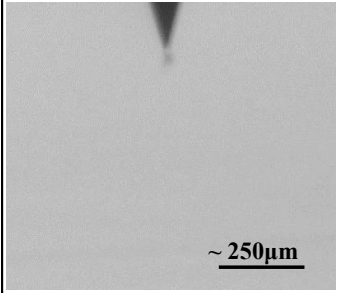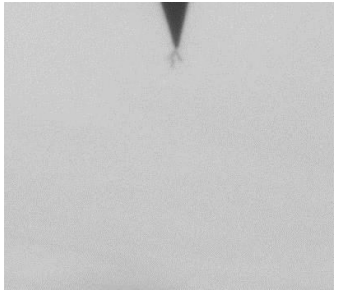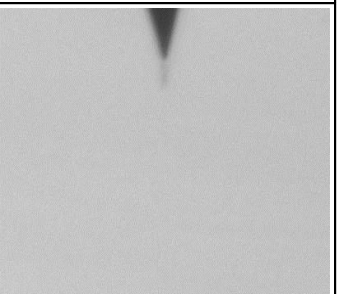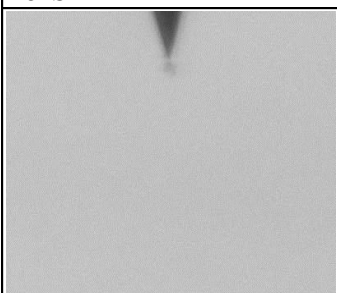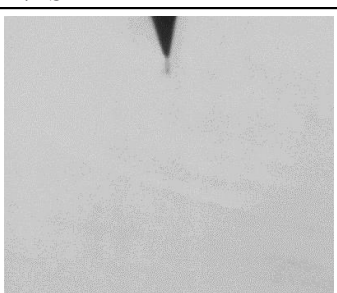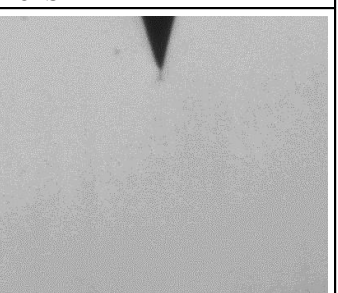
Appendix A-7: Initiation times and initial tree lengths for samples used in this study.

Quick Initiation	Sample ID	Stage 1: Tree initiation			Sample ID	Stage 1: Tree initiation			Sample ID	Stage 1: Tree initiation		
		Voltage kV(rms)	Time (min)	Tree length		Voltage kV(rms)	Time (min)	Tree length		Voltage kV(rms)	Time (min)	Tree length
AC initiation from 12kV rms	B6#S1	12	1	33	B7#S1	12	1	38	B8#S1	12	1	34
	B6#S2	12	1	25	B7#S2	12	1	27	B8#S2	12	1	28
	B6#S3	12	1	33	B7#S3	12	1	27	B8#S3	12	1	24
	B6#S4	12	1	41	B7#S4	12	1	42	B8#S4	12	1	27
	B6#S5	12	1	38	B7#S5	12	1	20	B8#S5	12	1	23
	B6#S6	12	1	41	B7#S6	12	1	43	B8#S6	12	1	37
	B6#S7	14	5	82	B7#S7	12	1	37	B8#S7	12	1	26
	B6#S8	12	1	43	B7#S8	12	1	29	B8#S8	12	1	30
	B6#S9	12	2	59	B7#S9	12	1	29	B8#S9	12	1	35
	B6#S10	12	2	49	B7#S10	12	1	18	B8#S10	12	1	18
	B6#S11	14	3	42	B7#S11	12	1	43	B8#S11	12	1	25
	B6#S12	12	1	32	B7#S12	12	1	31	B8#S12	12	1	30

Quick Initiation	Sample ID	Stage 1: Tree initiation			Sample ID	Stage 1: Tree initiation			Sample ID	Stage 1: Tree initiation		
		Voltage kV(rms)	Time (min)	Tree length		Voltage kV(rms)	Time (min)	Tree length		Voltage kV(rms)	Time (min)	Tree length
AC initiation from 12kV rms	B9#S1	12	1	33	B11#S1	14	4	28				
	B9#S2	12	1	53	B11#S2	16	9	49				
	B9#S3	12	1	38	B11#S5	12	1	40				
	B9#S4	12	1	33	B11#S8	12	1	36				
	B9#S5	12	1	52	B12#S1	12	1	29				
	B9#S6	12	1	29	B12#S3	12	1	86				
	B9#S7	12	1	23	B12#S4	12	1	70				
	B9#S8	12	1	39	B12#S5	12	1	36				
	B10#S2	12	1	89	B12#S7	16	8	41				
	B10#S4	12	1	45	B12#S9	12	1	76				
	B10#S5	12	1	33								
	B10#S6	12	1	86								

Verification tests

Sample Initiation	Sample ID	Tree initiation with 30 kV AC			Sample ID	Tree initiation with (AC+DC)			Sample ID	Tree initiation (AC-DC)		
		Voltage kV(pk)	Time (min)	Tree length		Voltage kV(pk)	Time (min)	Tree length		Voltage kV(pk)	Time (min)	Tree length
Initated samples during verificatiion tests @ 30 kV	B11#S4*	30	113	54	B13#S1	30	2	48	B14#S2	30	1	71
	B11#S10*	30	73	70	B13#S2	30	7	86	B14#S4	30	1	153
	B11#S12*	30	1	72	B13#S3	30	9	73	B14#S5	30	1	63
	B12#S2*	30	104	503	B13#S5	30	1	61	B14#S6	30	1	170
	B12#S8*	30	107	60	B13#S6	30	1	63	B14#S7	30	1	85
	B12#S10*	30	1	576	B13#S8	30	3	63	B14#S9	30	1	88
	B12#S11*	30	1	95	B13#S10	30	1	78	B14#S11	30	1	88
	B14#S1	30	1	122	B13#S11	30	2	46	B14#S12	30	1	54

* these samples did not initiate up to 16 kV rms during quick initiatin tests

Appendix A-8: Collated results from verification tests.

Experiments 1	1-stage test: Contionuos application of 30 kV peak AC from initiation for 2 hours		
AC test at 30 kV peak	Sample ID	Voltage stress time (min)	Comments
	B11#S4*	166	Sample initiated at 113 min and brokedown after 166 minutes
	B11#S12*	29	Sample initiated within 1 min and brokedown after 29 minutes
	B12#S2*	126	Sample initiated at 104 min and brokedown after 126 minutes
	B12#S11*	126	Sample initiated within 1 min and brokedown after 126 minutes
2	2-stage test: samples initiated with 30 kV peak AC and stressed with 15 kV pk AC ± 15 kV DC		
(AC+DC) test at 30 kV pk-pk	Sample ID	Voltage stress time (min)	Comments; 2-stage experiment
	B13#S2	50	Breakdown after 50 min
	B13#S5	40	Breakdown after 40 min
	B13#S8	48	Breakdown after 48 min
	B11#S8*	244	No breakdown; sample from -DC@60kV test that did not grow
	B11#S5*	153	No breakdown; sample from -DC@60kV test that did not grow
(AC-DC) test at 30 kV pk-pk	B14#S4	64	Breakdown after 64 min
	B14#S7	46	Breakdown after 46 min
	B14#S9	54	Breakdown after 54 min
	B14#S12	65	Breakdown after 65 min
	B12#S3	184	No breakdown

3	3-stage test: samples initiated with 30 kV peak AC and stressed with 15 kV pk AC ± 15 kV DC					
(AC+DC) test at 30 kV pk-pk	Sample ID	Voltage stress time (min)	Comments Stage 2	Stage 3	Voltage stress time (min)	Comments Stage 3
	B13#S1	41	to Stage 3	**AC test at 30 kV peak**	120	Stopped after 2 hours
	B13#S3	40	to Stage 3		120	Stopped after 2 hours
	B13#S6	25	to Stage 3		26	Breakdown occurred
	B13#S10	30	to Stage 3		120	
	B13#S11	41	to Stage 3		120	
(AC-DC) test at 30 kV pk-pk	B14#S2	50	to Stage 3	**AC test at 30 kV peak**	120	Stopped after 2 hours
	B14#S5	44	to Stage 3		120	BD after 2 hours
	B14#S6	47	to Stage 3		42	BD after 42 min
	B14#S11	51	to Stage 3		84	BD after 84 min
	B12#S5*	85	to Stage 3		120	Stopped after 2hrs
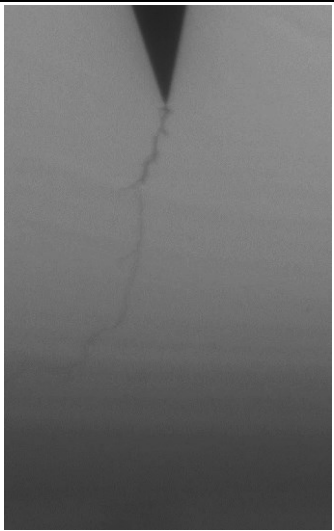
Appendix B-1: Images of AC pre-incepted initial trees.

Examples of AC pre-initiated trees		
B8#S1	B6#S2	B7#S3
~ 250μm		
B8#S4	B7#S6	B8#S8
B7#S9	B6#S10	B7#S11
B8#S12	B7#S1	B8#S2

Appendix B-2: Images of AC pre-incepted initial trees.

Examples of AC pre-Initiated trees		
B6#S1	B7#S2	B8#S3
~ **250μm**		
B6#S4	B7S4	B8S6
B7#S7	B6#S8	B8#S9
B7#S10	B6#S3	B8#S10

268
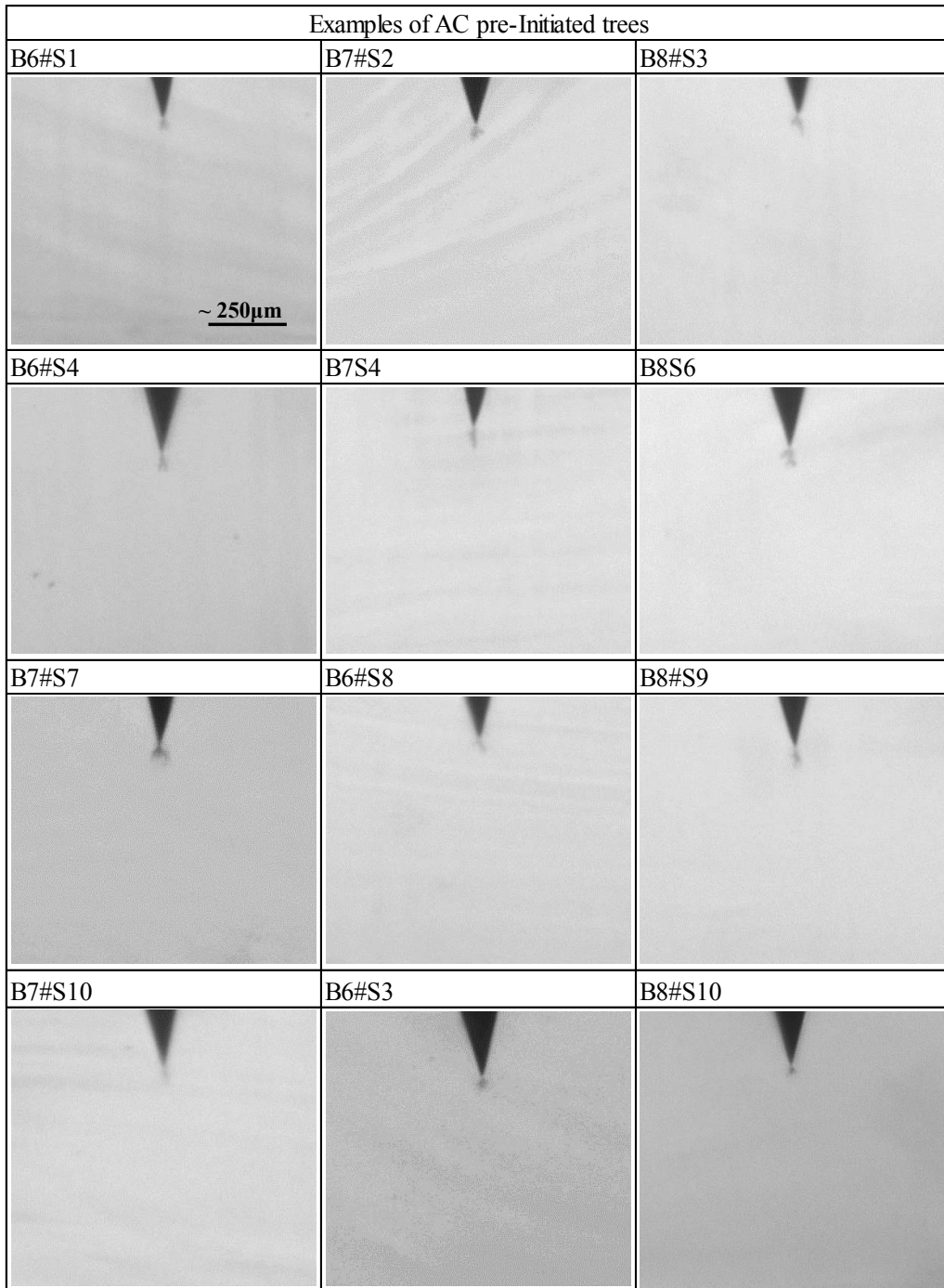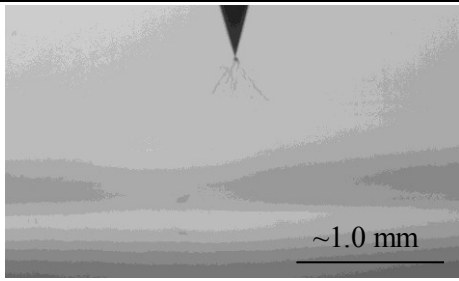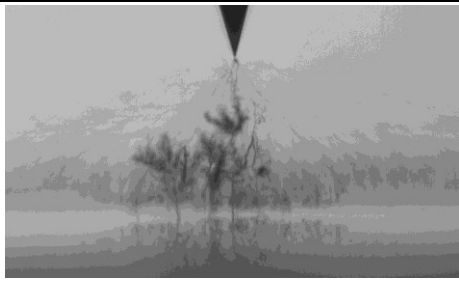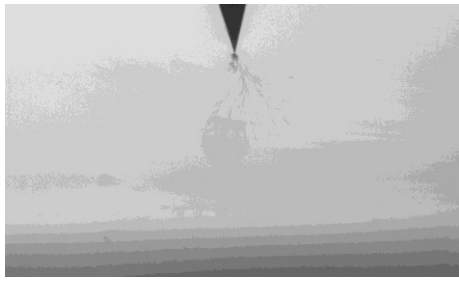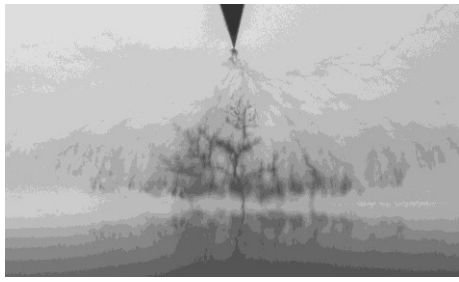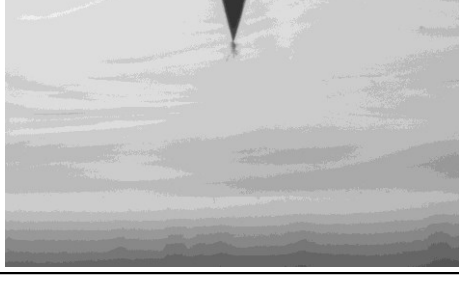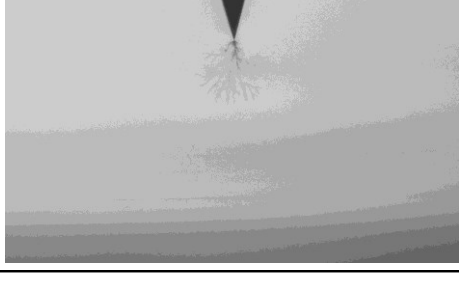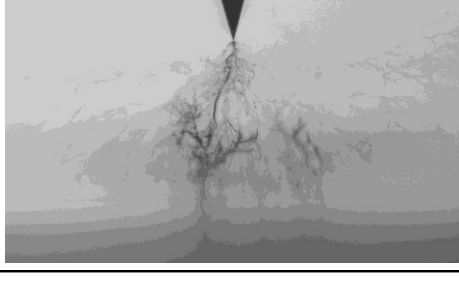
Appendix B-3: Tree images under +ve' DC test

Images of Propagated DC trees		
B9#S1_After 600 min	B10#S4_PTBD_322 min	B9#S4_After_600 min
B9#S6_After_600 min	B9#S5_PTBD_135 min	B9#S3_PTBD_271_min

Appendix B-4: Tree images under +ve' DC test

Images of Propagated DC trees		
B9#S7_After_600 min	B10#S6_PTBD_128 min	B10#S2_PTBD_92 min
B9#S8_PTBD_1 min	B9#S2_PTBD_611 min	B10#S5_PTBD_183 min

270
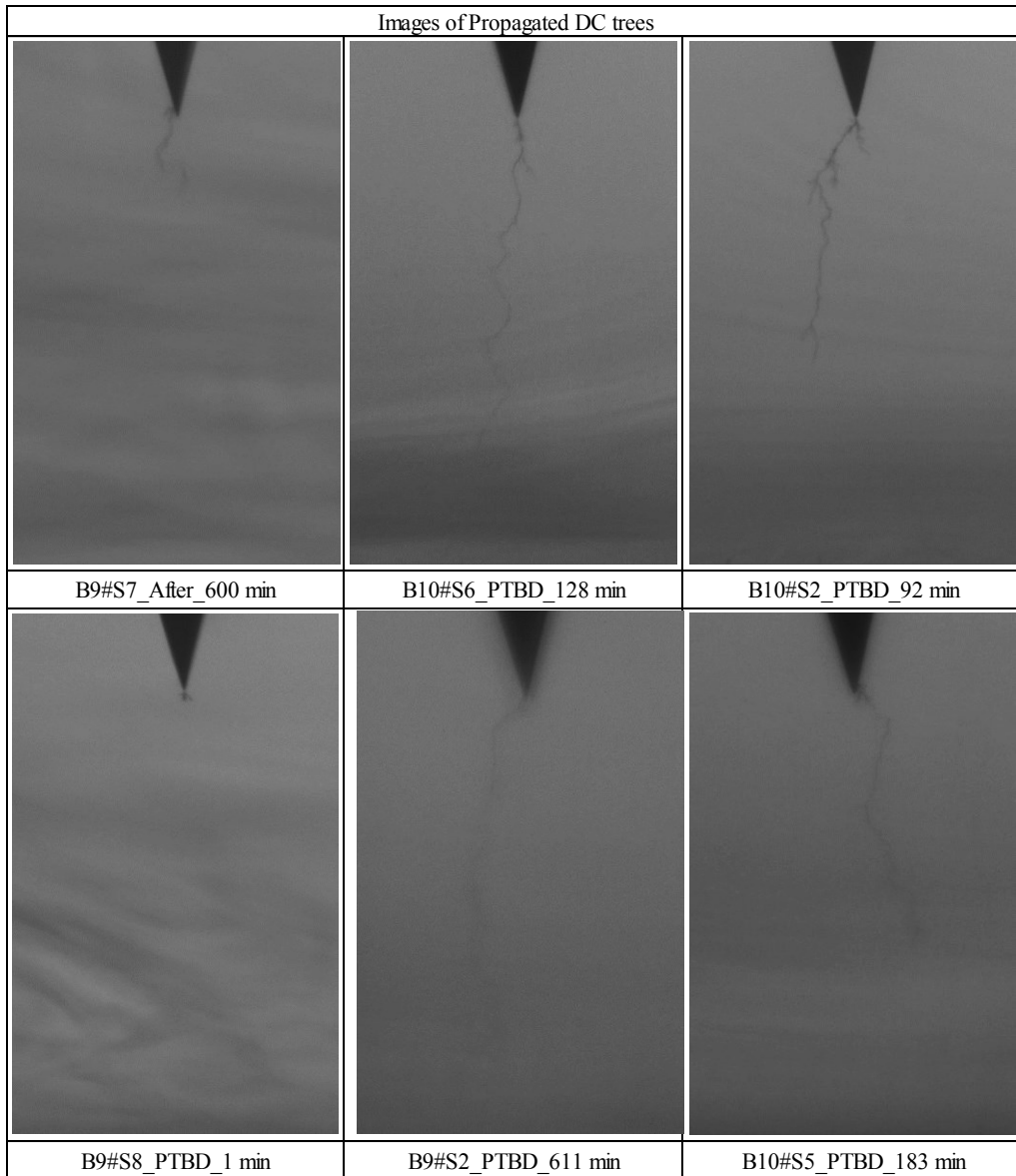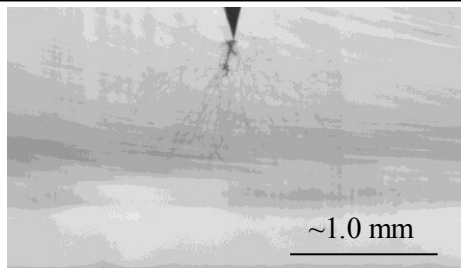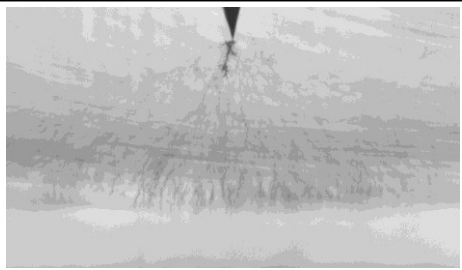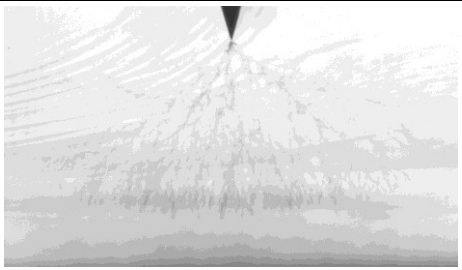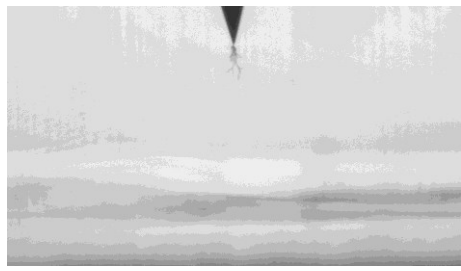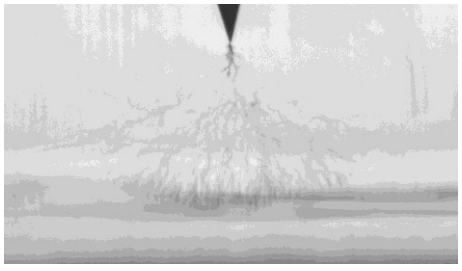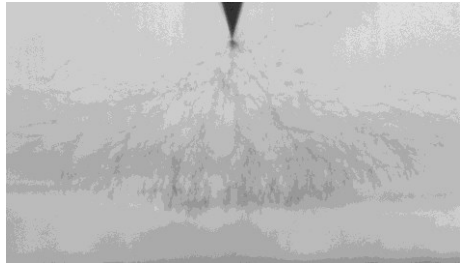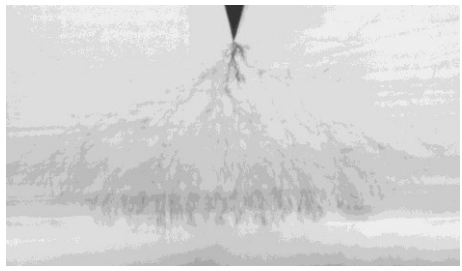
Appendix B-5: Tree images of AC test.

AC propagated trees	
~1.0 mm	
B8#S1_25 min	B8#S1_75 min
B6#S2_25 min	B6#S2_75 min
B7#S3_25 min	B7#S3_75 min
B8#S4_25 min	B8#S4_105 min
B7#S6_25 min	B7#S6_80 min
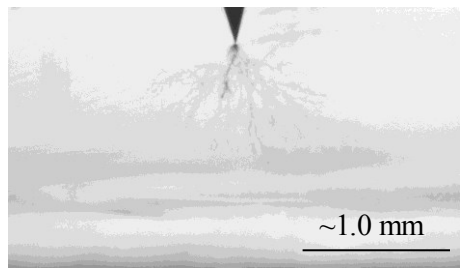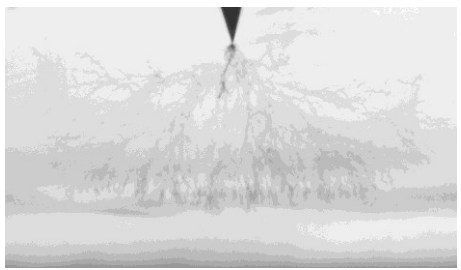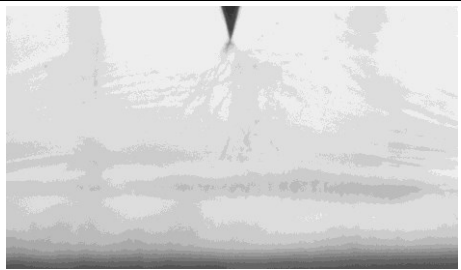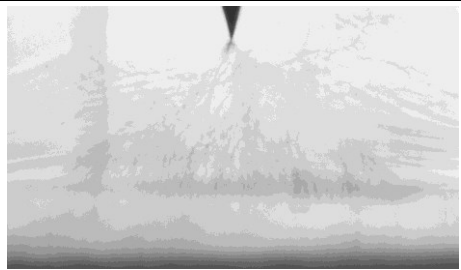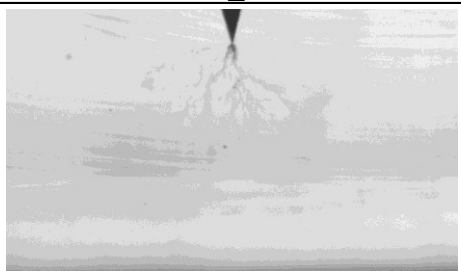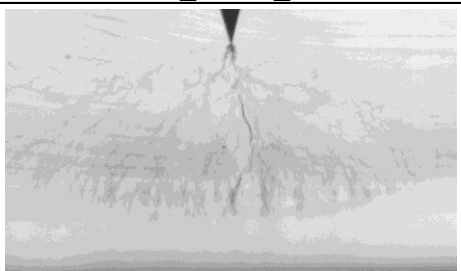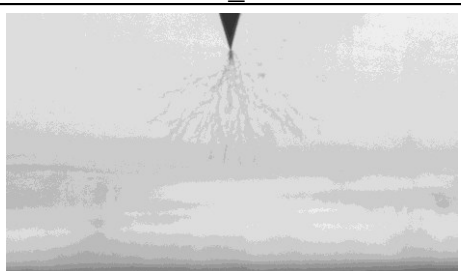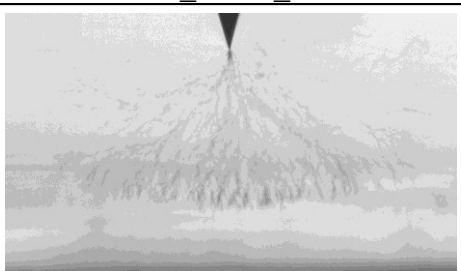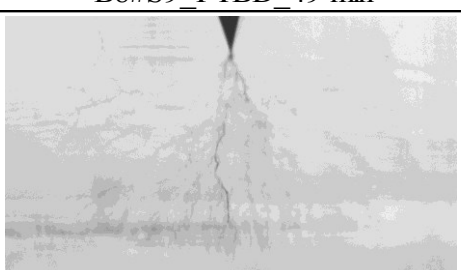
Appendix B-6: Tree images of AC test.

AC propagated trees	
~1.0 mm	
B8#S8_25 min	B8#S8_90 min
B7#S9_25 min	B7#S9_76 min
B6#S10_25 min	B6#S10_95 min
B7#S11_25 min	B7#S11_80 min
B8#S12_25 min	B8#S12_125 min
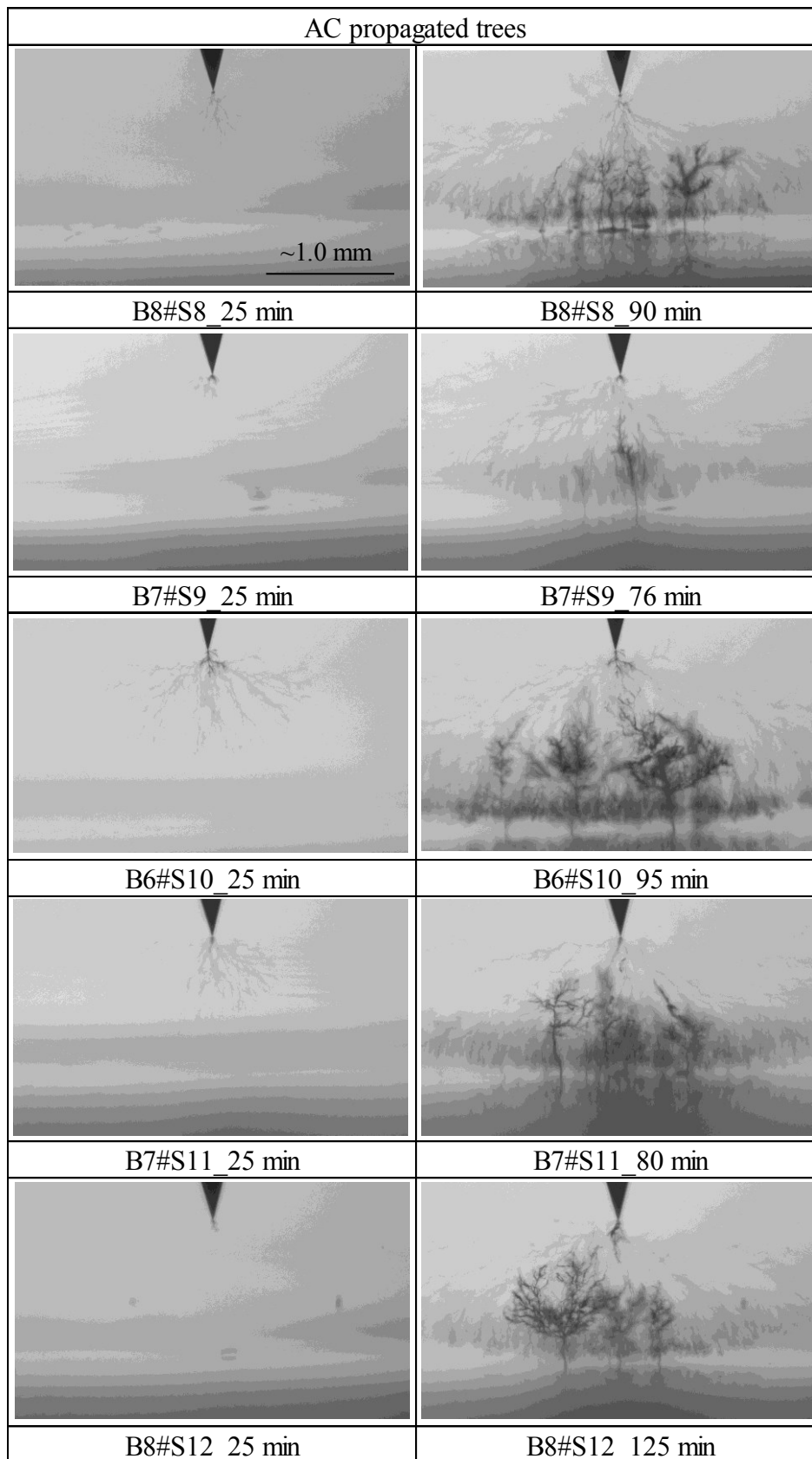
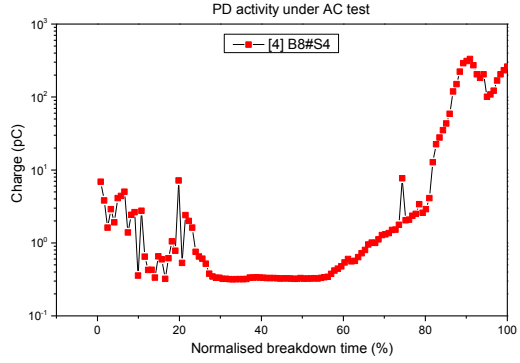# Appendix B-7: Tree images of AC superimposed +ve′ DC test.

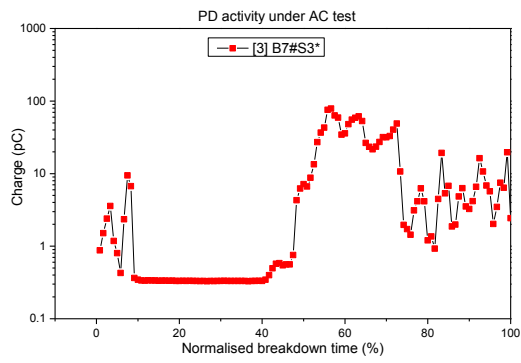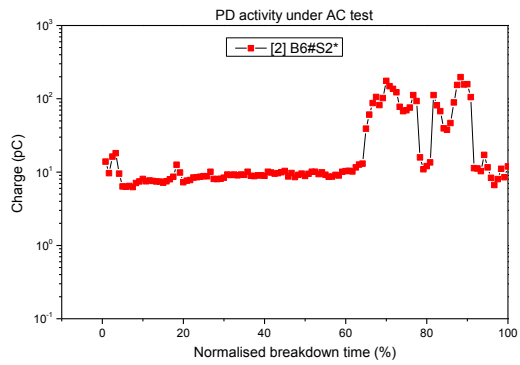| (AC+DC) propagated trees	
~1.0 mm	
B6#S1_25 min	B6#S1_PTBD_51 min
B7#S2_25 min	B7#S2_PTBD_53 min
B8#S3_25 min	B8#S3_PTBD_56 min
B6#S4_25 min	B6#S4_PTBD_69 min
B7#S5_25 min	B7#S5_PTBD_54 min

Appendix B-8: Tree images of AC superimposed +ve' DC test.

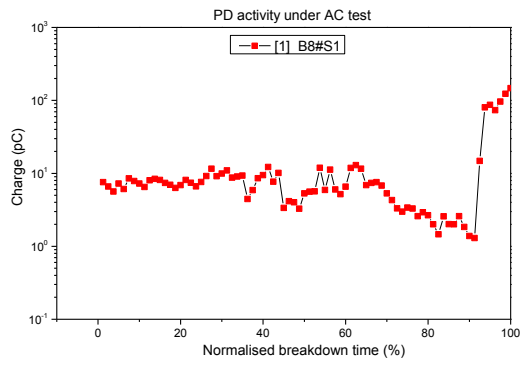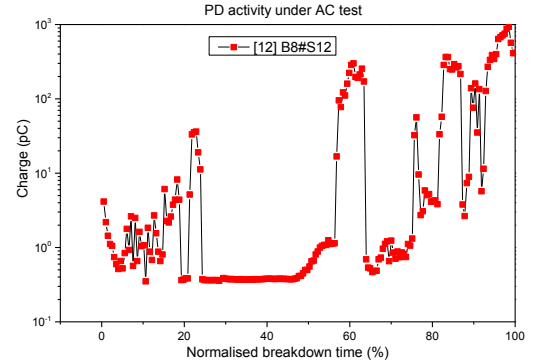| (AC+DC) propagated trees	
~1.0 mm	
B8#S6_25 min	B8#S6_PTBD_46 min
B7#S7_25 min	B7#S7_PTBD_45 min
B6#S8_25 min	B6#S8_PTBD_56 min
B8#S9_25 min	B8#S9_PTBD_49 min
B7#S10_25 min	B7#S10_PTBD_54 min

Appendix B-9: Tree images of AC superimposed –ve' DC test

(AC-DC) propagated trees	
B7#S1_25 min	B7#S1_PTBD_57 min
B8#S2_25 min	B8#S2_PTBD_46 min
B6#S3_25 min	B6#S3_PTBD_76 min
B7#S4_25 min	B7#S4_PTBD_66 min
B8#S5_25 min	B8#S5_PTBD_54 min

~1.0 mm
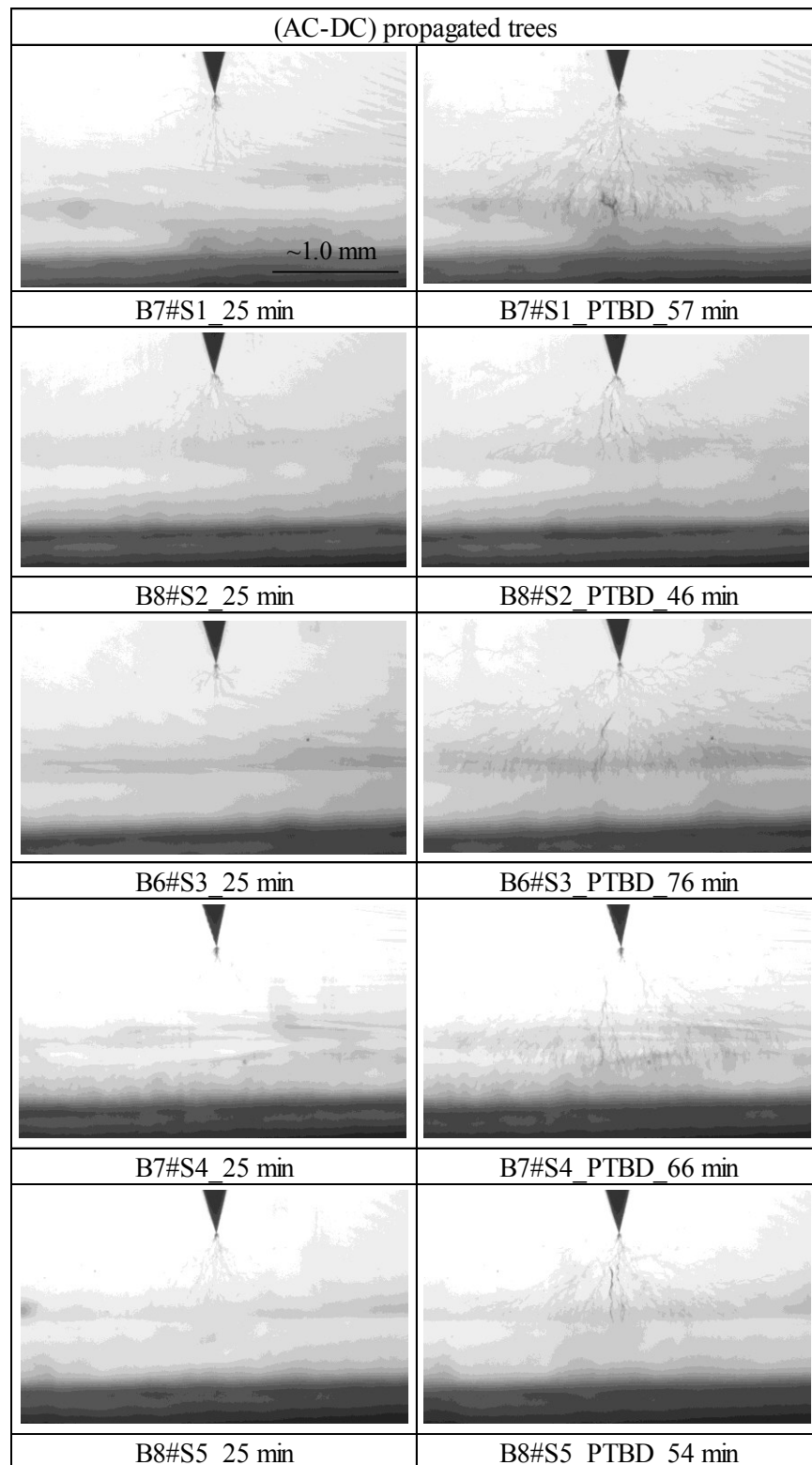
Appendix B-10: Tree images of AC superimposed –ve' DC test

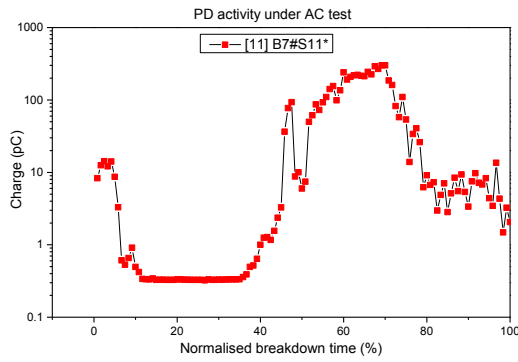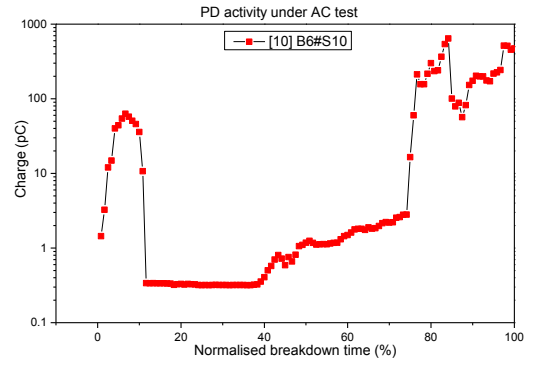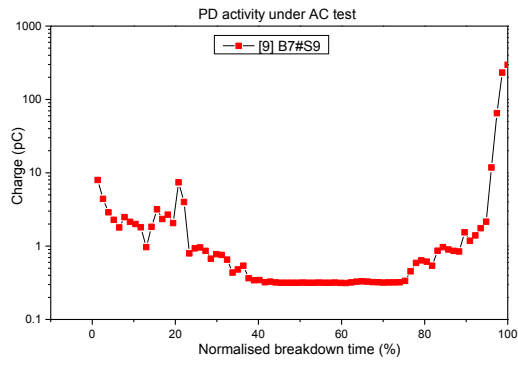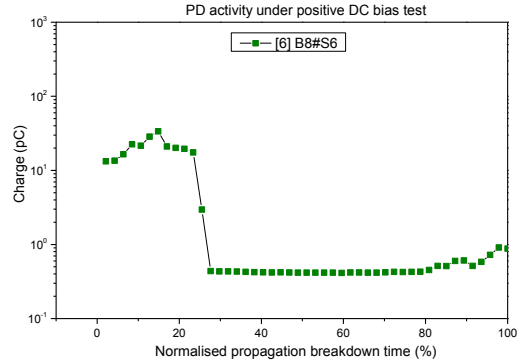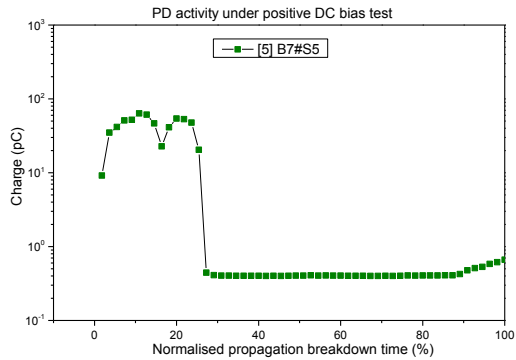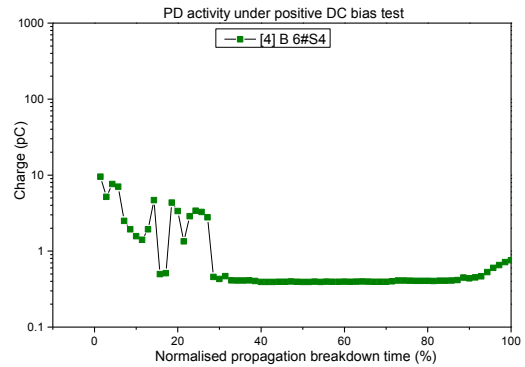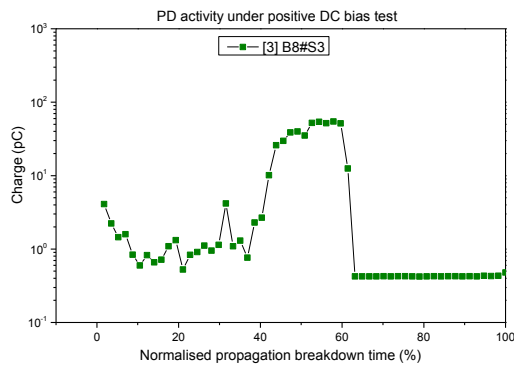| (AC-DC) propagated trees	
B6#S6_25 min	B6#S6_PTBD_74 min
B8#S7_25 min	B8#S7_PTBD_69 min
B7#S8_25 min	B7#S8_PTBD_184 min
B6#S9_25 min	B6#S9_PTBD_54 min
B8#S10_25 min	B8#S10_PTBD_91 min

~1.0 mm
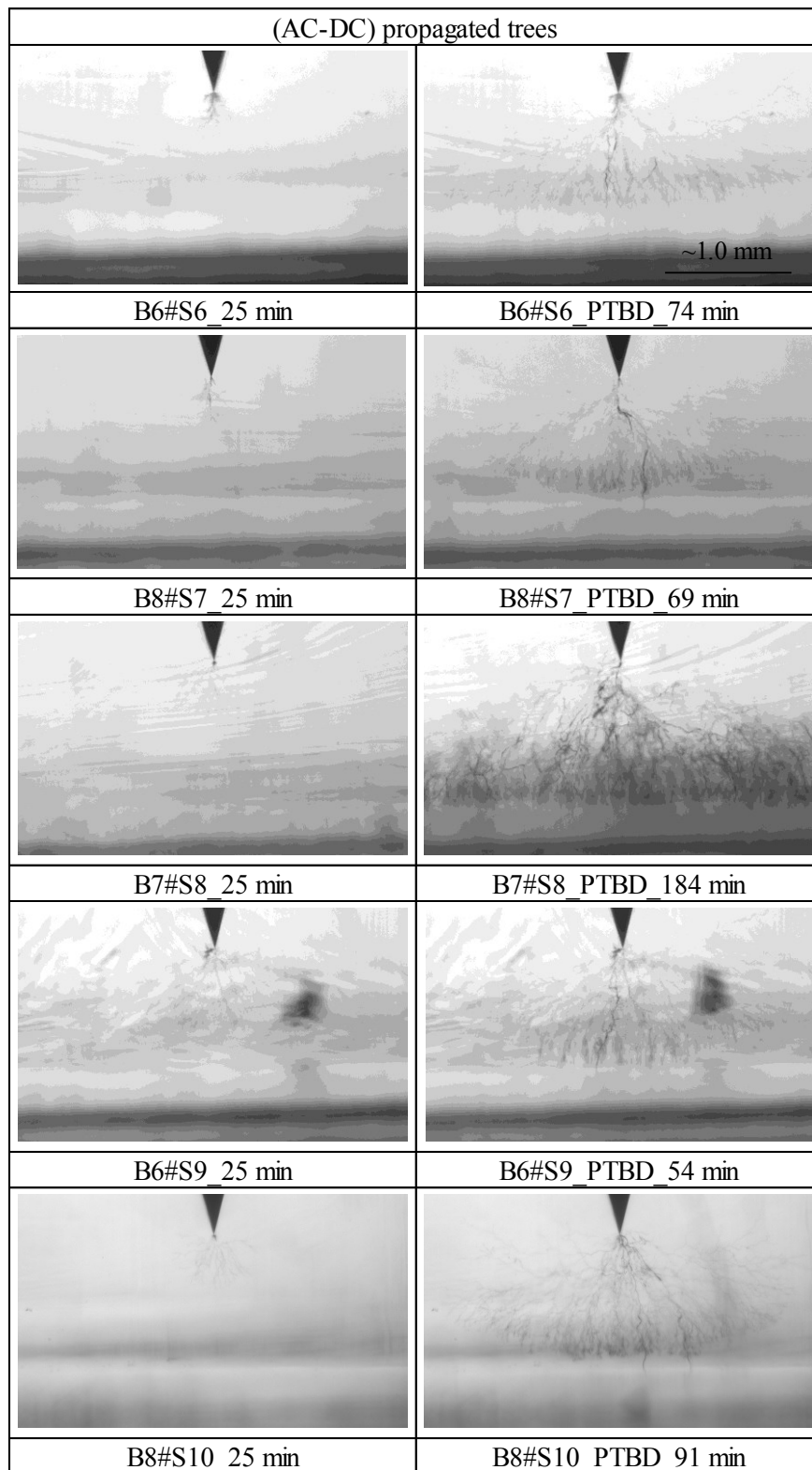
Appendix B-11: Typical examples of breakdown channels

Typical breakdown channels

Example 1	Example 1
Example 1	Example 1
Example 1	Example 1
Example 1	Example 1
Example 1	Example 1
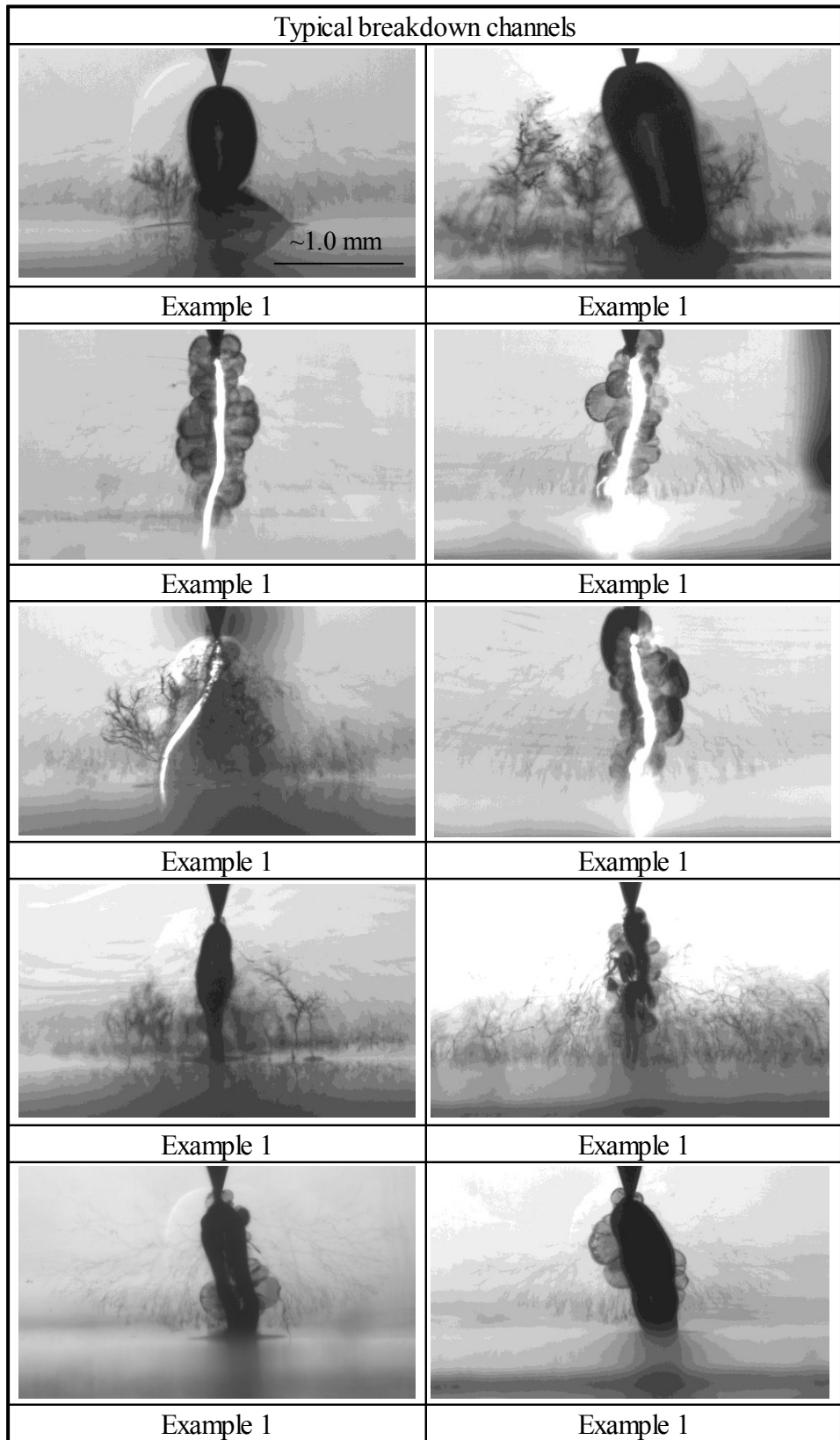
Appendix C-1: Individual PD plots under AC tests

PD activity under AC test — [1] B8#S1

PD activity under AC test — [2] B6#S2*

PD activity under AC test — [3] B7#S3*

PD activity under AC test — [4] B8#S4

PD activity under AC test — [6] B7#S6

PD activity under AC test — [8] B8#S8

PD activity under AC test — [9] B7#S9

PD activity under AC test — [10] B6#S10

PD activity under AC test — [11] B7#S11*

PD activity under AC test — [12] B8#S12

279
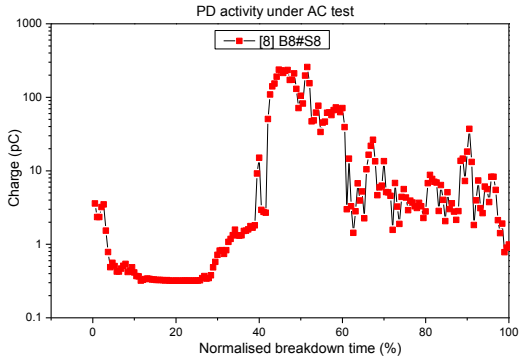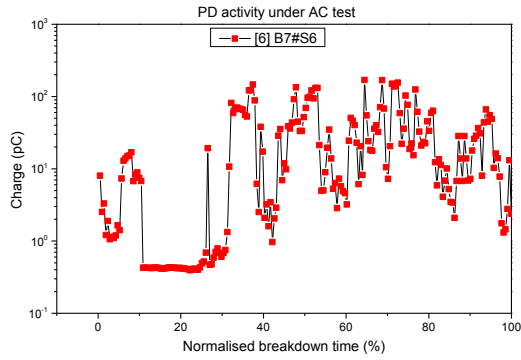
Appendix C-2: Individual PD plots under positive DC bias test

PD activity under positive DC bias test — [1] B6#S1

PD activity under positive DC bias test — [2] B7#S2

PD activity under positive DC bias test — [3] B8#S3

PD activity under positive DC bias test — [4] B 6#S4

PD activity under positive DC bias test — [5] B7#S5

PD activity under positive DC bias test — [6] B8#S6

PD activity under positive DC bias test — [7] B7#S7

PD activity under positive DC bias test — [8] B6#S8

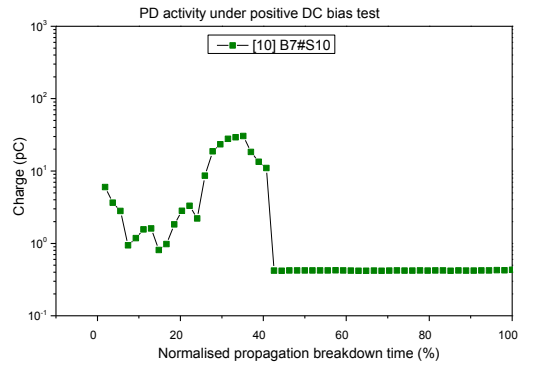PD activity under positive DC bias test — [9] B8#S9

PD activity under positive DC bias test — [10] B7#S10

Appendix C-3: Individual PD plots under negative DC bias test

PD activity under negative DC bias test — [4] B7#S4

PD activity under negative DC bias test — [5] B8#S5

PD activity under negative DC bias test — [6] B6#S6

PD activity under negative DC bias test — [7] B8#S7

PD activity under negative DC bias test — [8] B7#S8

PD activity under negative DC bias test — [9] B6#S9

PD activity under negative DC bias test — [10] B8#S10
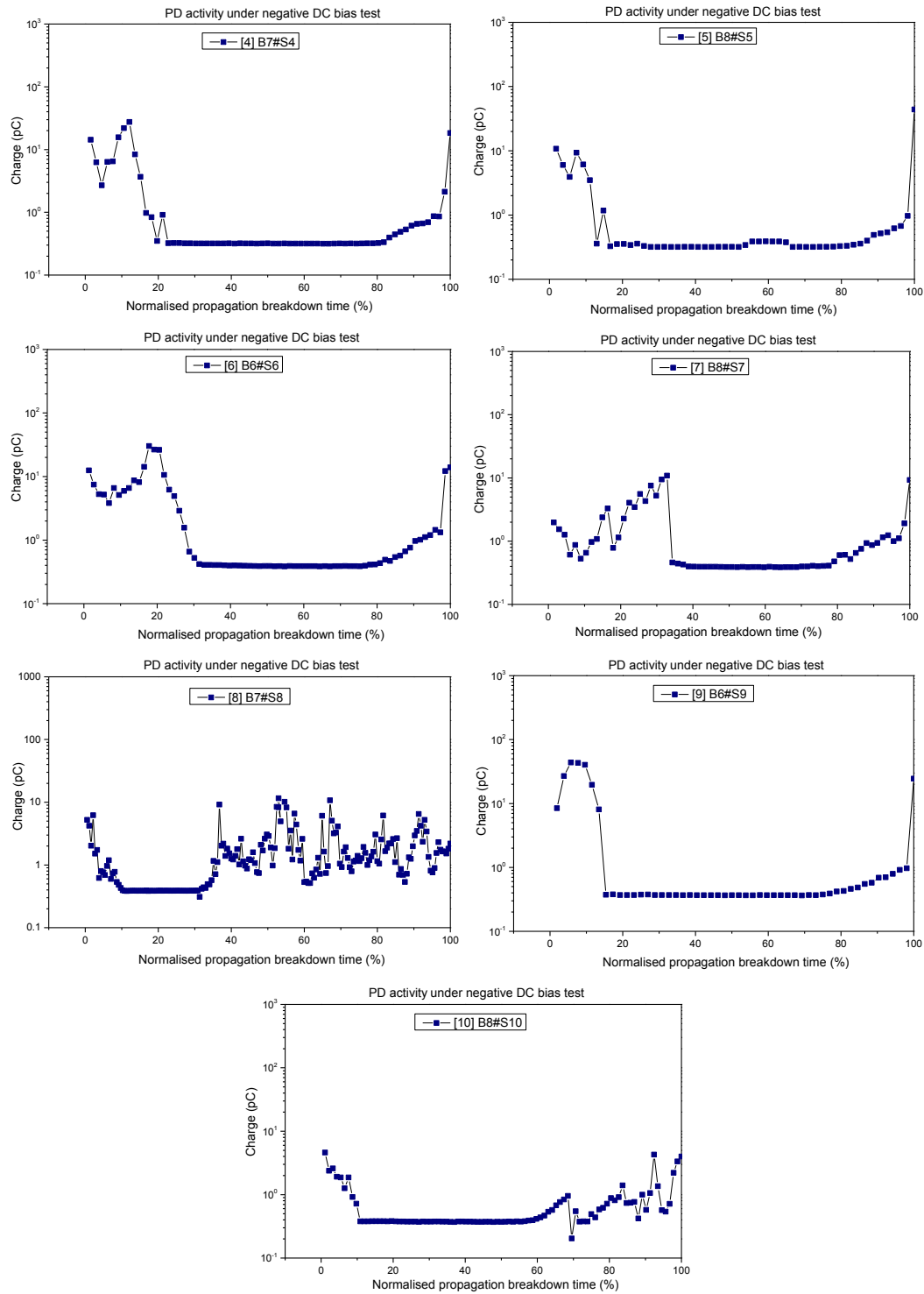
Appendix D: List of Publications

[1] **I. Iddrissu**, S. M. Rowland, and A. Tzimas, "The Impact of Interfaces and Space   Charge Formation on Breakdown Strength of Epoxy Resin," in *IEEE Annual Conference on Electrical Insulation and Dielectric Phenomena (CEIDP)*, 2014, pp. 90–93.

[2] **I. Iddrissu** and S. M. Rowland, "The Impact of DC Bias on Electrical Tree Growth Characteristics in Epoxy Resin Samples," in *IEEE Annual Conference on Electrical Insulation and Dielectric Phenomena (CEIDP)*, 2015, vol. 1, pp. 876–879.

[3] **I. Iddrissu**, H. Zehng, and S. M. Rowlan, "Electrical tree growth in epoxy resin under DC voltages," *Accepted for publication in IEEE International Conference on Dielectrics* (ICD) 2016.

[4] **I. Iddrissu**, Z. LV, and S. M. Rowlan, "The dynamic characters of partial discharge in epoxy resin at different stages of treeing," *Accepted for publication in IEEE International Confererence on Dielectrics* (ICD) 2016.